CISM International Centre for Mechanical Sciences 547
Courses and Lectures

Richard V. Craster
Julius Kaplunov
Editors

Dynamic Localization Phenomena in Elasticity, Acoustics and Electromagnetism

International Centre for Mechanical Sciences

Springer

CISM Courses and Lectures

Series Editors:

The Rectors
Friedrich Pfeiffer - Munich
Franz G. Rammerstorfer - Wien
Elisabeth Guazzelli - Marseille

The Secretary General
Bernhard Schrefler - Padua

Executive Editor
Paolo Serafini - Udine

The series presents lecture notes, monographs, edited works and proceedings in the field of Mechanics, Engineering, Computer Science and Applied Mathematics.
Purpose of the series is to make known in the international scientific and technical community results obtained in some of the activities organized by CISM, the International Centre for Mechanical Sciences.

International Centre for Mechanical Sciences

Courses and Lectures Vol. 547

For further volumes:
www.springer.com/series/76

Richard V. Craster · Julius Kaplunov
Editors

Dynamic Localization Phenomena in Elasticity, Acoustics and Electromagnetism

Springer

Editors

Richard V. Craster
Imperial College London

Julius Kaplunov
Keele University United Kingdom

ISSN 0254-1971
ISBN 978-3-7091-1618-0 ISBN 978-3-7091-1619-7 (eBook)
DOI 10.1007/978-3-7091-1619-7
Springer Wien Heidelberg New York Dordrecht London

All contributions have been typeset by the authors
Printed in Italy

Printed on acid-free paper

Springer is part of Springer Science+Business Media (www.springer.com)

PREFACE

A revolution is currently occurring in physics and engineering through the manufacture and application of smart structures with designer microstructure. Many of the applications: cloaking, invisibility, trapped and defect modes, resonances, ultra-refraction, all-angle-negative refraction, wave guiding along surfaces depend upon subtle properties of wave localization and are ubiquitous across several fields: examples are drawn from elasticity, acoustics and electromagnetism. There are also numerous applications in more traditional fields such as the non-destructive evaluation and testing of structures. For example, prestresses or coatings on elastic media can be used to manipulate surface and edge waves, and localized modes arise in coated or deformed waveguides and are modified by fluid flow. In addition, surface and guided waves play a key role in crack and flaw detection and a knowledge of surface and resonant modes is invaluable. Recent work has highlighted how localized defect modes arise in microstructured media and new homogenization theories can be used to create continuum descriptions of micromechanical systems, even at high frequencies.

The aim of these lecture notes is to introduce an interdisciplinary audience to a variety of interrelated dynamic localisation phenomena occurring in elasticity, acoustic and electromagnetism. In particular, these involve surface and edge waves and also trapped modes localised near defects, shape changes and the edges of elongated waveguides. The effects of layering, prestress, anisotropy, periodic microstructures as well as various multi-field phenomena are addressed with referencing to underlying industrial problems.

The course covered a wide range of subjects/techniques related to dynamic localisation phenomena. In particular, these includes asymptotic and perturbation methods, modern homogenization methodologies, variational methods, basics of non-linear elasticity, the general theory of surface waves, multimodal approach, and advanced applications of St Venant principle. The objective of the lectures is to cover the essential and up to date numerical, asymptotic, and analytical techniques as well as relevant continuum theories that are required to make progress in, and understand, wave localization and allied ef-

fects. A major focus is on the qualitative physical insight into the mechanisms of dynamic localisation.

The lectures were chosen to appeal to researchers, primarily but not exclusively graduate students and postdoctoral researchers, from Mechanical, Aerospace and Civil Engineering programs and should naturally also be of interest to Physicists and Applied Mathematicians and focus on recent work in localized modes and waves that are unlikely to appear in traditional university graduate courses; the lectures are also suitable for industrial researchers who encounter resonant or localised waves. The topics explore the applications in Engineering and Physics, notably in photonics, showing the interconnections with acoustics and elasticity that are normally treated independently. Both theoreticians and experimentalists are expected to gain useful knowledge from these lecture notes.

Richard Craster and Julius Kaplunov

CONTENTS

Modelling microstructured media: periodic systems and effective media

R. V. Craster & M. Makwana *

Abstract My aim in these lectures is to give a broad overview of the Mathematics and Physics of perfectly periodic systems, drawing heavily upon the literature of solid-state physics: it is essential to understand how structure on a micro-scale affects longer scale macro-scale behaviour and periodic systems are a naturally place to begin. Periodic systems are, on one hand, quite special and the constructive interference created by periodicity leads to strong effects that we shall see later, but on the other hand many natural and man-made structures exhibit, at least some, general periodic structure. After developing the language of periodic systems we will turn our attention to the development of asymptotic "effective" media that are posed entirely upon the macro-scale. Importantly we will develop asymptotic theories valid at high frequencies. A general approach valid for continua, semi-discrete (frame) and fully discrete (mass-spring) systems will be developed. If time allows we will then look further into some of the remarkable physics that can be seen when waves move through structured media: defect states, all-angle negative refraction and ultra-refraction.

1 Motivation

Periodic, or almost periodic, structures surround us and are of considerable technological importance. One of the most talked about materials at the moment is graphene, an almost perfect material constructed from a hexagonal lattice and graphene has truly remarkable properties some of which are related to the properties of the waves that pass through it. Many atomistic systems are remarkably regular in their structure mainly due to the energetic arguments that force the material to adopt such regular patterns. The attraction of one atom to its neighbour, or neighbours, can be modelled by discrete mass-string models with the physics of the attraction lumped into some effective string constants. Historically the study of perfect lattice-like systems originated in solid-state physics and a huge amount of effort and

*Department of Mathematics, Imperial College, London, SW7 2AZ, U.K.

R. Craster, J. Kaplunov (Eds.), *Dynamic Localization Phenomena in Elasticity, Acoustics and Electromagnetism*, CISM International Centre for Mechanical Sciences,
DOI 10.1007/978-3-7091-1619-7_1, © CISM, Udine 2013

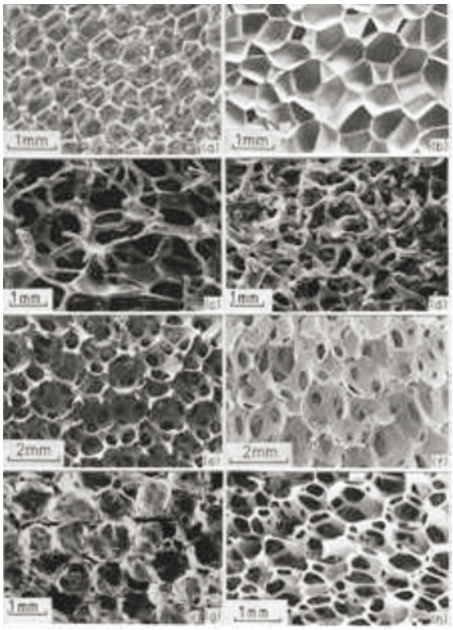

Figure 1: Photographs of cellular solids: (a) open-cell polyurethane (b) closed-cell polyurethane (c) nickel (d) copper (e) zirconia (f) mullite (g) glass (h) a polyether foam with both open and closed cells. Taken from the book of Gibson and Ashby [8].

scientific progress was made in that area: This is fortunate as we can then use that accumulated knowledge! The books of Kittel [11] and Brillouin [4] are the classical texts in this area and we will draw upon them in these lectures. It is also notable that considerable effort went into the properties of atomic systems with defects, i.e extra atoms or disruption/ disorder in the atomic structure [1].

Shifting to, yet, another area, that is, structural mechanics and designer materials one finds that the subjects of solid mechanics also abound with structured media. Cellular solids, engineering foams, or panels, created from honeycomb lattices are popular in industry for their lightweight, but strong, properties. A typical range of engineering foams are shown in Fig. 1, taken from [8], and although not perfectly regular, they still retain some periodic and regular structure. Once again waves passing through such a

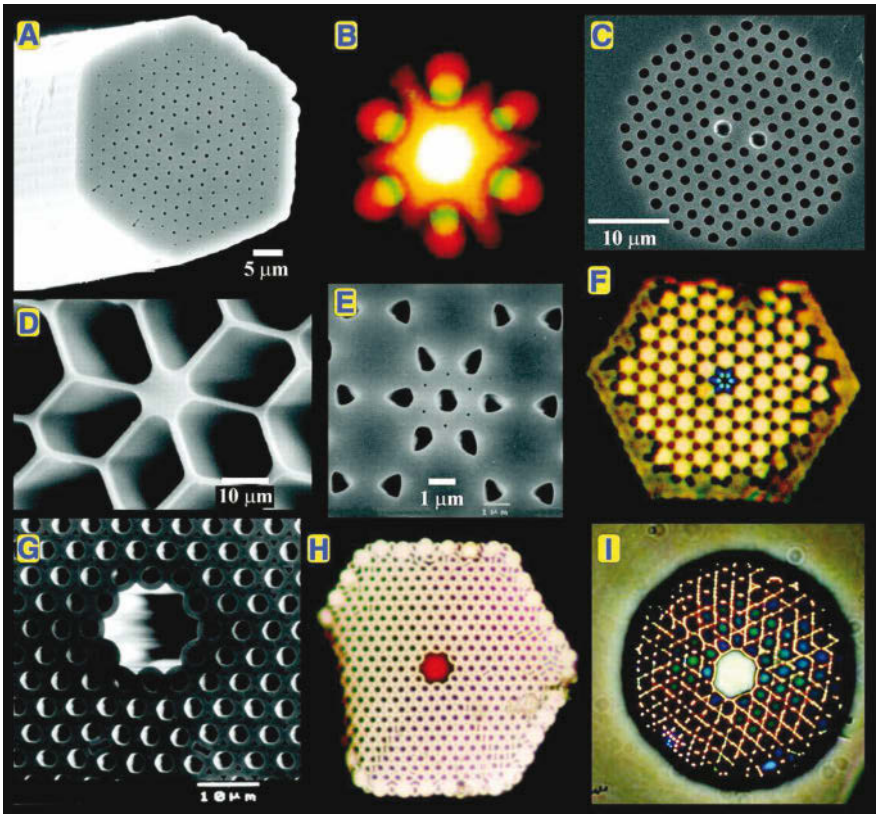

Figure 2: Micrographs of various Photonic Crystal Fibre structures taken from the review of Russell et al [15]. The regular array of holes allow for excellent (low-loss) waveguides in optics and have a host of applications: sensors, high bandwidth guides, optical filters.

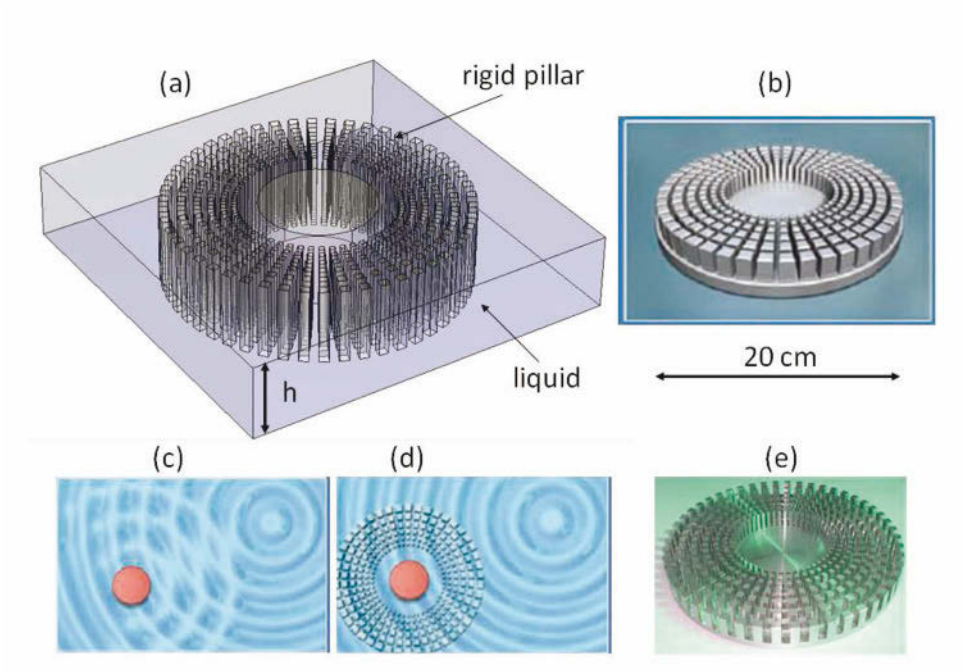

Figure 3: A water wave cloak: (a) Geometry of the structured cloak consisting of concentric arrays of rigid pillars immersed in a vessel of liquid of depth h; (b) Diagrammatic view of the cloak; (c-d) Scattering of water waves on a rigid obstacle (red disc) without (c) and with (d) the water wave cloak; (e) Photo of the micro-structured cloak used in experiments around 10 Hertz. Figure taken from [9].

structure are of interest, for instance, can one determine where or whether the honeycomb has sustained damage or whether some ligaments are broken. Similarly many buildings, bridges, roofs and other structures are created from a frame of beams or trusses, a famous example is the Eiffel tower and a common Civil Engineering task is to find the modes of vibration of such a structure in, for instance, Earthquake resistant design. Cellular microstructures also underlie many continuum models in micromechanics [14].

Modern physics and the new subjects of photonics and metamaterials utilise the properties of structured media to create the remarkable effects of cloaking, negative refraction, subwavelength imaging and almost perfect guiding, optical filtering, designer surfaces and much more. A selection of photonic crystal fibres are shown in Fig. 2, taken from [15], and interestingly, from our point of view, they consist of a large number of holes in a matrix material - all equally spaced - but with one or more holes filled, moved, or removed. So the structure is certainly not infinitely periodic, but has some features that are clearly regular. Later we will see that there exist, so-called, stop-bands which are windows of frequencies in which waves do not propagate through a perfect material: However, the destruction of perfect periodicity through the introduction, or removal, of additional features can create defect or localised modes. These modes only occur for single frequencies within the stop-band and thereby allow only specific waves to propagate. This striking result allows one to create very precise guiding structures which allow light to be controlled accurately - the books [10; 17] contain considerable discussion and demonstration of this.

Metamaterials are similarly dominated by the optics of structured media, actually it does not have to limited to optics as similar effects can be engineered in other wave systems such as acoustics or in water-waves. In the latter system, recent experiments have verified the efficacy of these cloaking systems and a recent example is shown in figure 3 taken from the book [9]. Quite incredibly one can make a piece of space, and whatever is enclosed by it, invisible to incoming waves - the lectures by Sebastien Guenneau will be covering this, and other exciting areas of metamaterials, and I do not want to encroach upon this, bar to say that clearly that understanding and modelling structured media is clearly important in that setting too.

There are three classes of structure of increasing technical difficulty and complexity: Completely discrete media created from point masses connected by conceptual springs, then semi-discrete frames, nets or trusses joined at points but these points are connected via strings or elastic beams that satisfy ordinary differential equations and finally fully continuum systems where, say, for holes in a photonic crystal the electromagetic waves obey Maxwell's

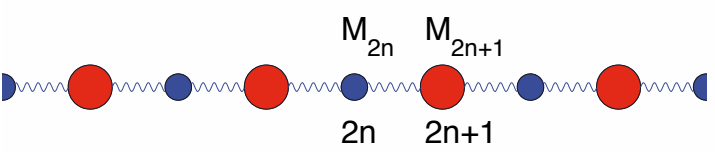

Figure 4: A chain of masses - the classical linear diatomic chain.

equations. In terms of the physics associated with microstructure one can go a long way in understanding the techniques and how the dominant physics can be encapsulated in a model by using the simplest, discrete, systems as "toy" problems. In these lectures I will endeavour to keep the Mathematics simple, and not obfuscate the physical ideas, and therefore the discrete systems are the toys of choice.

A key observation for all the motivational examples chosen is that there is a very regular structure on a small-scale, and that one might be interested in hundreds, thousands or even millions or repeating elementary cells, but that one would ideally be interested in modelling behaviour on some macro-scale. There is a potentially huge disparity in length-scales which one would wish to exploit in any asymptotic modelling. Another key observation is that there are actually three lengthscales in the problem: the micro-scale of the elementary cell, the macro-scale of the whole structure and finally the wavelength of oscillations we are interested in. Considerations of whether the waves are long relative to the elementary cell or short, so multiple scattering occurs, are important.

2 Perfect, infinite, systems

We begin by exploring the properties of the simplest periodic structures: linear chains, of which the diatomic chain is shown Figure 4 with the atoms interacting via nearest neighbour interactions; this is an oversimplification of the real atomic situation but rather good as a toy model that describes the essential features one expects to see. This is a toy model of salt, NaCl, in which there are two alternating atoms, Sodium and Chlorine, and one can label the displacements of each atom by y_{2n}, y_{2n+1} with the even and odd masses M_{2n}, M_{2n+1} taking values M_2, M_1 respectively. Scaling out the spring constants, and assuming nearest neighbour interactions one arrives at a model system:

$$y_{2n-1} + y_{2n+1} - 2y_{2n} = -\Omega^2 M_2 y_{2n} \tag{1}$$

$$y_{2n} + y_{2n+2} - 2y_{2n+1} = -\Omega^2 M_1 y_{2n+1} \tag{2}$$

where Ω is the wave frequency. Note that it is implicit that the time dependence of the system is $\exp(-i\Omega t)$. The difference equations simplify even further if we consider equal masses and then there is a single difference equation to consider:

$$y_{n+1} + y_{n-1} - 2y_n = -M\Omega^2 y_n. \tag{3}$$

Provided the lattice is infinite, and perfectly periodic, one can sidestep the explicit solution of the difference equation and instead pose quasi-periodic conditions. We simply consider one mass and say that as a wave moves from one mass to the next it undergoes a phase-shift, κ, so that

$$y_{n+1} = \exp(i\kappa) y_n. \tag{4}$$

This phase-shift can be interpreted as a wavenumber and it is often called the Bloch wavenumber and the quasi-periodic condition (4) is called a Bloch condition: It is more historically fair to call these Floquet-Bloch conditions, as a digresion Floquet proved one-dimensional results later generalised to three-dimensions by Bloch and often in one-dimension Floquet's name is used. The wave frequency Ω is related to the Bloch wavenumber κ via a dispersion relation

$$\Omega = \frac{2}{\sqrt{M}} \sin\left(\frac{\kappa}{2}\right). \tag{5}$$

Just to recall: dispersionless waves have the phase and group velocities equal and most linear wave systems such as those of acoustics, electromagnetism and elasticity have this property. One can see that in the limit of small wavenumber, long waves and low frequencies that equation (5) reduces to

$$\Omega \sim \frac{\kappa}{\sqrt{M}} \tag{6}$$

which is a linear relation and therefore the waves, in that limit, are dispersionless.

For the simple chain the dispersion relation is shown in Figure 5(a) from which we can see the relation is clearly non-linear - also shown are the asymptotics from homogenization theories.

To whet your appetite for how an "effective" medium would describe a large number of masses let us generate a continuum description of the discrete system in the long-wave, low frequency limit. We begin by introducing a long-scale continuous variable $\eta = \varepsilon n$ where ε is some small parameter, if

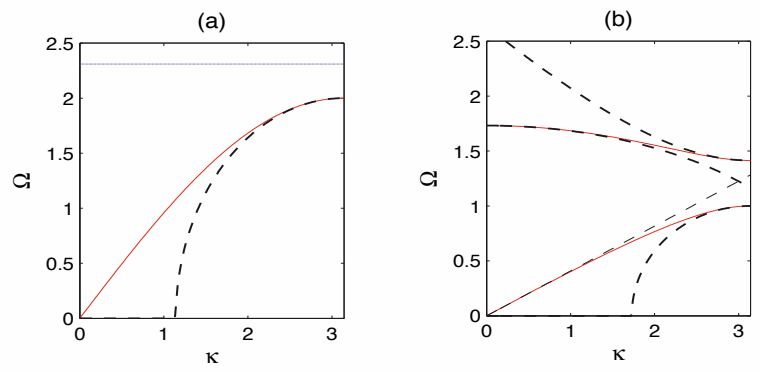

Figure 5: Dispersion curves for the one-dimensional uniform lattice, (a) and the diatomic lattice (b). The exact dispersion curves are the solid lines whilst the asymptotics in (a) and from [7] in (b)) of the perfect lattice are the dashed lines. In panel (a) the dashed line above the exact curve shows the frequency associated to the localised defect state. In panel (a) the mass value $M = 1$ whilst in (b) $M_1 = 2$ and $M_2 = 1$. Taken from [12].

we were practical people this could be found by considering the frequency, and the frequency is $\Omega = \varepsilon\hat{\Omega}$ (where $\hat{\Omega}$) is an order one quantity. Let us set

$$y_n = y(\eta), \quad y_{n\pm1} = y(\eta \pm \varepsilon) \tag{7}$$

and then the difference equation becomes, in this new language, that

$$y(\eta+\varepsilon) + y(\eta-\varepsilon) - 2y(\eta) - M\varepsilon^2\hat{\Omega}^2 y(\eta) = 0. \tag{8}$$

An expansion in a Taylor series

$$y(\eta+\varepsilon) \sim y(\eta) + \varepsilon y'(\eta) + \frac{\varepsilon^2}{2} y''(\eta) + \dots \tag{9}$$

yields, to leading order,

$$y_{\eta\eta} + M\hat{\Omega}^2 y = 0. \tag{10}$$

This is simply the wave equation (in one dimension with harmonic time dependence assumed) for a string and suggests (as we would expect) that, if the wave was long enough, it would see the collection of masses as being smeared out to produce an effective string. One could go to higher orders in the expansion and gradually dispersive effects would become evident. But

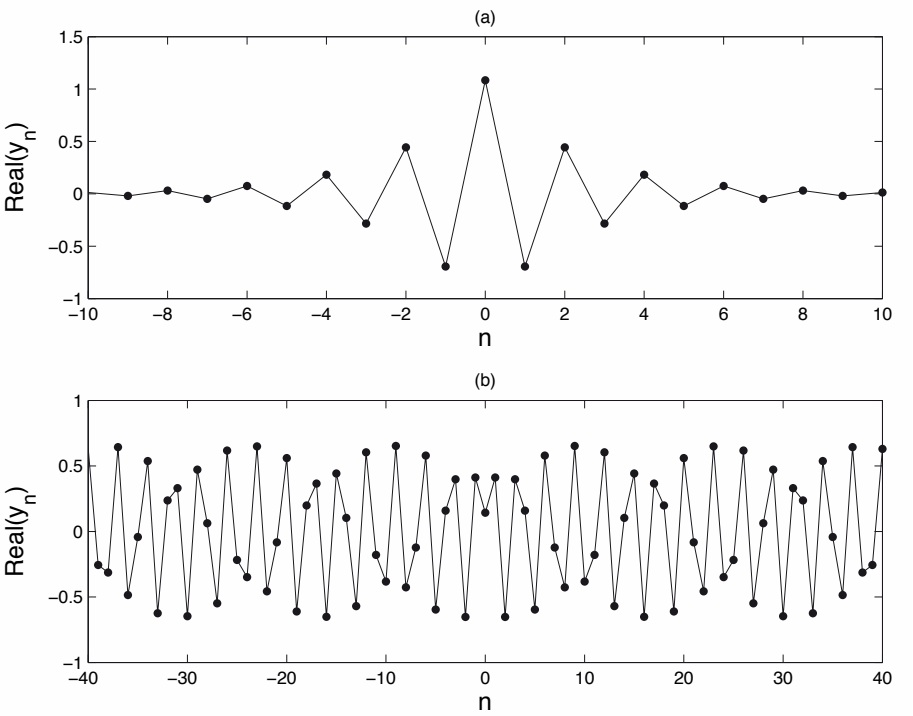

Figure 6: Forced lattice at origin. (a) Forcing frequency $\Omega = 2.05$ and (b) $\Omega = 1.8$.

going to higher orders tends, in general, to be a fair amount of effort for a reducing amount of increased knowledge (in my opinion). Notably the dispersion relation one obtains from the effective string is

$$\kappa = \sqrt{M}\Omega \tag{11}$$

when one replaces η with εn. Therefore this does indeed tie back in with (5) as one would hope.

If one forces the lattice close to the band-gap edge at $\Omega = 2$ (assuming $M = 1$) then one sees two distinct types of behaviour, as shown in figure

6, with spatially decaying solutions for frequencies within the stop-band, and oscillatory propagating solutions otherwise. Notably in figure 6(a) the masses are, at least roughly, out-of-phase from their neighbours and the decay appears exponential and in figure 6(b) the masses are, again, roughly out-of-phase and there is an apparent longer scale oscillation. Both the local behaviour and the long-scale features suggest that some asymptotic progress can be made.

As we have just witnessed some solutions are propagating within the system, a natural question is how, numerically, to mimic "infinity". In continuum systems a method due to Berenger [3] called perfectly matched layers is highy popular and widely used. Oddly, in discrete systems there does not appear to have been an analogous development. It is possible to generate a discrete PML (DPML) by following the arguments of, say, Turkel in the continuous case and discretise (after a further approximation) one gets

$$y_{n+1} + y_{n-1} - 2y_m + M\Omega^2 \left(1 - \frac{\sigma(n)}{i\Omega}\right)^2 y_n = \delta_{n,0} \tag{12}$$

[12] on a lattice $-N \leq n \leq N$ with $\sigma(n) = 0$ for $|n| < N_{pml}$. In PML computations it is often observed, and indeed proved [16], that nonlinear dependence in σ is advantageous. Here we take $\sigma(n) = (N_{pml} - n)^q/N$ for $n > N_{pml}$ and a symmetric formula for $n < -N_{pml}$; in computations $q = 2$ unless otherwise indicated. Physically the masses are taken to have a frequency dependent damping.

Also shown in Fig. 5 is the dispersion curve from the classical example of the diatomic chain of masses and springs. Notably there are two dispersion curves (the upper/lower ones called optical and acoustic branches respectively) separated by a so-called stop band, the stop-band of frequencies is one in which propagation is disallowed and even in this simple system one can use it as a filter. The Bloch wavenumber κ again plays a vital role as it is the phase shift across a cell - and is related to the frequency via a dispersion relation

$$M_1 M_2 \Omega^4 - 2(M_1 + M_2)\Omega^2 + 2(1 - \cos\kappa) = 0. \tag{13}$$

Note the range of κ (for 0 to π) caused by the periodicity of the system, and that there exist standing waves at end of Brillouin zone (the points $\kappa = 0$ and π.

2.1 Two-dimensions

There are naturally higher dimensional periodic structures, these are of more interest than one-dimensional chains, and the prototypical two-

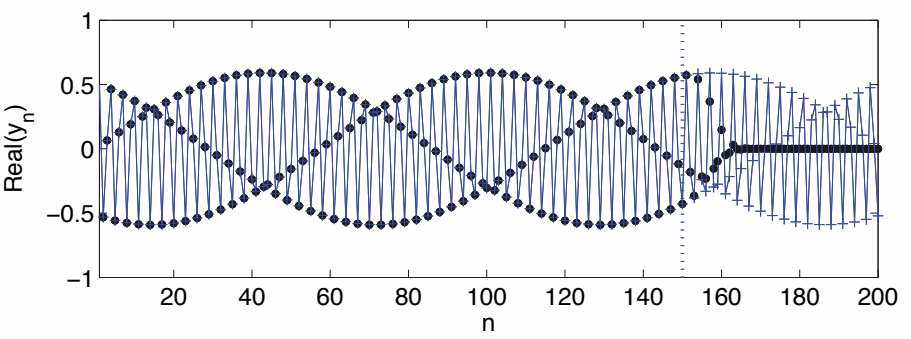

Figure 7: Comparing discrete PML with the exact solution for frequency $\lambda = 1.75$. The real part of y_n is shown with the exact solution as the crosses connected by lines, the PML numerics are solid circles; these are visually indistinguishable until we enter the PML region for $n > N_{pml} = 150$. Similar accuracy occurs for the imaginary part. Figure taken from [12].

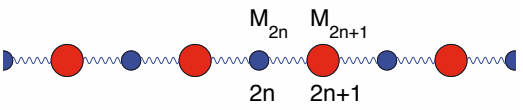

Figure 8: A schematic of the diatomic chain.

dimensional lattice is

$$y_{n+1,m} + y_{n-1,m} + y_{n,m+1} + y_{n,m-1} - 4y_{n,m} + \Omega^2 M y_{n,m} = 0 \qquad (14)$$

and now the scalar (in 1D) Bloch wavenumber is replaced by a vector $\kappa = (\kappa_1, \kappa_2)$ where

$$y_{n+\hat{N},m+\hat{M}} = \exp(i[\hat{N}\kappa_1 + \hat{M}\kappa_2])y_{n,m} \qquad (15)$$

for integer N, M and the resulting dispersion relation is

$$M\Omega^2 = 4 - 2(\cos\kappa_1 + \cos\kappa_2). \qquad (16)$$

The Brillouin zone [4] is no longer a simple line (as in 1D) but now a square in κ space. More conventionally one just plots the dispersion relation around

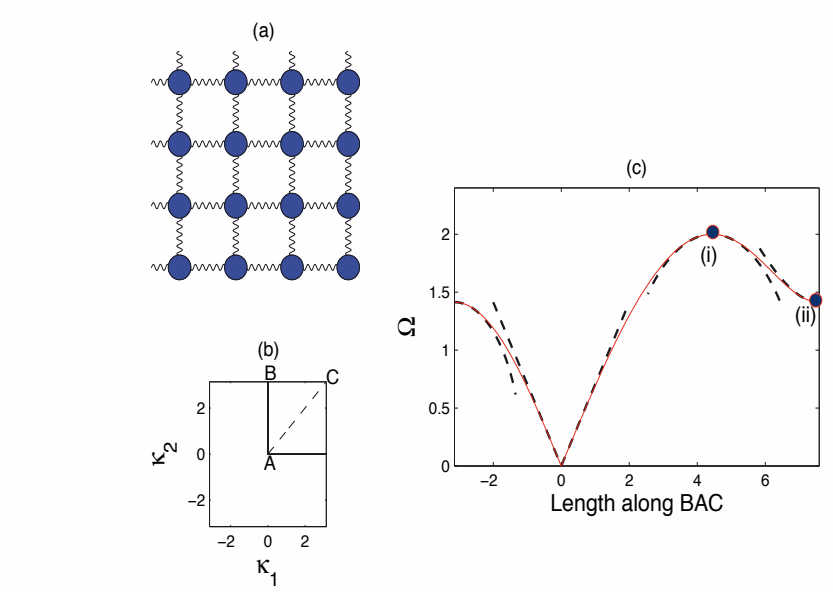

Figure 9: A uniform square lattice is shown in (a), with the irreducible Brillouin zone is the triangle A,B,C in (b). $M = 2$ in the dispersion curve (c); the dashed lines are from the HFH asymptotics. Figure taken from [12]

the edges of the irreducible Brillouin zone although that does carry some implications regarding the full iso-frequency surfaces [5]. The dispersion relation (16) is plotted in Fig. 9 and immediate observation is that the dispersion curves are linear near the origin, and a simple Taylor expansion then recovers an effective acoustic equation that can be obtained also by conventional homogenization. Another key observation is that standing waves occur at the wavenumber vector positions identified by A, B and C where they are perfectly in-phase/ out-of-phase in oscillation across the structure.

2.2 Homogenization

The homogenisation technique involves the confluence of two ideas: One mathematical, the idea of using a long-scale and a short-scale separation which is called the method of multiple scales. The other, physical, is that there exist standing wave frequencies, and associated eigenmodes, that en-

code the multiple scattering of near and far members of the periodic structure. This latter step is the key modification of standard homogenisation theory allowing one to model high frequency oscillations in periodic or nearly periodic structures. The full theory for lattices is in [7] and it can be extended to continuous systems [6].

In the simplest example of the diatomic lattice in one dimension (the basic idea carries across to higher dimensions with additional algebra) we introduce two scales: a long-scale, on the scale of the grid, characterised by $N \gg 1$ where N could be the number of lattice points and introduce a small parameter $\varepsilon = 1/N \ll 1$; the small parameter is crucial to the whole procedure. We introduce a new long-scale coordinate $\eta = 2n/N$ and take η to be a continuous, not discrete, variable. The other scale, the short-scale is taken to be the elementary cell and we specify an integer m that takes the values $m = -1, 0, 1, 2$; the elementary cell corresponds to the masses at $2n$, $2n + 1$ and their immediate neighbours. The two-scales are considered as independent variables, which is the standard multiple scales trick [2], and we take

$$y_{2n+m} = y(\eta + m\varepsilon, m) \sim y(\eta, m) + m\varepsilon y_\eta(\eta, m) + \frac{(m\varepsilon)^2}{2} y_{\eta\eta}(\eta, m) + \dots \quad (17)$$

as $\varepsilon \ll 1$. In particular the four displacements used in equations (1),(2) in this notation are $y_{2n-1} = y(\eta - \varepsilon, -1)$, $y_{2n} = y(\eta, 0)$, $y_{2n+1} = y(\eta + \varepsilon, 1)$ and $y_{2n+2} = y(\eta + 2\varepsilon, 2)$.

The asymptotic analysis only uses the displacements at y_{2n} and y_{2n+1}; their neighbouring displacements are related to these two via

$$[y_{2n-1}, y_{2n+2}] = [y(\eta - \varepsilon, -1), y(\eta + 2\varepsilon, 2)] = (-1)^J [y(\eta - \varepsilon, 1), y(\eta + 2\varepsilon, 0)] \quad (18)$$

as we assume that the motion, on the microscale of the elementary cell, is that of locally standing waves oscillating in-phase or out-of-phase ($J = 0, 1$ respectively) across the cell.

Equations (1),(2) to order ε^2 in matrix form become,

$$[A_0 - \lambda^2 M(1 + \varepsilon^2 \alpha g(\eta)) + \varepsilon A_1(\partial, \lambda) + \varepsilon^2 A_2(\partial^2, \lambda)]\mathbf{y}(\eta) = 0, \quad (19)$$

where ∂ denotes $\partial/\partial\eta$, $\mathbf{y}(\eta) = [y(\eta, 0),\ y(\eta, 1)]^T$ is the displacement vector, M is a diagonal matrix $M = \text{diag}\,[M_2,\ M_1]$, A_0 is a constant matrix and A_1 and A_2 are matrix differential operators. These matrices depend on periodicity conditions and, therefore, are different for in-phase and out-of-phase cases.

The natural separation of scales leads to a hierarchy of equations in powers of ε where the ansatz

$$\mathbf{y}(\eta) = \mathbf{y}_0(\eta) + \varepsilon \mathbf{y}_1(\eta) + \varepsilon^2 \mathbf{y}_2(\eta) + \dots \quad (20)$$

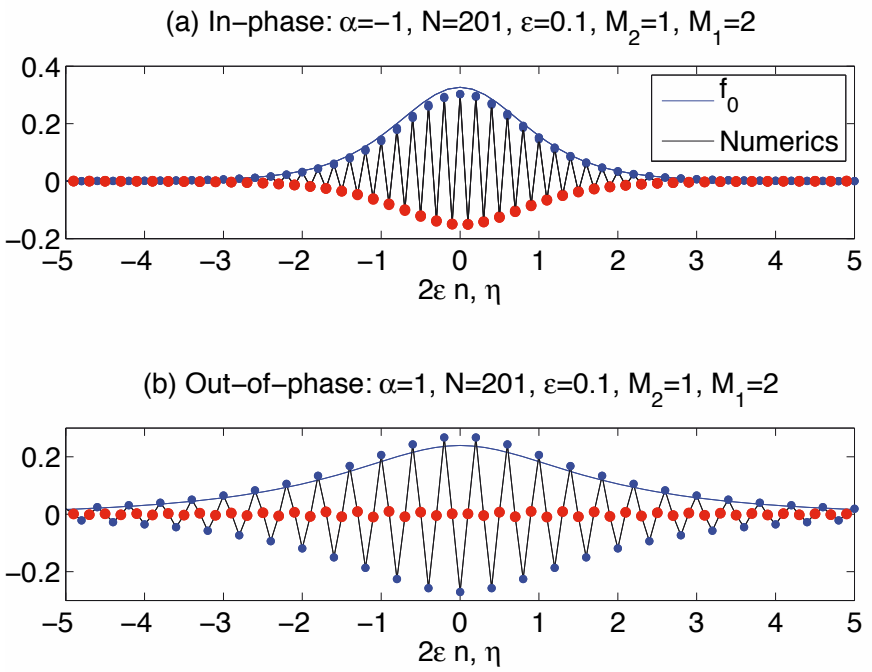

Figure 10: Localised modes for $M_1 = 2$, $M_2 = 1$ showing the numerical solution of (1,2) versus the f_0 from the asymptotic equations24), and its in-phase analogue, with the $g(\eta)$ =sech$^2(\eta)$. Panel (a) shows a localised in-phase solution for which the numerics give $\lambda^2 \sim 3.01896$ and the asymptotics give $\lambda^2 \sim 3.01880$ that differ in the fourth decimal place. Panel (b) shows the localised out-of-plane eigensolution for $\alpha = 1$ and the numerics give $\lambda^2 = 1.99239$ with the asymptotics as $\lambda^2 = 1.99236$. This figure is taken from [7].

$$\lambda^2 = \lambda_0^2 + \varepsilon\lambda_1^2 + \varepsilon^2\lambda_2^2 + \dots \tag{21}$$

is adopted. Substituting the ansatz into the lattice equations (19) gives differential-difference equations that are treated order-by-order in ε.

Let us now look at an example in detail: Standing waves with complete phase-shift across the structure lead to periodic conditions for the masses

which are $y(\eta,-1) = -y(\eta,1)$ and $y(\eta,0) = -y(\eta,2)$ (c.f. (18)) at each order. Matrices A_0, A_1 and A_2 become

$$A_0 = \begin{pmatrix} 2 & 0 \\ 0 & 2 \end{pmatrix},\ A_1 = \begin{pmatrix} 0 & -2\partial \\ 2\partial & (2-\lambda^2 M_1)\partial \end{pmatrix},\ A_2 = \begin{pmatrix} 0 & 0 \\ 2\partial^2 & (1-\tfrac{1}{2}\lambda^2 M_1)\partial^2 \end{pmatrix}. \tag{22}$$

At leading order, the separation of scales, and lack of explicit dependence upon η, leads to $y_0(\eta) = f_0(\eta)Y_0$. The vector Y_0 is defined on the scale of the elementary cell and displacements of the masses are chosen that lead to standing waves:

$$\mathbf{Y}_0 = (1,0)^T, \qquad \lambda_0^2 = \frac{2}{M_2} \tag{23}$$

and solutions at first and second order lead to the differential eigenvalue problem that determines $f_0(\eta)$ and λ_2^2 as

$$\frac{2}{(M_1 - M_2)} f_{0\eta\eta} + \lambda_2^2 f_0 = 0. \tag{24}$$

For $\alpha = 0$ the Bloch relation yields the local behaviour as $\varepsilon k \to \pi$ that

$$\lambda^2 \sim \frac{2}{M_2} + \frac{(\varepsilon k - \pi)^2}{2(M_1 - M_2)} + \dots \tag{25}$$

which also follows from expanding the explicit dispersion relation. The main point though is that this is a systematic way of deriving the long-scale behaviour.

One can extend these ideas to non-periodic systems where, say, the masses vary slowly as

$$M_{2n} = M_2(1 + \varepsilon^2 \alpha g(\eta)), \qquad M_{2n+1} = M_1(1 + \varepsilon^2 \alpha g(\eta)) \tag{26}$$

and (24)

$$\frac{2}{(M_1 - M_2)} f_{0\eta\eta} + [\lambda_2^2 + \alpha \lambda_0^2 g(\eta)] f_0 = 0. \tag{27}$$

This is a differential-eigenvalue problem that allows one to identify localized defect states, these are non-zero eigensolutions that exponentially decay at infinity; typically these occur at frequencies within the stop-bands of the perfect system. An example, taken from [7], is shown in Fig. 10. It is notable that the details such as the local oscillation from one mass to the next emerge naturally through the asmyptotic theory. Another nice detail is that the asymptotic ODE is just Schroedinger's equation and so one can take the entire (and considerable) theory from Physics and apply it to show when localised defect tates occur and to find estimates.

Extending all this to two-dimensions (and indeed three) is certainly possible [12; 7] and the asymptotic ODE for f_0 gets replaced by a PDE that captures the long-scale effective anisotropy of the system in its simplest manner.

3 Conclusions

These lectures have concentrated upon the toy system of masses and springs, but the underlying ideas are relevant to continuous periodic, or near periodic, systems [6] and frame structures [13]. One can take any periodic system, not necessarily on a square lattice, and homogenize it to create effective equations that encapsulate the essential physics within just long-scale equations.

Acknowledgements

The author gratefully acknowledges the hospitality of CISM where these lectures were given. Much of the work presented is the outcome of joint work with Julius Kaplunov, Evgeniya Nolde, Aleksey Pichugin, Sebastien Guenneau, Tryfon Antonakakis, Lina Joseph and Julia Postnova and it is a pleasure to thank them for their input to all of this.

Bibliography

[1] A. S. Barker Jr and A. J. Sievers, *Optical studies of the vibrational properties of disordered solids*, Rev. Mod. Phys., 47 (1975), pp. S1–S179.

[2] C. M. Bender and S. A. Orszag, *Advanced mathematical methods for scientists and engineers*, McGraw-Hill, New York, 1978.

[3] J.-P. Berenger, *A perfectly matched layer for the absorption of electromagnetic waves*, J. Comp. Phys., (1994), pp. 185–200.

[4] L. Brillouin, *Wave propagation in periodic structures: electric filters and crystal lattices*, Dover, New York, second ed., 1953.

[5] R. V. Craster, T. Antonakakis, M. Makwana, and S. Guenneau, *Dangers of using the edges of the Brillouin zone*, Phys. Rev. B, 86 (2012), p. 115130.

[6] R. V. Craster, J. Kaplunov, and A. V. Pichugin, *High frequency homogenization for periodic media*, Proc R Soc Lond A, 466 (2010), pp. 2341–2362.

[7] R. V. Craster, J. Kaplunov, and J. Postnova, *High frequency asymptotics, homogenization and localization for lattices*, Q. Jl. Mech. Appl. Math., 63 (2010), pp. 497–519.

[8] L. J. Gibson and M. F. Ashby, *Cellular solids: structures and properties*, Cambridge University Press, Cambridge, 2nd ed., 1997.

[9] S. Guenneau and R. V. Craster, eds., *Acoustic Metamaterials*, Springer-Verlag, 2012.

[10] J. D. Joannopoulos, S. G. Johnson, J. N. Winn, and R. D. Meade, *Photonic Crystals, Molding the Flow of Light*, Princeton University Press, Princeton, second ed., 2008.

[11] C. Kittel, *Introduction to solid state physics*, John Wiley & Sons, New York, 7th ed., 1996.

[12] M. Makwana and R. V. Craster, *Localized defect states for high frequency homogenized lattice models.* To appear Q. Jl. Mech. Appl. Math., 2013.

[13] E. Nolde, R. V. Craster, and J. Kaplunov, *High frequency homogenization for structural mechanics*, J. Mech. Phys. Solids, 59 (2011), pp. 651–671.

[14] M. Ostoja-Starzewski, *Lattice models in micromechanics*, Appl. Mech. Rev., 55 (2002), pp. 35–60.

[15] P. S. Russell, E. Marin, A. Diez, S. Guenneau, and A. B. Movchan, *Sonic band gap PCF preforms: enhancing the interaction of sound and light*, Opt. Exp., 11 (2003), p. 2555.

[16] E. A. Skelton, S. D. M. Adams, and R. V. Craster, *Guided elastic waves and perfectly matched layers*, Wave Motion, 44 (2007), pp. 573–592.

[17] F. Zolla, G. Renversez, A. Nicolet, B. Kuhlmey, S. Guenneau, and D. Felbacq, *Foundations of photonic crystal fibres*, Imperial College Press, London, 2005.

Multiscale models of electromagnetic and plasmonic metamaterials

Sébastien Guenneau*‡

* Institut Fresnel, UMR CNRS 7149, Aix-Marseille Université, France

Abstract In this chapter, we discuss paradigms central to electromagnetic metamaterials and their plasmonic counterparts. We start with a slab lens with unlimited resolution, which is made possible using the concept of negative refraction, when the permittivity and permeability of a medium change sign simultaneously. Pendry's perfect lens heavily relies upon existence of surface plasmons that exist on its boundaries. Correspondences with acoustics are then investigated in light of spring-mass models which bridge the field of electromagnetic and acoustic metamaterials, which are composites within which light or other (e.g. elastic, liquid surface) waves experience inverted Snell-Descartes laws of refraction upon resonance of micro-scale resonators. Next, we explain how geometric transforms introduced for computational easiness in helicoidal fibres, were given a twist by Pendry's team in 2006 in order to design invisibility cloaks. Finally, we apply these mathematical tools to the control of surface plasmons propagating at structured metal-dielectric interfaces. We illustrate transformational plasmonics with a broadband plasmonic invisibility carpet which has been experimentally validated by Quidant's group in 2010 at near infrared frequencies.

1 Introduction: Towards super lenses

A fundamental issue with imaging systems is the constraint on resolution imposed by the diffraction limit. In ordinary imaging systems that image only the propagating modes of radiation, features on the object smaller than the wavelength cannot be reproduced in the image. Images with subwavelength details can be assembled from scanning probes that can sense the electromagnetic near-fields (popularly known as scanning near-field optical microscopy). However, the scanning process severely limits image frame rates, and the probes require near direct contact with the object. The perfect lens proposed by Sir John Pendry in 2000 began to address these issues by providing for the possibility of image transfer of both the near- and far-field components or radiation with a free-space working distance [14]. The

R. Craster, J. Kaplunov (Eds.), *Dynamic Localization Phenomena in Elasticity, Acoustics and Electromagnetism*, CISM International Centre for Mechanical Sciences,
DOI 10.1007/978-3-7091-1619-7_2, © CISM, Udine 2013

cornerstone of this flat lens is the concept of negative refraction - foreseen by Victor Veselago in the late sixties [16] - whereby both permittivity and permeability take negative values and lead to negative refractive index and near-field enhancements. The subwavelength details of the source are transmitted through the system because they couple to the surface plasmons that exist on the boundaries between the negative refractive index material and the dielectric medium. This plasmonic mechanism forms also the basis for the current interest in metallic structures for super-resolution imaging at optical frequencies. Although such a near-field magnifier for electrostatic fields in the cylindrical geometry was proposed back in 1994 by McPhedran, Nicorovici and Milton [4], these perfect lenses can be flat and can be generalized to a variety of geometries including the cylindrical and spherical geometries [7]. There are some fundamental differences in the different geometries, for example, the focal surfaces. The cylindrical lens has curved object and image surfaces, whereas the perfect lens has planar object and image planes that better match typical detector arrays, and display formats. These imaging devices enabled by negative refractive index metamaterials have attracted a lot of attention and activity during the past decade [8].

It has nevertheless been realized that the image resolution of these extraordinary devices made of negative refractive index materials suffers from serious limitations due to the presence of dissipation and spatial dispersion [9] that is inherent to the structured composite resonant metamaterials. Pendry had originally proposed [14] that a thin film of silver that has negative dielectric permittivity alone can approximately act as a superlens with subwavelength image resolution at visible and near ultra-violet frequencies for p-polarized light. Refinements of what Pendry christened the poor man's lens were subsequently considered to improve the performance using the metamaterials at hand: the superlens effect was generalized to an asymmetric system, for example, a silver film with glass on one side and air on the other which made the system mechanically more robust. Further, the image resolution obtained by an asymmetric lens could be better under certain conditions. This proposal by Pendry and Ramakrishna to use a film of silver, which displays a (complex valued) negative dielectric constant in the visible spectrum, with air on one side and other media such as glass or GaAs on the other side [10] led to the demonstration of subwavelength imaging through negative refraction by Zhang's team in 2005 [1].

2 Square root of $\varepsilon\mu$ for negative ε and μ: Positively negative

Let us understand why should a medium with $\Re e(\epsilon) < 0$ and $\Re e(\mu) < 0$ be considered to have a negative refractive index. We start with the case of passive media.

Before embarking on our journey through the looking glass, we recall that Maxwell's equations in an isotropic heterogeneous medium described by relative permittivity ε and relative permeability μ take the following form in the absence of charges:

$$\nabla \times \mathcal{E} = -\mu_0 \frac{\partial \mu \mathcal{H}}{\partial t} \ , \text{ and } \nabla \times \mathcal{H} = \varepsilon_0 \frac{\partial \varepsilon \mathcal{E}}{\partial t} \ , \tag{1}$$

where $\nabla = (\partial/\partial x, \partial/\partial y, \partial/\partial z)$ is a gradient acting on the three space variables and t is the time variable. Moreover, $(\mathcal{E}, \mathcal{H})$ is the electromagnetic field and $\mu_0\varepsilon_0$ is a constant equal to the inverse of the square of the speed of light in vacuum usually denoted c.

Assuming a time harmonic dependence in $\exp(-i\omega t)$ with ω the angular frequency, and a spatial oscillation $\exp(i\mathbf{x}\cdot\mathbf{k})$ with $\mathbf{k} = (k_x, k_y, k_z)$ the vector wavenumber, that is $(\mathcal{E}, \mathcal{H}) = (\mathbf{E}, \mathbf{H})\exp(i(\mathbf{x}\cdot\mathbf{k} - \omega t))$, we obtain

$$\mathbf{k} \times \mathbf{E} = -\mu_0 \mu \omega \mathbf{H} \ , \text{ and } \mathbf{k} \times \mathbf{H} = \varepsilon_0 \varepsilon \omega \mathbf{E} \ , \tag{2}$$

which shows that if $\varepsilon < 0$, $\mu < 0$, $\mathbf{k}$, $\mathbf{E}$, $\mathbf{H}$ form a left-handed triad. However, the Poynting vector $\mathbf{S} = \mathbf{E} \times \mathbf{H}$ remains unchanged, implying that $\mathbf{k}$ and $\mathbf{S}$ are in opposite directions in a medium with $\varepsilon < 0$, $\mu < 0$. Physically, this means the phase velocity and the group velocity (energy flow) are in opposite direction, which is a hallmark of negative refraction.

2.1 Choosing the negative root in passive media

There is a subtlety with the definition of the refractive index through the Maxwell relation $n = \sqrt{\varepsilon\mu}$ in the negative layer. Care has to be taken for the choice of the square root in the definition of n. Indeed, the constitutive parameters for a medium with both $\Re e(\epsilon) < 0$ and $\Re e(\mu) < 0$ satisfy

$$\varepsilon = |\ \varepsilon\ | e^{i\Phi_\varepsilon} \ , \ \mu = |\ \mu\ | e^{i\Phi_\mu} \ , \text{ where } \Phi_\varepsilon \ , \ \Phi_\mu \in]\tfrac{\pi}{2}, \pi]. \tag{3}$$

This leads to an ambiguity in the expression for the refractive index n:

$$\begin{array}{rl} n & = |\ n\ | e^{i\Phi_n} \ , \text{with } \Phi_n = \frac{1}{2}(\Phi_\mu + \Phi_\varepsilon) \in]\frac{\pi}{2}, \pi] \\ & \text{or } \Phi_n = \frac{1}{2}(\Phi_\mu + \Phi_\varepsilon) - \pi \in] -\frac{\pi}{2}, 0] \ , \end{array} \tag{4}$$

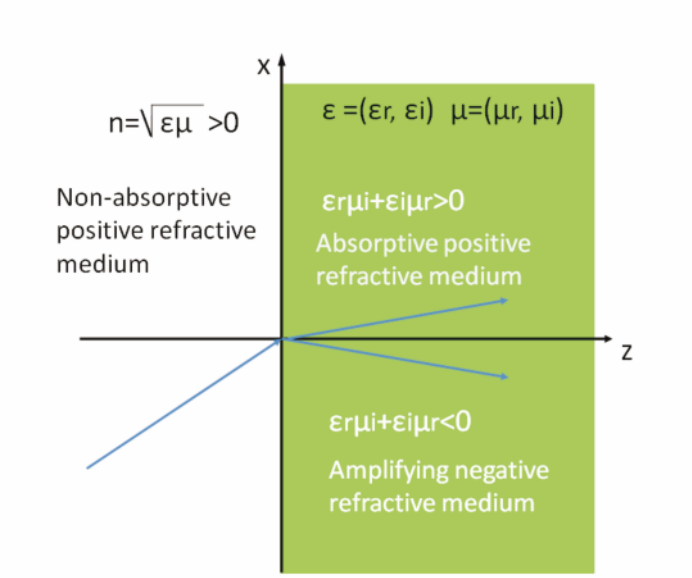

Figure 1. Refraction of a light ray (blue arrows) through an interface separating a non-absorptive positive refractive medium, and an absorptive positive refractive medium (upper right corner), or an amplifying negative refractive medium (lower right corner).

depending upon the choice for the square root. We infer from (4) that the wave is either left-handed with respect to the wave vector $\mathbf{k}$ and right-handed with respect to the direction of the energy flow $\mathbf{S}$ ($\Re e(n) < 0$ and $\Im m(n) > 0$) or right-handed with respect to $\mathbf{k}$ and $\mathbf{S}$ ($\Re e(n) > 0$ and $\Im m(n) < 0$). Either physical situation seems acceptable.

As we are particularly interested in the case of small loss, we can take the following two ansatz [8; 15]

$$\varepsilon = \varepsilon_r + i\eta\varepsilon_i \text{ and } \mu = \mu_r + i\eta\mu_i \text{ where } 0 < \eta \ll 1 \,, \tag{5}$$

where ε_r and μ_r are negative reals, whereas ε_i and μ_i are positive reals. We obtain

$$n = \pm\sqrt{\mid \varepsilon_r\mu_r \mid}\left[1 - i\frac{\eta}{2}\left(\frac{\varepsilon_i}{\mid \varepsilon_r \mid} + \frac{\mu_i}{\mid \mu_r \mid}\right)\right] + O(\eta^2) \,. \tag{6}$$

We note that a refractive index n such that $\Re e(n) > 0$ and $\Im m(n) < 0$ corresponds to an exponentially growing wave in a dissipative medium and

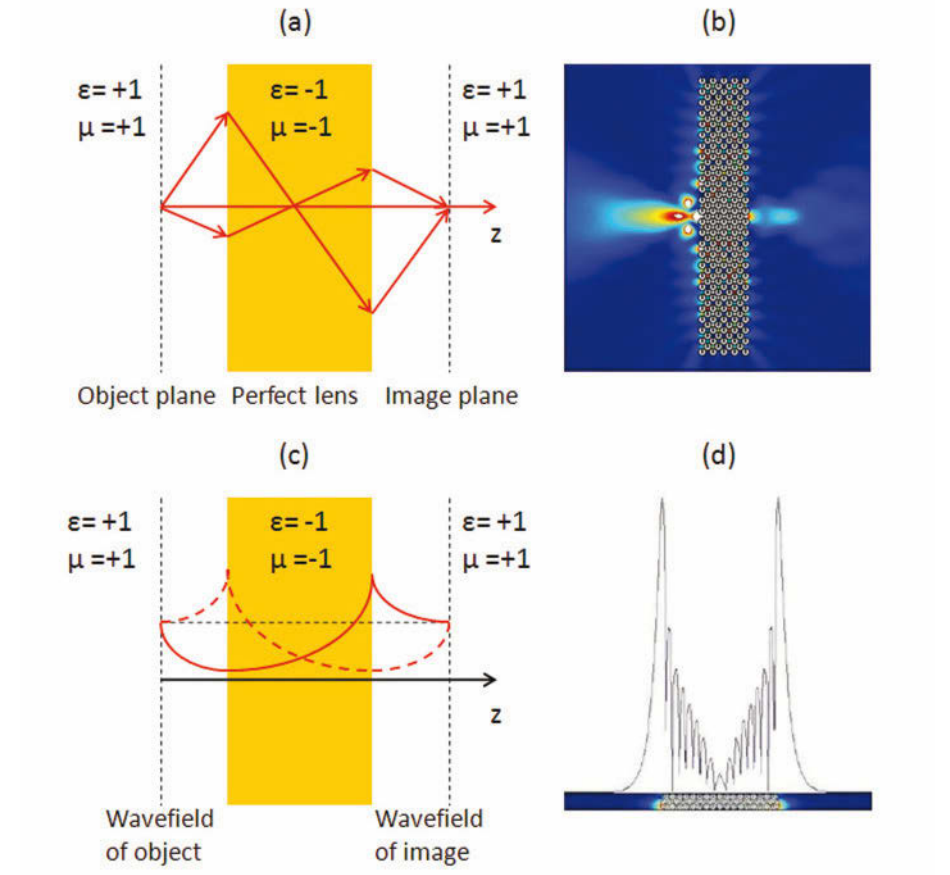

Figure 2. Super lenses via negative refraction: (a) Schematic diagram depicting the focussing of rays by the Pendry-Veselago lens ($\varepsilon = \mu = -1$). (b) Numerical simulation demonstrating the imaging effect for TE waves through an array of SRRs (plot of the longitudinal magnetic field intensity). (c) The perfect lens in (a) and the poor man's lens in (b) work by excitation of surface plasmons. (d) Profile of the longitudinal magnetic field in (b) along the line passing through the source and the image.

should therefore be disregarded in (6). Taking the limit of zero absorption (η goes to zero) in (6) for $\Re e(n) < 0$ and $\Im m(n) > 0$, gives $n = -\sqrt{\mid \varepsilon_r \mu_r \mid}$.

This is a standard practice in physics to obtain the causal solution by considering a lossy medium and taking the limit of zero loss.

2.2 Overcoming the wavelength limit to resolution

Let us now say a few words on the wavelength limit to resolution in the perfect lens [14] wherein in the limit of zero absorption $\varepsilon = \mu = -1$ leading to a negative refractive index $n = -1$ impedanced matched to vacuum as we have seen above.
Each wave has a wavevector $\mathbf{k} = (k_x, k_y, k_z)$ responsible for driving the wave from object to image, which from (2) satisfies the dispersion relation

$$k_z = \sqrt{\omega^2/c^2 - k_x^2 - k_y^2}\,, \tag{7}$$

where k_x and k_y define the components of the image.

The larger the magnitude of k_x, k_y we can propagate to the image plane the better the resolution. The problem is that making these transverse wave vectors too large gives k_z an imaginary value and the wave decays exponentially along the z-axis. These decaying components of the object field are often referred to as the near field. They are confined to the vicinity of the object and serve to lock away high-resolution information. Hence the biggest Fourier component that we can capture has magnitude $k =\mid \mathbf{k} \mid = \omega/c$ and the wavelength restriction on resolution follows. How does our negative slab avoid this limit? The secret it deploys is a surface resonance which is used to amplify evanescent waves and restore them to the values taken in the object plane, which is the bold claim which Pendry makes in his seminal paper on negative refraction makes a perfect lens [14]. Given time, a resonance can build a substantial amplitude using energy drawn from the source. Absorption is the great enemy of resonances so low loss materials are essential if we are to approach the resolution offered by the perfect lens.

For the perfect lens a problem of field divergence [22] is particularly acute because behind the image the fields continue to grow as we trace them back towards the lens. For very large values of k_x, k_y, essential for high resolution, the fields grow very rapidly. In fact there is a limit to this process because absorption will eventually damp the resonances responsible for amplification and the gain provided by the slab will be replaced by attenuation for the very highest values of k_x, k_y, capping the divergence in the fields but at the same time limiting resolution. For example in the instance of a lossy dielectric, $\varepsilon = \varepsilon_r + i\varepsilon_i$, the resolution limit is given by [17]

$$\Delta = 2\pi d/\ln(\varepsilon_i)\,, \tag{8}$$

where d is the thickness of the slab. This shows that reducing loss is essential in order to achieve a high resolution with the nearly perfect lens.

2.3 Resolving the wavevector in negative refractive media

For simplicity, we only considered the case of passive media, but the general issue of resolving the wave vector in negative refractive media with gain can be also addressed. For this, one has to consider the analytic behavior of the wave vector $\mathbf{k}$ in the complex plane, with a total of eight physically distinct cases in the four quadrants of two Riemann sheets [15]. The eight cases along with the different media and circumstances are shown in Figure 3 where they are located in different regions of the $\Re e(k_z) - \Im m(k_z)$ plane, k_z being the normal component of the wave-vector in the refraction process between vacuum and the given medium. Primarily, we draw the readers attention to the regions of the $\Re e(k_z) - \Im m(k_z)$ plane where the media with $\Re e(\epsilon) < 0$ and $\Re e(\mu) < 0$ lie. It is seen that they both have $\Re e(k_z) < 0$. Second, we also stress that refraction of waves is primarily a propagation effect that is interesting only when the waves can propagate long distances. While it has been theoretically shown that waves in some highly absorptive media can refract negatively across an interface, the propagation length of the wave inside the medium is usually so short to preclude even its experimental study in most cases.

During the past few years, there has been some controversy regarding the assignment of various physical media to these eight regions [15; 23; 24; 25; 26]. It has been wrongly suggested [23; 24] that for light incident on a semi-infinite gain medium with $\Im m(\epsilon) < 0$, the presence of gain in the medium could imply a negative sign for the refractive index even if $\Re e(\epsilon) > 0$ and $\Re e(\mu) > 0$. It has also been mistakenly claimed [24] that evanescent waves that exponentially grow into bulk of the medium would exist at the interface of such a positive medium that has gain. While we will not get into a detailed analysis of this controversy here, we first note that for a finite medium such as a finite slab or a sphere, all the relevant physical quantities such as the transmission, reflection or scattering coefficients are invariant with the sign of the wave-vector or the index [26]. Hence the choice of the wave-vector in an infinite medium is primarily of academic curiosity. Second, the choice of the wave-vector that causes an exponential increase of the evanescent waves into the bulk of the medium would be contrary to the presence of surface plasmon waves at the interface between a metal and a gain medium that has been experimentally measured recently [27]. In any case, if the evanescent waves were to decay exponentially in absorptive media and amplify exponentially in amplifying media,

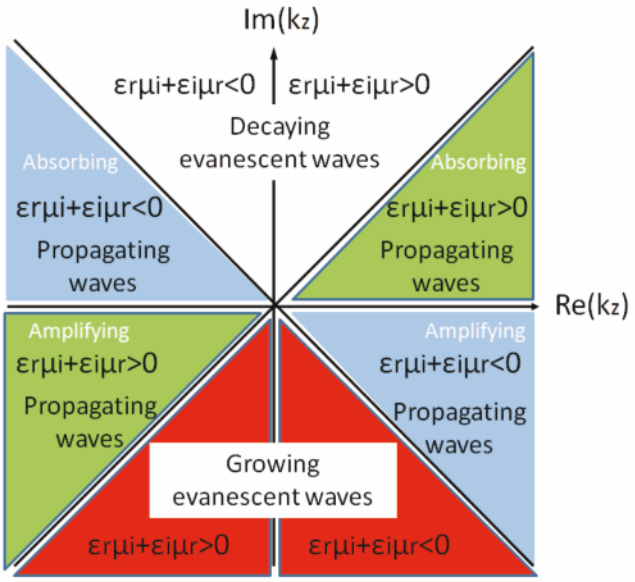

Figure 3. A scheme for the classification of electromagnetic media into combinations of positive refractive or negative refractive media and absorbing or amplifying media, as proposed by Ramakrishna and Martin [15].

the limit of zero dissipation or gain would become ill-defined. Hence the choice of a wave-vector that causes exponential amplification for evanescent waves in gain media is inconsistent. Finally, we should point out that the choice of the wave-vector in a gain medium has been investigated with careful experiments a long time ago [18]. The experimental results described therein clearly show that the sign for the square-root (or the wave-vector) in an amplifying medium is definitely positive. Hence we stress here that while there are two mathematically valid choices for the branch, the physical relevant branch for a medium can be chosen only by the imposition of physical boundary conditions. What boundary condition is physically correct can only be decided by experiments and there is unambiguous experimental evidence [18; 27] that the choice of the signs for the wave-vector in various media and circumstances originally set out in Ref. [15] are the physically reasonable ones. We also note an attempt to obtain the limit of semi-infinite media by considering finite slabs with gain and taking the limit of infinite slab thickness [19] and remark that any such attempt would be

futile for perfectly coherent, monochromatic waves as the steady-state solution is effectively obtained at infinite time where all the multiple reflections from both the interfaces, however far apart, are included in the solution.

3 Engineering negative effective medium parameters

While the negative dielectric permittivity demonstrated by a plasma and highly conducting metals at visible and ultra-violet frequencies has been known for over a century, negative magnetic permeability was relatively unknown except in some narrow frequencies ranges in some magnetic materials at microwave frequencies [8]. Natural materials with simultaneously negative dielectric and magnetic permeability were unknown and such effects became possible only with certain artificially structured materials, examples of which were first engineered at the turn of the new Millenium [20; 13; 21].

In this section, we discuss how negative effective medium parameters can be obtained using Pendry's split ring resonators (SRRs): these are associated with an anti-phased over-screened response at frequencies slightly greater than the resonance frequency of a forced oscillator with low levels of dissipation. We shall see that from a mechanical standpoint SRRs are simply Helmholtz's resonators which can be modelled via springs and masses. Newton's laws meet Maxwell's equations in SRRs!

3.1 Asymptotic modelling of resonators with a thin domain: Spring-mass model behind electromagnetic metamaterials

In what follows, we model the famous split ring resonator introduced by John Pendry's team in 1998 [13] in order to achieve artificial magnetism. Our aim is to better understand the underlying mechanism leading to its resonant features, using the powerful tool of asymptotic analysis of multi-structures [3]. The following derivation is adapted from [5] (see also [6] for the analogous case of transverse electric waves propagating within thin-walled photonic crystal fibres). We shall see that the derivation unveils a link between a spring-mass model and a split ring resonator, as schematically depicted in Figure 4 i.e. it bridges the discrete and continuous models.

Mathematically, electromagnetic waves propagating in dielectric cylindrical media (i.e. invariant along the z direction) are characterized by a relative permittivity, $\varepsilon(x, y)$ related to the refractive index n through $\varepsilon = n^2$. The magnetic field $\mathbf{H}(x, y)$ is solution of the time-harmonic vector Maxwell's equations. Harmonic time dependence, $\exp(-i\omega t)$, with ω as wave frequency allows us to work directly in the spectral domain, i.e. with the Maxwell operator. If we consider infinite conducting cylindrical

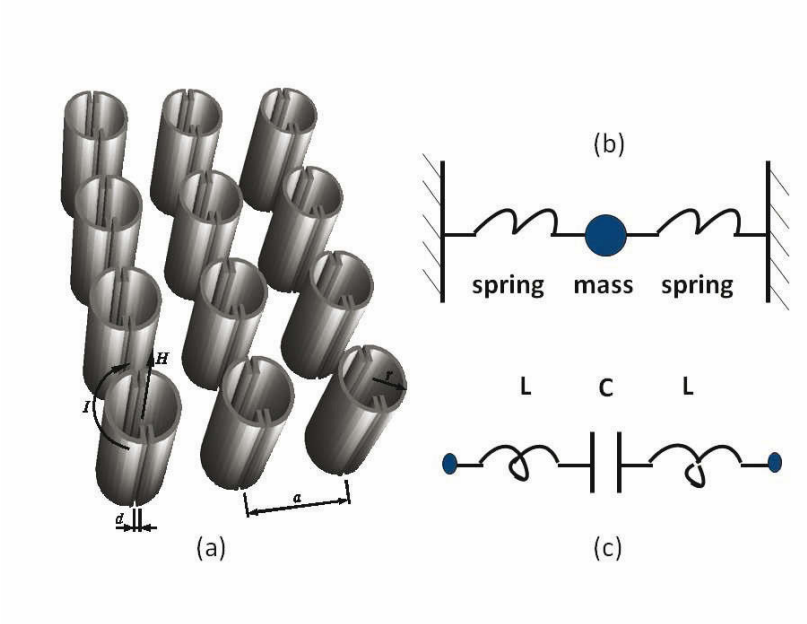

Figure 4. (a) Square array of cylinders with capacitive splits (so-called thin bridges of thickness d small compared to the pitch a) that respond resonantly to radiation with the (longitudinal) magnetic field along the cylindrical axes. Circulating currents I around the rings tend to shield the interior due to the inductance while the capacitance due to the gaps gives rise to a resonance, the so-called artificial magnetism (picture adapted from [2]). (b) A split ring acts as a Helmholtz resonator: a mass (counterpart of the capacitance C in electric circuits) is connected to walls via springs (counterparts of inductance L, say in solenoids) [5]. The physical interpretation is a negative effective permeability upon resonance. (c) Resonant LC circuit counter part of a Hemholtz resonator.

inclusions in this dielectric medium (e.g. SRRs as in Figure 4), the problem (with weak derivatives in $\mathbb{R}^3$) takes the form:

$$\nabla \times \left(\varepsilon^{-1}\nabla \times \mathbf{H}\right) = \frac{\omega^2}{c^2}\mathbf{H}\,, \mathbf{n} \times (\varepsilon^{-1}\nabla \times \mathbf{H})\,|_{\partial D} = \mathbf{0}\,, \tag{9}$$

with c the speed of light in vacuum, and $\mathbf{n}$ the unit outward normal to the boundary ∂D of the infinite conducting inclusions D.

If we consider transverse electric waves propagating in a homogeneous dielectric matrix (ε is a constant) with infinite conducting SRRs of cross-section Ω, then the longitudinal component u of the magnetic field $\mathbf{H} = (0, 0, u)$ satisfies the following equation and boundary condition:

$$\nabla \cdot (\nabla u) + \varepsilon k^2 u = 0\,,\ \frac{\partial u}{\partial n}\,|_{\partial\Omega} = 0\,, \tag{10}$$

where $k = 2\pi/\lambda = \omega/c$ is the wavenumber in vacuum, with λ the (fixed) wavelength, ω the radian frequency and $\partial u/\partial n = \mathbf{n} \cdot \nabla \mathbf{u}$.
We denote by Ω the double-split rings as shown in Figure 4. Formally,

$$\Omega = \{r_0 < \sqrt{x^2 + y^2} < r_1\} \setminus \overline{\bigcup_{j=1}^{N} \Pi_\eta^{(j)}} \tag{11}$$

where r_0 and r_1 are functions of variables x, y unless the rings are circular and

$$\Pi_\eta^{(j)} = \left\{(x, y)\ :\ 0 < x < l_j\,,\ |\ y\ | < \eta h_j/2\right\}\,, \tag{12}$$

is a thin ligament of length l_j between the 'ends of the letter C'. Here ηh_j the thickness of the j-th bridge, with η a small positive non-dimensional parameter. In our case, we have two thin-bridges $\Pi_\eta^{(1)}$ and $\Pi_\eta^{(2)}$.
To derive the asymptotic expansions, we introduce the scaled variable $\xi = y/\eta$ so that $\xi \in (-h_j/2,\, h_j/2)$ within $\Pi_\eta^{(j)}$, and

$$\frac{\partial^2 v}{\partial y^2} = \frac{1}{\eta^2}\frac{\partial^2 v}{\partial \xi^2}. \tag{13}$$

In $\Pi_1^{(j)}$, the time-harmonic wave equation (10) takes the rescaled form

$$\left(\frac{1}{\eta^2}\frac{\partial^2}{\partial \xi^2} + \frac{\partial^2}{\partial x^2}\right) u + \varepsilon\frac{\omega^2}{c^2}u = 0\,, \tag{14}$$

where the derivatives are taken in classical sense (the relative permittivity ε is constant in the thin-bridge), and c is the speed of light in vacuum. The longitudinal magnetic field u is approximated in the form

$$u \sim U^{(0)}(x, y) + \eta^2 U^{(1)}(x, y)\,. \tag{15}$$

Assuming some Neumann (perfect conducting in TE polarization) boundary conditions hold on the lower and upper edges of the thin-domain [1], to leading order we obtain (see (14) and (15))

$$\frac{\partial^2 U^{(0)}}{\partial \xi^2} = 0\,,\ |\ \xi\ | < h_j/2\ ,\ \frac{\partial U^{(0)}}{\partial \xi}\big|_{\xi=\pm h/2} = 0\,. \tag{16}$$

Hence, $U^{(0)} = U^{(0)}(x)$ (it is ξ-independent). Assuming that $U^{(0)}$ is given, we derive that the function $U^{(1)}$ satisfies the following model problem on the scaled cross-section of Π_1

$$\begin{aligned} \frac{\partial^2 U^{(1)}}{\partial \xi^2} = -\frac{\partial^2 U^{(0)}}{\partial x^2} + \frac{\varepsilon\omega^2}{c^2} U^{(0)}, \qquad & |\ \xi\ | < h_j/2 \\ \frac{\partial U^{(1)}}{\partial \xi}_{\ |\xi=\pm h_j/2} \quad = \quad & 0\,. \end{aligned} \tag{17}$$

The condition of solvability for the problem (17) has the form

$$\frac{d^2 U^{(0)}}{dx^2} + \frac{\varepsilon\omega^2}{c^2} U^{(0)} = 0\,, \quad 0 < x < l_j\ . \tag{18}$$

Hence we have shown that to the leading order we can approximate the longitudinal magnetic field u within the thin bridge $\Pi_\eta^{(j)}$ by the function $U^{(0)}$ which satisfies the time-harmonic wave equation in one-space dimension.
We now assume that the longitudinal magnetic field is periodic over each unit cell Y within an array of SRRs: this is a legitimate assumption for a configuration like in Figure 4(a) as the field is localised inside the core region of the SRR. This shows that the average of the eigenfield over the cell vanishes. Indeed, let χ_1 denote the value of the field in the large body Σ of the multi-structure Ω (union of the two C-shaped voids) and let χ_2 (which we normalize to 1) denote the value of the field within the complementary area of the macro-cell $Y \setminus \Omega$ excluding the ligaments. Applying Green's formula, we deduce that

$$\frac{\omega^2}{c^2} \int_Y \varepsilon u\ dxdy = \int_{Y\cup\Omega} \nabla\cdot\nabla u\ dxdy = \int_{\partial Y\cup\partial\Omega} \frac{\partial u}{\partial n}\ dl = 0\ , \tag{19}$$

since u is periodic on ∂Y (and the normal anti-periodic) and Neumann data hold on $\partial\Omega$.

[1] If one assumes Dirichlet (perfect conducting in TM polarization) conditions hold on the upper and lower edges of the thin-domain, this kills the field oscillations in the split ring resonator. This explains why SRRs only work for TE polarization.

This shows that the average of the longitudinal magnetic field u over Y vanishes, hence by neglecting the area of the thin bridges, we obtain

$$\chi_1 \mathcal{S}_\Sigma + \chi_2 \mathcal{S}_{Y\setminus\Omega} = O(\eta)\,. \tag{20}$$

Since we have two thin bridges, we have two separate eigensolutions V_j, $j = 1, 2$, corresponding to the vibrations of the longitudinal magnetic field in the thin domains $\Pi_\eta^{(j)}$:

$$V_j''(x) + \varepsilon \frac{\omega^2}{c^2} V_j(x) = 0\,,\ 0 < x < l_j\,, \tag{21}$$

$$V_j(0) = \chi_2 = -\chi_1 \frac{\mathrm{meas}(\Xi)}{\mathrm{meas}(Y \setminus \Omega)}\,, \tag{22}$$

$$\varepsilon^{-1} \eta h_j V_j' l_j = M\omega^2 V(l_j)\,, \tag{23}$$

where ηh_j and l_j are the thickness and the length of the thin ligament $\Pi_\eta^{(j)}$, and $M = \varepsilon \mathrm{meas}(\Xi)$ is the area of the body Ξ. The bridges are both connected to Ξ, hence $V_1(l_1) = V_2(l_2) = V$, where V is the constant longitudinal magnetic field in the body Ξ. In the context of acoustics, V is a displacment field, M is the mass of the body Ξ, and the left hand side in (23) has the physical dimension of a force, hence (23) is nothing but Newton's second law (the forces acting on the body equal its mass times its acceleration).

We note that $V_j(0)$ is equal to a non-zero constant unlike in [5] (in that case we assumed that $\chi_2 = 0$ i.e. $u = 0$ where the bridges meet the region outside Ω). Here, the constant is chosen in such a way that the average of the field over the basic cell vanishes, as should be expected for a localised (stationary) field.
The solution of the problem (21)-(23) has the form

$$V_j(x) = -\frac{\chi_2 \cos(\frac{\omega}{c} l_j) - 1}{\sin(\frac{\omega}{c} l_j)} \sin(\frac{\omega}{c} x) + \chi_2 \cos(\frac{\omega}{c} x)\,, \tag{24}$$

where $c = \sqrt{\mu/\rho}$ and the frequency ω is given as the solution of the following equation

$$\eta \left(h_1 \cot(\frac{\omega l_1}{c}) + h_2 \cot(\frac{\omega l_2}{c}) + 2C \right) = \varepsilon M c \omega\,. \tag{25}$$

Looking at a first low frequency, we deduce an explicit asymptotic approximation

$$\omega \sim \sqrt{\frac{\eta h_1}{l_1} + \frac{\eta h_2}{l_2}} \sqrt{\frac{1}{\varepsilon M}} \Big(1 + \frac{\mathrm{meas}(\Xi)}{\mathrm{meas}(Y \setminus \Omega)} \Big)\,. \tag{26}$$

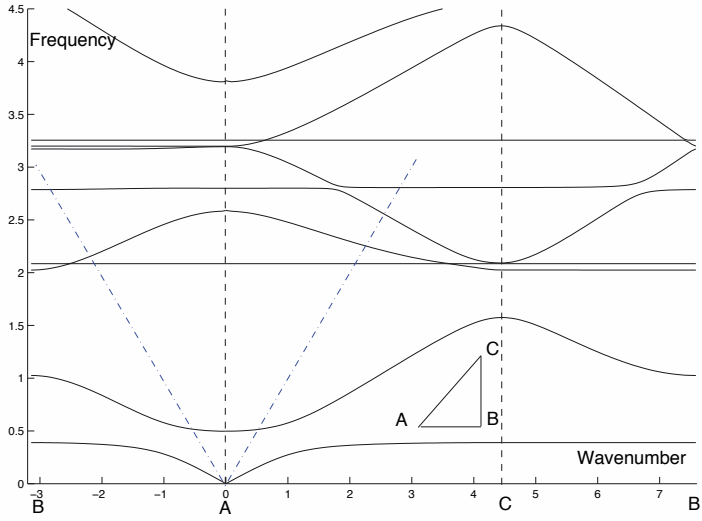

Figure 5. Band diagram corresponding to a square array of split ring resonators as in Fig. 4. The wavenumber is a projection of the Bloch vector which describes the first Brillouin zone ABC with $A = (0, 0)$, $B = (\pi/d, 0)$ and $C = (\pi/d, \pi/d)$, where d is the pitch of the array. Dispersion curves correspond to frequencies of transverse electric waves propagating within the array. The resonance associated with a constant longitudinal magnetic field inside each infinite conducting cylinder, see Fig. 6(b), creates a low frequency stop band (range of frequencies for which no waves can propagate within the array) near the normalised frequency $\omega d/c = 0.57$ (with c speed of light in vacuum) above which the effective permeability displays a negative real part [28]. The dotted lines emerging from point A show the light cone. Its intersection with the second dispersion curve along AC direction gives the onset of all-angle-negative refraction (also known as dynamic anisotropy) [29], for which light emanating from a source in vacuum couples to an array of SRRs and forms an image underneath according the inverted Snell-Descartes laws of refraction, see Fig. 6(a).

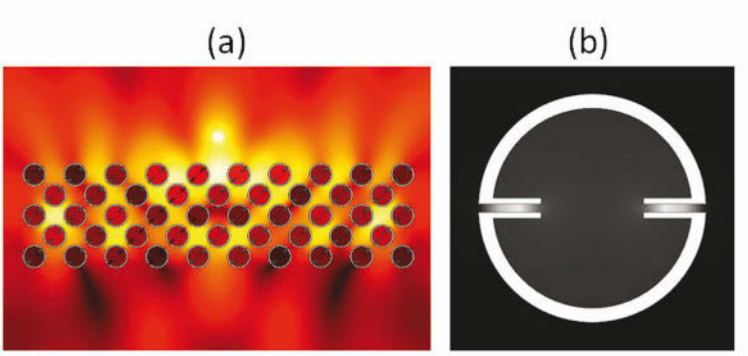

Figure 6. Imaging effect for transverse electric waves: (a) An electric line source placed on the upper side of an array of infinite conducting cylinders (with cross-sections shaped as split ring resonators (SRRs)) is imaged on the lower side. The asymptotic formula (26) provides us with the resonant frequency of SRRs (b) at which lensing occurs.

This estimate actually holds for the frequency of the upper edge of the first phononic band gap of Figure 5. It matches that of a LC resonant circuit as schematically shown in Figure 4(c).

We report in Figure 5 finite element computations for a periodic cell of side length d with a double C-shaped void. The central disk has a radius of $0.3d$ and the two cuts have the same length $0.22d$ and a thickness $0.03d$. We deduce the frequency estimate is $\omega^* d/c = 0.57$, which is in good agreement with the finite element value $\omega^{**} d/c = 0.59$ for the lowest point on the second dispersion curve on Figure 5 occurring at the Γ point (where the Bloch wavenumber $\mathbf{k}$ vanishes). Above this value, one can see that the group velocity for waves propagating in the CA direction is negative, hence by tilting the square array through an angle $\pi/4$, one can achieve some form of negative refraction. This leads to a lensing effect most visible for a source of frequency $\omega d/c = 0.7$ placed above a tilted array of 48 SRRs, see Fig. 6. Time has now come to make some connections with acoustic waves, as it seems fairly obvious from the spring mass model underpinning the split ring resonators that mechanical vibrations should also be enhanced in SRRs, which opens also routes towards negative refraction for acoustic waves. Actually, it is enough to look at wave equation (19) to convince oneself that a simple change of parameter, say replacing the permittivity ε by the shear modulus μ makes all the section valid for anti-plane shear waves

propagating in an isotropic elastic material with cracks shaped as SRRs, in which case u is the anti-plane shear displacement. One could also get rid of the parameter ε (take it to be 1 and supply (19) with the dispersion equation for surface liquid waves: $\omega^2 = gk(1 + k^2d^2)\tanh(kh)$, where ω is the surface liquid wave frequency, g the constant of gravity, d the liquid capillarity length, and h the liquid depth. The Neumann condition now stands for a no-flow condition on rigid cylinders plunging into the liquid, the equation takes place on the free surface and u is related to the liquid elevation away from the still surface (in the absence of waves).

Let us now move to the next section, which is concerned with another electromagnetic paradigm: transformational optics and invisibility cloaks. Note that the first realization of an invisibility cloak by the group of Smith and Pendry was based upon split ring resonators [76].

4 A brief history of transformational optics: From helicoidal fibers to invisibility cloaks

Geometric transforms in computational electromagnetics have been applied as a mere mathematical tool for over 20 years [32], for instance to map unbounded domains onto finite ones, a trick known as perfectly matched layers in the finite element community [31], and further reinterpreted by mathematicians in more abstract frameworks [54]. Researchers from the electric engineering [50; 51; 63] and photonics [64; 65; 66; 67] communities have made use of geometric transforms in order to study twisted fibers, since the Maxwell's equations take a particularly tractable form in helicoidal coordinates. However, these works remained some kind of academic curiosity until six years ago, when a handful of photonics groups announced transparency could be achieved in metamaterials [37; 30], and the bold claim of cloaking via anomalous resonance by Milton and Nicorovici[61]. A renewed interest followed in gradient index materials (whose paradigm is the Luneburg lens [59]) in optics and acoustics owing to their links with transformational optics and acoustics. Mass media got suddenly interested when two research groups (those of Pendry, Schurig and Smith [74] and Leonhardt [55]) independently proposed a systematic way to control wave trajectories in curvilinear coordinate systems. These two groups designed a cloak that renders any object inside it invisible to electromagnetic radiation. The former team theorized that a coating consisting of a meta-material whose physical properties are deduced from a coordinate transformation in the Maxwell system displays anisotropy and heterogeneity of permittivity and permeability working as a deformation of the optical space around the object. The physicists consider the blowup of a point, thereby tearing apart the metric

space. Though this may seem haphazardous, this can be legitimated by making use of advanced mathematical treatments [44; 53]. The experimental validation [76] of their theoretical considerations was given in 2006 for a copper cylinder invisible to an incident plane wave at 8.5 GHz. In 2008, our group in Marseille proposed a broadband metallic cloak displaying an effective anisotropic permittivity, which has been experimentally shown to cloak some metallic obstacle from 7 to 9 Ghz [41]. In 2009, the group of de Lustrac proposed a non-magnetic version of Pendry's cloak which was experimentally demonstrated at microwave frequencies [52]. However, Leonhardt's team used mathematical tools of complex analysis in order to conformally map the Helmholtz equation, thereby ensuring that the (spatially varying) refractive index be isotropic. These two approaches to cloaking (conformal and non-conformal) markedly enhance our capabilities to manipulate light, even in the intense near field limit [82]. Other research groups looked at how governing equations behave under geometric transforms in other areas of physics, such as the conductivity equation [42], the Schrödinger equation for matter waves [43; 80; 38; 45], the acoustic wave equation [36; 35; 71] and the Navier equation for elastodynamics [60; 34].

5 Transformed conductivity equation: Correspondences with electrostatics and magnetostatics

Maybe the simplest way to introduce the field of cloaking is through the emblematic example of the conductivity equation as it avoids any unnecessary technicalities whilst encapsulating much of the physics of invisibility.

Let us consider the two-dimensional conductivity equation in a bounded cylindrical domain Ω with no source

$$\nabla \cdot (\kappa(\mathbf{x}) \nabla u) = 0 \,, \tag{27}$$

where u represents the static (heat, electric, magnetic) field, at each point $\mathbf{x} = (x, y)$ in Ω. Moreover, κ is the thermal conductivity, permittivity, permeability depending upon the context. Upon a change of variable $\mathbf{x} = (x, y) \to \mathbf{x}' = (x', y')$ described by a Jacobian matrix $\mathbf{J} = \partial(x', y')/\partial(x, y)$, this equation takes the form:

$$\nabla \cdot \left(\mathbf{J}^{-T} \kappa(\mathbf{x}') \mathbf{J}^{-1} \det(\mathbf{J}) \nabla u \right) = 0 \,. \tag{28}$$

We note that (27) and (28) have the same structure, except that the transformed conductivity

$$\underline{\underline{\kappa}}' = \mathbf{J}^{-T} \kappa \mathbf{J}^{-1} \det(\mathbf{J}) = \kappa \mathbf{J}^{-T} \mathbf{J}^{-1} \det(\mathbf{J}) = \kappa \mathbf{T}^{-1} \,, \tag{29}$$

is matrix-valued, with $\mathbf{T}$ the metric tensor.
An elegant way to derive (28) is to multiply (27) by a smooth function $\phi \in C_0^\infty(\Omega)$ (that is an infinitely differentiable function with a compact support on Ω) and to further integrate by parts, which yields the following variational form:

$$\int_\Omega (\nabla\phi \cdot \kappa\nabla u)\, dxdy - \int_{\partial\Omega} (\kappa\nabla u \cdot \mathbf{n}\phi - \kappa\nabla\phi \cdot \mathbf{n}u)\, dl = 0\ , \tag{30}$$

where $\mathbf{n}$ is the unit outward normal to the boundary $\partial\Omega$ of the integration domain Ω.

We now apply to (30) the coordinate change $\mathbf{x} = (x, y) \to \mathbf{x}' = (x', y')$ and noting that $\nabla = \mathbf{J}^{-1}\nabla'$, where ∇' is the gradient in the new coordinates, we end up with

$$\begin{aligned} &\int_\Omega \left\{ \left(\mathbf{J}^{-1}\nabla'\phi \cdot \kappa\mathbf{J}^{-1}\nabla' u\right) \det(\mathbf{J}) \right\} dx'dy' \\ &-\int_{\partial\Omega} \left\{ \left(\kappa\mathbf{J}^{-1}\nabla' u \cdot \mathbf{n}\phi - \kappa\mathbf{J}^{-1}\nabla'\phi \cdot \mathbf{n}u\right) \det(\mathbf{J}) \right\} dl' = 0 \end{aligned} \tag{31}$$

Upon integration by parts, using $\mathbf{J}^{-1}\nabla'\phi \cdot \kappa\mathbf{J}^{-1}\nabla' u = (\nabla'\phi)^T \mathbf{J}^{-T}\kappa\mathbf{J}^{-1}\nabla' u$ we obtain the variational form of (28) which lays the foundation of transformation optics in the static case. Indeed, in the electrostatic case, the coefficient in (27) plays the role of the inverse of the permittitivy ($\kappa = \varepsilon^{-1}$), while in the magnetostatic case, it plays the role of the inverse of the permeability ($\kappa = \mu^{-1}$). The forms of the transformed permittivity $\underline{\underline{\varepsilon}}'$ and permeability $\underline{\underline{\mu}}'$ follow from (29).

6 Transformational optics: Geometrical transformations and equivalent materials

Beside Cartesian coordinates, cylindrical and spherical coordinates, and even the other orthogonal systems [78], have been commonly used to set up electromagnetic problems. Using results of the previous section, much more general coordinate systems are discussed since they do not need to be orthogonal (and not even real valued). Here, we have used a simple approach to derive the transformed permittivity and permeability, requiring only knowledge of changes of variables in integral calculus. However, when one moves to the time-dependent Maxwell system, a modern approach is to write the equations of electromagnetism in the language of exterior calculus that is covariant, i.e. independent of the choice of the coordinate system [32]. In this way, the Maxwell equations involve only the exterior derivative

and are purely topological and differential while all the metric information is contained in the material properties via a Hodge star operator. This looks rather abstract but can nevertheless be encapsulated in a very simple and practical *equivalence rule* co-discovered by A. Nicolet and F. Zolla during the 2002 IUTAM symposium organized by A.B. Movchan at Liverpool University [81; 62]:

When you change your coordinate system, all you have to do is to replace your initial material (electric permittivity tensor $\underline{\underline{\varepsilon}}$ *and magnetic permeability tensor* $\underline{\underline{\mu}}$*) properties by equivalent material properties given by the following rule:*

$$\underline{\underline{\varepsilon'}} = \mathbf{J}^{-1}\underline{\underline{\varepsilon}}\mathbf{J}^{-T}\det(\mathbf{J}) \quad \textit{and} \quad \underline{\underline{\mu'}} = \mathbf{J}^{-1}\underline{\underline{\mu}}\mathbf{J}^{-T}\det(\mathbf{J}) \tag{32}$$

where $\mathbf{J}$ *is the Jacobian matrix of the coordinate transformation consisting of the partial derivatives of the new coordinates with respect to the original ones (*$\mathbf{J}^{-T}$ *is the transposed of its inverse).*

In Eq.(32), the right hand sides involve matrix products where the matrix associated with a second rank tensor involving the coefficients of its representation in the initial Cartesian coordinate system. The obtained matrix provides the new coefficients of the tensor corresponding to the equivalent material. Eq.(32) is consistent with (29), which should not come as a surprise as the tensors of permittivity and permeability should have the same form in the Maxwell system and the electrostatic and magnetostatic equations.

However, one word on the modern differential geometry viewpoint of transformation optics would be in order [2]. Explicitly, a map from a coordinate system $\{u, v, w\}$ to the coordinate system $\{x, y, z\}$ is given by the transformation characterized by $x(u, v, w)$, $y(u, v, w)$ and $z(u, v, w)$. As we start with a given set of equations in a given coordinate system, it seems at first sight that we have to map these coordinates on the new ones. Nevertheless it is the opposite that has to be done: the new coordinate system is mapped on the initial one (i.e. the new coordinates are defined as explicit functions of the initial coordinates) and the equations are then pulled back, according to differential geometry [32], on the new coordinates. This provides directly the functions whose derivatives are involved in the computation of the Jacobian matrix. The Jacobian is directly given by:

$$\mathbf{J}_{xu} = \begin{pmatrix} \frac{\partial x}{\partial u} & \frac{\partial x}{\partial v} & \frac{\partial x}{\partial w} \\ \frac{\partial y}{\partial u} & \frac{\partial y}{\partial v} & \frac{\partial y}{\partial w} \\ \frac{\partial z}{\partial u} & \frac{\partial z}{\partial v} & \frac{\partial z}{\partial w} \end{pmatrix} = \frac{\partial(x, y, z)}{\partial(u, v, w)} \, . \tag{33}$$

[2] The author wishes to thank A. Nicolet from Aix-Marseille University for his wisdom and guidance through the wonderland of differential forms over the past fifteen years.

The *equivalence rule* (32) can be extended to more general material properties such as local Ohm's law and bianisotropic materials [62]. Moreover, the rule given by Eq. (1) may be easily applied to a composition of transformations. Let us consider three coordinate systems $\{u, v, w\}$, $\{X, Y, Z\}$, and $\{x, y, z\}$.
The two successive changes of coordinates are given by the sets of functions $\{X(u, v, w), Y(u, v, w), Z(u, v, w)\}$ and $\{x(X, Y, Z), y(X, Y, Z), z(X, Y, Z)\}$. They lead to the Jacobians $\mathbf{J}_{Xu}$ and $\mathbf{J}_{xX}$ so that the global Jacobian

$$\mathbf{J}_{xu} = \frac{\partial(x, y, z)}{\partial(u, v, w)} = \frac{\partial(x, y, z)}{\partial(X, Y, Z)} \frac{\partial(X, Y, Z)}{\partial(u, v, w)} = \mathbf{J}_{xX}\mathbf{J}_{Xu} \tag{34}$$

The compound transformation can therefore be considered either as involving this global Jacobian or as successive applications of Eq. (1). This rule naturally applies for an arbitrary number of coordinate systems. Note that the maps are defined from the final u, v, w to the original x, y, z coordinate system and that the product of the Jacobians, corresponding to the composition of the pull back maps, is in the opposite order.

When the initial material properties ε and μ are isotropic and described by a scalar, they generally lead to anisotropic properties and are given via a transformation matrix $\mathbf{T} = \mathbf{J}^T\mathbf{J}/\det(\mathbf{J})$ related to the metric expressed in the new coordinates so that the *Nicolet-Zolla equivalence rule* (32) becomes

$$\underline{\underline{\varepsilon}}' = \varepsilon\mathbf{T}^{-1}\,, \quad \text{and} \quad \underline{\underline{\mu}}' = \mu\mathbf{T}^{-1}\,. \tag{35}$$

We note that there is no change in the impedance of the media since the permittivity and permeability suffer the same transformation. As inhomogeneous and anisotropic equivalent materials are obtained and as the theoretical framework is the exterior calculus, the (Whitney) finite element method is perfectly adapted to the numerical algorithm implementation [33; 39; 40]. In fact, this goes beyond simple change of coordinates as we will also consider active transformations, i.e. changes of space (i.e. of manifold) where the equations are written.

6.1 Useful Jacobians in polar in spherical coordinates

It is very often useful to use radial transformations. In this case, the most simple way is to first perform a transformation to cylindrical or spherical coordinates and to perform the inverse transformation once the radial transformation has been made. First, the classical transformation from Cartesian coordinates (x, y, z) to polar coordinates (ρ, θ, z) is introduced

via a map from ρ, θ to x, y:

$$\begin{cases} x(\rho,\theta) = \rho\cos\theta \\ y(\rho,\theta) = \rho\sin\theta. \end{cases} \tag{36}$$

The associated Jacobian is

$$\mathbf{J}_{x\rho}(\rho,\theta) = \frac{\partial(x,y,z)}{\partial(\rho,\theta,z)} = \begin{pmatrix} \cos\theta & -\rho\sin\theta & 0 \\ \sin\theta & \rho\cos\theta & 0 \\ 0 & 0 & 1 \end{pmatrix} = \mathbf{R}(\theta)\ \mathbf{diag}(1,\rho,1), \tag{37}$$

with

$$\mathbf{R}(\theta) = \begin{pmatrix} \cos\theta & -\sin\theta & 0 \\ \sin\theta & \cos\theta & 0 \\ 0 & 0 & 1 \end{pmatrix} \text{ and } \mathbf{diag}(1,\rho,1) = \begin{pmatrix} 1 & 0 & 0 \\ 0 & \rho & 0 \\ 0 & 0 & 1 \end{pmatrix}.$$

$\mathbf{R}(\theta)$ is a matrix of rotation through an angle θ about the z-axis which has the well known properties: $\mathbf{R}(\theta)^{-1} = \mathbf{R}(\theta)^T = \mathbf{R}(-\theta)$.

Furthermore, the inverse transformation of (36) is given by the map:

$$\begin{cases} \rho(x,y) = \sqrt{x^2+y^2} \\ \theta(x,y) = 2\arctan\left(\frac{y}{x+\sqrt{x^2+y^2}}\right), \end{cases} \tag{38}$$

and is associated with the Jacobian:

$$\mathbf{J}_{\rho x}(x,y) = \mathbf{J}_{x\rho}^{-1}(\rho(x,y),\theta(x,y)) = \mathbf{diag}(1, \frac{1}{\rho(x,y)}, 1)\ \mathbf{R}(-\theta(x,y)). \tag{39}$$

Similarly, the spherical coordinates are described via a map from ρ, θ, φ to x, y, z:

$$\begin{cases} x = \rho\cos\theta\sin\varphi \\ y = \rho\sin\theta\sin\varphi \\ z = \rho\cos\varphi. \end{cases} \tag{40}$$

The spherical Jacobian:

$$\mathbf{J}_{x\rho}(\rho,\theta,\varphi) = \begin{pmatrix} \cos\theta\sin\varphi & -\rho\sin\theta\sin\varphi & \rho\cos\theta\cos\varphi \\ \sin\theta\sin\varphi & \rho\cos\theta\sin\varphi & \rho\sin\theta\cos\varphi \\ \cos\varphi & 0 & -\rho\sin\varphi \end{pmatrix}, \tag{41}$$

can be written as $\mathbf{J}_{x\rho} = \mathbf{R}(\theta)\mathbf{M}_2(\varphi)\mathbf{diag}(1,\rho\sin\varphi,\rho)$ still involving the $\mathbf{R}(\theta)$ matrix together with:

$$\mathbf{M_2}(\varphi) = \begin{pmatrix} \sin\varphi & 0 & \cos\varphi \\ 0 & 1 & 0 \\ \cos\varphi & 0 & -\sin\varphi \end{pmatrix}, \tag{42}$$

with the properties: $\mathbf{M}_2^{-1}(\varphi) = \mathbf{M}_2^T(\varphi) = \mathbf{M}_2(\varphi)$. All this, and much more, can be found in [70; 69].

7 Problems with open boundary conditions

One of the primary applications of non orthogonal coordinates is the modelling of infinite domains [57]. In the electrostatic or magnetostatic case as well as in the eddy current case, the solution decreases to zero at infinity. Several types of infinite elements have been introduced (when the problem was not brutally truncated at finite distance) but the most efficient ones correspond to a mapping of a finite domain on the exterior infinite domain [51; 63].

In the case of propagation problems, a transformation of an infinite domain into a finite one as presented above would contract the wavelength to an infinitely small value as the outer boundary is approached so that a well adapted mesh would be difficult to obtain. In this case, the solution is to introduce the Perfectly Matched Layers (PML).Such regions have been introduced by Berenger [31] and, nowadays, in the time harmonic case, the most natural way to introduce PML is to consider them as maps on a complex space [54] so that the corresponding change of (complex) coordinates leads to equivalent ε and μ (that are complex, anisotropic, and inhomogeneous even if the original ones were real, isotropic, and homogeneous). This leads automatically to an equivalent medium with the same impedance as the one of the initial ambient medium since ε and μ are transformed in the same way and this insures that the interface with the layer is non-reflecting. Moreover, a correct choice of the complex map leads to an absorbing medium able to dissipate the outgoing waves. The problem can therefore be properly truncated under the condition that the artificial boundary is situated in a region where the field is damped to a negligible value.

For isotropic uniform media outside the region of interest, the cylindrical PML is an annulus whose characteristics are obtained by multiplying ε and μ by the following complex matrix:

$$\mathbf{T}_{PML}^{-1} = \mathbf{J}_{PML}^{-1}\mathbf{J}_{PML}^{-T}\det(\mathbf{J}_{PML}) = \mathbf{R}(\theta)\mathbf{diag}(\frac{\tilde{\rho}}{s_\rho\rho}, \frac{s_\rho\rho}{\tilde{\rho}}, \frac{s_\rho\tilde{\rho}}{\rho})\mathbf{R}(-\theta).$$

This latest expression is the metric tensor in Cartesian coordinates (x, y, z) for the cylindrical PML. $\theta, \rho, \tilde{\rho}$, and $s_\rho(\rho)$ are explicit functions of the vari-

ables x and y, *i.e.* $\theta = 2\arctan\left(\frac{y}{x+\sqrt{x^2+y^2}}\right)$, $\rho = \sqrt{x^2+y^2}$, $s_\rho(\rho) = s_\rho(\sqrt{x^2+y^2})$, and $\tilde{\rho} = \int_0^{\sqrt{x^2+y^2}} s_\rho(\rho')d\rho'$ where $s_\rho(\rho')$ is an arbitrary but well chosen complex valued function of a real variable that describes the radial stretch relating the initial radial distance ρ to the complex one $\tilde{\rho}$.

Another remarkable property of the PML is that they provide the correct extension to non-Hermitian operators (since $\mathbf{T}_{PML}$ is complex and symmetric) that allows the computation of the leaky modes in waveguides [66] and this may be obtained via a correct choice of the PML parameters, namely R^*, R^{trunc} such that $R^* < \rho < R^{trunc}$, and $s_\rho(\rho)$ [72].

8 Helicoidal geometries and twisted optical fibres

The purpose of this section is to show how the *Nicolet-Zolla equivalence rule* (32) can be used to study the propagation of modes in twisted waveguides via a two-dimensional model though the translational invariance of the geometry is lost.

Figure 7. A twisted structure that may be described by the helicoidal coordinates (courtesy of F. Zolla, Institut Fresnel).

Let us introduce an helicoidal coordinate system [56; 50] (ξ_1, ξ_2, ξ_3) deduced from rectangular Cartesian coordinates (x, y, z) in the following way

$$\begin{cases} x = \xi_1 \cos(\alpha\xi_3) + \xi_2 \sin(\alpha\xi_3) \\ y = -\xi_1 \sin(\alpha\xi_3) + \xi_2 \cos(\alpha\xi_3) \\ z = \xi_3 \ , \end{cases} \tag{43}$$

where α is a parameter which characterizes the torsion of the structure. A *twisted structure* is a structure for which both geometrical and physical characteristics (here the permittivity ε and the permeability μ) together

with the boundary conditions only depend on ξ_1 and ξ_2. Note that such a structure is invariant along ξ_3 but $\frac{2\pi}{\alpha}$-periodic along z (the period may be shorter depending on the symmetry of the cross section).

This general coordinate system is characterized by the Jacobian of the transformation (43):

$$\mathbf{J}_{hel}(\xi_1,\xi_2,\xi_3) = \begin{pmatrix} \cos(\alpha\xi_3) & \sin(\alpha\xi_3) & \alpha\xi_2\cos(\alpha\xi_3) - \alpha\xi_1\sin(\alpha\xi_3) \\ -\sin(\alpha\xi_3) & \cos(\alpha\xi_3) & -\alpha\xi_1\cos(\alpha\xi_3) - \alpha\xi_2\sin(\alpha\xi_3) \\ 0 & 0 & 1 \end{pmatrix}, \quad (44)$$

which does depend on the three variables ξ_1, ξ_2 and ξ_3. On the contrary, the transformation matrix $\mathbf{T}_{hel}$:

$$\mathbf{T}_{hel}(\xi_1,\xi_2) = \frac{\mathbf{J}_{hel}^T\mathbf{J}_{hel}}{det(\mathbf{J}_{hel})} = \begin{pmatrix} 1 & 0 & \alpha\xi_2 \\ 0 & 1 & -\alpha\xi_1 \\ \alpha\xi_2 & -\alpha\xi_1 & 1+\alpha^2(\xi_1^2+\xi_2^2) \end{pmatrix}, \quad (45)$$

which describes the change in the material properties, only depends on the first two variables ξ_1 and ξ_2 [64; 65; 66]. This matrix may also conveniently be expressed in terms of twisted cylindrical coordinates:

$$\begin{aligned} &\mathbf{R}(\varphi)\begin{pmatrix} 1 & 0 & 0 \\ 0 & 1 & -\rho\alpha \\ 0 & -\rho\alpha & 1+\rho^2\alpha^2 \end{pmatrix}\mathbf{R}(-\varphi) \\ &= \begin{pmatrix} 1 & 0 & \alpha\rho\sin(\varphi) \\ 0 & 1 & -\alpha\rho\cos(\varphi) \\ \alpha\rho\sin(\varphi) & -\alpha\rho\cos(\varphi) & 1+\rho^2\alpha^2 \end{pmatrix}, \end{aligned}$$

with $\varphi = 2\arctan\left(\frac{\xi_2}{\xi_1+\sqrt{\xi_1^2+\xi_2^2}}\right)$, $\rho = \sqrt{\xi_1^2+\xi_2^2}$.

Helicoidal coordinates have also been combined with PML to compute the leaky modes in twisted microstructured optical fibres [66].

$$\mathbf{T}_{hPML} = \mathbf{R}(\varphi)\begin{pmatrix} \frac{\rho s_\rho}{\tilde\rho} & 0 & 0 \\ 0 & \frac{\tilde\rho}{\rho s_\rho} & -\alpha\frac{\tilde\rho}{s_\rho} \\ 0 & -\alpha\frac{\tilde\rho}{s_\rho} & \frac{\rho(1+\alpha^2\tilde\rho^2)}{\tilde\rho s_\rho} \end{pmatrix}\mathbf{R}(-\varphi). \quad (46)$$

This is the expression of the "twisted cylindrical PML tensor" in "helicoidal Cartesian modelling coordinates" ξ_1,ξ_2 and all the quantities involved in the previous expression can be given as explicit functions of these two variables, joining $s_\rho(\rho) = s_\rho(\sqrt{\xi_1^2+\xi_2^2})$ and $\tilde\rho = \int_0^{\sqrt{\xi_1^2+\xi_2^2}} s_\rho(\rho')d\rho'$ to the expressions for ρ and φ given here above.

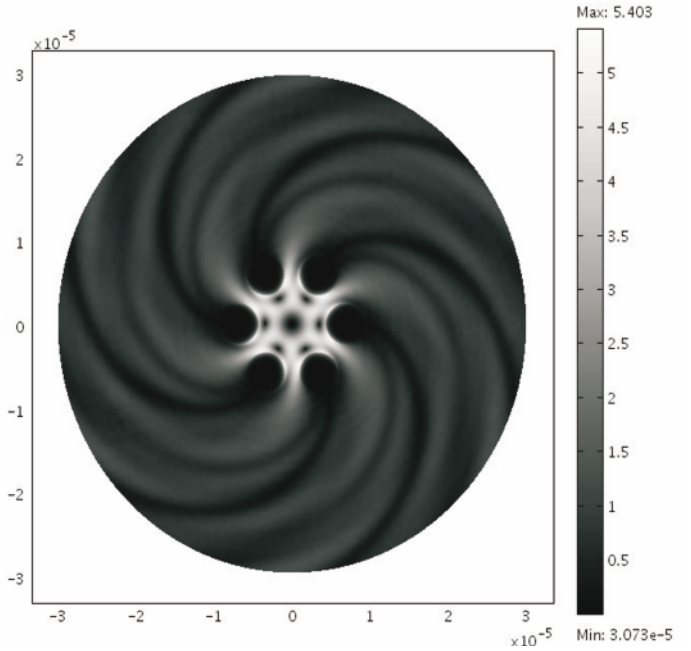

Figure 8. Map of the norm of the longitudinal component of the electric field for a strongly twisted fibre ($\alpha = 50,000\, m^{-1}$) with very large losses.The map is truncated at the inner boundary of the PML, the field unit on the gray scale is arbitrary, and dimensions on the axes are in m (courtesy of F. Zolla, Institut Fresnel).

The fact that the equivalent materials are independent from the longitudinal coordinate ξ_3 allows a two-dimensional model for the determination of the propagation modes and of the leaky modes via a classical model provided it allows completely anisotropic and inhomogeneous media. Luckily, the finite element method allows such a numerical computation.

Figure (8) shows a microstructured optical fibre or MOF [46; 47; 48; 49; 81]. It is a dielectric waveguide whose structure consists of a bulk of silica (supposed to be unbounded) drilled by six air holes with a center-to-center spacing $\Lambda = 6.75\,\mu m$. Each hole is circular with a radius equal to $r_s = 2.5\,\mu m$. A given wavelength $\lambda_0 = 1.55\,\mu m$ is considered for which the index of silica is about $\sqrt{\varepsilon_{\mathrm{Si}}} = n_{\mathrm{Si}} = 1.444024$. Note that for this structure no propagating mode can be found and the fundamental mode is a leaky mode. The figure shows the norm of the longitudinal component of the

electric field for the "fundamental mode" in the case of a very strong twist ($\alpha = 50,000\, m^{-1}$) for which the losses are very large.

9 Invisibility cloaking

The geometrical transformations can also be used in the reverse sense to design new materials. In this case, a geometrical transformation is applied to free space to guess interesting material properties given by the *Nicolet-Zolla equivalence rule*. A new device can be built if the new material properties may be approximated, *e.g.* using electromagnetical metamaterials [75]. For instance, a convex domain is mapped on a holey domain with the same exterior boundary. The structure made of the transformed equivalent material is an invisibility cloak and any object can be perfectly hidden in the central hole [74; 82].

To compute the transformation matrix $\mathbf{T}$ associated with the cloak, we first map Cartesian coordinates onto polar co-ordinates (ρ, θ, z). The associated Jacobian matrix is given by (37). Let us now consider a 2D object we want to cloak located within a disk of radius R_1. As proposed in [74], we consider a geometric transformation which maps the field within the disk $\rho \leq R_2$ onto the annulus $R_1 \leq \rho \leq R_2$:

$$\begin{cases} \rho' = R_1 + \rho(R_2 - R_1)/R_2 \ , \ 0 \leq \rho \leq R_2 \\ \theta' = \theta \ , \ 0 < \theta \leq 2\pi \\ z' = z \ , \ z \in \mathbb{R} \ , \end{cases} \tag{47}$$

where ρ', θ' and z' are "radially contracted cylindrical coordinates". Moreover, this transformation maps the field for $\rho \geq R_2$ onto itself through the identity transformation. This leads to

$$\mathbf{J}_{\rho\rho'} = \frac{\partial(\rho, \theta, z)}{\partial(\rho', \theta', z')} = \mathbf{diag}(c_{11}, 1, 1) \tag{48}$$

where $c_{11} = R_2/(R_2 - R_1)$ for $0 \leq \rho \leq R_2$ and $c_{11} = 1$ for $\rho > R_2$.

Last, we need to go to Cartesian coordinates x', y', z', which are "radially contracted Cartesian coordinates" where the modeling takes place to obtain a representation of the metric tensor in the suitable coordinate system. The associated Jacobian matrix is given by (39):

$$\mathbf{J}_{\rho' x'}(x', y') = \frac{\partial(\rho', \theta', z')}{\partial(x', y', z')} = \mathbf{J}_{\rho x}^T(\frac{1}{\rho'}, \theta') = \mathbf{diag}(1, \frac{1}{\rho'}, 1)\ \mathbf{R}(-\theta'). \tag{49}$$

Applying the composition rule twice, $\mathbf{J}_{xx'} = \mathbf{J}_{x\rho}\mathbf{J}_{\rho\rho'}\mathbf{J}_{\rho' x'}$, hence the material properties of the invisibility cloak are described by the transformation

matrix $\mathbf{T} = \mathbf{J}_{xx'}^T \mathbf{J}_{xx'}/det(\mathbf{J}_{xx'})$. We will also need its inverse that we give explicitly, taking into account that $\rho(\rho') = c_{11}(\rho' - R_1)$:

$$\mathbf{T}^{-1} = \mathbf{R}(\theta')\mathbf{diag}(\frac{\rho' - R_1}{\rho'}, \frac{\rho'}{\rho' - R_1}, \frac{c_{11}^2(\rho' - R_1)}{\rho'})\mathbf{R}(-\theta'). \qquad (50)$$

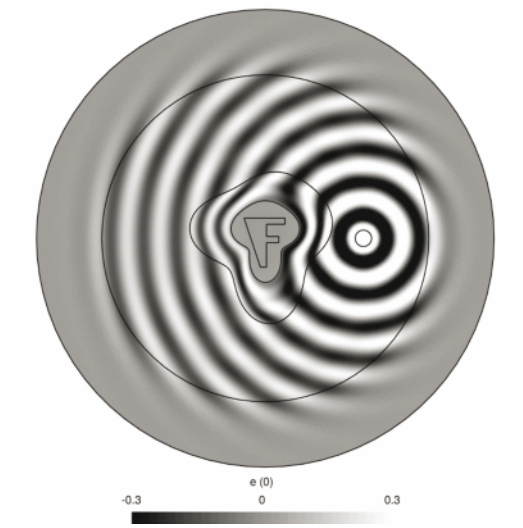

Figure 9. Cloak with a general shape surrounding a F-shaped metallic object in presence of a line electric source generating transverse electric waves. Plot of the real part of the longitudinal magnetic field. (courtesy of A. Nicolet, Institut Fresnel).

A quite general situation is considered in Fig. 9, where the shape of the cloak is described by two arbitrary functions $R_1(\theta)$ and $R_2(\theta)$ giving an angle dependent distance from the origin corresponding respectively to the interior and exterior boundary of the cloak [70; 69].

Three dimensional cloaks

The three-dimensional cloaks may be determined following the same guidelines but using the spherical coordinates : The Jacobian of the radial contraction $\mathbf{J}_{\rho\rho'} = \mathbf{diag}(c_{11}, 1, 1)$ is still the same (ρ is now the radius of a

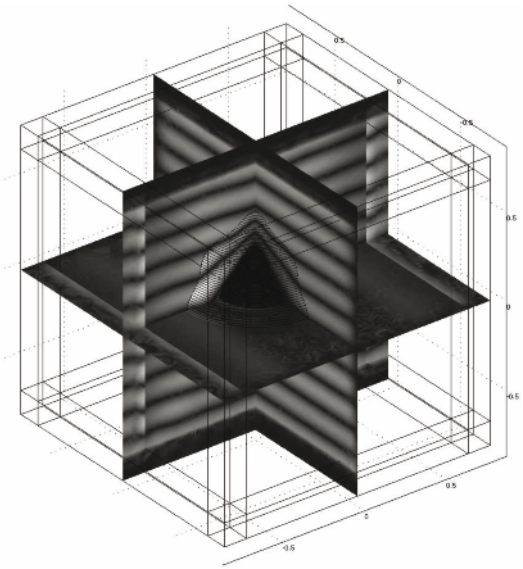

Figure 10. Three-dimensional cloak with a general shape of revolution about one axis given by Fourier series (courtesy of G. Dupont, Institut Fresnel).

sphere). The total Jacobian is therefore :

$$\begin{array}{l}\mathbf{R}(\theta)\mathbf{M}_2(\varphi)\mathbf{diag}(1,\rho\sin\varphi,\rho)\mathbf{diag}(c_{11},1,1)\mathbf{diag}(1,1/(\rho'\sin\varphi'),1/\rho')\\ \mathbf{M}_2(\varphi')\mathbf{R}^T(\theta') = \mathbf{R}(\theta)\mathbf{M}_2(\varphi)\mathbf{diag}(c_{11},\rho/\rho',\rho/\rho')\mathbf{M}_2(\varphi)\mathbf{R}^T(\theta)\end{array},$$

where we used the fact that $\varphi = \varphi'$ and $\theta = \theta'$. The matrix for the equivalent media is finally:

$$\mathbf{T}^{-1} = \mathbf{R}(\theta)\mathbf{M}_2(\varphi)\mathbf{diag}(\frac{\rho^2}{c_{11}\rho'^2}, c_{11}, c_{11})\mathbf{M}_2(\varphi)\mathbf{R}^T(\theta). \tag{51}$$

Three-dimensional arbitrary cloaks can be found by varying their interior and exterior radii with respect to the angular coordinates: $R_1(\theta,\varphi), R_2(\theta,\varphi)$. An illustrative example is shown in Fig. 10, whereby a plane wave incident from below is smoothly detoured around the central region inside the cloak (the amplitude of the electromagnetic field vanishes there).

Let us now move to the last part of the chapter, which introduces the field of plasmonics and its connections to metamaterials.

10 Introduction to plasmonics and structured surfaces

At the beginning of the last century, R.M. Wood [148] showed that when he sends a polarised light on a diffraction grating on metal plate, a very unusual reflected pattern of dark and light bands can be observed. That was the first noticed observation of uncommon attenuated reflection on gratings. A few years later, in 1907, Lord Rayleigh [136] showed theoretically some basic properties of gratings using a plane wave expansion of the scattered electromagnetic field. He found that the scattered field was singular at wavelengths for which one of the spectral orders emerged from the grating at the grazing angle. He then observed that these wavelengths corresponded to the Wood anomalies. Furthermore, these singularities appeared only when the electric field was polarized perpendicular to the grooves. When the magnetic field was perpendicular, there was no anomaly [149]. More explanations were given by Palmer [127] for deep gratings.

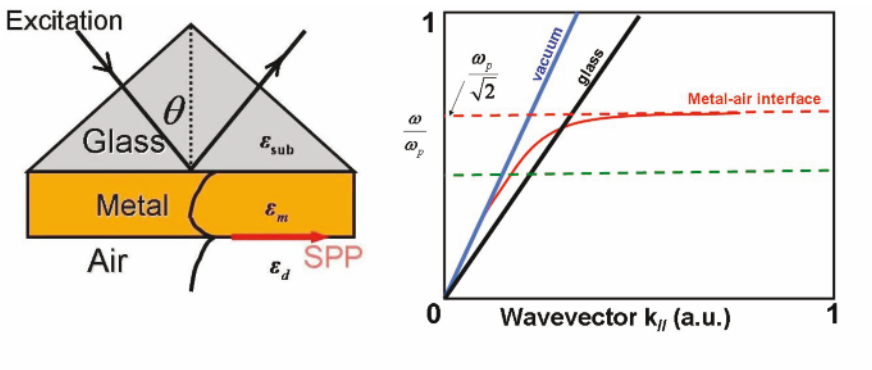

Figure 11. (a) Kretschmann's configuration [106]: the metal film is evaporated onto the glass prism. The light is incident through the glass substrate. The surface plasmon polaritons (SPPs) are excited on the metal-air interface. One of the mandatory conditions for the excitation of the plasmon is that the projection of the wavevector $k_{//}$ of light matches the one of the plasmon. We represent the dispersion curves for metal-air interface (red curve) as well as the light line in air (blue line) and glass (black line). Curves show how a SPP can be excited on this metal-air interface through a glass substrate in the region between the blue and the black lines.

Pines [132; 133] suggested that the energy losses of the Wood anomalies are due to the excitation of conducting electrons associated with a plasmon. The term surface plasmon polariton (SPP) was coined by Stewart, Hessel

and Ritchie [142], [94] and [137]. It is only in 1968 that Kretschmann [106] and Otto [124] demonstrated how to generate Surface Plasmon excitations. Since then SPPs have found many applications in biology [114] and chemistry [108]. As the list of references is extensive, we refer to other books and papers that describe a complete history of SPPs [120], [97], [135], [88] and [89]. However, in order to exemplify the mechanism leading to the excitation of SPPs, we present a classical experimental setup (Figure 11) to generate an SPP.

One word on the SPP terminology would be in order. Surface plasmons (SPs) are defined as electromagnetic waves associated with a collective oscillation of the electrons in the free electrons plasma on the surface of a metal. Polaritons are quasiparticles resulting from strong coupling of electromagnetic waves with an electric or magnetic dipole excitation. They result in the crossing of the dispersion of light with any interacting resonance. It corresponds to the mixing of a photon with an excitation of a material. The most frequently discussed types of polaritons are :

- phonon-polaritons: corresponding to the coupling of an infrared photon with an optic phonon,
- exciton-polaritons, corresponding to the coupling of visible light with an exciton,
- surface plasmon-polaritons: corresponding to the coupling of surface plasmons with light

A polariton can be associated with that wave and is called surface plasmon polariton (SPP). In Figure 12 the electromagnetic field distribution of these surface waves is shown. The field has its maximum amplitude at the interface and decays exponentially in the direction normal to the interface. Figure 12 shows how a SPP can be excited on this metal-air interface trough a glass substrate. The required momentum matching is fulfilled there. From the theoretical point of view the condition to fulfill is:

$$k_{inc//} = k_{SP} \ , \tag{52}$$

where k_{inc} is the wave vector of the incident electromagnetic field through the glass substrate and k_{SP} is the wave vector for a surface plasmon on the air-metal interface. We note this SPP cannot be excited directly from the *air* side (as $k_{sp} > \omega/c$). An approximation of this condition can be done if the metal is thick enough:

$$k_{inc} = n_{glass} k_0 \quad , k_{inc//} = n_{glass} k_0 \sin\theta \quad \text{and} \quad k_{SP} = \frac{\omega}{c}\sqrt{\frac{\varepsilon_1 \varepsilon_2}{\varepsilon_1 + \varepsilon_2}} \ , \tag{53}$$

where c is the speed of light in a vacuum, ε_1 and ε_2 are respectively dielectric functions (dielectric (air) and metal (gold)) and ω is the angular frequency.

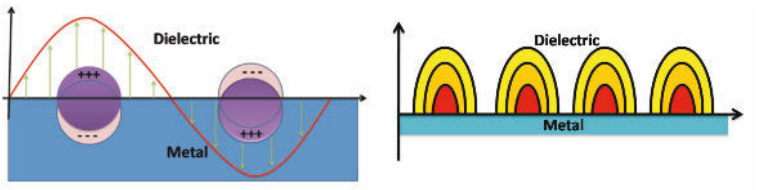

Figure 12. Schematic representation of the electric field of a Surface Plasmon oscillation (left) and amplitude of the magnetic component(right).

We note that there are many different ways of exciting an SPP using rough surfaces but in this chapter we will assume that we have launched successfully the SPP on the metal surface.

11 Origin of the Drude model for metals

Many models have been developed for physical properties of materials such as permittivity and permeability for metal. In the sequel we will mainly use the Drude model as well as some experimental data from [126].

Free electron gas model The simplest case is to consider a free electron gas without any collision. In this case the only force applied to the electron is the Coulomb force. Let us consider that a charge $-e$ (with a mass m) is located in an electric field $\mathbf{E}(t) = \mathbf{E}_0 e^{-i\omega t}$ (where e is the charge of an electron, t the time variable, $\mathbf{r}$ the position vector and ω the angular frequency).
The equation of motion is given by Newton's second law:

$$m\frac{d^2\mathbf{r}}{dt^2} - e\mathbf{E} = \mathbf{0} \tag{54}$$

The immediate solution is given by:

$$\mathbf{r}(t) = \frac{e}{m\omega^2}\mathbf{E}(t) \tag{55}$$

Let us now introduce the dielectric displacement $\mathbf{D}$ and the polarisation $\mathbf{P}$, which are functions of the electric field $\mathbf{E}$, the electron density n and the

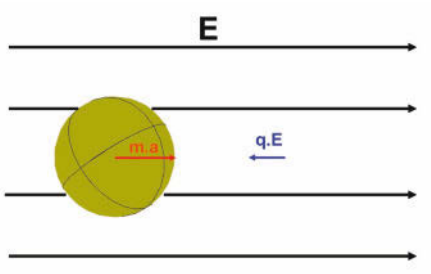

Figure 13. An electron in an electric field: $\mathbf{E}$ is the electric field, q the charge of an electron, $\mathbf{a} = d^2\mathbf{r}/dt^2$ is the acceleration and m the mass of the charge.

displacement $\mathbf{r}$:

$$\mathbf{D} = \varepsilon_0\mathbf{E} + \mathbf{P} \ , \ \mathbf{P} = -n(e\mathbf{r}) \tag{56}$$

Using the definition of the polarisation $\mathbf{P}$ and substituting in Eq. 55, we find:

$$\mathbf{P}(t) = -\frac{ne^2}{m\omega^2}\mathbf{E}(t) \tag{57}$$

Introducing $\mathbf{P}$ in the definition of $\mathbf{D}$ we have:

$$\mathbf{D}(t) = \varepsilon(\omega).\varepsilon_0.\mathbf{E}(t) = \varepsilon_0\mathbf{E}(t) - \frac{ne^2}{m\omega^2}\mathbf{E}(t) \tag{58}$$

Finally we obtain:

$$\varepsilon(\omega) = 1 - \frac{ne^2}{\varepsilon_0 m\omega^2} \tag{59}$$

And if we call ω_p the plasma fraquency with

$$\omega_p^2 = \frac{ne^2}{\varepsilon_0 m} \tag{60}$$

we end up with the common formula for the free electron gas (perfect metal):

$$\varepsilon(\omega) = 1 - \frac{\omega_p^2}{\omega^2} \tag{61}$$

We note that there are no losses in this case, henceforth this consideration is clearly not adapted in the optical region for metals.

Lossy metal By rewriting the equation of motion of an electron of the plasma sea in an electric field $\mathbf{E}$ in presence of collision of electrons, we have to introduce the collision frequency γ so that the motion equation takes the new form:

$$m\frac{d^2\mathbf{r}}{d^2t} + m\gamma\frac{d\mathbf{r}}{dt} = -e\mathbf{E} \tag{62}$$

where $\mathbf{r}$ is the position vector, t the time variable, m the mass and e the charge of an electron.
As in the previous paragraph, using the solution of 62 and the definition of the polarisation, we end up with the complex permittivity of the free electron gas:

$$\varepsilon(\omega) = 1 - \frac{\omega_p^2}{\omega^2 + i\gamma\omega} \tag{63}$$

This function is complex valued and takes into account losses in metal (collision). We will use this model to fit the permittivity of the metal.

12 Basic properties of Surface Plasmon Polaritons

Considering the surface plasmon polariton (SPP) as an electromagnetic mode localized at the interface between dielectric and metal, we will look at the relation between the frequency ω and the wave vector $\mathbf{k}$. This wave is linked to the wave vector $\mathbf{k}$ by a dispersion relation. We show the existence conditions of surface plasmons from the Maxwell's equations using the outgoing wave condition (ow.c) and the conditions at the boundary between the two media. We consider two semi-infinite media, one consisting of a dielectric environment with real permittivity ε_d and the other one of a metal of complex permittivity $\varepsilon = \varepsilon_m^{'} + \imath\varepsilon_m^{''}$. As a first step we will consider perfect non-absorbent metal i.e. $\varepsilon_m^{''} = 0$. Figure 14 shows the layout of the system. The $xy-$ plane is defined as the interface and the z direction is perpendicular to the interface. The plasmon propagates along the x direction: this means that the system is translationally invariant along the $y-$ direction. In this section we will consider both media non magnetic (i.e. $\mu = \mu_0$) and we take the general form of the field as follows:
We define Φ_j (with $j = d, m$: dielectric or metal) the transverse component of the EM field with E being the electrical field and H the magnetic field:

$$\Phi_j = \begin{cases} E_{jy} & \text{for a transverse electric polarization (TE), or s-polarization} \\ H_{jy} & \text{for a transverse magnetic polarization (TM), or p-polarization} \end{cases}, \quad . \tag{64}$$

We consider a time dependency of the form $e^{-i\omega t}$, where ω is the angular frequency and c the light velocity. In this case the vector Maxwell's

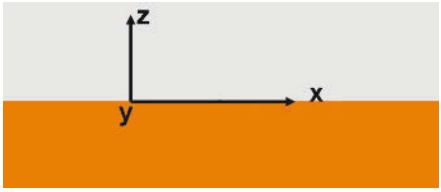

Figure 14. Layout of the system: two semi-infinite layers

equations reduce to the scalar Helmholtz equation:

$$\Delta\Phi_j + \varepsilon_j \frac{\omega^2}{c^2}\Phi_j = 0 \ , \tag{65}$$

where ε_j is the dielectric constant of the medium j (with $j = d, m$: dielectric or metal).
Here, $k = \mid \mathbf{k} \mid$ is the angular wave number. As $\mathbf{k}$ is a vector it can be written as a sum of two vector components: $\mathbf{k} = k_x\mathbf{e}_x + k_z\mathbf{e}_y$, with $\mathbf{e}_x$ and $\mathbf{e}_y$ the vectors attached to the Cartesian coordinates. Taking into account the evanescent behavior in $z-$ direction and the propagation in $x-$ direction we need to satisfy $\alpha_d > 0$ and $k'_x > 0$ (with $k_x = k'_x + k''_x 1$). Finally, the field has the following form in the dielectric and in the metal respectively:

$$\Phi_d = A_d e^{\alpha_d z} e^{i(k_x x - \omega t)} \ , \ \Phi_m = A_d e^{-\alpha_m z} e^{i(k_x x - \omega t)} \ . \tag{66}$$

For a TE wave (and non magnetic media), the transmission conditions through the interface $z = 0$ take the form:

$$\begin{array}{ll} E_d \Big|_{z=0^+} & = E_m \Big|_{z=0^-} \\ \dfrac{\partial E_d}{\partial z}\Big|_{z=0^+} & = \dfrac{\partial E_m}{\partial z}\Big|_{z=0^-} \end{array} \ .$$

Using Eq. 66, this leads to:

$$A_d = A_m \ , \ -\alpha_d A_d = \alpha_m A_m \ , \tag{67}$$

so that $-\alpha_d = \alpha_m$, which is impossible as these are positive reals. This means there is no solution for a TE wave: for this light polarization, one cannot excite any SPP on a planar metal-dielectric interface.

Considering now the TM mode, the transmission condition at the dielectric-metal interface $z = 0$ becomes:

$$\begin{array}{ll} H_d \Big|_{z=0^+} & = H_m \Big|_{z=0^-} \quad , \\ \dfrac{1}{\varepsilon_d} \dfrac{\partial H_d}{\partial z} \Big|_{z=0^+} & = \dfrac{1}{\varepsilon_m} \dfrac{\partial H_m}{\partial z} \Big|_{z=0^-} \quad . \end{array}$$

By the same way as above we find:

$$\frac{-\alpha_d}{\varepsilon_d} = \frac{\alpha_m}{\varepsilon_m} \, . \tag{68}$$

As α_d and α_m, are positive this means that we have a special existence condition for surface plasmons (keeping in mind here we assume that the metal is not lossy i.e. ε_m is real):

$$\varepsilon_d \varepsilon_m < 0 \, . \tag{69}$$

This existence condition for a p-polarized SPP can be fulfilled for a planar dielectric-metal interface.
Considering the magnetic component in Eq. 66, and using the transmission condition in Eq. 68, we obtain the dispersion relation of the propagative wave vector $\mathbf{k}$ along the $x-$ axis:

$$k_x = \frac{\omega}{c} \left(\frac{\varepsilon_d \varepsilon_m}{\varepsilon_d + \varepsilon_m} \right)^{1/2} \, . \tag{70}$$

13 From transformational optics to plasmonics

We now wish to apply transformational optics to the case of a (p-polarized) SPP propagating in the positive x direction at the interface $z = 0$ between metal ($z < 0$) and air ($z > 0$):

$$\begin{cases} \mathbf{H}_2 & = (0, H_{y2}, 0) \exp\{\imath(k_{x2} x - \omega t) - k_{z2} z\} \, , z > 0 \, , \\ \mathbf{H}_1 & = (0, H_{y1}, 0) \exp\{\imath(k_{x1} x - \omega t) + k_{z1} z\} \, , z < 0 \, , \end{cases} \tag{71}$$

where c is the speed of light in vacuum and $\varepsilon_2 = 1 - \frac{\omega_p^2}{\omega^2 + i\gamma\omega}$ has the usual Drude form in the metal($z < 0$), for which ω_p is the plasma frequency (2175 THz) of the *free electron gas* and γ is a characteristic collision frequency of about 4.35 THz [126]. As seen previously, even if the main part of the energy is located in the dielectric medium, SPP is propagating in both media

(metal and dielectric) and we have to satisfy the existence condition for that wave.
The idea is to apply the transformation optics tools for both media. SPPs are particular solutions of Maxwell's equations so that the same rules should be used. Moreover, both media (d':transformed dielectric,m':transformed metal) will be described by spatially varying tensors of permittivity $\underline{\underline{\varepsilon'_{d,m}}}$ and permeability $\underline{\underline{\mu'_{d,m}}}$. In the case of a cloak (and rotator, concentrator...) both sides will be transformed in order to preserve the existing boundary condition at the interface between the metal and the dielectric part. It is the natural condition for a cylindrical cloak as the cloak is invariant in the direction of the cylinder. Here we start with the case of a carpet. Only the top medium will be transformed.

13.1 Surface plasmon between a metal and an anisotropic medium

If we assume that both tensors of permittivity and permeability can be represented in a diagonal basis i.e. $\underline{\underline{\varepsilon'}} = \mathrm{diag}(\varepsilon_{xx2}, \varepsilon_{yy2}, \varepsilon_{zz2})$ and $\underline{\underline{\mu'}} = \mathrm{diag}(\mu_{xx2}, \mu_{yy2}, \mu_{zz2})$.

From the first Maxwell equation, we know that:

$$\left\{ \begin{array}{ll} \nabla \times \mathbf{H}_2 & = -i\omega\varepsilon_0 \underline{\underline{\varepsilon'}} \mathbf{E}_2,\ z > 0\ , \\ \nabla \times \mathbf{H}_1 & = -i\omega\varepsilon_0 \varepsilon_1 \mathbf{E}_1,\ z < 0\ , \end{array} \right. \tag{72}$$

where H_j is defined by:

$$\left\{ \begin{array}{ll} \mathbf{H}_2 & = (0,\ H_{y_2},\ 0) \exp\{\imath(k_{x2}x - \omega t) - k_{z2}z\},\ z > 0\ , \\ \mathbf{H}_1 & = (0,\ H_{y_1},\ 0) \exp\{\imath(k_{x1}x - \omega t) + k_{z1}z\},\ z < 0\ , \end{array} \right.$$

with $\Re(k_{z1})$ and $\Re(k_{z1})$ strictly positive in order to maintain evanescent fields above and below the interface $z = 0$. This leads to

$$\left\{ \begin{array}{ll} \mathbf{E}_2 & = -\frac{c}{\omega} H_{y_2} (\frac{k_{z2}}{\varepsilon_{xx2}},\ 0,\ \frac{k_{x2}}{\varepsilon_{zz2}}) \exp\{\imath(k_x x - \omega t) - k_{z2}z\},\ z > 0\ , \\ \mathbf{E}_1 & = -\frac{c}{\omega} H_{y_1} (\frac{k_{z1}}{\varepsilon_1},\ 0,\ \frac{k_{x2}}{\varepsilon_1}) \exp\{\imath(k_x x - \omega t) - k_{z1}z\},\ z < 0\ , \end{array} \right.$$

with $\mathbf{E}_j = (E_{xj}, 0, E_{zj})$. The transverse wave numbers are found by invoking the other Maxwell equation

$$\left\{ \begin{array}{ll} \nabla \times \mathbf{E}_2 & = i\omega\mu_0 \underline{\underline{\mu'}} \mathbf{H}_2,\ z > 0\ , \\ \nabla \times \mathbf{E}_1 & = i\omega\mu_0 \mathbf{H}_1,\ z < 0\ , \end{array} \right. \tag{73}$$

which leads to

$$k_{zi} = \sqrt{\varepsilon_{xx2} \left(\frac{k_x^2}{\varepsilon_{zz2}} - \mu_{yy2} \left(\frac{\omega}{c} \right)^2 \right)}\ ,\ j = 1\ , 2\ , \tag{74}$$

The boundary condition at the interface $z = 0$ requires continuity of the tangential components of the electromagnetic field, which is ensured if

$$\frac{k_{z1}}{\varepsilon_1} + \frac{k_{z2}}{\varepsilon_{xx2}} = 0\,. \tag{75}$$

Substituting (74) into (75), we obtain the dispersion relation for a surface plasmon at the interface between a metal and an invisibility carpet [100] [104]:

$$k_x = \frac{\omega}{c}\sqrt{\frac{\varepsilon_{zz2}\varepsilon_1(\mu_{yy2}\varepsilon_1 - \varepsilon_{xx2})}{\varepsilon_1^2 - \varepsilon_{xx2}\varepsilon_{zz2}}}\,. \tag{76}$$

These properties have been studied in gyrotropic materials and purely anisotropic dielectrics [92]. The main point of this condition is to preserve the existence condition of the SPP between a metal and a transformed medium which is anisotropic and heterogeneous. We see that the new query can come from the geometrical deformation (i.e. the shape of the bump) in the case of the carpet of Pendry.

14 Plasmonic carpet: Design of plasmonic paradigms

In the present section we start by showing the particular condition for a SPP to propagate on a bumped surface then we show numerically that one can control the SPP on these surfaces using transformational plasmonics.

14.1 Surface plasmon carpets: theoretical study

We now wish to apply transformational optics to plasmonics to hide under a SPP carpet. In presence of a bump, the electromagnetic field will scatter on a bumped mirror as shown in Figure 15. We want to avoid this phenomenon. All the following work stand on the fact that we want to build a similar carpet as the one of Li and Pendry for SPP. Figure 15 shows what the SPP cloak-carpet should do. However, we now wish to analyse the interaction of this SPP with a specific anisotropic heterogeneous structure, in the present case a three dimensional invisibility carpet [100], deduced from the following geometric transformation:

$$\begin{cases} x' &= x \\ y' &= y \\ z' &= \dfrac{z_2 - z_1}{z_2} z + z_1. \end{cases} \tag{77}$$

Here z' is a stretched coordinate. It is easily seen that this linear geometric transform maps the surface $z_0(x, y)$ of the horizontal plane $z(x, y) = 0$ onto

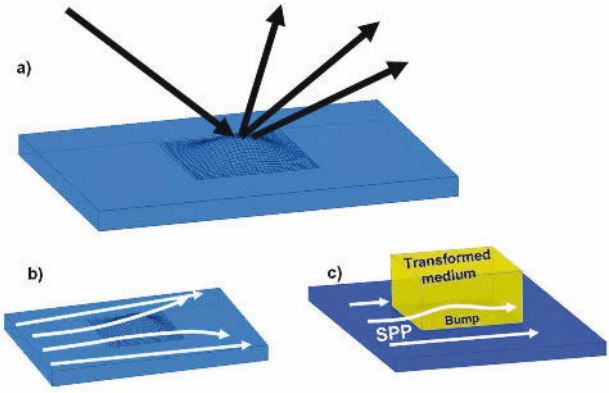

Figure 15. Principle of a three-dimensional invisibility carpet for electromagnetic fields: (a) Light incident upon a curved surface undergoes different orders of diffraction (shown as black arrows); (b) SPP propagating on a curved surface is scattered away from the metal interface (typical trajectories shown as white arrows); (c) Light incident upon a curved surface with an invisibility carpet (yellow box) undergoes the same diffraction as light incident upon a flat metal surface. SPP propagating inside the carpet stays on the curved metal surface.

the surface $z(x,y) = z_1(x,y)$, and it leaves the surface $z(x,y) = z_2(x,y)$ unchanged.
The surfaces z_1 and z_2 are assumed to be differentiable, and this ensures that the carpet won't display any singularity on its inner boundary.
The symmetric tensors $\underline{\underline{\varepsilon'}}$ and $\underline{\underline{\mu'}}$ are fully described by five non vanishing entries in a Cartesian basis:
The transformation is done only in the $z-$ direction:

$$\mathbf{J}_{zz'} = \begin{pmatrix} 1 & 0 & 0 \\ 0 & 1 & 0 \\ \dfrac{\partial z}{\partial x'} & \dfrac{\partial z}{\partial y'} & \alpha^{-1} \end{pmatrix} \tag{78}$$

where $\alpha = (z_2 - z_1)/z_2$ and with $\mathbf{J}$ the Jacobian matrix of the transformation.

It follows that transformed tensors of permittivity and permeability are:

$$\underline{\underline{\varepsilon}}' = \underline{\underline{\mu}}' = \begin{pmatrix} \alpha^{-1} & 0 & -\dfrac{\partial z}{\partial x'} \\ 0 & \alpha^{-1} & -\dfrac{\partial z}{\partial y'} \\ -\dfrac{\partial z}{\partial x'} & -\dfrac{\partial z}{\partial y'} & \alpha\left(1+\left(\dfrac{\partial z}{\partial x'}\right)^2+\left(\dfrac{\partial z}{\partial y'}\right)^2\right) \end{pmatrix} \tag{79}$$

The purpose of the next section is to show that such carpets work equally well for electromagnetic and plasmonic fields. This is due to the fact that the transformed medium is valid for any field solution of the Maxwell equations (which is obviously the case for SPPs). Importantly, we note that this material is not only heterogeneous anisotropic but also magnetic, which seems a far technological reach. However, these constraints can be further relaxed using some quasi-conformal grids in the spirit of Li and Pendry's work for two-dimensional carpets [113].

14.2 Gaussian shaped bump in a flat box

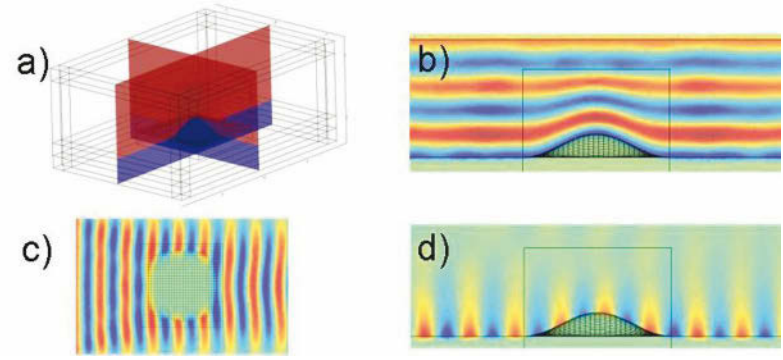

Figure 16. Amplitude (a) and real part (b) of the scattered magnetic field for a plane wave incident from the top on the carpet. (c-d) Top and side views of the real part of the magnetic field for a SPP launched from the left at the metal-dielectric interface. Courtesy of M. Kadic, Institut Fresnel.

We now wish to apply the recipe for the design of 3D carpets to specific geometrical transformations in order to hide smooth and conical shaped bumps on a metallic surface. We first present the projection of the flat sur-

face on a smooth $\cos^2$ shaped surface. This shape of the bump is described by:

$$z_1 = h_0 \cos\left(\frac{\pi x}{l}\right)^2 \cos\left(\frac{\pi y}{l}\right)^2 \text{ with } h = 2.10^{-7}\ ;\ l = 1.25\ 10^{-6}\ z_2 = 7.5\ 10^{-7} \tag{80}$$

$$\frac{\partial z_1}{\partial x} = -2h_o \cos\left(\frac{\pi x}{l}\right) .cos\left(\frac{\pi y}{l}\right)^2 . \sin\left(\frac{\pi x}{l}\right) . \frac{\pi}{l} \tag{81}$$

$$\frac{\partial z_1}{\partial y} = -2h_o \cos\left(\frac{\pi y}{l}\right) \cos\left(\frac{\pi x}{l}\right)^2 . \sin\left(\frac{\pi y}{l}\right) . \frac{\pi}{l} \tag{82}$$

We report in Figure 16 the finite element computations which exemplify the role played by the carpet in the control of the reflection of a plane wave on the bumped surface with the transformed medium, see Figure 16(panels: a and b). The bump with the transformed medium is mimicking a flat mirror. The same result is obtained for a SPP propagating on the metal surface through the transformed medium without any scattering, see Figure 16(panels: c and d).

15 Plasmonic carpet: Experimental demonstration

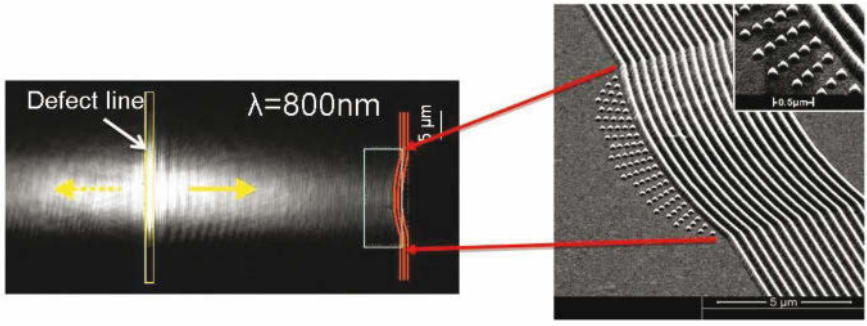

Figure 17. SEM micrograph of the structure realized by single-step electron-beam-lithography. The defect line is used to launch the SPP from the left to the structure (bump with cloak) (right). The carpet-cloak is made of TiO2 cones as shown in the zoom (right). Courtesy of J. Renger and R. Quidant, ICFO Barcelone.

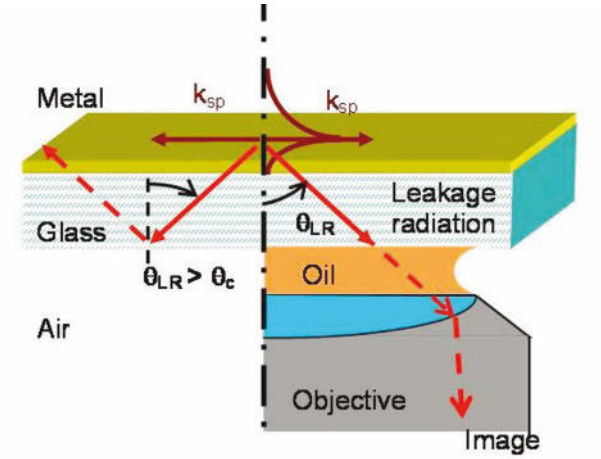

Figure 18. Leakage radiation principle. Using the Kretschmann configuration principle we can deduce that by reciprocity, a SPP propagating at the surface of thin film leaks into the substrate. Mapping the leak provides a direct information about the intensity of the surface field propagating at the interface. Courtesy of M. Kadic, Institut Fresnel.

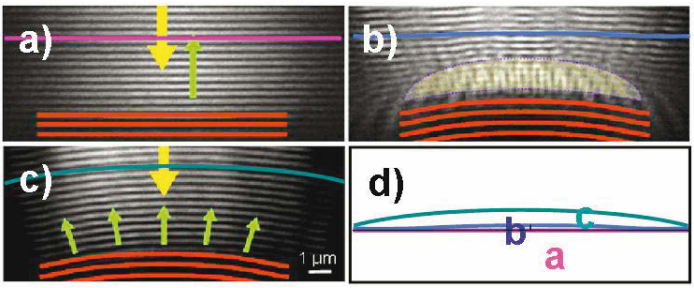

Figure 19. Experimental diffraction of a SPP incident from the top (magnetic field) (a) The SPP hits the straight reflector. (b) Cloak in front of the curved reflector nearly compensates for the curved reflector. (c) The SPP hits the curved reflector. d) Comparison of averaged curvature of SPP wavefronts in cases a) b) and c). Courtesy of J. Renger and R. Quidant, ICFO Barcelone.

The experimental results presented in this section have been obtained in ICFO in Barcelona by the team of Professor Romain Quidant. The work has been carried out by Dr. Jan Renger. As pointed out by the numerical simulations, we choose a configuration in which a gold surface is structured with TiO2 nanostructures. The TiO2 particles are placed in the crescent-moon-like carpet and are first fabricated on top of a 60-nm-thin Au film by combining electron-beam lithography and reactive ion etching. In a second lithography step, a curved Bragg-type reflector (formed by 15 gold lines (section = 150 nm 150 nm) periodically separated by half the SPP wavelength) is added, acting as the object to be hidden behind the carpet. The shape of the obtained TiO2 particles is conical (h = 200 nm, r = 210 nm) as a consequence of the etching anisotropy. The SPP was launched at a ripple-like, 200-nm-wide TiO2-line placed 44 μm away from the reflector. SPPs propagating on thin metal films deposited on dielectric substrate have radiative losses into the substrates. This leakage radiation was collected using a high-numerical aperture objective to map the SPP fields. Additionally for the sake of clarity, we employed spatial filtering in the conjugated (Fourier-) plane to suppress the direct transmitted light from the excitation spot and scattered light in order to isolate the carpet properties. Original attempts at reflecting SPPs with flat and curved homogeneous metallic step-like mirror turned out to be inefficient because the SPPs tend to radiate in open space. We therefore decided to consider instead flat and curved Bragg mirrors, formed by periodically arranged metal ridges, which show a much higher reflectivity. The leakage radiation microscopy (LRM) images map the distribution of the SPPs propagating at the gold/air interface and interacting with the different structures fabricated at the gold surface. In the case of a bare curved Bragg-reflector, the reflected SPPs are propagating into different directions depending on their relative angle to the normal to the mirror lines (see green arrows in Figure 19(c)), thus leading to a curved wave front. Conversely, adding the crescent-moon-like TiO2 carpet re-establishes a fringe pattern with a nearly straight wave front (see Figure 19(b)) very similar to the case of a flat Bragg-mirror. The remaining small lateral modulations are attributed to imperfections in the manufacturing. Further, we quantify the reduction in the wave front curvature induced by the presence of the crescent-moon-like TiO2 carpet. Comparing the areas under the numerically averaged curves b (curved mirror with carpet) and c (curved mirror without carpet) leads to reduction by a factor 3.7 as shown in Figure 19(d). Figure 20 further numerically demonstrates that the plasmonic carpet cloak should work from 650nm to 1000nm.

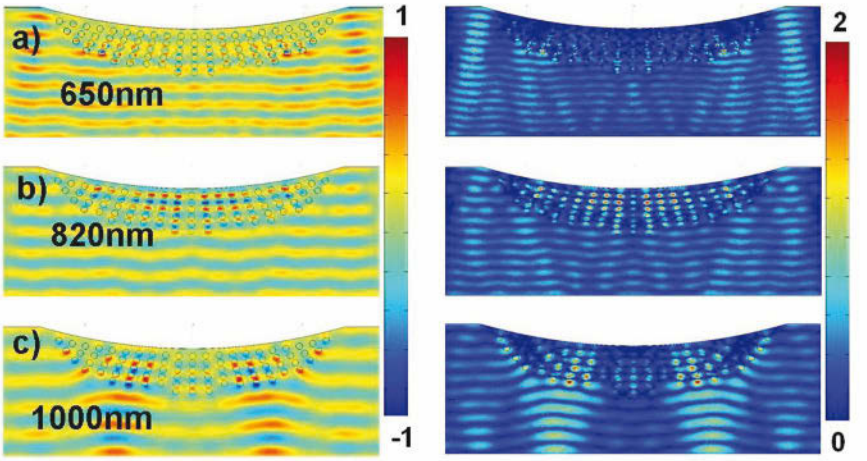

Figure 20. Broadband aspect for the SPP carpet. Numerical simulation for a range of wavelengths (phase and amplitude are represented respectively on the left and right side): (a) 650nm; (b) 850nm; (c) 1000nm. Courtesy of M. Kadic, Institut Fresnel.

16 Conclusion

In this chapter, we have reviewed the properties of media with negative permittivity and permeability. We discussed the choice of the sign of the refractive index. We also proposed a multi-structured point of view for the lensing effect associated with a simplified version of the perfect lens (the poor man's lens) consisting of infinite conducting split ring resonators (SRRs). In this way, we have bridged electromagnetic and acoustic metamaterials using some spring mass model approximation for SRRs, which allowed us to approximate the frequencies at which an array of SRRs behaves effectively as a homogeneous medium with negative permittivity, or shear modulus, depending upon whether we consider transverse electric waves or anti-plane shear waves. We then noted that SRRs have been also used to fabricate an invisibility cloak by Pendry's team in 2006. Its design is based upon geometrical transformations which may be viewed as a unified formalism bridging several techniques in electromagnetism: treatment of unbounded domains and of twisted structures, design of invisibility cloaks... The cornerstone of the method is to remark that the conductivity equation, and in the same way electrostatic, magnetostatic and electromagnetic equations, can be written

in a form such that all the metric properties are encapsulated in the material properties. The change of coordinates may therefore generate exotic equivalent material properties, via the *Nicolet-Zolla equivalence rule* (32), and the rest of the computation is dealt with just as if rectangular Cartesian coordinates were used. Though this technique is completely general, the fact that the obtained materials are usually anisotropic and inhomogeneous makes it of particular interest in the context of the finite element method where it provides very interesting models that do not require a modification of the existing code (and thus provides examples whereby the power of this method unfolds). It further provides a tool to design new electromagnetic devices such as the invisibility cloaks. It gives also an interpretation of negative refractive index materials together with a pictural view of the perfect lens that corresponds to a "folding" of the space [73; 58; 77]. Nevertheless, it should be emphasized that the space transformations that do not correspond to a diffeomorphism lead to material properties that are, if not impossible to obtain , at least challenging for the optical metamaterial science (even in a small frequency range). Thus far, experimental verification of invisibility cloaks was chiefly achieved for microwaves [76; 52]. Finally, we looked into plasmonics, which is an emergent subject in photonics allowing for a markedly enhanced control of surface electromagnetic waves propagating at structured metal- dielectric interfaces. A design of a broadband plasmonic carpet was discussed, and its experimental demonstration put forward.

Bibliography

[1] N. Fang, H. Lee, C. Sun and X. Zhang, Science **3**08, 534 (2005)
[2] S. Guenneau, S.A. Ramakrishna, *Negative refractive index, perfect lenses and checkerboards: Trapping and imaging effects in folded optical spaces*, Comptes Rendus Physique **10**, 352–378 (2009)
[3] V. Kozlov, V. Mazya, A.B. Movchan, *Asymptotic Analysis of Fields in Multistructures*, Oxford Science Publications (1999)
[4] R.C. McPhedran, N.A. Nicorovici, G.W. Milton, *Optical and dielectric properties of partially resonant composites*, Phys. Rev. B **4**9, 8479 (1994).
[5] A.B. Movchan, S. Guenneau, *Localised modes in split ring resonators*, Phys. Rev. B **70**, 125,116 (2004)
[6] A.B. Movchan, N.V. Movchan, S. Guenneau, R.C. McPhedran, *Asymptotic estimates for localized electromagnetic modes in doubly periodic structures with defects*, Proc. R. Soc. A **463**, 1045 (2007)
[7] J.B. Pendry, *Perfect cylindrical lenses*, Opt. Express **1**1(7), 755-760 (2003)

[8] S.A. Ramakrishna and T.M. Grzegorczyk, *Physics and applications of negative refractive index materials* (CRC Press, Boca Raton, 2009)

[9] D.R. Smith, D. Schurig, M. Rosenbluth, S. Schultz, S.A. Ramakrishna and J.B. Pendry, *Limitations on subdiffraction imaging with a negative refractive index slab*, Appl. Phys. Lett. **8**2(10), 1506 (2003).

[10] S.A. Ramakrishna and J.B. Pendry, *The asymmetric lossy near-perfect lens*, J. Mod. Opt. **4**9(10), 1747-1762 (2002).

[11] J.B. Pendry and S.A. Ramakrishna, *Focussing light using negative refraction*, J. Phys. Cond. Matt. **1**5, 6345-6364 (2003).

[12] J.B. Pendry, A.J. Holden, D.J. Robbins and W.J. Stewart, *Extremely low frequency plasmons in metallic mesostructures*, Physical Review Letters **76**, 4763 (1996)

[13] J.B. Pendry, A.J. Holden, W.J. Stewart and I. Youngs, *Magnetism from conductors and enhanced nonlinear phenomena*, IEEE Trans. Micr. Theory and Techniques **47**, 2075-2084 (1996)

[14] J.B. Pendry, *Negative refraction makes a perfect lens*, Phys. Rev. Lett. **85**, 3966-3969 (2000)

[15] S.A. Ramakrishna and O.J.F. Martin, *Resolving the wave vector in negative refractive index media*, Opt. Letters **3**0(19), 2626 (2005).

[16] V.G. Veselago, *The electrodynamics of substances with simultaneously negative values of ϵ and μ*, Sov. Phys. Usp. **10**, 509-514 (1968)

[17] S.A. Ramakrishna, J.B. Pendry, M.C.K. Wiltshire and W.J. Stewart, *Imaging the near field*, J. Mod. Optics **5**0, 1419 (2003)

[18] M. P. Silverman, *And Yet It Moves*, 151-163 (Cambridge Univ. Press, New York, NY, USA, 1993).

[19] V. U. Nazarov and Y. C. Chang, *Resolving the wave vector and the refractive index from the coefficient of reflectance*, Opt. Lett. **3**2, 2939-2941 (2007).

[20] J.B. Pendry, A.J. Holden, D.J. Robbins and W.J. Stewart, *Low frequency plasmons in thin-wire structures*, J. Phys.: Condens. Matter **1**0, 4785-4809 (1998).

[21] D. R. Smith, W.J. Padilla, V. C. Vier, S. C. Nemat-Nasser, and S. Schultz, *Composite Medium with Simultaneously Negative Permeability and Permittivity* Phys. Rev. Lett. **8**4, 4184 (2000)

[22] D. Maystre and S. Enoch, *Perfect lenses made with left-handed materials: Alice's mirror?*, J. Opt. Soc. Am A **2**1, 122-131 (2004).

[23] Y. F. Chen, P. Fischer, and F. W. Wise, *Negative refraction at optical frequencies in nonmagnetic two component molecular media*, Phys. Rev. Lett. **9**5, 067402 (2005).

[24] J. Skaar, *On resolving the refractive index and the wave vector*, Opt. Lett. **3**1, 3372-3374 (2006).

[25] S.A. Ramakrishna, *Comment on 'Negative refraction at optical frequencies in nonmagnetic two component molecular media'*, Phys. Rev. Lett. **9**8, 059701 (2007).

[26] A. Lakhtakia, J. B. Geddes III, and T. G. Mackay, *When does the choice of the refractive index of a linear, homogeneous, isotropic, active, dielectric medium matter?*, Opt. Express **1**5, 17709-17714 (2007).

[27] J. Seidel, F. Grafström and L. Eng, *Stimulated emmission of surface plasmons at the interface between a silver film and an optically pumped dye solution*, Phys. Rev. Lett. **9**4, 177401 (2005).

[28] S. A. Ramakrishna *Physics of negative refractive index materials*, Rep. Prog. Phys. **6**8, 449-521 (2005).

[29] S. Guenneau, R. Craster, A. Antonakakis, K. Cherednichenko, S. Cooper, *Homogenization techniques for periodic structures*, Chapter 11 in Gratings: Theory and numeric applications, E. Popov editor, Institut Fresnel/CNRS/Aix-Marseille-University (2012) ISBN: 2-85399-860-4 (www.fresnel.fr/numerical-grating-book)

[30] A. Alu and N. Engheta, *Achieving transparency with plasmonic and metamaterial coatings*, Phys. Rev. E **95**, 016623 (2005).

[31] J.-P. Berenger *A Perfectly Matched Layer for the Absorption of Electromagnetic Waves*,Journal of Computational Physics **114**, 185-200 (1994)

[32] A. Bossavit, *Notions de géométrie differentielle pour l'étude des courants de Foucault et des méthodes numériques en Electromagnétisme*, *Méthodes numériques en électromagnétisme* (A. Bossavit, C. Emson, I. Mayergoyz), Eyrolles, Paris, 1-147 (1991)

[33] A. Bossavit, *A Rationale for 'Edge-Elements' in 3-D Fields Computations*, *IEEE Trans. Mag.***24**(1), 74-79 (1998)

[34] M. Brun, S. Guenneau and A.B. Movchan, *Achieving control of in-plane elastic waves*, Appl. Phys. Lett. **94**, 061903 (2009)

[35] H. Chen and C.T. Chan, *Acoustic cloaking in three dimensions using acoustic metamaterials*, Appl. Phys. Lett. **91**, 183518 (2007).

[36] S.A. Cummer and D. Schurig, *One path to acoustic cloaking*, New J. Phys. **9**, 45 (2007).

[37] F.J.G. de Abajo, G. Gomez-Santos, L.A. Blanco, A.G. Borisov and S.V. Shabanov, *Tunneling mechanisms of light transmission through metallic films*, Phys. Rev. Lett. **95**, 067403 (2005).

[38] A. Diatta and S. Guenneau, *Non singular cloaks allow mimesis*, J. Optics **13**, 024012 (2011)

[39] P. Dular, J.-Y. Hody, A. Nicolet, A. Genon and W. Legros, *Mixed Finite Elements Associated with a Collection of Tetrahedra, Hexahedra and Prisms*,IEEE Trans. Mag.**30**(5), 2980-2983 (1994)

[40] P. Dular, A. Nicolet, A. Genon and W. Legros, *A Discrete Sequence Associated with Mixed Finite Elements and its Gauge Condition for Vector Potentials*,IEEE Trans. on Mag.**31**(3), 1356-1359 (1995)

[41] A. Farhat, S. Guenneau, A.B. Movchan, S. Enoch, *Achieving invisibility over a finite range of frequencies*, Opt. Express **16**, 5656-5661 (2008)

[42] A. Greenleaf, M. Lassas and G. Uhlmann, *On nonuniqueness for Calderon's inverse problem*, Math. Res. Lett. **10**, 685-693 (2003)

[43] A. Greenleaf, Y. Kurylev, M. Lassas and G. Uhlmann, *Isotropic transformation optics: approximate acoustic and quantum cloaking*, New J. Phys. **10**, 115024 (2008)

[44] A. Greenleaf, Y. Kurylev, M. Lassas and G. Uhlmann, *Full-wave invisibility of active devices at all frequencies*, Comm. Math. Phys. **275**(3) 749-789 (2007)

[45] A. Greenleaf, Y. Kurylev, M. Lassas and G. Uhlmann, *Schrödinger's Hat: Electromagnetic, acoustic and quantum amplifiers via transformation optics*, (preprint:arXiv:1107.4685v1)

[46] S. Guenneau, A. Nicolet, F. Zolla, C. Geuzaine and B. Meys, *A finite element formulation for spectral problems in optical fibers*,COMPEL**20**(1), 120-131 (2001)

[47] S. Guenneau, A. Nicolet, F. Zolla and S. Lasquellec, *Modeling of photonic crystal optical fibers with finite elements*,IEEE Trans. Mag.**38**(2), 1261-1264 (2002)

[48] S. Guenneau, S. Lasquellec, A. Nicolet and F. Zolla, *Design of photonic band gap optical fibers using finite elements*, COMPEL**21**(4), 534-539 (2002)

[49] S. Guenneau, A. Nicolet, F. Zolla and S. Lasquellec, *Theoretical and numerical study of photonic crystal fibers*, Progress In Electromagnetic Research**41**, 271-305 (2003)

[50] H. Igarashi and T. Honma, *A finite element analysis of TE modes in twisted waveguides*, *IEEE Trans. Mag.***27**(5), 4052-4055 (1991)

[51] J.-F. Imhoff, G. Meunier, X. Brunotte and J. C. Sabonnadiere, *An Original Solution for Unbounded Electromagnetic 2D- and 3D- problems Throughout the Finite Element Method*,IEEE Trans. Mag.**26**(5), 1659-1661 (1990)

[52] B. Kanté, D. Germain, and A. de Lustrac, *Experimental demonstration of a nonmagnetic metamaterial cloak at microwave frequencies*, Phys. Rev. B **80**, 201104(R) (2009)

[53] R. V. Kohn, H. Shen, M.S. Vogelius and M. I. Weinstein, *Cloaking via change of variables in electric impedance tomography*, Inverse Problems **24** 015016 (2008).

[54] M. Lassas and E. Somersalo, *Analysis of the PML equations in general convex geometry*, Proceedings of the Royal Society of Edinburgh, Sect. A. Mathematics **131**(5), 1183-1207 (2001)
[55] U. Leonhardt, T. G. Philbin, *General relativity in electrical engineering*;New J. Phys.**8**(10), 247 (2006)
[56] L. Lewin and T. Ruehle, *Propagation in twisted square waveguide*,IEEE Trans. MTT**28**(1), 44-48 (1980)
[57] D. A. Lowther, E. M. Freeman, and B. Forghani, *A Sparse Matrix Open Boundary Method for the Finite Element Analysis*, IEEE Trans. Mag.**25**(4), 2810-2812 (1989)
[58] U. Leonhardt, *Optical Conformal Mapping*, Science **312**, 1777 (2006)
[59] R. K. Luneburg, *Mathematical theory of optics*, University of California Press, Berkeley (1964)
[60] G.W. Milton, M. Briane and J.R. Willis, *On cloaking for elasticity and physical equations with a transformation invariant form*, New J. Phys. **8**, 248 (2006)
[61] G.W. Milton and N.A. Nicorovici, *On the cloaking effects associated with anomalous localised resonance*, Proc. R. Soc. A **462**, 3027-3059 (2006)
[62] G. W. Milton, M. Briane and J. R. Willis, *On the cloaking for elasticity and physical equations with a transformation invariant form*, *New J. Phys.***8**(248),1-20 (2006)
[63] A. Nicolet, J.-F. Remacle, B. Meys, A. Genon and W. Legros, *Transformation methods in computational electromagnetics*, Journal of Applied Physics**75**(10), 6036-6038 (1994)
[64] A. Nicolet, F. Zolla and S. Guenneau, *Modelling of twisted optical waveguides with edge elements*, Eur. Phys. J. Appl. Phys.**28**, 153-157 (2004)
[65] A. Nicolet, A. B. Movchan, S. Guenneau and F. Zolla, *Asymptotic modelling of weakly twisted electrostatic problems*, C. R. Mecanique**334**(2), 91-97 (2006)
[66] A. Nicolet and F. Zolla, *Finite Element Analysis of Helicoidal Waveguides*, IET Science, Measurement & Technology**1**(1), 67-70 (2007)
[67] A. Nicolet, A. B. Movchan, C. Geuzaine, F. Zolla and S. Guenneau, *High order asymptotic analysis of twisted electrostatic problems*, Physica B**394**(2), 335-338 (2007)
[68] A. Nicolet, F. Zolla, Y. A. Ould and S. Guenneau, *Leaky Modes in Twisted Microstructured Optical Fibres*, Waves in Complex and Random Media**17**(4), 559-570 (2007)
[69] A. Nicolet, F. Zolla, Y. Ould Agha and S. Guenneau, *Geometrical transformations and equivalent materials in computational electromagnetism*, COMPEL**27**(4), 806-819 (2008)

[70] A. Nicolet, F. Zolla and S. Guenneau, *Finite element analysis of cylindrical invisibility cloaks of elliptical cross section*, IEEE Trans. Mag.**33**(14), 1584-1586 (2008)

[71] A. Norris, *Acoustic cloaking theory*, Proc. R. Soc. Lond. **464**, 2411 (2008)

[72] Y. Ould Agha, F. Zolla, A. Nicolet and S. Guenneau, *On the use of PML for the computation of leaky modes: an application to Microstructured Optical Fibres*, COMPEL**27**(1), 95-109 (2008)

[73] J. B. Pendry and D. R. Smith, *Reversing light with negative refraction*, Physics Today**57**(6), 37-43 (2004)

[74] J. B. Pendry and D. Shurig and D. R. Smith, *C*ontrolling electromagnetic fields, Science**3**12, 1780-1782 (2006)

[75] S. A. Ramakrishna, *Physics of negative refractive index materials*, Reports Progress Physics**68**(2), 449-521 (2005)

[76] D. Schurig, J. J. Mock, B. J. Justice, S. A. Cummer, J. B. Pendry, A. F. Starr and D. R. Smith, *Metamaterial electromagnetic cloak at microwave frequency*, Science**314**(5801), 977-980 (2006)

[77] D. Schurig, J. B. Pendry and D. R. Smith, *Transformation-designed optical elements*, Optics Express**15**(22), 14772-14782 (2007)

[78] J. A. Stratton, *Electromagnetic Theory*, (McGraw-Hill, New-York, 1941)

[79] H. Yabe and Y. Mushiake, *An analysis of a hybrid-mode in a twisted rectangular waveguide*, IEEE Trans. MTT**32**(1), 65-71 (1984)

[80] S. Zhang, D.A. Genov, C. Sun and X. Zhang, *Cloaking of matter waves*, Phys. Rev. Lett. **100**, 123002 (2008)

[81] F. Zolla, G. Renversez, A. Nicolet, B. Khulmey, S. Guenneau and D. Felbacq, *Foundations of Photonic Crystal Fibres*, (Imperial College Press, London, 2005)

[82] F. Zolla, S. Guenneau, A. Nicolet and J. B. Pendry, *Electromagnetic analysis of cylindrical invisibility cloaks and the mirage effect*, Optics Letters**32**(9), 1069-1071 (2007)

[83] A.A. Maradudin A.V. Zayats and I.I. Smolyaninov. Nano-optics of surface plasmon polaritons. *Phys. Rep.*, 408:131–314, (2005).

[84] T.A. Leskova B. Baumeier and A.A. Maradudin. Cloaking from surface plasmon polaritons by a circular array of point scatterers. *Phys. Rev. Lett.*, 103:246809 (2009).

[85] L. Brillouin. Wave propagation in periodic structures. (Dover, New York, 1953).

[86] B.J. Justice S.A. Cummer J.B. Pendry A.F. Starr D.R. Smith D. Schurig, J.J. Mock. Metamaterial electromagnetic cloak at microwave frequencies. *Science*, 314:977 (2006).

[87] A. Doppler. Uber das farbige licht der doppelsterne und einige andere gestirne des himmels. (1842).
[88] L. Tsonev E. Popov and D. Maystre. Losses of plasmon surface wave on metallic grating. *J. Mod. Opt.*, 37:379–387 (1990).
[89] L. Tsonev E. Popov and D. Maystre. Lamellar diffraction grating anomalies. *Appl. Opt.*, 33:5214–5219 (1994).
[90] A. Nicolet J.B. Pendry F. Zolla, S. Guenneau. Electromagnetic analysis of cylindrical invisibility cloaks and the mirage effect. *Opt. Lett.*, 32(1):1069–1071 (2007).
[91] L.A. Blanco A.G. Borisov F.J. Garcia de Abajo, G. Gomez-Santos and S.V. Shabanov. Tunneling mechanism of light transmission through metallic films. *Phys. Rev. Lett.*, 95:067403 (2005).
[92] Y. Fu and X. Zhou. Plasmonic lenses: A review. *Plasmonics*, 1–24 (2010).
[93] S. Guenneau and S.A. Ramakrishna. Negative refractive index, perfect lenses and checkerboards: Trapping and imaging effects in folded optical spaces. *Comptes rendus Physique*, 10:352–378 (2009).
[94] A. Hessel and A. A. Oliner. A new theory of woods anomalies on optical gratings. *Appl. Opt*, 4:1275–1297 (1965).
[95] Y. Huang. Electromagnetic cloaking by layered structure of homogeneous isotropic materials. *Opt. Express*, 15(1):11133–11141 (2007).
[96] P.A. Huidobro. Transformation optics for plasmonics. *Nano Letters*, 10(1):1985–1990 (2010).
[97] M.C. Hutley. Diffraction gratings. *(Academic Press 1982).*
[98] C.C. Davis I.I. Smolyaninov, Y-J. Hung. Imaging and focusing properties of plasmonic metamaterial devices. *Phys. Rev. B*, 76:205424 (2007).
[99] J.-F. Imhoffl. On original solution for unbounded electromagnetic 2d and 3d- problems throughout the finite element method. *IEEE Transactions on Magnetics*, 26(5) (1990).
[100] M. Kadic J. Renger. Hidden progress: broadband plasmonic invisibility. *Opt. Express*, 18(1):15757–15768 (2010).
[101] T. Zentgraf G. Bartal J. Valentine, J. Li and X. Zhang. An optical cloak made of dielectrics. *Nature Mater.*, 8:569–571 (2009).
[102] D. Schurig J.B. Pendry and D.R. Smith. Controlling electromagnetic fields. *Science*, 312:1780 (2006).
[103] L. Martin-Moreno J.B. Pendry and F.J. Garcia-Vidal. Mimicking surface plasmons with structured surfaces. *Science*, 305:847 (2004).
[104] M. Kadic. Transformational plasmonics: cloak, concentrator and rotator for spps. *Opt. Express*, 18(1):12027–12032 (2010).
[105] Muamer Kadic, Sebastien Guenneau, Stefan Enoch, and S. Anantha Ramakrishna. Plasmonic space folding: Focusing surface plasmons via negative refraction in complementary media. *ACS Nano*, 5(9):6819–6825 (2011).

[106] E. Kretschmann and H. Reather. Radiative decay of nonradiative surface plasmon excited by light. *Z.Naturf.*, 23A:2135–2136 (1968).
[107] P Lalanne, J Hazart, P Chavel, E Cambril, and H Launois. A transmission polarizing beam splitter grating. *J. Opt. A: Pure Appl. Opt.*, 1:215–219 (1999).
[108] C.R. Lawrence. Surface plasmon resonance studies of immunoreactions utilizing disposable diffraction gratings. *Biosens.Bioelectron.*, 11:389–400 (1996).
[109] U. Leonhardt. Optical conformal mapping. *Science*, 312:1777 (2006).
[110] U. Leonhardt and T. G. Philbin. Transformation optics and the geometry of light. *Prog. Opt.*, 53:69–152 (2009).
[111] U. Leonhardt and T. Tyc. Broadband invisibility by non-euclidean cloaking. *Science*, 323:110 (2009).
[112] C.B. Poitras L.H. Gabrielli, J. Cardenas and M. Lipson. Silicon nanostructure cloak operating at optical frequencies. *Nat. Photonics*, 8:461–463 (2009).
[113] Jensen Li and J. B. Pendry. Hiding under the carpet: A new strategy for cloaking. *Phys. Rev. Lett.*, 101(20):203901 (2008).
[114] B. Liedberg. Surface plasmon resonance for gas detection and biosensing. *Lab.Sensors Actuat.*, 4:299–304 (1983).
[115] Y. Liu. Transformational plasmon optics. *Nano Letters*, 10(1):1991–1997 (2010).
[116] A.B. Movchan M. Farhat, S. Guenneau and S. Enoch. Achieving invisibility over a finite range of frequencies. *Opt. Express*, 16:5656–5661 (2008).
[117] D.A. Roberts S.A. Cummer D.R. Smith M. Rahm, D. Schurig and J.B. Pendry. 'design of electromagnetic cloaks and concentrators using form-invariant coordinate transformations of maxwell's equations. *Photon. Nanostruct. Fundam Appl.*, 6:87–95 (2008).
[118] S. Maier. Plasmonics: Fundamentals and applications. *New York, Springer (2007).*
[119] J.C. Maxwell. The scientific papers of James Clerk Maxwell. *reprinted by Dover Publications, New York, 1:285 (1953).*
[120] D. Maystre. General study of grating anomalies from electromagnetic surface modes. *Chapter 17 of Electromagnetic Surface Modes*, A. D. Boardman, John Wiley and Sons:661–724 (1982).
[121] D. Maystre and S. Enoch. Perfect lenses made with left handed materials: Alice's mirror. *J. Opt. Soc. Am. A.*, 21:122–131 (2004).
[122] M. Kafesaki Th. Koschny E. Ozbay E. N. Economou N. H. Shen, S. Foteinopoulou and C. M. Soukoulis. Compact planar far-field superlens based on anisotropic left-handed metamaterials. *Phys. Rev. B*, 80:115123 (2009).

[123] R.C. McPhedran N.A. Nicorovici and G.W. Milton. Optical and dielectric properties of partially resonant composites. *Phys. Rev. B*, 49:8479–8482 (1994).

[124] A. Otto. Exitation of nonradiative surface plasma waves in silver by the method of frustrated total reflection. *Z. Phys.*, 216:398–410 (1968).

[125] L. C. Botten R. C. McPhedran P. J. Bliek, R. Deleuil and D. Maystre. Inductive grids in the region of diffraction anomalies - theory, experiment, and applications. *IEEE MTT*, 10:1119–1125 (1980).

[126] E.D. Palik. Handbook of optical constants of solids. *Academic, London (1985).*

[127] C.H. Palmer. Parallel diffraction grating anomalies. *J.Opt.Soc.Am.*, 42:269 (1952).

[128] J.B. Pendry. Negative refraction makes a perfect lens. *Phys. Rev. Lett.*, 85:3966–3969 (2000).

[129] J.B. Pendry. Perfect cylindrical lenses. *Opt. Express*, 11:755– 760 (2003).

[130] J.B. Pendry and S. Anantha Ramakrishna. Near field lenses in two dimensions. *J. Phys.: Condens. Matter*, 14:8463–8479 (2002).

[131] J.B. Pendry and S.A. Ramakrishna. Focussing light with negative refractive index. *J. Phys. Cond. Matter*, 15:6345 (2003).

[132] D. Pines. A collective description of electron interactions. i. magnetic interactions. *Physical Review*, 82:625–634 (1951).

[133] D. Pines. A collective description of electron interactions. ii. collective vs individual particle aspects of the interactions. *Physical Review*, 85:338–353 (1952).

[134] J.J. Mock J.Y. Chin T.J. Cui R. Liu, C. Ji and D.R. Smith. Broadband ground-plane cloak. *Science*, 323:366 (2008).

[135] H. Raether. Surface plasmons on smooth and rough surfaces and on gratings. *Springer Tracts in Modern Physics, New York: Springer-Verlag., 111 (1988).*

[136] Lord Rayleigh. Dynamical theory of the grating. *Proc.Roy.Soc.*, A79:399 (1907).

[137] J.J. Cowan R.H. Ritchie, E.T. Arakawa and R.N. Hamm. Surface-plasmon resonance effect in grating diffraction. *Phys. Rev. Letters*, 21:1530–1533 (1968).

[138] M.S. Vogelius R.V. Kohn, H. Shen and M.I. Weinstein. Cloaking via change of variables in electric impedance tomography. *Inverse Problems*, 24:015016 (2008).

[139] S.A. Ramakrishna S. Chakrabarti and S. Guenneau. Finite checkerboards of dissipative negative refractive index. *Optics Express*, 14:12950–12957 (2006).

[140] A.C. Vutha S. Guenneau and S.A. Ramakrishna. Negative refraction in 2d checkerboards related by mirror anti-symmetry and 3d corner lenses. *New Journal of Physics*, 7:164 (2005).

[141] B. Gralak S. Guenneau and J.B. Pendry. Perfect corner reflector. *Opt. Lett.*, 30:146 (2005).

[142] J.E. Stewart and W.S. Gallaway. Diffraction anomalies in grating spectrophotometers. *Appl. Opt.*, 1:421–429 (1962).

[143] H. F. Ghaemi T. Thio P. A. Woff T. W. Ebbesen, H. J. Lezec. Extraordinary optical transmission through sub-wavelength hole arrays. *Nature*, 391:667 (1998).

[144] S.A. Maier. Plasmonics: Fundamentals and Applications *New York, Springer (2007).*

[145] V.G. Veselago. The electrodnamics of substances with simultaneously negative values of permitivity and permeability. *Soviet Physics Uspekhi*, 10(4) (1968).

[146] R.H. Baughman V.M. Agranovich, Y.R. Shen and A.A. Zakhidov. Optical bulk and surface waves with negative refraction. *Journal of Luminescence*, 110:167–173 (2004).

[147] A.V. Kildiev W. Cai, U.K. Chettiar and V.M. Shalaev. Optical cloaking with metamaterials. *Nature Photonics*, 1:224–227 (2007).

[148] R.W. Wood. On a remarkable case of uneven distribution of light in a diffraction grating spectrum. *Philosophical magazine*, 4:396–402 (1902).

[149] R.W. Wood. Anomalous diffracting gratings. *Physical Review*, 48:928–937 (1935).

[150] X.M. Yang Q. Cheng R. Liu W.X. Jiang, T.J. Cui and D.R. Smith. Invisibility cloak without singularity. *Phys. Lett.*, 93:194102 (2008).

[151] G. Bartal Y. Liu, T. Zentgraf and X. Zhang. Transformational plasmon optics. *Nano Lett.*, 6:1991–1997 (2010).

Explicit Models for Surface, Interfacial and Edge Waves

J. Kaplunov[1] and D. A. Prikazchikov[2],
[1]Department of Mathematics, Keele University,
Staffordshire, ST5 5BG, UK,
[2] Department of Computational Mathematics and Mathematical Physics,
The Bauman Moscow State Technical University,
2^{nd} Baumanskaya str., 5, Moscow, 105005, Russia

Abstract We derive explicit asymptotic formulations for surface, interfacial and edge waves in elastic solids. The effects of mixed boundary conditions and layered structure are incorporated. A hyperbolic-elliptic duality of surface and interfacial waves is emphasized along with a parabolic-elliptic duality of the edge bending wave on a thin elastic plate. The validity of the model for the Rayleigh wave is illustrated by several moving load problems.

1 Introduction

Surface elastic waves as well as their interfacial and edge analogues seem to be 'hidden' within the general equations of elastodynamics. At the same time the contribution of these waves to the overall dynamic response sometimes is more substantial than that of bulk waves. As an example, we mention a resonant behaviour of elastic solids caused by high speed moving loads.

This chapter is centered on explicit models for surface, interfacial and edge waves, that neglect the effect of bulk waves. We study the classical Rayleigh surface wave (Rayleigh 1885) along with Schölte-Gogoladze (Schölte 1949 and Gogoladze 1948) and Stoneley (1924) interfacial waves, and the edge bending wave on a thin plate discovered by Konenkov (1960), relying on the methodology established in our recent publications (Kaplunov *et al.* 2006, 2010, 2013, Dai *et al.* 2010, Erbaş *et al.* 2012). General formulations for homogenous surface and interfacial waves were also developed last years by Achenbach (1998), Kiselev & Rogerson (2009), Kiselev & Parker (2010), Parker (2012).

R. Craster, J. Kaplunov (Eds.), *Dynamic Localization Phenomena in Elasticity, Acoustics and Electromagnetism*, CISM International Centre for Mechanical Sciences,
DOI 10.1007/978-3-7091-1619-7_3, © CISM, Udine 2013

Our approach is based upon a fundamental result by Friedlander (1948) and Chadwick (1976) regarding representation of plane homogenous surface and interfacial waves in terms of harmonic functions. On perturbing the Rayleigh wave eigensolution in slow time we derive in paragraph 2.4 a *hyperbolic-elliptic* model for plane strain near-surface motion. The model consists of a *pseudo-static elliptic* equation governing decay into the interior, subject to the Dirichlet boundary condition in the form of a *hyperbolic* equation describing propagation of the Rayleigh wave under prescribed surface stresses. It reveals a hyperbolic-elliptic duality of the Rayleigh wave and also has obvious advantages for numerical computations. Indeed, we split the original vector hyperbolic problem into a scalar hyperbolic equation and a time independent elliptic problem over the interior.

With the help of the Radon integral transform, we extend the consideration above to 3D case including a pseudo-differential formulation for a coated half-space, see paragraphs 2.4 and 2.6. In addition, the proposed approach appears to be very promising for mixed dynamic problems for cracks and stamps, see paragraph 2.5.

In Section 3 we demonstrate that the *hyperbolic-elliptic* models for interfacial waves are not more difficult than that for the Rayleigh wave. The results of this section may also be easily generalised to 3D problems.

Resonant effect of moving loads studied in Section 4, is virtually the ideal setup for testing derived models. We consider a variety of plane strain problems taking into account mixed boundary conditions along with layered structure. A number of elegant approximate solutions are obtained in a surprisingly straightforward manner.

The dispersive nature of the edge bending wave on a thin plate leads to a *parabolic-elliptic* asymptotic theory. We arrive at a beam-like fourth-order equation modelling propagation of disturbances along the edge, see Section 5.

2 Surface waves

We derive an asymptotic *hyperbolic-elliptic* model for the surface Rayleigh wave. The plane strain motion is studied in great detail including mixed boundary value problems. The obtained results are extended to 3D case.

2.1 Equations of linear elastodynamics

Consider an elastic half-space given by

$$H^+_{(3)} = \left\{(x_1; x_2; x_3) \,\middle|\, -\infty < x_1 < \infty, \quad -\infty < x_2 < \infty, \quad 0 \le x_3 < \infty\right\}.$$

The equations of motion in 3D elasticity are taken in the form (see e.g. Achenbach 1973)

$$\frac{\partial \sigma_{im}}{\partial x_m} = \rho \frac{\partial^2 u_i}{\partial t^2}, \qquad i = 1, 2, 3, \tag{2.1.1}$$

where ρ is volume density, t is time, u_i are displacement vector components, σ_{im} are stress tensor components, and summation over repeated suffices is assumed. In case of a free surface wave homogeneous boundary conditions over the surface $x_3 = 0$ are imposed, yielding

$$\sigma_{3i} = 0. \tag{2.1.2}$$

Below we also consider more general boundary conditions.

The constitutive relations are given by

$$\sigma_{ik} = \delta_{ik} \lambda \operatorname{div} \mathbf{u} + 2\mu \left(\frac{\partial u_i}{\partial x_k} + \frac{\partial u_k}{\partial x_i} \right), \tag{2.1.3}$$

where $\mathbf{u} = \{u_1, u_2, u_3\}$, δ_{ik} is the Kronecker delta, and λ and μ are the Lamé elastic moduli. In view of the constitutive relations (2.1.3) the equations of motion take the form

$$(\lambda + \mu) \operatorname{grad} \operatorname{div} \mathbf{u} + \mu \Delta_3 \mathbf{u} = \rho \frac{\partial^2 \mathbf{u}}{\partial t^2}, \tag{2.1.4}$$

where $\Delta_3 = \dfrac{\partial^2}{\partial x_1^2} + \dfrac{\partial^2}{\partial x_2^2} + \dfrac{\partial^2}{\partial x_3^2}$ is the 3D Laplace operator.

2.2 Plane harmonic Rayleigh wave

Let us begin with a 2D problem for a half-plane

$$H^+_{(2)} = \left\{ (x_1; x_3) \,\middle|\, -\infty < x_1 < \infty, \quad 0 \le x_3 < \infty \right\},$$

adapting the plane strain assumptions

$$u_2 = 0, \qquad u_i = u_i(x_1, x_3, t), \quad (i = 1, 3).$$

In this case, the displacement field $\{u_1, u_3\}$ may be expressed through the elastic wave potentials ϕ and ψ as

$$u_1 = \frac{\partial \phi}{\partial x_1} - \frac{\partial \psi}{\partial x_3}, \qquad u_3 = \frac{\partial \phi}{\partial x_3} + \frac{\partial \psi}{\partial x_1}. \tag{2.2.1}$$

Then, the equations of motion (2.1.4) are rewritten in the form

$$\Delta \phi - \frac{1}{c_1^2} \frac{\partial^2 \phi}{\partial t^2} = 0, \qquad \Delta \psi - \frac{1}{c_2^2} \frac{\partial^2 \psi}{\partial t^2} = 0, \tag{2.2.2}$$

where $c_1 = \sqrt{(\lambda + 2\mu)/\rho}$ and $c_2 = \sqrt{\mu/\rho}$ denote the longitudinal and shear wave speeds, respectively, and $\Delta = \dfrac{\partial^2}{\partial x_1^2} + \dfrac{\partial^2}{\partial x_3^2}$. The wave potentials may then be found in the form of travelling wave solutions

$$\phi = \phi(x_1 - ct, \alpha x_3) = A \exp\left[ik\left(x_1 - ct\right) - k\alpha x_3\right], \tag{2.2.3}$$

$$\psi = \psi(x_1 - ct, \beta x_3) = B \exp\left[ik\left(x_1 - ct\right) - k\beta x_3\right], \tag{2.2.4}$$

decaying as $x_3 \to \infty$, where c is the sought for wave speed, and as it readily follows from (2.2.2),

$$\alpha = \sqrt{1 - \frac{c^2}{c_1^2}}, \qquad \beta = \sqrt{1 - \frac{c^2}{c_2^2}}. \tag{2.2.5}$$

It is clear that each of the functions ϕ and ψ in (2.2.3) and (2.2.4) are harmonic over the half-plane $H^+_{(2)}$. We also remark that all the speculations in what follows are equally valid for the wave travelling in the opposite direction, i.e. for the functions ϕ and ψ depending on $x_1 + ct$. The boundary conditions (2.1.2) can now be expressed in terms of the wave potentials as

$$\begin{aligned} &2\frac{\partial^2 \phi}{\partial x_1 \partial x_3} + \frac{\partial^2 \psi}{\partial x_1^2} - \frac{\partial^2 \psi}{\partial x_3^2} = 0, \\ &\left(\kappa^2 - 2\right)\frac{\partial^2 \phi}{\partial x_1^2} + \kappa^2 \frac{\partial^2 \phi}{\partial x_3^2} + 2\frac{\partial^2 \psi}{\partial x_1 \partial x_3} = 0, \end{aligned} \tag{2.2.6}$$

with

$$\kappa = \frac{c_1}{c_2} = \sqrt{\frac{2 - 2\nu}{1 - 2\nu}},$$

where ν is the Poisson ratio. Substitution of the formulae (2.2.3), (2.2.4) into (2.2.6) results in the homogeneous algebraic system in A and B

$$\begin{aligned} &2i\alpha A + (1 + \beta^2)B = 0 \\ &(1 + \beta^2)A - 2i\beta B = 0 \end{aligned} \tag{2.2.7}$$

which possesses a non-trivial solution provided that the related determinant equals zero, i.e.

$$4\alpha\beta = (1 + \beta^2)^2, \tag{2.2.8}$$

originating from the classical paper by Lord Rayleigh (1885) and having a unique root $c = c_R$, provided that

$$\alpha = \alpha_R = \sqrt{1 - \frac{c_R^2}{c_1^2}}, \qquad \beta = \beta_R = \sqrt{1 - \frac{c_R^2}{c_2^2}}. \tag{2.2.9}$$

2.3 Plane surface wave of arbitrary profile

We follow the approach in Friedlander (1948) and Chadwick (1976) in order to generalize the sinusoidal Rayleigh wave solution derived in the previous subsection to a surface wave of arbitrary profile

$$\phi = \phi(x_1 - ct, \alpha x_3), \qquad \psi = \psi(x_1 - ct, \beta x_3), \tag{2.3.1}$$

with α and β defined above, see (2.2.5), and plane harmonic functions ϕ and ψ satisfying the elliptic equations

$$\frac{\partial^2 \phi}{\partial x_3^2} + \alpha^2 \frac{\partial^2 \phi}{\partial x_1^2} = 0, \qquad \frac{\partial^2 \psi}{\partial x_3^2} + \beta^2 \frac{\partial^2 \psi}{\partial x_1^2} = 0, \tag{2.3.2}$$

arising from the wave equations (2.2.2). On substituting the harmonic functions (2.3.1) into the boundary conditions (2.2.6), we obtain

$$\begin{aligned} &2\frac{\partial^2 \phi(x_1 - ct, 0)}{\partial x_1 \partial x_3} + \left(1 + \beta^2\right) \frac{\partial^2 \psi(x_1 - ct, 0)}{\partial x_1^2} = 0, \\ &-\left(1 + \beta^2\right) \frac{\partial^2 \phi(x_1 - ct, 0)}{\partial x_1^2} + 2\frac{\partial^2 \psi(x_1 - ct, 0)}{\partial x_1 \partial x_3} = 0. \end{aligned} \tag{2.3.3}$$

Throughout this chapter we employ the Cauchy-Riemann identities for a plane harmonic function $f(x, ky)$. They are given by

$$\frac{\partial f}{\partial y} = -k \frac{\partial \overline{f}}{\partial x}, \qquad \frac{\partial f}{\partial x} = \frac{1}{k} \frac{\partial \overline{f}}{\partial y}, \qquad \overline{\overline{f}} = -f, \tag{2.3.4}$$

where bar indicates a harmonic conjugate.

With the help of these identities the conditions (2.3.3) may be transformed to

$$\begin{aligned} &2\alpha \frac{\partial^2 \phi}{\partial x_1^2} + \left(1 + \beta^2\right) \frac{\partial^2 \overline{\psi}}{\partial x_1^2} = 0, \\ &\left(1 + \beta^2\right) \frac{\partial^2 \phi}{\partial x_1^2} + 2\beta \frac{\partial^2 \overline{\psi}}{\partial x_1^2} = 0, \end{aligned} \tag{2.3.5}$$

leading to the Rayleigh equation (2.2.8). In this case the sought for harmonic eigenfunctions

$$\phi = \phi(x_1 - c_R t, \alpha_R x_3), \qquad \psi = \psi(x_1 - c_R t, \beta_R x_3) \tag{2.3.6}$$

are related to each other on the surface $x_3 = 0$ as

$$\frac{\partial \psi}{\partial x_1} = -\frac{2}{1 + \beta_R^2} \frac{\partial \phi}{\partial x_3}, \tag{2.3.7}$$

see $(2.3.3)_1$. Moreover, the last relation specified on the surface may be extended to the whole interior region as

$$\psi(x_1 - c_R t, \beta_R x_3) = \frac{2\alpha_R}{1+\beta_R^2}\,\overline{\phi}(x_1 - c_R t, \beta_R x_3), \tag{2.3.8}$$

or

$$\phi(x_1 - c_R t, \alpha_R x_3) = -\frac{2\beta_R}{1+\beta_R^2}\,\overline{\psi}(x_1 - c_R t, \alpha_R x_3), \tag{2.3.9}$$

for more details see Chadwick (1976). Thus, the wave potentials are related through the Hilbert transform, and consequently the Rayleigh wave field may be expressed through a single harmonic function.

2.4 Hyperbolic-elliptic model

Plane strain problem Consider now non-homogeneous boundary conditions

$$\sigma_{31} = Q(x_1, t), \qquad \sigma_{33} = P(x_1, t), \tag{2.4.1}$$

imposed along the surface $x_3 = 0$ of the half-plane $H^+_{(2)}$. These may be reformulated in terms of the wave potentials as

$$\begin{gathered} 2\frac{\partial^2\phi}{\partial x_1 \partial x_3} + \frac{\partial^2\psi}{\partial x_1^2} - \frac{\partial^2\psi}{\partial x_3^2} = \frac{Q}{\mu}, \\ \left(\kappa^2 - 2\right)\frac{\partial^2\phi}{\partial x_1^2} + \kappa^2\frac{\partial^2\phi}{\partial x_3^2} + 2\frac{\partial^2\psi}{\partial x_1 \partial x_3} = \frac{P}{\mu}. \end{gathered} \tag{2.4.2}$$

Let us we perturb the surface wave eigensolutions (2.3.6) in slow time

$$\tau = \varepsilon t, \qquad (\varepsilon \ll 1). \tag{2.4.3}$$

Throughout this paragraph we assume that the deviation of the analysed perturbed motion $\{\phi(x_1 - c_R t, x_3, \tau),\, \psi(x_1 - c_R t, x_3, \tau)\}$ from the homogeneous Rayleigh wave field (2.3.6) is small. On inserting slow time τ into the original equations of motion (2.2.2) at $\alpha = \alpha_R$ and $\beta = \beta_R$, and taking into account the operator identity $\dfrac{\partial}{\partial t} = -c_R\dfrac{\partial}{\partial x_1} + \varepsilon\dfrac{\partial}{\partial \tau}$, we have

$$\begin{gathered} \frac{\partial^2\phi}{\partial x_3^2} + \alpha_R^2\frac{\partial^2\phi}{\partial x_1^2} + 2\frac{\varepsilon}{c_R}\left(1-\alpha_R^2\right)\frac{\partial^2\phi}{\partial x_1 \partial \tau} - \frac{\varepsilon^2}{c_R^2}\left(1-\alpha_R^2\right)\frac{\partial^2\phi}{\partial \tau^2} = 0, \\ \frac{\partial^2\psi}{\partial x_3^2} + \beta_R^2\frac{\partial^2\psi}{\partial x_1^2} + 2\frac{\varepsilon}{c_R}\left(1-\beta_R^2\right)\frac{\partial^2\psi}{\partial x_1 \partial \tau} - \frac{\varepsilon^2}{c_R^2}\left(1-\beta_R^2\right)\frac{\partial^2\psi}{\partial \tau^2} = 0. \end{gathered} \tag{2.4.4}$$

Next, we expand the potentials in asymptotic series as

$$\begin{aligned}\phi(x_1-c_Rt,x_3,\tau)&=\phi_0(x_1-c_Rt,\alpha_Rx_3,\tau)+\varepsilon\phi_1(x_1-c_Rt,x_3,\tau)+\ldots,\\ \psi(x_1-c_Rt,x_3,\tau)&=\psi_0(x_1-c_Rt,\beta_Rx_3,\tau)+\varepsilon\psi_1(x_1-c_Rt,x_3,\tau)+\ldots,\end{aligned}\tag{2.4.5}$$

where the leading order terms ϕ_0 and ψ_0 coincide with the surface wave eigensolutions (2.3.6) to within a parametric dependence of slow time.

On substituting the expansion (2.4.5) into the perturbed equations of motion (2.4.4) we get expressions for $O(\varepsilon)$ terms. They are written as

$$\begin{aligned}\phi_1&=\phi_{10}-x_3\frac{1-\alpha_R^2}{\alpha_Rc_R}\frac{\partial\overline{\phi}_0}{\partial\tau},\\ \psi_1&=\psi_{10}-x_3\frac{1-\beta_R^2}{\beta_Rc_R}\frac{\partial\overline{\psi}_0}{\partial\tau},\end{aligned}\tag{2.4.6}$$

where $\phi_{10}=\phi_{10}(x_1-c_Rt,\alpha_Rx_3,\tau)$ and $\psi_{10}=\psi_{10}(x_1-c_Rt,\beta_Rx_3,\tau)$ are arbitrary functions, harmonic in the first two variables, for more details see Kaplunov *et al.* (2006).

It is convenient to treat the two sub-problems for boundary conditions, namely, the cases of vertical ($Q=0,P\neq0$) and horizontal ($P=0,Q\neq0$) loading. Let us consider first the effect of a vertical force normalizing it by $P=\varepsilon P_\varepsilon$. On introducing the formulae (2.4.5) and (2.4.6) into the boundary conditions (2.4.2) we get at $x_3=0$

$$\begin{aligned}2\frac{\partial^2\phi_{10}}{\partial x_1\partial x_3}+\left(1+\beta_R^2\right)\frac{\partial^2\psi_{10}}{\partial x_1^2}-\frac{2(1-\alpha_R^2)}{c_R\alpha_R}\frac{\partial^2\overline{\phi}_0}{\partial x_1\partial\tau}&\\ +\frac{2(1-\beta_R^2)}{c_R\beta_R}\frac{\partial^2\overline{\psi}_0}{\partial x_3\partial\tau}=0,&\\ -\left(1+\beta_R^2\right)\frac{\partial^2\phi_{10}}{\partial x_1^2}+2\frac{\partial^2\psi_{10}}{\partial x_1\partial x_3}-\frac{2(1-\alpha_R^2)\kappa^2}{c_R\alpha_R}\frac{\partial^2\overline{\phi}_0}{\partial x_3\partial\tau}&\\ -\frac{2(1-\beta_R^2)}{c_R\beta_R}\frac{\partial^2\overline{\psi}_0}{\partial x_1\partial\tau}=\frac{P_\varepsilon}{\mu}.&\end{aligned}\tag{2.4.7}$$

Then, using the Cauchy-Riemann identities (2.3.4) along with the relations

$$\overline{\psi}_0(x_1-c_Rt,0)=-\frac{2\alpha_R}{1+\beta_R^2}\,\phi_0(x_1-c_Rt,0)=-\frac{1+\beta_R^2}{2\beta_R}\,\phi_0(x_1-c_Rt,0),\tag{2.4.8}$$

following from (2.3.8) and (2.3.9), we rewrite the boundary conditions (2.4.7)

as

$$\begin{aligned} &2\alpha_R \frac{\partial^2 \phi_{10}}{\partial x_1^2} + \left(1+\beta_R^2\right) \frac{\partial^2 \overline{\psi}_{10}}{\partial x_1^2} = \frac{2}{c_R}\left[\frac{1-\beta_R^4}{2\beta_R} - \frac{1-\alpha_R^2}{\alpha_R}\right] \frac{\partial^2 \phi_0}{\partial x_1 \partial \tau}, \\ &-\left(1+\beta_R^2\right) \frac{\partial^2 \phi_{10}}{\partial x_1^2} - 2\beta_R \frac{\partial^2 \overline{\psi}_{10}}{\partial x_1^2} = \frac{2}{c_R}\left[1-\beta_R^2 - \frac{1-\beta_R^4}{2\beta_R^2}\right] \frac{\partial^2 \phi_0}{\partial x_1 \partial \tau} + \frac{P_\varepsilon}{\mu}. \end{aligned} \tag{2.4.9}$$

It is clear that the determinant of the left hand side of (2.4.9) equals zero. The solvability condition is

$$\frac{2}{c_R} \frac{\partial^2 \phi_0}{\partial x_1 \partial \tau} = \frac{1+\beta_R^2}{2\mu B} P_\varepsilon, \tag{2.4.10}$$

where

$$B = \frac{\beta_R}{\alpha_R}(1-\alpha_R^2) + \frac{\alpha_R}{\beta_R}(1-\beta_R^2) - (1-\beta_R^4). \tag{2.4.11}$$

Let the load on the right hand side of (2.4.10) evolve in slow time as

$$P_\varepsilon(x_1, t) = \frac{\partial^2 p_\varepsilon}{\partial \tau \partial x_1}, \tag{2.4.12}$$

with $p_\varepsilon = p_\varepsilon(x_1 - c_R t, \tau)$. Then we readily infer from (2.4.10) that

$$\phi_0 = \frac{\left(1+\beta_R^2\right) c_R}{4\mu B} p_\varepsilon, \tag{2.4.13}$$

i. e. $\phi_0 = \phi_0(x_1 - c_R t, \tau)$ as was initially assumed.

It is evident, however, that for an arbitrary vertical load P the solution of the equation (2.4.10) may demonstrate a more general time dependence. Nevertheless, this equation always enables a correct evaluation of the Rayleigh wave contribution to the overall dynamic response. Moreover, the developed perturbation procedure is a counterpart of a routine relying on computation of the residues corresponding to the Rayleigh wave poles, see the Appendix in Kaplunov *et al.* (2006). It is also very crucial that the solution of (2.4.10) will often dominate in the near-surface zone, in particular for impulse and near-resonant moving loads. For the latter the slow time may be defined as

$$\tau = \left|1 - \frac{c}{c_R}\right| t, \quad c \approx c_R, \tag{2.4.14}$$

where c is the speed of the load.

Finally, applying the operator asymptotic relationship

$$\frac{2\varepsilon}{c_R}\frac{\partial^2}{\partial x_1 \partial \tau} = \frac{\partial^2}{\partial x_1^2} - \frac{1}{c_R^2}\frac{\partial^2}{\partial t^2} + O\left(\varepsilon^2\right),$$

we present the equation (2.4.10) for $\phi = \phi_0$ in terms of the original time t as

$$\frac{\partial^2 \phi}{\partial x_1^2} - \frac{1}{c_R^2}\frac{\partial^2 \phi}{\partial t^2} = \frac{1+\beta_R^2}{2\mu B} P. \tag{2.4.15}$$

Thus, the asymptotic formulation for the Rayleigh wave has been reduced to a scalar problem for the pseudo-static elliptic equation $(2.3.2)_1$ derived in the previous subsection subject to the Dirichlet boundary condition at $x_3 = 0$ in the form of the wave equation (2.4.15). The shear potential ψ may then be restored from the relation (2.3.8).

In case of tangential loading a similar asymptotic model consists of a scalar problem for the elliptic equation $(2.3.2)_2$ subject to a boundary condition at $x_3 = 0$, given by the following hyperbolic equation

$$\frac{\partial^2 \psi}{\partial x_1^2} - \frac{1}{c_R^2}\frac{\partial^2 \psi}{\partial t^2} = \frac{1+\beta_R^2}{2\mu B} Q, \tag{2.4.16}$$

with the potential ϕ determined through the Hilbert transform from (2.3.9).

We remark that the established approximate formulation is oriented to the Rayleigh wave only and does not incorporate the effect of bulk waves. The range of validity of the model (see (2.3.2), (2.3.8), (2.3.9), (2.4.15), and (2.4.16)) covers the problems of near-surface dynamics with the dominant contribution of the Rayleigh wave.

The consideration above reveals a dual *hyperbolic-elliptic* nature of the Rayleigh wave. It is worth noting however that not all the displacement components demonstrate a wave behaviour along the surface. In particular, in case of vertical loading only the horizontal displacement u_1 is governed by a hyperbolic equation. The latter follows from (2.4.15) (see also (2.3.3)) and can be written as

$$\frac{\partial^2 u_1}{\partial x_1^2} - \frac{1}{c_R^2}\frac{\partial^2 u_1}{\partial t^2} = \frac{1-\beta_R^4}{4\mu B}\frac{\partial P}{\partial x_1}. \tag{2.4.17}$$

3D problem Let us generalise the plane strain formulation obtained in the previous subsection, to the 3D case. We start from the equations of motion (2.1.4), in case of vertical surface loading modelled by the boundary conditions at $x_3 = 0$

$$\sigma_{31} = \sigma_{32} = 0, \qquad \sigma_{33} = P(x_1, x_2, t). \tag{2.4.18}$$

The Radon integral transform

$$f^{(\alpha)}(\chi,\alpha,x_3,t)=\int\limits_{-\infty}^{\infty} f\left(\chi\cos\alpha-\eta\sin\alpha,\chi\sin\alpha+\eta\cos\alpha,x_3,t\right)d\zeta, \quad (2.4.19)$$

where

$$\chi=x_1\cos\alpha+x_2\sin\alpha, \qquad \eta=-x_1\sin\alpha+x_2\cos\alpha,$$

with the angle α varying over the interval $0\le\alpha<2\pi$, reduces the original 3D elastodynamics problem to a 2D problem for associated transforms, for more details see Georgiadis & Lykotrafitis (2001) and references therein. In (2.4.19) and below the Radon transforms are denoted by suffice (α). We also define transformed displacements in the Cartesian frame (χ,η) as

$$u_\chi^{(\alpha)}=u_1^{(\alpha)}\cos\alpha+u_2^{(\alpha)}\sin\alpha, \qquad u_\eta^{(\alpha)}=-u_1^{(\alpha)}\sin\alpha+u_2^{(\alpha)}\cos\alpha, \quad (2.4.20)$$

and set $u_\eta^{(\alpha)}=0$ assuming that the the anti-plane motion does not induce surface waves.

It is clear that the aforementioned 2D problem for Radon transforms is formally identical to that in the theory of plane strain. Then, we introduce an analogue of wave potentials

$$u_\chi^{(\alpha)}=\frac{\partial\phi^{(\alpha)}}{\partial\chi}-\frac{\partial\psi^{(\alpha)}}{\partial x_3}, \qquad u_3^{(\alpha)}=\frac{\partial\phi^{(\alpha)}}{\partial x_3}+\frac{\partial\psi^{(\alpha)}}{\partial\chi} \quad (2.4.21)$$

and follow the perturbation procedure developed in the previous subsection. The asymptotic formulation for the Rayleigh wave (expressed through Radon transforms) contains the elliptic equations

$$\frac{\partial^2\phi^{(\alpha)}}{\partial x_3^2}+\alpha_R^2\frac{\partial^2\phi^{(\alpha)}}{\partial\chi^2}=0, \qquad \frac{\partial^2\psi^{(\alpha)}}{\partial x_3^2}+\beta_R^2\frac{\partial^2\psi^{(\alpha)}}{\partial\chi^2}=0, \quad (2.4.22)$$

over the interior, along with the hyperbolic equation

$$\frac{\partial^2\phi^{(\alpha)}}{\partial\chi^2}-\frac{1}{c_R^2}\frac{\partial^2\phi^{(\alpha)}}{\partial t^2}=\frac{1+\beta_R^2}{2\mu B}P^{(\alpha)}, \quad (2.4.23)$$

specified on the surface $x_3=0$. The relation between the potentials $\phi^{(\alpha)}$ and $\psi^{(\alpha)}$ on the surface now becomes

$$\frac{\partial\psi^{(\alpha)}}{\partial\chi}=-\frac{2}{1+\beta_R^2}\frac{\partial\phi^{(\alpha)}}{\partial x_3}. \quad (2.4.24)$$

Next, we introduce a pair of the potentials $\psi_1^{(\alpha)} = \psi^{(\alpha)} \cos\alpha$ and $\psi_2^{(\alpha)} = \psi^{(\alpha)} \sin\alpha$ in order to invert the formulae (2.4.22)-(2.4.24). As a result, we get

$$\frac{\partial^2 \phi}{\partial x_3^2} + k_1^2 \Delta\phi = 0, \tag{2.4.25}$$

$$\frac{\partial^2 \psi_i}{\partial x_3^2} + k_2^2 \Delta\psi_i = 0, \tag{2.4.26}$$

where now $\Delta = \dfrac{\partial^2}{\partial x_1^2} + \dfrac{\partial^2}{\partial x_2^2}$, and $i = 1, 2$, subject to the boundary conditions ($x_3 = 0$)

$$\Delta\phi - \frac{1}{c_R^2} \frac{\partial^2 \phi}{\partial t^2} = \frac{1 + \beta_R^2}{2\mu B} P, \tag{2.4.27}$$

and

$$\frac{\partial \psi_1}{\partial x_1} = \frac{\partial \psi_2}{\partial x_2} = -\frac{2}{1 + \beta_R^2} \frac{\partial \phi}{\partial x_3}. \tag{2.4.28}$$

In the formulae above the potentials ϕ, ψ_1 and ψ_2 satisfy the vector relation (Dai *et al.* 2010)

$$\mathbf{u} = \mathrm{grad}\phi + \mathrm{curl}\Psi, \tag{2.4.29}$$

where $\Psi = (-\psi_2, \psi_1, 0)$.

2.5 Plane mixed problems

The methodology in 2.4.1 may also be adapted for mixed boundary value problems arising in dynamics of cracks and stamps. Consider first a *vertical stamp* applied to the surface of the elastic half-plane $H_{(2)}^+$. The boundary conditions at $x_3 = 0$ include zero tangential stresses

$$\sigma_{31} = 0, \tag{2.5.1}$$

along with normal stresses P and vertical displacements U_3 prescribed on the disjoint parts of the surface S_1 and S_2, respectively ($S_1 \cup S_2 = R$). Thus

$$\begin{aligned} &\sigma_{33} = P(x_1, t), \quad \text{at} \quad x_1 \in S_1, \\ &u_3 = U_3(x_1, t), \quad \text{at} \quad x_1 \in S_2, \end{aligned} \tag{2.5.2}$$

see Fig. 1.

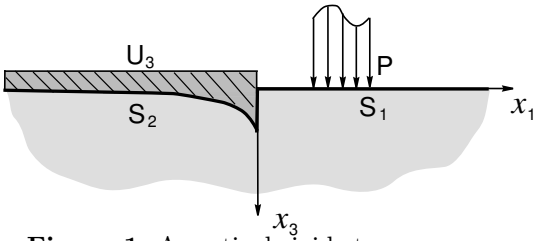

Figure 1. A vertical rigid stamp

On utilizing the formulae (2.3.2), (2.3.8) and (2.4.15), we arrive at a scalar mixed problem for the elliptic equation (see Erbaş *et al.* 2012)

$$\frac{\partial^2\phi}{\partial x_3^2}+\alpha_R^2\frac{\partial^2\phi}{\partial x_1^2}=0 \tag{2.5.3}$$

subject to the boundary conditions ($x_3=0$)

$$\frac{\partial^2\phi}{\partial x_1^2}-\frac{1}{c_R^2}\frac{\partial^2\phi}{\partial t^2}=\frac{1+\beta_R^2}{2\mu B}P,\quad \text{at}\quad x_1\in S_1, \tag{2.5.4}$$

and

$$\frac{\partial\phi}{\partial x_3}=\frac{1+\beta_R^2}{1-\beta_R^2}U_3,\quad \text{at}\quad x_1\in S_2. \tag{2.5.5}$$

As before, the shear potential ψ is expressed by the relation (2.3.8).

A similar formulation may be deduced for an elastic half-plane, part of which is coated by a flexible inextensible membrane not resisting to vertical motion. In this case the boundary conditions on the surface $x_3=0$ may be written as

$$\begin{aligned}&\sigma_{33}=0,\quad \text{at}\quad x_3=0,\\ &\sigma_{31}=Q(x_1,t),\quad \text{at}\quad x_1\in S_1,\\ &u_1=U_1(x_1,t)\quad \text{at}\quad x_1\in S_2.\end{aligned} \tag{2.5.6}$$

where Q and U_1 denote the given horizontal stresses and displacements, respectively, see Fig. 2.

Now a scalar setup for the shear potential ψ is given by the equation

$$\frac{\partial^2\psi}{\partial x_3^2}+\beta_R^2\frac{\partial^2\psi}{\partial x_1^2}=0 \tag{2.5.7}$$

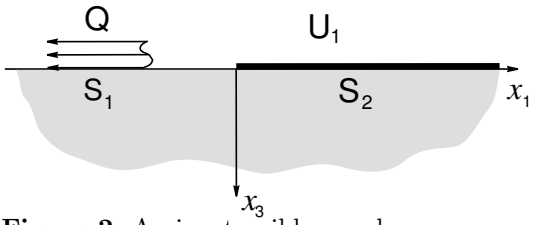

Figure 2. An inextensible membrane

along with the boundary conditions ($x_3 = 0$)

$$\frac{\partial^2\psi}{\partial x_1^2} - \frac{1}{c_R^2}\frac{\partial^2\psi}{\partial t^2} = \frac{1+\beta_R^2}{2\mu B}\,Q, \quad \text{at} \quad x_1 \in S_1, \tag{2.5.8}$$

and

$$\frac{\partial\psi}{\partial x_3} = \frac{1+\beta_R^2}{1-\beta_R^2}\,U_1, \quad \text{at} \quad x_1 \in S_2. \tag{2.5.9}$$

2.6 Long wave asymptotic model for a surface wave on a coated half-space

The asymptotic formulation for the Rayleigh wave may also be extended to a coated half-space in the framework of long-wave approximation. Consider the elastic half-space $H^+_{(3)}$ coated by an elastic layer occupying the region $-h \le x_3 \le 0$, see Fig. 3.

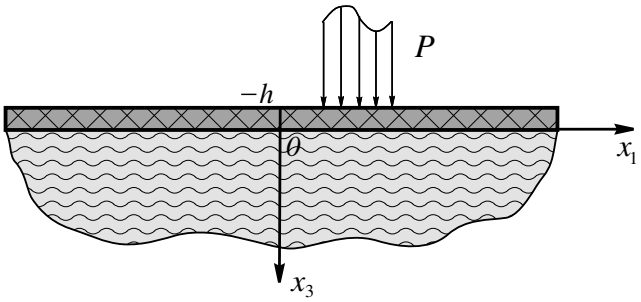

Figure 3. A half-space coated by an elastic layer

As in subsection 2.4.2, we impose the boundary conditions (2.4.18) on the upper face of the coating $x_3 = -h$. We also assume continuity of all displacements and stresses at the interface $x_3 = 0$.

A standard asymptotic long-wave technique applied to the coating (here and below in this subsection for more details see Dai *et al.* (2010) and

references therein) results in effective boundary conditions on the interface $x_3 = 0$, namely

$$\sigma_{i3} = \rho_0 h \left\{ \frac{\partial^2 u_i}{\partial t^2} - c_{20}^2 \left[\frac{\partial^2 u_i}{\partial x_j^2} + 4\left(1-\kappa_0^{-2}\right)\frac{\partial^2 u_i}{\partial x_i^2} + \left(3-4\kappa_0^{-2}\right)\frac{\partial^2 u_j}{\partial x_i \partial x_j} \right] \right\},$$
$$\sigma_{33} = \rho_0 h \frac{\partial^2 u_3}{\partial t^2} + P, \qquad 1 \le i \ne j \le 2, \tag{2.6.1}$$

where ρ_0 is density of the coating, c_{10} and c_{20} are associated bulk wave speeds, and $\kappa_0 = c_{10}/c_{20}$. The boundary conditions (2.6.1) coincide with those earlier proposed by Tiersten (1969).

Thus, the initial problem is reduced to analysis of the uncoated half-space H_3^+ subject to the boundary conditions (2.6.1) imposed on its surface $x_3 = 0$. In this case the transformed equations

$$\frac{\partial^2 \phi^{(\alpha)}}{\partial \chi^2} + \frac{\partial^2 \phi^{(\alpha)}}{\partial x_3^2} - \frac{1}{c_1^2}\frac{\partial^2 \phi^{(\alpha)}}{\partial t^2} = 0,$$
$$\frac{\partial^2 \psi^{(\alpha)}}{\partial \chi^2} + \frac{\partial^2 \psi^{(\alpha)}}{\partial x_3^2} - \frac{1}{c_2^2}\frac{\partial^2 \psi^{(\alpha)}}{\partial t^2} = 0, \tag{2.6.2}$$

are accompanied by the boundary conditions ($x_3 = 0$)

$$\mu\left[2\frac{\partial^2 \phi^{(\alpha)}}{\partial \chi \partial x_3} + \frac{\partial^2 \psi^{(\alpha)}}{\partial \chi^2} - \frac{\partial^2 \psi^{(\alpha)}}{\partial x_3^2}\right] = \mu_0 h\left[c_{20}^{-2}\left(\frac{\partial^3 \phi^{(\alpha)}}{\partial \chi \partial t^2} - \frac{\partial^3 \psi^{(\alpha)}}{\partial x_3 \partial t^2}\right) - 4\left(1-\kappa_0^{-2}\right)\left(\frac{\partial^3 \phi^{(\alpha)}}{\partial \chi^3} - \frac{\partial^3 \psi^{(\alpha)}}{\partial x_3 \partial \chi^2}\right)\right],$$
$$\mu\left[\left(\kappa^2-2\right)\frac{\partial^2 \phi^{(\alpha)}}{\partial \chi^2} + \kappa^2 \frac{\partial^2 \phi^{(\alpha)}}{\partial x_3^2} + 2\frac{\partial^2 \psi^{(\alpha)}}{\partial \chi \partial x_3}\right] = \mu_0 h c_{20}^{-2}\left(\frac{\partial^3 \phi^{(\alpha)}}{\partial x_3 \partial t^2} + \frac{\partial^3 \psi^{(\alpha)}}{\partial \chi \partial t^2}\right) - P^{(\alpha)}. \tag{2.6.3}$$

A perturbation procedure similar to that in subsection 2.4.1, leads to a singularly perturbed hyperbolic equation on the surface. It is given by

$$\frac{\partial^2 \phi^{(\alpha)}}{\partial \chi^2} - \frac{1}{c_R^2}\frac{\partial^2 \phi^{(\alpha)}}{\partial t^2} + \frac{bh}{\alpha_R}\frac{\partial^3 \phi^{(\alpha)}}{\partial \chi^2 \partial x_3} = \frac{1+\beta_R^2}{2\mu B} P^{(\alpha)}, \tag{2.6.4}$$

with

$$b = \frac{\mu_0}{2\mu B}(1-\beta_R^2)\left[(1-\beta_{R0}^2)(\alpha_R+\beta_R) - 4\beta_R(1-\kappa_0^{-2})\right]. \tag{2.6.5}$$

In the original variables, we get from (2.6.4)

$$\Delta\phi - \frac{1}{c_R^2}\frac{\partial^2\phi}{\partial t^2} + \frac{bh}{\alpha_R}\frac{\partial}{\partial x_3}(\Delta\phi) = \frac{1+\beta_R^2}{2\mu B}P, \tag{2.6.6}$$

which is a boundary condition for the elliptic equation (2.4.25), where now $\Delta = \dfrac{\partial^2}{\partial x_1^2} + \dfrac{\partial^2}{\partial x_2^2}$.

The perturbed hyperbolic equation (2.6.6) can also be presented in a pseudo-differential form, i.e.

$$\Delta\phi - \frac{1}{c_R^2}\frac{\partial^2\phi}{\partial t^2} - bh\sqrt{-\Delta}\,(\Delta\phi) = \frac{1+\beta_R^2}{2\mu B}P. \tag{2.6.7}$$

In the plane strain case the last equation becomes

$$\frac{\partial^2\phi}{\partial x_1^2} - \frac{1}{c_R^2}\frac{\partial^2\phi}{\partial t^2} - bh\sqrt{-\frac{\partial^2}{\partial x_1^2}}\frac{\partial^2\phi}{\partial x_1^2} = \frac{1+\beta_R^2}{2\mu B}P. \tag{2.6.8}$$

This equation may also be written through the Hilbert transform. Therefore, the presence of a coating inevitably leads to an integro-differential formulation.

In addition, the equation (2.6.8) enables a simple approximation of the exact dispersion relation, see e.g. Shuvalov & Every (2008) and references therein. Indeed, we easily deduce from (2.6.8) that

$$v = c_R\left(1 - \frac{b}{2}|kh| + \dots\right), \tag{2.6.9}$$

demonstrating that the Rayleigh wave speed c_R is a local extremum over the long wave domain $kh \ll 1$, where k denotes wave number.

3 Interfacial waves

The results obtained for the Rayleigh wave are now generalized to interfacial waves. In view of the existing representation in terms of a single harmonic function (Kiselev & Parker 2010), we may expect similar hyperbolic-elliptic formulations for both Schölte-Gogoladze and Stoneley waves, see also Prikazchikov (2011). In this section we restrict ourselves to plane strain assumptions, however, 3D formulations may be easily derived using the Radon transform similarly to what has been done for the Rayleigh wave. We show that the analysis of interfacial wave fields may be also reduced to scalar problems for the elliptic equations. As a result, a tedious algebra, traditionally associated with investigation of interfacial waves, seems to be mainly overcome.

3.1 Schölte-Gogoladze wave

Consider an elastic half-plane $H^+_{(2)}$, joint with a fluid half-plane

$$H^-_{(2)} = \left\{(x_1; x_3) \,\middle|\, -\infty < x_1 < \infty, \quad x_3 < 0\right\},$$

and concentrate on the interfacial Schölte-Gogoladze wave propagating along the line $x_3 = 0$ and decaying away from it. This wave has been discovered independently by Schölte (1949) and Gogoladze (1948).

The equations of motion for an elastic medium are given by (2.2.2), whereas fluid motion is governed by the Helmholz equation

$$\Delta\theta - \frac{1}{c_f^2}\frac{\partial^2\theta}{\partial t^2} = 0, \tag{3.1.1}$$

where θ is the displacement potential, $\Delta = \dfrac{\partial^2}{\partial x_1^2} + \dfrac{\partial^2}{\partial x_3^2}$, and c_f is the fluid wave speed. Below we assume zero tangential stresses and continuity of normal displacements along the interface $x_3 = 0$, leading to the boundary conditions

$$\sigma_{31} = 0, \qquad u_3 = v, \qquad \sigma_{33} - p = P(x_1, t), \tag{3.1.2}$$

where v and p are the vertical displacement and pressure in fluid, respectively, given by

$$v = \frac{\partial\theta}{\partial x_3}, \qquad p = \rho_f \frac{\partial^2\theta}{\partial t^2},$$

with ρ_f denoting the volume density of the fluid, and P standing for prescribed vertical stresses along the interface. The boundary conditions (3.1.2) expressed in terms of the potentials ϕ, ψ and θ become

$$2\frac{\partial^2\phi}{\partial x_1 \partial x_3} - \frac{\partial^2\psi}{\partial x_1^2} + \frac{\partial^2\psi_0}{\partial x_3^2} = 0,$$

$$\frac{\partial\phi_0}{\partial x_3} + \frac{\partial\psi}{\partial x_1} - \frac{\partial\theta}{\partial x_3} = 0, \tag{3.1.3}$$

$$\mu\left[\left(\kappa^2 - 2\right)\frac{\partial^2\phi_0}{\partial x_1^2} + \kappa^2\frac{\partial^2\phi}{\partial x_3^2} - 2\frac{\partial^2\psi}{\partial x_1 \partial x_3}\right] - \rho_f\frac{\partial^2\theta}{\partial t^2} = P.$$

The equation for the interfacial Schölte-Gogoladze wave speed follows from (2.2.2), (3.1.1), and (3.1.3) at $P = 0$. It takes the form

$$4\alpha_{SG}\beta_{SG} - \left(1 + \beta_{SG}^2\right)^2 = \frac{\rho_f}{\rho}\frac{\alpha_{SG}}{\gamma_{SG}}\left(1 - \beta_{SG}^2\right)^2, \tag{3.1.4}$$

where

$$\alpha_{SG} = \sqrt{1 - \frac{c_{SG}^2}{c_1^2}}, \qquad \beta_{SG} = \sqrt{1 - \frac{c_{SG}^2}{c_2^2}}, \qquad \gamma_{SG} = \sqrt{1 - \frac{c_{SG}^2}{c_f^2}}, \quad (3.1.5)$$

and c_{SG} is the sought for speed of the Schölte-Gogoladze wave. Similarly to the consideration in 2.4.1, we obtain an approximate hyperbolic-elliptic formulation for the contribution of the Schölte-Gogoladze wave to the general dynamic response. The decay into the interior is again governed by the *elliptic* equation

$$\frac{\partial^2 \phi}{\partial x_3^2} + \alpha_{SG}^2 \frac{\partial^2 \phi}{\partial x_1^2} = 0, \quad (3.1.6)$$

while the interfacial dynamics is described by the *hyperbolic* equation ($x_3 = 0$)

$$\frac{\partial^2 \phi}{\partial x_1^2} - \frac{1}{c_{SG}^2} \frac{\partial^2 \phi}{\partial t^2} = AP, \quad (3.1.7)$$

where

$$A = \frac{1 + \beta_{SG}^2}{\mu \left[2B_{SG} - \dfrac{\rho_f}{\rho} \dfrac{(1 - \beta_{SG}^2)^2 \left(\gamma_{SG}^2 - \alpha_{SG}^2 - 4\alpha_{SG}^2 \gamma_{SG}^2 \right)}{2\alpha_{SG} \gamma_{SG}^3} \right]}, \quad (3.1.8)$$

and B_{SG} takes the form (2.4.11) to within the substitutions $\alpha_R = \alpha_{SG}$ and $\beta_R = \beta_{SG}$. It is readily observed that at $\rho_f = 0$ the equation (3.1.7) is identical to that for the Rayleigh wave, see (2.4.15).

The potentials ψ and θ are related to the potential ϕ as

$$\psi(x_1 - c_{SG}t, \beta_{SG}x_3) = \frac{2\alpha_{SG}}{1 + \beta_{SG}^2} \overline{\phi}(x_1 - c_{SG}t, \beta_{SG}x_3), \quad (3.1.9)$$

and

$$\theta(x_1 - c_{SG}t, \gamma_{SG}x_3) = -\frac{1 - \beta_{SG}^2}{1 + \beta_{SG}^2} \phi(x_1 - c_{SG}t, \gamma_{SG}x_3). \quad (3.1.10)$$

3.2 Stoneley wave

Next, we study two joint elastic half-planes $H_{(2)}^+$ and $H_{(2)}^-$ in order to develop an asymptotic model for the Stoneley interfacial wave, see Stoneley (1924). The equations of motion are now expressed in terms of two sets of elastic potentials $\phi^{(k)}$ and $\psi^{(k)}$ $(k = 1, 2)$ as

$$\Delta\phi^{(k)} - \frac{1}{c_{1k}^2} \frac{\partial^2 \phi^{(k)}}{\partial t^2} = 0, \qquad \Delta\psi^{(k)} - \frac{1}{c_{2k}^2} \frac{\partial^2 \psi^{(k)}}{\partial t^2} = 0, \quad (3.2.1)$$

where $c_{1k} = \sqrt{(\lambda_k + 2\mu_k)/\rho_k}$ and $c_{2k} = \sqrt{\mu_k/\rho_k}$ are the associated bulk wave speeds for the medium k; in doing so, all the elastic parameters have to satisfy pretty sophisticated existence conditions for the Stoneley wave examined by Schölte (1947).

As before, we only consider a jump of normal stresses at the interface. Thus, we have at $x_3 = 0$

$$\begin{aligned}
&\frac{\partial \phi^{(1)}}{\partial x_1} - \frac{\partial \phi^{(2)}}{\partial x_1} + \frac{\partial \psi^{(1)}}{\partial x_3} - \frac{\partial \psi^{(2)}}{\partial x_3} = 0,\\
&\frac{\partial \phi^{(1)}}{\partial x_3} - \frac{\partial \phi^{(2)}}{\partial x_3} - \frac{\partial \psi^{(1)}}{\partial x_1} + \frac{\partial \psi^{(2)}}{\partial x_1} = 0,\\
&2\mu_1 \frac{\partial^2 \phi^{(1)}}{\partial x_1 \partial x_3} - 2\mu_2 \frac{\partial^2 \phi^{(2)}}{\partial x_1 \partial x_3} + \mu_1 \left[\frac{\partial^2 \psi^{(1)}}{\partial x_3^2} - \frac{\partial^2 \psi^{(1)}}{\partial x_1^2} \right]\\
&\qquad\qquad - \mu_2 \left[\frac{\partial^2 \psi^{(2)}}{\partial x_3^2} - \frac{\partial^2 \psi^{(2)}}{\partial x_1^2} \right] = 0,\\
&\lambda_1 \frac{\partial^2 \phi^{(1)}}{\partial x_1^2} + (\lambda_1 + 2\mu_1) \frac{\partial^2 \phi^{(1)}}{\partial x_3^2} - \lambda_2 \frac{\partial^2 \phi^{(2)}}{\partial x_1^2}\\
&- (\lambda_2 + 2\mu_2) \frac{\partial^2 \phi^{(2)}}{\partial x_3^2} - 2\mu_1 \frac{\partial^2 \psi^{(1)}}{\partial x_1 \partial x_3} + 2\mu_2 \frac{\partial^2 \psi^{(2)}}{\partial x_1 \partial x_3} = P,
\end{aligned} \tag{3.2.2}$$

where $P = P(x_1, t)$ is a given vertical force.

The transcedental equation for the Stoneley wave speed $c = c_S$ (Stoneley 1924) is

$$c_S^4 \left((\rho_1 - \rho_2)^2 - a_1 a_2 \right) + 2c_S^2 m_{12} (\rho_2 b_1 - \rho_1 b_2) + m_{12}^2 b_1 b_2 = 0, \tag{3.2.3}$$

in which

$$\begin{aligned}
a_1 = (\rho_1 \alpha_{2S} + \rho_2 \alpha_{1S}), \qquad a_2 = (\rho_1 \beta_{2S} + \rho_2 \beta_{1S}),\\
b_k = 1 - \alpha_{kS} \beta_{kS}, \qquad m_{12} = 2\left(\mu_1 - \mu_2\right),
\end{aligned} \tag{3.2.4}$$

and

$$\alpha_{kS} = \sqrt{1 - \frac{c_S^2}{c_{1k}^2}}, \qquad \beta_{kS} = \sqrt{1 - \frac{c_S^2}{c_{2k}^2}}, \qquad (k = 1, 2). \tag{3.2.5}$$

The asymptotic model for the Stoneley wave arising from the boundary value problem (3.2.1) and (3.2.2), contains the *elliptic* equation

$$\frac{\partial^2 \phi^{(1)}}{\partial x_3^2} + \alpha_{1S}^2 \frac{\partial^2 \phi^{(1)}}{\partial x_1^2} = 0 \tag{3.2.6}$$

governing the decay into the interior. The rest of wave potentials is determined by the following relations between the potentials at the interface $x_3 = 0$

$$\begin{aligned}
\psi^{(2)}(x_1 - c_S t, \beta_{2S} x_3) &= \frac{g_4}{g_1 \beta_{2S}} \overline{\phi}^{(1)}(x_1 - c_S t, \beta_{2S} x_3), \\
\phi^{(2)}(x_1 - c_S t, \alpha_{2S} x_3) &= \frac{g_2}{g_1} \phi^{(1)}(x_1 - c_S t, \alpha_{2S} x_3), \\
\psi^{(1)}(x_1 - c_S t, \beta_{1S} x_3) &= \frac{g_3}{g_4} \psi^{(2)}(x_1 - c_S t, \beta_{1S} x_3),
\end{aligned} \tag{3.2.7}$$

where

$$\begin{aligned}
g_1 &= (m_{12} - \rho_1 c_S^2) b_2 + \rho_2 c_S^2 (1 + \alpha_{2S} \beta_{1S}), \\
g_2 &= (\rho_2 c_S^2 + m_{12}) b_1 - \rho_1 c_S^2 (1 + \alpha_{1S} \beta_{2S}), \\
g_3 &= \rho_2 c_S^2 (\alpha_{1S} + \alpha_{2S}) - m_{12} \alpha_{1S} b_2, \\
g_4 &= \rho_1 c_S^2 (\alpha_{1S} + \alpha_{2S}) - m_{12} \alpha_{2S} b_1.
\end{aligned} \tag{3.2.8}$$

Finally, the *hyperbolic* equation for $\phi^{(1)}$ on the interface $x_3 = 0$ is written as

$$\frac{\partial^2 \phi^{(1)}}{\partial x^2} - \frac{1}{c_S^2} \frac{\partial^2 \phi^{(1)}}{\partial t^2} = \frac{g_1 P_S}{c_S^2 B_S}, \tag{3.2.9}$$

where the constant B_S is given by

$$\begin{aligned}
B_S = &-2c_S^2 \left[(\rho_1 - \rho_2)^2 - a_1 a_2 \right] - m_{12} c_S^2 \left(\rho_2 f_2 - \rho_1 f_1 \right) \\
&- \frac{m_{12}^2}{2} \left(b_2 f_1 + b_1 f_2 \right) - \frac{c_S^4}{2} \left(d_1 a_2 + d_2 a_1 \right) + 2 m_{12} \left(\rho_2 b_1 - \rho_1 b_2 \right),
\end{aligned} \tag{3.2.10}$$

with

$$d_k = \frac{\rho_2}{\alpha_{kS} c_{1k}^2} + \frac{\rho_1}{\beta_{kS} c_{2k}^2}, \qquad f_k = \frac{\alpha_{kS}}{\beta_{kS} c_{k2}^2} + \frac{\beta_{kS}}{\alpha_{kS} c_{k1}^2}, \qquad (k = 1, 2).$$

It is remarkable that the models for the interfacial Stoneley and Schölte-Gogoladze waves are not more difficult than that for the Rayleigh wave due to the relations for wave potentials, see (3.1.9), (3.1.10), and (3.2.7).

4 Moving load problems

We illustrate the efficiency of the derived hyperbolic-elliptic formulations for the Rayleigh wave by modelling near-resonant regimes of moving loads. As might be expected, the dynamic response caused by a load travelling at a speed close to the Rayleigh wave speed is not strongly affected by bulk waves.

4.1 Steady-state motion of a point force

We begin with the the classical plane strain problem for a steadily moving vertical point force, see Fig. 4 (see e.g. Cole & Huth 1958).

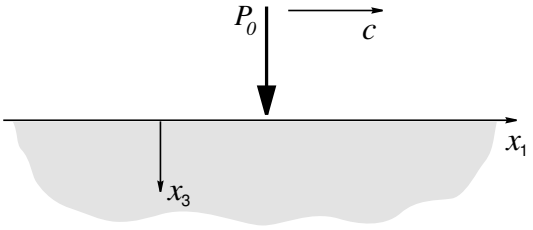

Figure 4. A point force travelling along the surface of a half-plane.

The equations of motion are given by (2.2.2), with boundary conditions on the surface $x_3 = 0$ written as

$$\sigma_{31} = 0, \qquad \sigma_{33} = P_0 \delta(x_1 - ct), \tag{4.1.1}$$

where c is a constant speed of the load.

The asymptotic model for the Rayleigh wave developed in subsection 2.4, now consists of the scalar boundary value problem

$$\frac{\partial^2 \phi}{\partial x_3^2} + \alpha_R^2 \frac{\partial^2 \phi}{\partial s^2} = 0, \tag{4.1.2}$$

subject to the boundary condition ($x_3 = 0$)

$$\left(1 - \frac{c^2}{c_R^2}\right) \frac{\partial^2 \phi}{\partial s^2} = \frac{1 + \beta_R^2}{2\mu B} P_0 \, \delta(s), \tag{4.1.3}$$

where $s = x_1 - ct$ is a moving coordinate. Remarkably, a resonant effect may be immediately observed from (4.1.3) due to degeneration at $c = c_R$. This scalar problem may be reformulated as a Dirichlet problem for the derivative $\phi_s = \dfrac{\partial \phi}{\partial s}$ as

$$\frac{\partial^2 \phi_s}{\partial x_3^2} + \alpha_R^2 \frac{\partial^2 \phi_s}{\partial s^2} = 0, \tag{4.1.4}$$

subject to

$$\phi_s(s, 0) = \frac{\left(1 + \beta_R^2\right) c_R^2 P_0}{2\mu B \left(c_R^2 - c^2\right)} \left(H(s) - \frac{1}{2}\right), \tag{4.1.5}$$

where a constant of integration is chosen because of symmetry. In fact, the 2D steady-state solution is defined to within the rigid body motion of a half-plane, which may be determined from the associated transient problem only, see Kaplunov (1986).

The problem (4.1.4) is easily solved by exploiting the Poisson formula (e.g. Courant & Hilbert 1989), giving

$$\phi_s(s,x_3)=\frac{\left(1+\beta_R^2\right)P_0c_R^2}{2\pi\mu B\left(c_R^2-c^2\right)}\arctan\frac{s}{\alpha_R\,x_3}. \tag{4.1.6}$$

Therefore (see (2.3.8)),

$$\psi_s(s,x_3)=\frac{\partial\psi}{\partial s}=-\frac{\alpha_RP_0c_R^2}{2\pi\mu B\left(c_R^2-c^2\right)}\ln\left(s^2+\beta_R^2\,x_3^2\right). \tag{4.1.7}$$

As a result, the steady-state displacement field is given by

$$\begin{aligned}
u_1^{st}(\xi)&=\frac{(1+\beta_R^2)P_0v_R^2}{2\mu\pi B(v_R^2-v^2)}\left[\arctan\frac{\xi}{\alpha_R}-\frac{1+\beta_R^2}{2}\arctan\frac{\xi}{\beta_R}\right],\\
u_2^{st}(\xi)&=-\frac{(1+\beta_R^2)P_0v_R^2\alpha_R}{4\mu\pi B(v_R^2-v^2)}\left[\ln\left(\xi^2+\alpha_R^2\right)-\frac{2}{1+\beta_R^2}\ln\left(\xi^2+\beta_R^2\right)\right],
\end{aligned} \tag{4.1.8}$$

with the following dimensionless parameters

$$\xi=\frac{s}{x_3},\qquad v=\frac{c}{c_2},\qquad v_R=\frac{c_R}{c_2}.$$

It may be verified that the displacement components in (4.1.8) are the leading order terms in the Taylor expansion of the exact solution in Cole & Huth (1958) around the resonant Rayleigh wave speed $c=c_R$.

4.2 Transient motion of a point force

Let us now consider the associated transient problem. In this case the same equation (4.1.2) is subject to the following hyperbolic boundary condition on the surface $x_3=0$

$$\frac{\partial^2\phi}{\partial s^2}-\frac{1}{c_R^2}\frac{\partial^2\phi}{\partial t^2}=\frac{1+\beta_R^2}{2\mu B}P_0\delta(s). \tag{4.2.1}$$

The solution of the latter can be written as (here and below in this subsection see Kaplunov *et al.* (2010) for more detail)

$$\phi(s,0,t)=B_1\int_0^t\left[H\left(s+(c-c_R)r\right)-H\left(s+(c+c_R)r\right)\right]dr. \tag{4.2.2}$$

with

$$B_1 = \frac{\left(1+\beta_R^2\right) c_R P_0}{4\mu B}, \tag{4.2.3}$$

and the *resonant* ($c = c_R$) case arising immediately from the analysis of the integrand.

For the *sub-Rayleigh* regime ($c < c_R$) we get from (4.2.2)

$$\phi(s,0,t) = \begin{cases} B_1 \dfrac{s-s_1}{c_R-c}, & 0 \le s < s_1; \\ B_1 \dfrac{s-s_2}{c_R+c}, & s_2 < s < 0; \\ 0, & \text{otherwise}, \end{cases} \tag{4.2.4}$$

with the values s_1 and s_2 given by

$$s_1 = t(c_R - c), \qquad s_2 = -t(c_R + c). \tag{4.2.5}$$

For the *super-Rayleigh regime* ($c > c_R$) we have

$$\phi(s,0,t) = \begin{cases} 2B_1 \dfrac{c_R s}{c^2 - c_R^2}, & s_1 \le s \le 0; \\ -B_1 \dfrac{s-s_2}{c_R+c}, & s_2 < s < s_1; \\ 0, & \text{otherwise}. \end{cases} \tag{4.2.6}$$

Finally, if $c = c_R$, we obtain

$$\phi(s,0,t) = \begin{cases} -B_1 \dfrac{s-s_2}{2c_R}, & s_2 \le s \le 0; \\ 0, & \text{otherwise}, \end{cases} \tag{4.2.7}$$

with s_2 given now by $s_2 = -2c_R t$.

The solutions on the surface (4.2.4), (4.2.6) and (4.2.7) provide an immediate insight into the physics of the original problem. In particular, Fig. 5 shows a clear distinction of the resonant regime from the two others. In this figure the function $\phi(s,0,t)$ at a fixed time t is plotted for all three aforementioned cases. If $c \neq c_R$, the solution in question is continuous in s, see Figs 5(a) and 5(b). At the same time, the limiting resonant solution in Fig. 5(c), demonstrates a discontinuity under a line moving force ($s = 0$), which is linearly increasing in time. As a result we should not expect a steady-state regime at $c = c_R$. Thus, a rather straightforward analysis of an infinite string under a moving load immediately reveals the resonant phenomena associated with the Rayleigh wave.

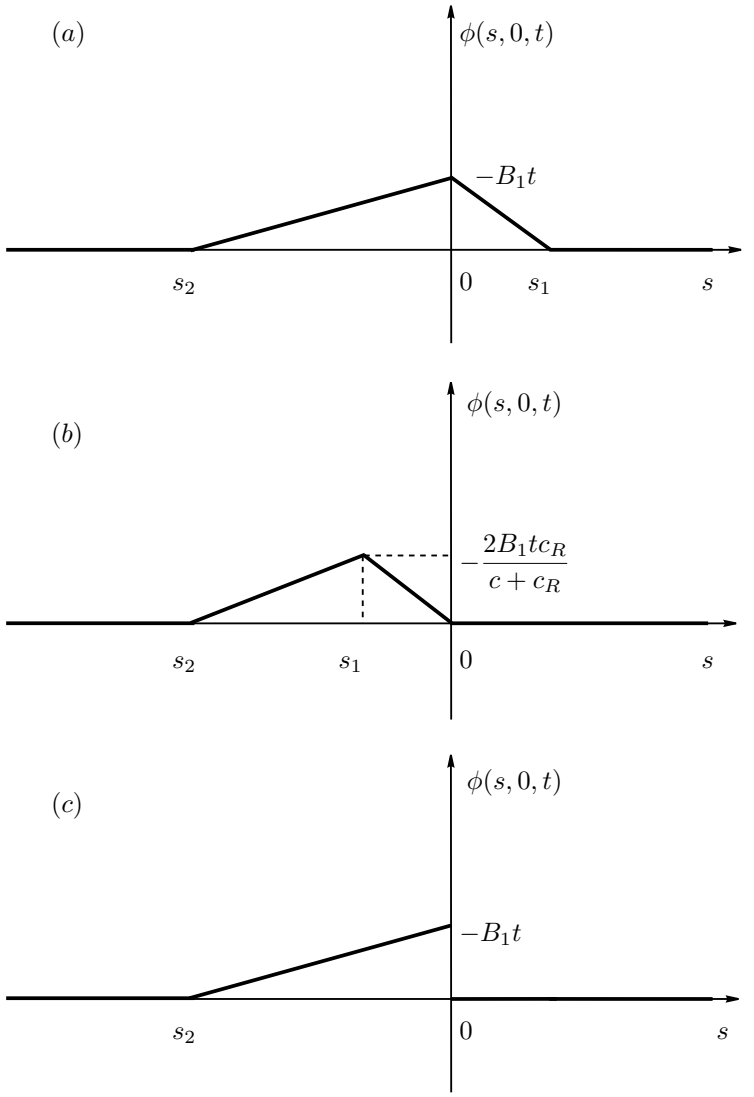

Figure 5. The wave potential ϕ vs. the moving co-ordinate s on the surface $x_3 = 0$: (a) the sub-Rayleigh regime ($c < c_R$); (b) the super-Rayleigh regime ($c > c_R$); (c) resonant regime ($c = c_R$).

Once the potential is determined at the surface $x_3 = 0$, the solution is then restored over the interior through the Poisson formulae. In the *sub-*

Rayleigh and *super-Rayleigh* regimes the displacement components become

$$\begin{aligned} u_1(\xi,\tau) = {} & \frac{2B_1\, v_R}{\pi c_2(v_R^2 - v^2)}\left[\arctan\frac{\xi}{\alpha_R} - \frac{1+\beta_R^2}{2}\arctan\frac{\xi}{\beta_R}\right] \\ & - \frac{B_1}{\pi c_2(v_R+v)}\left[\arctan\frac{\xi-\xi_2}{\alpha_R} - \frac{1+\beta_R^2}{2}\arctan\frac{\xi-\xi_2}{\beta_R}\right] \\ & - \frac{B_1}{\pi c_2(v_R-v)}\left[\arctan\frac{\xi-\xi_1}{\alpha_R} - \frac{1+\beta_R^2}{2}\arctan\frac{\xi-\xi_1}{\beta_R}\right], \end{aligned} \tag{4.2.8}$$

$$\begin{aligned} u_3(\xi,\tau) = {} & \frac{B_1\,\alpha_R}{2\pi c_2(v_R+v)}\left[\ln\frac{(\xi-\xi_2)^2+\alpha_R^2}{\xi^2+\alpha_R^2} - \frac{2}{1+\beta_R^2}\ln\frac{(\xi-\xi_2)^2+\beta_R^2}{\xi^2+\beta_R^2}\right] \\ & + \frac{B_1\,\alpha_R}{2\pi c_2(v_R-v)}\left[\ln\frac{(\xi-\xi_1)^2+\alpha_R^2}{\xi^2+\alpha_R^2} - \frac{2}{1+\beta_R^2}\ln\frac{(\xi-\xi_1)^2+\beta_R^2}{\xi^2+\beta_R^2}\right], \end{aligned} \tag{4.2.9}$$

with

$$\tau = \frac{c_2 t}{x_3}, \qquad \xi_1 = \frac{s_1}{x_3} = (v_R - v)\tau, \qquad \xi_2 = \frac{s_2}{x_3} = -(v + v_R)\tau, \tag{4.2.10}$$

and s_1, s_2 defined by (4.2.5). In the *resonant* regime the corresponding displacement components may be found as

$$\begin{aligned} u_1(\xi,\tau) = {} & \frac{B_1\alpha_R\tau}{\pi c_2}\left[\frac{1}{\xi^2+\alpha_R^2} - \frac{2\beta_R^2}{(1+\beta_R^2)(\xi^2+\beta_R^2)}\right] \\ & + \frac{\beta}{2\pi c_2 v_R}\left[\arctan\frac{\xi}{\alpha_R} - \arctan\frac{\xi-\xi_2}{\alpha_R}\right] \\ & - \frac{B_1(1+\beta_R^2)}{4\pi c_2 v_R}\left[\arctan\frac{\xi}{\beta_R} - \arctan\frac{\xi-\xi_2}{\beta_R}\right], \end{aligned} \tag{4.2.11}$$

$$\begin{aligned} u_3(\xi,\tau) = {} & \frac{B_1\alpha_R\xi\tau}{\pi c_2}\left[\frac{2}{(1+\beta_R^2)(\xi^2+\beta_R^2)} - \frac{1}{\xi^2+\alpha_R^2}\right] \\ & + \frac{B_1\alpha_R}{4\pi c_2 v_R}\left[\ln\frac{(\xi-\xi_2)^2+\alpha_R^2}{\xi^2+\alpha_R^2} - \frac{2}{1+\beta_R^2}\ln\frac{(\xi-\xi_2)^2+\beta_R^2}{\xi^2+\beta_R^2}\right], \end{aligned} \tag{4.2.12}$$

with $\xi_2 = -2v_R\tau$.

The obtained displacements (4.2.8)-(4.2.12) are expressed in elementary functions in contrast to the integral exact solution of the problem, see Appendix of Kaplunov *et al.* (2010). Nevertheless, the approximate solution demonstrates key features of the problem, in particular, an important large time limit as $\tau \to \infty$ immediately follows from the formulae above. In the sub-Rayleigh regime we have

$$u_i(\xi,\tau) \sim u_i^{\infty}(\xi,\tau), \qquad u_i^{\infty}(\xi,\tau) = u_i^{st}(\xi) + u_i^{r}(\tau) \qquad (i = 1, 2), \tag{4.2.13}$$

where u_i^{st} $(i = 1, 2)$ are displacements in the related steady-state problem (4.1.8), and

$$u_1^r(\tau) = u_1^{r0}, \qquad u_2^r(\tau) = u_2^{r0} + u_2^{r\tau}(\tau), \tag{4.2.14}$$

with

$$\begin{aligned} u_1^{r0} &= \frac{B_1 v \left(1 - \beta_R^2\right)}{2c_2(v_R^2 - v^2)}, \\ u_2^{r0} &= -\frac{B_1 \alpha_R (1 - \beta_R^2)}{\pi c_2 (1 + \beta_R^2)} \left[\frac{\ln(v_R + v)}{v_R + v} + \frac{\ln|v_R - v|}{v_R - v} \right], \\ u_2^{r\tau}(\tau) &= -\frac{2B_1 v_R \alpha_R (1 - \beta_R^2)}{\pi c_2 (v_R^2 - v^2)(1 + \beta_R^2)} \ln \tau. \end{aligned} \tag{4.2.15}$$

Here u_i^r $(i = 1, 2)$ are components of the rigid body motion of the half-plane. It is remarkable that the rigid body motion along the vertical axe demonstrates a logarithmic growth in time, see (4.2.14) and (4.2.15), observed earlier in Kaplunov (1986). This means that a steady-state regime in subsection 4.1 cannot be achieved at a large time limit.

The formulae (4.2.13)-(4.2.15) are also valid for the super-Rayleigh case, except the expression for the rigid body motion component along the horizontal axe, which now becomes

$$u_1^{r0} = -\frac{B_1 v_R \left(1 - \beta_R^2\right)}{2c_2(v_R^2 - v^2)}. \tag{4.2.16}$$

In the resonant case the limiting behaviour as $\tau \to \infty$ is

$$u_i(\xi, \tau) \sim u_i^{\infty}(\xi, \tau) \qquad (i = 1, 2), \tag{4.2.17}$$

with

$$u_1^{\infty}(\xi, \tau) = \frac{B_1 \alpha_R \tau}{\pi c_2} \left[\frac{1}{\xi^2 + \alpha_R^2} - \frac{2\beta_R^2}{(1 + \beta_R^2)(\xi^2 + \beta_R^2)} \right], \tag{4.2.18}$$

$$\begin{aligned} u_2^{\infty}(\xi, \tau) = {} & \frac{B_1 \alpha_R \xi \tau}{\pi c_2} \left[\frac{2}{(1 + \beta_R^2)(\xi^2 + \beta_R^2)} - \frac{1}{\xi^2 + \alpha_R^2} \right] \\ & + \frac{B_1 \alpha_R (\beta_R^2 - 1)}{4\pi c_2 v_R (\beta_R^2 + 1)} \ln \tau. \end{aligned} \tag{4.2.19}$$

Thus, the displacements demonstrate linear growth in time apart from the vertical displacement at $\xi = 0$, which increases as $\ln \tau$.

Another interesting observation is related to the resonant regime of a moving semi-infinite strip, in which $P = P_0 H(x - c_R t)$. In this case the

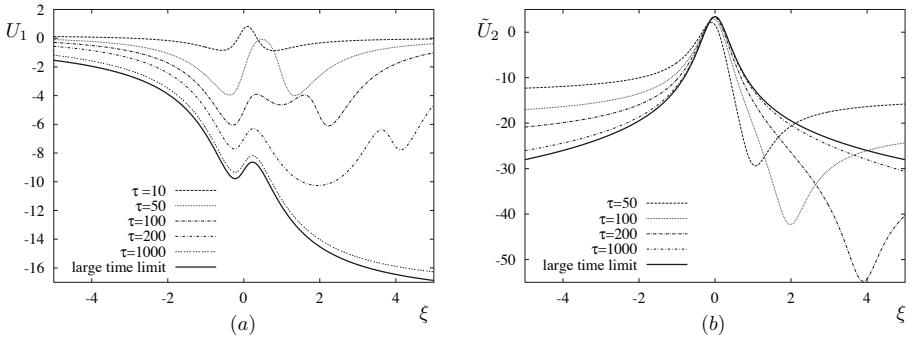

Figure 6. The sub-Rayleigh transient (a) horizontal and (b) vertical displacements (4.2.8) and (4.2.9) and the large time limits (4.2.13) for $v = 0.9$.

asymptotic model recovers the classical result of Goldstein (1965) with less effort.

Numerical illustrations are presented in Fig. 6-8 for the Poisson ratio $\nu = 0.25$ corresponding to $v_R \approx 0.9194$.

We plot the dimensionless displacements

$$U_k = \frac{\pi\mu u_k}{P_0}, \quad \tilde{U}_2 = \frac{\pi\mu}{P_0}\left(u_2(\xi,\tau) - u_2^{r\tau}(\tau)\right).$$

Here we subtract from the vertical displacement $u_2(\xi,\tau)$ the function $u_2^{r\tau}(\tau)$ having a logarithmic growth in time, see (4.2.14) and (4.2.15). In this case we depict only a bounded in time component in order to show convergence at a large time limit.

The sub-Rayleigh displacements of the half-space (4.2.8) and (4.2.9) are plotted in Fig. 6 for $v = 0.9$ and several values of time τ. Similar results for the super-Rayleigh regime ($v = 0.95$) are presented in Fig. 7. The solid line corresponds to the limits (4.2.13) with (4.2.14)–(4.2.15) and (4.2.16). As might be expected, transient displacements tend to their large time values as time increases. The resonant displacements (4.2.11) and (4.2.12) are displayed in Fig. 8 for $\tau = 10$, 30, 50 and 100. They demonstrate a linear growth in time according to the formulae (4.2.11) and (4.2.12).

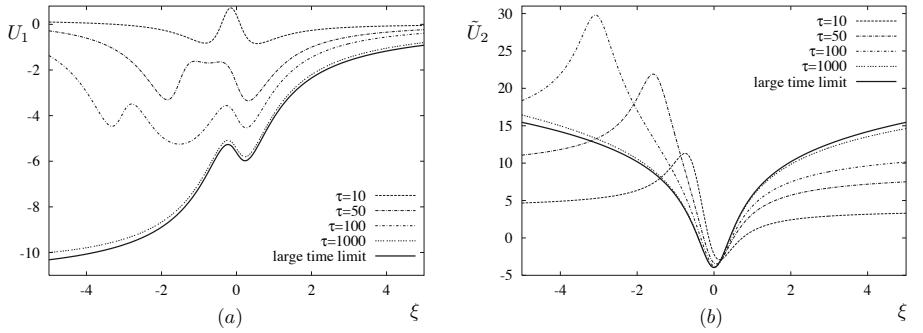

Figure 7. The super-Rayleigh transient (a) horizontal and (b) vertical displacements (4.2.8) and (4.2.9) and the large time limits (4.2.13) for $v = 0.95$.

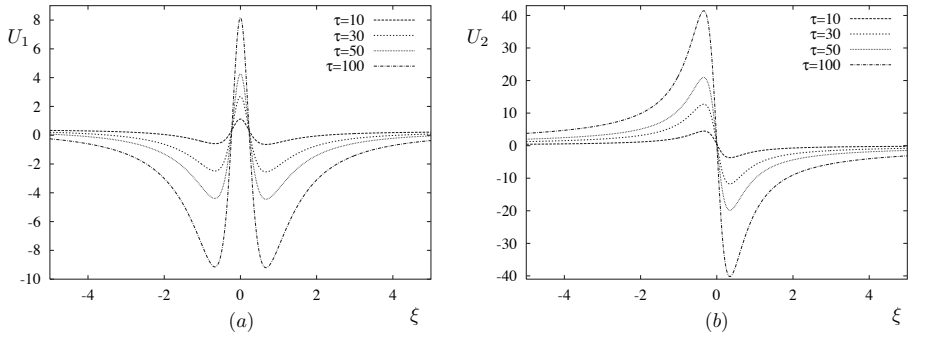

Figure 8. The resonant transient (a) horizontal and (b) vertical displacements (4.2.11) and (4.2.12) for $v = v_R$.

4.3 Steady-state motion of a stamp

Consider the steady-state motion of a rigid stamp, see Fig. 9, assuming

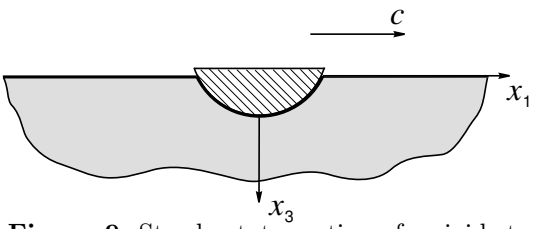

Figure 9. Steady-state motion of a rigid stamp

that its effect results in a prescribed surface displacements $U_3(x_1,t) = f(x_1 - ct)$. We also set $P = 0$ in the equation (2.5.4) governing the surface motion outside the stamp. The formulation of the mixed boundary value problem, obtained in subsection 2.5, may then be specified for the scaled normal derivative

$$\chi(s,p) = \frac{\beta_R^2 - 1}{\beta_R^2 + 1}\,\frac{\partial \phi}{\partial s}, \tag{4.3.1}$$

where $s = x_1 - ct,\ p = \alpha_R x_3$, for more details see Erbaş *et al.* (2012). Thus, we arrive at a canonical problem for the Laplace equation

$$\frac{\partial^2 \chi}{\partial p^2} + \frac{\partial^2 \chi}{\partial s^2} = 0, \tag{4.3.2}$$

with the mixed boundary conditions ($p = 0$)

$$\chi = f(s), \quad \text{at} \ \ s \in S_2 \tag{4.3.3}$$

and

$$\frac{\partial \chi}{\partial p} = 0, \quad \text{at} \ \ s \in S_1, \tag{4.3.4}$$

where and S_1 and S_2 are the traction free and constrained parts of the surface $p = 0$, respectively.

As an example, we consider an exponential stamp $f(s) = be^{-as}$, where a and b are positive constants. In this case (e.g. see Sveshnikov & Tikhonov 1978)

$$\chi(s,p) = b\mathrm{Re}\left\{e^{-aq}\left[1 - \mathrm{erf}\left(\sqrt{-aq}\right)\right]\right\}, \tag{4.3.5}$$

where $q = s + ip$ and $\mathrm{erf}(q)$ is the error function.

A resonant nature of the Rayleigh wave is clearly seen from the formula for the normal stress under the stamp

$$\sigma_{33}(s,0) = \frac{2\mu B\alpha_R^3\left(c^2 - c_R^2\right)}{(\beta_R^2 - 1)c_R^2}\,\chi(s,0)\,, \quad \text{at} \;\; s \in S_2. \tag{4.3.6}$$

Thus, the resonant limit as $c \to c_R$, corresponds to an asymptotically vanishing stress induced by a displacement of finite magnitude.

4.4 Moving load on a coated half-plane

Let a coated half-plane be loaded by a distributed force of the form (see Fig. 10)

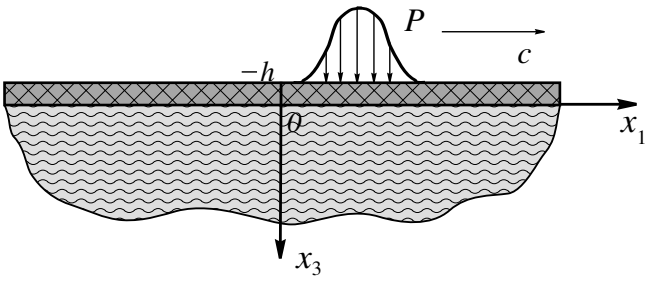

Figure 10. Distributed moving load on a coated half-plane.

$$P(x_1,t) = \frac{P_0 l}{\pi\left[l^2 + s^2\right]},$$

where l is a typical length, and $s = x_1 - ct$. We restrict ourselves to analysis of the surface motion ($x_3 = 0$), governed by the perturbed hyperbolic equation (2.6.8). We introduce the dimensionless moving coordinate $s_l = s/l$ along with the parameters

$$g = 1 - \frac{c^2}{c_R^2}, \qquad h_l = \frac{bh}{l} \tag{4.4.1}$$

and rewrite (2.6.8) as

$$g\theta - h_l\sqrt{-\frac{\partial^2}{\partial s_l^2}}\,\theta = \frac{1}{1+s_l^2}, \tag{4.4.2}$$

where

$$\theta = \frac{AP_0}{\pi l}\frac{\partial^2\phi}{\partial s_l^2}$$

denotes scaled normal surface stresses, here and below in this subsection see Dai *et al.* (2010) for further detail.

We remark that g and h_l are key problem parameters characterising the thickness of the coating and the proximity of the speed of the load to the Rayleigh wave speed, respectively. Then, using the Fourier transform, we present the solution of (4.4.2) as

$$\theta = -\frac{1}{2h_l}\sum_{n=1}^{2} e^{q_n}\mathrm{Ei}(1,q_n) \tag{4.4.3}$$

where

$$q_n = -\frac{g}{h_l}\left[1+(-1)^n i s_l\right], \qquad n=1,2,$$

and Ei is the integral exponent.

Two limiting cases may then be investigated. The first limit corresponds to the solution for an uncoated half-plane as $h_l/g \to 0$, whereas the second one $g/h_l \to 0$ reveals that the presence of a coating does not remove the resonance at $c = c_R$. The reason is that, despite of the dispersion due to the influence of the coating, the maximum or minimum of the phase speed is still given by the Rayleigh wave speed.

5 Edge bending wave

In this section we apply the proposed philosophy to the bending wave propagating along the edge of a semi-infinite thin elastic plate. We show that the dispersive edge bending wave has a *parabolic-elliptic* duality in contrast to a *hyperbolic-elliptic* duality of the non-dispersive surface and interfacial waves considered above.

5.1 Dispersion relation

Let the geometry of the plate of thickness $2h$ be given by $-\infty < x_1 < \infty$, $0 \le x_2 < \infty$, $-h \le x_3 \le h$, see Fig. 11. We start from the approximate 2D equation in the classical Kirchhoff theory for plate bending, given by

$$D\Delta^2 W + 2\rho h\frac{\partial^2 W}{\partial t^2} = 0, \tag{5.1.1}$$

where $W(x_1,x_2,t)$ is the deflection of the plate, $\Delta = \dfrac{\partial^2}{\partial x_1^2} + \dfrac{\partial^2}{\partial x_2^2}$, and

$$D = \frac{2Eh^3}{3\left(1-\nu^2\right)} \tag{5.1.2}$$

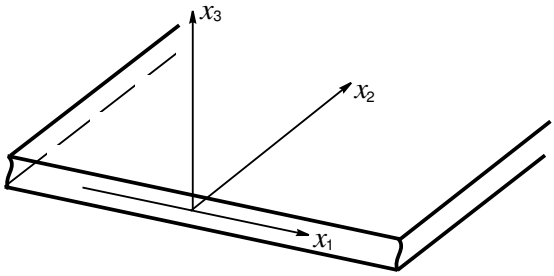

Figure 11. Thin elastic plate.

is bending stiffness, with E and ν denoting the Young modulus and the Poisson ratio, respectively.

The boundary conditions at the edge $x_2 = 0$ can be written as

$$\begin{aligned} &\frac{\partial^2 W}{\partial x_2^2} + \nu \frac{\partial^2 W}{\partial x_1^2} = -\frac{M}{D}, \\ &\frac{\partial^3 W}{\partial x_2^3} + (2-\nu)\,\frac{\partial^3 W}{\partial x_1^2 \partial x_2} = -\frac{N}{D}, \end{aligned} \tag{5.1.3}$$

where $M = M(x_1, t)$ and $N = N(x_1, t)$ are prescribed bending moment and shear force, respectively.

The travelling wave solution of (5.1.1) may be found in the form

$$W(x_1, x_2, t) = \sum_{j=1}^{2} C_j e^{i(kx_1 - \omega t) - k\lambda_j x_2}, \tag{5.1.4}$$

where

$$\lambda_j = \sqrt{1 + (-1)^j \sqrt{\frac{2\rho h}{D}}\,\frac{\omega}{k^2}}, \qquad j = 1, 2. \tag{5.1.5}$$

Substitution of (5.1.4) into the homogeneous edge boundary conditions ($M = N = 0$ in (5.1.3)) leads to the dispersion relation

$$Dk^4 \gamma_e^4 = 2\rho h \omega^2, \tag{5.1.6}$$

originating from Konenkov (1960) and subsequent contributions, see also Lawrie & Kaplunov (2012) and Norris *et al.* (2000) and references therein. Here the coefficient

$$\gamma_e = \left[(1-\nu)\left(3\nu - 1 + 2\sqrt{2\nu^2 - 2\nu + 1}\right)\right]^{1/4} \tag{5.1.7}$$

depends on the Poisson ratio only. In view of the dispersion relation (5.1.6), we have

$$\lambda_j = \lambda_{j0} = \sqrt{1 + (-1)^j \gamma_e^2}, \qquad j = 1, 2. \tag{5.1.8}$$

5.2 Edge bending wave of arbitrary profile

Here we generalise the travelling wave solution to that expressed through arbitrary plane harmonic function. The equation (5.1.1), written in terms of the dimensionless variables

$$\zeta_i = \frac{x_i}{h}, \qquad t_h = \frac{t}{h}\sqrt{\frac{E}{3\rho(1-\nu^2)}}, \qquad i = 1, 2 \tag{5.2.1}$$

becomes

$$\Delta^2 W + \frac{\partial^2 W}{\partial t_h^2} = 0, \tag{5.2.2}$$

where $\Delta = \dfrac{\partial^2}{\partial \zeta_1^2} + \dfrac{\partial^2}{\partial \zeta_2^2}$.

Let us assume that

$$\gamma^4 \frac{\partial^4 W}{\partial \zeta_1^4} + \frac{\partial^2 W}{\partial t_h^2} = 0, \tag{5.2.3}$$

where γ is a dimensionless parameter. This is a key assumption, leading below to transformation of the parabolic equation (5.2.2) to an elliptic equation and finally resulting in the sought for representation in terms of a plane harmonic function. The philosophy underlying (5.2.3) essentially mirrors that of subsection 2.3 (see Chadwick 1976), where the surface wave solution was obtained in the form of a travelling wave of arbitrary profile. Indeed, while an elastic string seems to be a right 1D object for understanding surface wave propagation, see the classical wave equation (2.4.15), its counterpart for the edge bending wave is a beam.

The equation (5.2.2) then becomes

$$\left(1 - \gamma^4\right) \frac{\partial^4 W}{\partial \zeta_1^4} + 2\frac{\partial^4 W}{\partial \zeta_1^2 \partial \zeta_2^2} + \frac{\partial^4 W}{\partial \zeta_2^4} = 0. \tag{5.2.4}$$

It also may be expressed in an operator form as

$$\Delta_1 \Delta_2 W = 0, \tag{5.2.5}$$

where

$$\Delta_j = \frac{\partial^2}{\partial \zeta_2^2} + \lambda_j^2 \frac{\partial^2}{\partial \zeta_1^2}, \qquad j = 1, 2, \tag{5.2.6}$$

and

$$\lambda_j^2 = 1 + (-1)^j \gamma^2. \tag{5.2.7}$$

The solution of (5.2.5) is expressed through two decaying as $\zeta_2 \to \infty$ plane harmonic functions W_j as

$$W = \sum_{j=1}^{2} W_j \left(\zeta_1, \lambda_j \zeta_2, t_h\right). \tag{5.2.8}$$

Let us substitute the latter into the homogeneous boundary conditions (5.1.3) rewritten in terms of dimensionless variables, using the Cauchy-Riemann identities (2.3.4). The result is

$$\begin{aligned} &\left(\nu - \lambda_1^2\right) \frac{\partial^2 W_1}{\partial \zeta_1^2} + \left(\nu - \lambda_2^2\right) \frac{\partial^2 W_2}{\partial \zeta_1^2} = 0, \\ &\lambda_1 \left(\lambda_1^2 - 2 + \nu\right) \frac{\partial^3 W_1}{\partial \zeta_1^3} + \lambda_2 \left(\lambda_2^2 - 2 + \nu\right) \frac{\partial^3 W_2}{\partial \zeta_1^3} = 0, \end{aligned} \tag{5.2.9}$$

leading to

$$\lambda_2(\nu - \lambda_1^2)^2 - \lambda_1(\nu - \lambda_2^2)^2 = 0. \tag{5.2.10}$$

Due to (5.2.7), the last relation may be re-cast in the form

$$1 - \gamma^4 - (2\nu - 2)\sqrt{1 - \gamma^4} - \nu^2 = 0. \tag{5.2.11}$$

Then,

$$\gamma^4 = (1 - \nu)\left(3\nu - 1 + 2\sqrt{2\nu^2 - 2\nu + 1}\right) = \gamma_e^4, \tag{5.2.12}$$

which coincides with the root of the dispersion relation (5.1.6) implying $\lambda_j = \lambda_{j0}$.

Similarly to subsection 2.3.1, the harmonic functions W_1 and W_2 may be related to each other. Consequently, a representation in terms of a single harmonic function may be established from the boundary conditions (5.2.9), namely

$$W\left(x_1, x_2, t\right) = W_j\left(x_1, \lambda_{j0} x_2, t\right) - \frac{\nu - \lambda_{j0}^2}{\nu - \lambda_{m0}^2} W_j\left(x_1, \lambda_{m0} x_2, t\right). \tag{5.2.13}$$

where $1 \le j \ne m \le 2$.

It is remarkable that (5.2.13) is even simpler than its Rayleigh wave counterpart (Chadwick 1976), since it does not involve harmonic conjugate functions.

5.3 Parabolic-elliptic model

Now we proceed with the development of an explicit model for the edge bending wave. In parallel with subsection 2.4, we perturb the equation (5.1.1) around the edge wave eigensolution constructed in the subsection 5.2. However, this procedure is now less trivial because of a multi-scale behaviour in time. Accordingly, we introduce fast ($\tau_f = t_h$) and slow ($\tau_s = \varepsilon t_h$) time variables, where as before $\varepsilon \ll 1$ is a small parameter. The equation (5.2.2) may now be written in terms of specified two time-scales as

$$\Delta^2 W + \left(\frac{\partial^2 W}{\partial \tau_f^2} + 2\varepsilon \frac{\partial^2 W}{\partial \tau_f \partial \tau_s} + \varepsilon^2 \frac{\partial^2 W}{\partial \tau_s^2} \right) = 0. \tag{5.3.1}$$

The deflection W may be then expanded in an asymptotic series, i. e.

$$W = \frac{h^2}{D} \left(W^{(0)} + \varepsilon W^{(1)} + ... \right). \tag{5.3.2}$$

Next, we substitute the expansion (5.3.2) into the governing equation (5.3.1), having at leading order

$$\Delta^2 W^{(0)} + \frac{\partial^2 W^{(0)}}{\partial \tau_f^2} = 0, \tag{5.3.3}$$

which may be readily transformed to

$$\left(1 - \gamma_e^4\right) \frac{\partial^4 W^{(0)}}{\partial \zeta_1^4} + 2 \frac{\partial^4 W^{(0)}}{\partial \zeta_1^2 \partial \zeta_2^2} + \frac{\partial^4 W^{(0)}}{\partial \zeta_2^4} = 0, \tag{5.3.4}$$

by making use of the assumption (5.2.3) at $\gamma = \gamma_e$. The solution of (5.3.4) is then given by a combination of harmonic functions, yielding

$$W^{(0)} = \sum_{j=1}^{2} W_j^{(0)} \left(\zeta_1, \lambda_{j0} \zeta_2, \tau_f, \tau_s \right), \tag{5.3.5}$$

where the scaling factors λ_{j0} $(j = 1, 2)$ are defined by (5.1.8).

At next order we obtain from (5.3.1)

$$\Delta^2 W^{(1)} + \frac{\partial^2 W^{(1)}}{\partial \tau_f^2} + 2 \frac{\partial^2 W^{(0)}}{\partial \tau_f \partial \tau_s} = 0, \tag{5.3.6}$$

which, in view of (5.2.3), may be re-written as

$$\Delta_1 \Delta_2 W^{(1)} = -2 \frac{\partial^2 W^{(0)}}{\partial \tau_f \partial \tau_s}. \tag{5.3.7}$$

For the sake of definiteness, we specify (5.2.3) as

$$i\gamma_e^2 \frac{\partial^2 W_j^{(0)}}{\partial \zeta_1^2} + \frac{\partial W_j^{(0)}}{\partial \tau_f} = 0, \qquad j = 1, 2. \tag{5.3.8}$$

Further analysis of (5.3.7) also requires separate consideration for both plane harmonic functions $W_j^{(1)}$, $j = 1, 2$. Let us first concentrate on $W_1^{(1)}$. Using properties of harmonic functions we deduce that

$$\Delta_2 W_1^{(0)} = (\lambda_{20}^2 - \lambda_{10}^2)\frac{\partial^2 W_1^{(0)}}{\partial \zeta_1^2} = 2\gamma_e^2 \frac{\partial^2 W_1^{(0)}}{\partial \zeta_1^2} = 2i\frac{\partial W_1^{(0)}}{\partial \tau_f}. \tag{5.3.9}$$

Therefore, the equation (5.3.7) may be presented as

$$\Delta_1 W_1^{(1)} = i\,\frac{\partial W^{(0)}}{\partial \tau_s}. \tag{5.3.10}$$

It is convenient now to define the function $\Phi_1^{(1)} = \dfrac{\partial W_1^{(1)}}{\partial \zeta_2}$. Then the equation (5.3.10) is rewritten as

$$\Delta_1 \Phi_1^{(1)} = i\,\frac{\partial^2 W_1^{(0)}}{\partial \zeta_2 \partial \tau_s}. \tag{5.3.11}$$

Similarly to (2.4.6), the solution of (5.3.11) may be found as

$$\Phi_1 = \frac{\partial W_1}{\partial \zeta_2} = \frac{\partial W_1^{(0)}}{\partial \zeta_2} + \varepsilon \left(\Phi_1^{(1,0)} + \frac{1}{2}\, i\zeta_2\, \frac{\partial W_1^{(0)}}{\partial \tau_s} \right) + \ldots \quad . \tag{5.3.12}$$

We also have for W_2

$$\Delta_2 W_2^{(1)} = -i\,\frac{\partial W_2^{(0)}}{\partial \tau_s}, \tag{5.3.13}$$

resulting in

$$\Phi_2 = \frac{\partial W_2}{\partial \zeta_2} = \frac{\partial W_2^{(0)}}{\partial \zeta_2} + \varepsilon \left(\Phi_2^{(1,0)} - \frac{1}{2}\, i\zeta_2\, \frac{\partial W_2^{(0)}}{\partial \tau_s} \right) + \ldots \quad . \tag{5.3.14}$$

Finally, we obtain for the normal derivative

$$\begin{aligned} \frac{\partial W}{\partial \zeta_2} = \frac{h^2}{D} \Bigg[& \frac{\partial \left(W_1^{(0)} + W_2^{(0)} \right)}{\partial \zeta_2} \\ & + \varepsilon \left(\Phi_1^{(1,0)} + \Phi_2^{(1,0)} + i\frac{\zeta_2}{2}\, \frac{\partial \left(W_1^{(0)} - W_2^{(0)} \right)}{\partial \tau_s} \right) + \ldots \Bigg]. \end{aligned} \tag{5.3.15}$$

Now we are in position to treat the non-homogeneous boundary conditions (5.1.3). As above in 2.4.1, the problem may be decomposed into two separate sub-problems involving a prescribed edge bending moment or shear force only. First, we study the effect of an edge bending moment normalized as $M = \varepsilon M_\varepsilon$. The boundary conditions rewritten in terms of dimensionless coordinates, are

$$\begin{aligned} &\frac{\partial^2 W}{\partial \zeta_2^2} + \nu \frac{\partial^2 W}{\partial \zeta_1^2} = -\frac{\varepsilon h^2}{D} M_\varepsilon, \\ &\frac{\partial^3 W}{\partial \zeta_2^3} + (2-\nu) \frac{\partial^3 W}{\partial \zeta_1^2 \partial \zeta_2} = 0. \end{aligned} \tag{5.3.16}$$

On substituting the asymptotic expansion (5.3.15) into the latter we obtain at leading order

$$\begin{aligned} &\left(\nu - \lambda_{10}^2\right) \frac{\partial^2 W_1^{(0)}}{\partial \zeta_1^2} + \left(\nu - \lambda_{20}^2\right) \frac{\partial^2 W_2^{(0)}}{\partial \zeta_1^2} = 0, \\ &\lambda_{10} \left(\lambda_{10}^2 - 2 + \nu\right) \frac{\partial^3 W_1^{(0)}}{\partial \zeta_1^3} + \lambda_{20} \left(\lambda_{20}^2 - 2 + \nu\right) \frac{\partial^3 W_2^{(0)}}{\partial \zeta_1^3} = 0, \end{aligned} \tag{5.3.17}$$

which is an analogue of (5.2.9). It results in the dispersion relation (5.2.10), implying $\lambda_j = \lambda_{j0}$, $j = 1, 2$, see also (5.1.8).

At next order, the boundary conditions (5.3.16) are given by

$$\begin{aligned} &\frac{\partial^2 W^{(1)}}{\partial \zeta_2^2} + \nu \frac{\partial^2 W^{(1)}}{\partial \zeta_1^2} = -M_\varepsilon, \\ &\frac{\partial^3 W^{(1)}}{\partial \zeta_2^3} + (2-\nu) \frac{\partial^3 W^{(1)}}{\partial \zeta_1^2 \partial \zeta_2} = 0. \end{aligned} \tag{5.3.18}$$

The relations (5.3.10) and (5.3.13) may be used to deduce that

$$\left.\frac{\partial^2 W^{(1)}}{\partial \zeta_1^2}\right|_{\zeta_2 = 0} = \frac{1}{\lambda_{10}^2} \left(\frac{i}{2} \frac{\partial W_1^{(0)}}{\partial \tau_s} - \frac{\partial \Phi_1^{(1,0)}}{\partial \zeta_2} \right) - \frac{1}{\lambda_{20}^2} \left(\frac{i}{2} \frac{\partial W_2^{(0)}}{\partial \tau_s} + \frac{\partial \Phi_2^{(1,0)}}{\partial \zeta_2} \right). \tag{5.3.19}$$

The boundary conditions (5.3.18) taking into account (5.3.15) and (5.3.19),

become

$$\begin{aligned}
&\left(1-\frac{\nu}{\lambda_{10}^2}\right)\frac{\partial\Phi_1^{(1,0)}}{\partial\zeta_2}+\left(1-\frac{\nu}{\lambda_{20}^2}\right)\frac{\partial\Phi_2^{(1,0)}}{\partial\zeta_2}\\
&\qquad+\frac{i}{2}\left(1+\frac{\nu}{\lambda_{10}^2}\right)\frac{\partial W_1^{(0)}}{\partial\tau_s}-\frac{i}{2}\left(1+\frac{\nu}{\lambda_{20}^2}\right)\frac{\partial W_2^{(0)}}{\partial\tau_s}=-M_\varepsilon,\\
&\left(2-\nu-\lambda_{10}^2\right)\frac{\partial^2\Phi_1^{(1,0)}}{\partial\zeta_1^2}+\left(2-\nu-\lambda_{20}^2\right)\frac{\partial^2\Phi_2^{(1,0)}}{\partial\zeta_1^2}\\
&\qquad+i\,\frac{\partial^2 W_1^{(0)}}{\partial\zeta_2\partial\tau_s}-i\,\frac{\partial^2 W_2^{(0)}}{\partial\zeta_2\partial\tau_s}=0.
\end{aligned}\tag{5.3.20}$$

Finally, we obtain using also the formula (5.2.13),

$$\frac{2i\gamma_e^2}{Q}\frac{\partial^2 W^{(0)}}{\partial\zeta_1\partial\tau_s}=-\frac{\partial M_\varepsilon}{\partial\xi},\tag{5.3.21}$$

where

$$Q=\frac{\eta\,(\nu+\eta)}{1-\nu+\eta},\tag{5.3.22}$$

with

$$\eta=\lambda_{10}\lambda_{20}=\sqrt{1-\gamma_e^4}.\tag{5.3.23}$$

Here the coefficient Q depends on the Poisson ratio only, see Fig. 12.

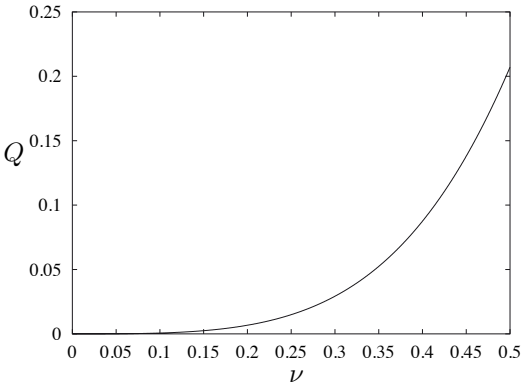

Figure 12. Coefficient Q vs. the Poisson ratio ν

The equation (5.3.21) enables calculation of the edge wave contribution to the overall dynamic response. This observation also follows from a similarity of the developed perturbation procedure and the routine in Kaplunov et al. (2013a) relying on computation of the residues corresponding to edge wave poles.

The operator relationship

$$\frac{\partial}{\partial \tau_s} = \varepsilon^{-1}\left(i\gamma_e^2 \frac{\partial^2}{\partial \zeta_1^2} + \frac{\partial}{\partial t_h}\right), \tag{5.3.24}$$

along with the condition (5.3.8), allow transformation of (5.3.21) to a parabolic equation at the edge $\zeta_2 = 0$. It is given by

$$\gamma_e^4 \frac{\partial^4 W^{(0)}}{\partial \zeta_1^4} + \frac{\partial^2 W^{(0)}}{\partial t_h^2} = Q\frac{\partial^2 M}{\partial \zeta_1^2}. \tag{5.3.25}$$

The equation (5.3.25) (see (5.3.2)) may be re-cast in terms of original variables as ($x_2 = 0$)

$$D\gamma_e^4 \frac{\partial^4 W}{\partial x_1^4} + 2\rho h \frac{\partial^2 W}{\partial t^2} = Q\frac{\partial^2 M}{\partial x_1^2}. \tag{5.3.26}$$

The established approximate formulation also contains the elliptic equation

$$\Delta_1 \Delta_2 W = 0, \tag{5.3.27}$$

where

$$\Delta_j = \frac{\partial^2}{\partial x_2^2} + \lambda_{j0}^2 \frac{\partial^2}{\partial x_1^2}, \qquad j = 1, 2, \tag{5.3.28}$$

which should be solved together with the parabolic equation (5.3.26).

In fact, the representation in terms of a single harmonic function (5.2.13) simplifies things even further since

$$W(x, 0, t) = \frac{\lambda_{i0}^2 - \lambda_{j0}^2}{\nu - \lambda_{j0}^2} W_i(x, 0, t), \quad 1 \le i \ne j \le 2. \tag{5.3.29}$$

The explicit model for the edge bending wave is then given by a Dirichlet problem for any of the following two pseudo-static elliptic equations

$$\frac{\partial^2 W_j}{\partial y^2} + \lambda_{j0}^2 \frac{\partial^2 W_j}{\partial x^2} = 0, \qquad (j = 1, 2) \tag{5.3.30}$$

with the boundary data originating from the parabolic equation (5.3.26). Then, we exploit the relations (5.2.13) and (5.3.29) to restore the overall 2D

bending field. Thus, we reveal a dual *parabolic-elliptic nature* of the studied wave.

The second type of boundary conditions is given by

$$\begin{aligned} &\frac{\partial^2 W}{\partial \zeta_2^2} + \nu \frac{\partial^2 W}{\partial \zeta_1^2} = 0, \\ &\frac{\partial^3 W}{\partial \zeta_2^3} + (2-\nu)\frac{\partial^3 W}{\partial \zeta_1^2 \partial \zeta_2} = -\frac{h^3}{D} N, \end{aligned} \tag{5.3.31}$$

leading to a parabolic beam-like equation. The analysis is rather similar to that presented in the previous case. Remarkably, now the boundary conditions lead to a parabolic equation for the rotation angle $\theta = \dfrac{\partial W}{\partial x_2}$ evaluated at the edge $x_2 = 0$, namely

$$D\gamma_e^4 \frac{\partial^4 \theta}{\partial x_1^4} + 2\rho h \frac{\partial^2 \theta}{\partial t^2} = -Q \frac{\partial^2 N}{\partial x_1^2}, \tag{5.3.32}$$

with the coefficient Q defined by (5.3.22).

The explicit model for a prescribed shear force contains the elliptic equation (5.3.30) which is to be solved in conjunction with the parabolic equation (5.3.32), and also the relations (5.2.13) and (5.3.29) as above.

6 Concluding remarks

The context of this chapter is restricted to the framework of linear isotropic elasticity. We expect various extensions of the developed asymptotic methodology to elastic solids demonstrating a more sophisticated constitutive behaviour, arising from numerous insights into the properties of surface, interfacial and edge waves, taking into consideration pre-stress (Dowaikh & Ogden 1990, 1991, Rogerson & Sandiford 1999, Pichugin & Rogerson 2012) and anisotropy (Fu 2003, 2005, Destrade 2004, 2007, Zakharov 2004, Norris 1994), see also Prikazchikov 2013. The illustrative examples presented in Section 4 are limited to plane moving load problems associated with the Rayleigh wave. There is a clear potential for 3D generalisations (Kaplunov *et al.* 2013b) and also for analysis of near-interfacial dynamics (Kennedy & Herrmann 1973a,b). In addition, we mention important industrially motivated problems involving viscoelastic coatings.

Acknowledgments

The research is partly supported by the Grant of the Russian Foundation for Basic Research, Ref. 12-01-33049.

Bibliography

[1] J.D. Achenbach, *Wave propagation in elastic solids*, North-Holland, Amsterdam, 1973.

[2] J.D. Achenbach, Explicit solutions for carrier waves supporting surface waves and plate waves, *Wave Motion* 28 (1998) 89–97.

[3] P. Chadwick, Surface and interfacial waves of arbitrary form in isotropic elastic media, *J. Elast.* 6 (1976) 73–80.

[4] J. Cole and J. Huth, Stresses produced in a half plane by moving loads, *J. Appl. Mech.* 25 (1958) 433–436.

[5] R. Courant and D. Hilbert, *Methods of Mathematical Physics*, Vol. 2, John Wiley & Sons, New York, 1989.

[6] H.H. Dai, J. Kaplunov, D.A. Prikazchikov, A long-wave model for the surface elastic wave in a coated half-space, *Proc. Roy. Soc. A.* 466 (2010) 3097–3116.

[7] M. Destrade, Surface acoustic waves in rotating orthorhombic crystals, *Proc. Roy. Soc. A.* 460 (2004) 653–665.

[8] M. Destrade, Seismic Rayleigh waves on an exponentially graded, orthotropic half-space, *Proc. Roy. Soc. A.* 463 (2007) 495–502.

[9] M.A. Dowaikh, R.W. Ogden. On surface waves and deformations in a pre-stressed incompressible elastic solid. *IMA Jl Appl Math.* 44 (1990) 261–284.

[10] M.A. Dowaikh, R.W. Ogden. On surface waves and deformations in a compressible elastic half-space. *SAACM*, 1 (1991) 27–45.

[11] B. Erbaş, J. Kaplunov and D.A. Prikazchikov, The Rayleigh wave field in mixed problems for a half-plane, *IMA Jl Appl. Math.* (2012) doi: 10.1093/imamat/hxs010.

[12] F.G. Friedlander, On the total reflection of plane waves, *Quart. J. Mech. Appl. Math.* 1 (1948) 376–384.

[13] Y.B. Fu, Existence and uniqueness of edge waves in a generally anisotropic elastic plate, *Q. J. Mech. Appl. Math.* 56 (2003) 605–616.

[14] Y.B. Fu, An explicit expression for the surface-impedance matrix of a generally anisotropic incompressible elastic material in a state of plane strain, *Int. J. Non-linear Mech.* 40 (2005) 229–239.

[15] H.G. Georgiadis, G. Lykotrafitis, A method based on the Radon transform for three-dimensional elastodynamic problems of moving loads. *J. Elast.* 65 (2001) 87–129.

[16] V. G. Gogoladze, Rayleigh waves on the interface between a compressible fluid medium and a solid elastic half-space. *Trudy Seism. Inst. Acad. Nauk. USSR* 127 (1948) 27–32.

[17] R.V. Goldstein, Rayleigh waves and resonance phenomena in elastic bodies, *J. Appl. Math. Mech.* (PMM) 29(3) (1965) 516–525.

[18] T.C. Kennedy and G. Herrmann, Moving load on a fluid-solid interface: supersonic regime, *J. Appl. Mech.* 40 (1973a) 137–142.

[19] T.C. Kennedy and G. Herrmann, Moving load on a fluid-solid interface: subsonic and intersonic regimes, *J. Appl. Mech.* 40 (1973b) 885–890.

[20] J. Kaplunov, *Transient dynamics of an elastic half-plane subject to a moving load*, Preprint No.277, Institute for Problems in Mechanics, Moscow, 1986 (*in Russian*).

[21] J. Kaplunov, E.L. Kossovich, R.R. Moukhomodiarov and O.V. Sorokina, Explicit models for bending and interfacial in thin elastic plates, *Izvestia SGU, Math. Mech. Inf.*, 13(1), (2013) 56–63.

[22] J. Kaplunov, E. Nolde and D.A. Prikazchikov, A revisit to the moving load problem using an asymptotic model for the Rayleigh wave, *Wave Motion* 71 (2010) 440–451.

[23] J. Kaplunov, D.A. Prikazchikov, B. Erbaş and O. Şahin. On a 3D moving load problem for an elastic half space, *Wave Motion* (2013) (doi: 10.1016/j.wavemoti.2012.12.008)

[24] J. Kaplunov, A. Zakharov and D.A. Prikazchikov, Explicit models for elastic and piezoelastic surface waves, *IMA J. Appl. Math.* 71 (2006) 768–782.

[25] A.P. Kiselev and D.F. Parker, Omni-directional Rayleigh, Stoneley and Schölte waves with general time dependence, *Proc. Roy. Soc. A.* 466 (2010) 2241–2258.

[26] A.P. Kiselev, G.A. Rogerson, Laterally dependent surface waves in an elastic medium with a general depth dependence. *Wave Motion* 46(8) (2009), 539–547.

[27] Yu.K. Konenkov, A Rayleigh-type bending wave, *Sov. Phys. Acoust.* 6, (1960) 122–123.

[28] J.B. Lawrie, J. Kaplunov, Edge waves and resonance on elastic structures: an overview. *Math. Mech. Solids* 17(1), (2012) 4–16 (doi: 10.1177/1081286511412281).

[29] Lord J.W.S. Rayleigh, On waves propagated along the plane surface of an elastic solid, *Proc. R. Soc. Lond.* 17 (1885) 4–11.

[30] A.N. Norris, Bending edge waves, *J. Sound Vib.* 174 (1994) 571–573 .

[31] A.N. Norris, V.V. Krylov, and I.D. Abrahams. Bending edge waves and comments on "A new bending wave solution for the classical plate equation". *J. Acoust. Soc. Am.* 107, (2000) 1781–1784 .

[32] D.F. Parker and A.P. Kiselev, Rayleigh waves having generalised lateral dependence, *Quart. J. Mech. Appl. Math.* 62 (2009) 19–30.

[33] D.F. Parker, Evanescent Schölte waves of arbitrary profile and direction, *Europ. J. Appl. Math.* 23 (2012) 267–287. (doi: 10.1017/S0956792511000362).

[34] A.V. Pichugin, G.A. Rogerson, Extensional edge waves in pre-stressed incompressible plates, *Math. Mech. Solids* 17, (2012) 27–42.

[35] D.A. Prikazchikov, Development of the asymptotic models for surface and interfacial waves, *Vestnik NGU*, 4(4) (2011) 1713–1715 (*in Russian*).

[36] D.A. Prikazchikov, Rayleigh waves of arbitrary profile in anisotropic media, *Mech. Rec. Comm*, (2013, to appear). (doi: 10.1016/j.mechrescom.2013.03.009).

[37] J.G. Schölte, The range of existence of Rayleigh and Stoneley waves, *Roy. Astron. Soc. Lond. Month. Not. Geophys. Suppl.* 5(3) (1947) 120–126.

[38] J.G. Schölte, On true and pseudo Rayleigh waves, *Proc. Konink. Ned. Akad. Wetensch.* 52 (1949) 652–653.

[39] A.L. Shuvalov, A.G. Every, On the long-wave onset of dispersion of the surface-wave velocity in coated solids. *Wave Motion* 45(6) (2008) 857–863.

[40] R. Stoneley, Elastic waves at the surface of separation of two solids, *Proc. Roy. Soc. A* 106 (1924) 416–428.

[41] A.G. Sveshnikov, A.N. Tikhonov, *The Theory of Functions of a Complex Variable*. Moscow: Mir Publishers, 1978.

[42] H.F. Tiersten, Elastic surface waves guided by thin films, *J. Appl. Phys.* 40(2) (1969) 770–789.

[43] D.D. Zakharov, Analysis of the acoustical edge bending mode in a plate using refined asymptotics. *J. Acoust. Soc. Am.* 116(2) (2004) 872–878.

Elastodynamic End Effects in Structural Mechanics

B. Karp[1] and D. Durban[2],
[1]Department of Mechanical Engineering, Ben-Gurion University of the Negev,
P.O.B. 653, Beer-Sheva 84105, Israel
[2] Faculty of Aerospace Engineering, Technion - Israel Institute of Technology,
Haifa 32000, Israel
Corresponding author: B. Karp, E-mail: bkarp@bgu.ac.il

Abstract Current status of research on decay of dynamic end effects in elastic structures aiming at formulation of a dynamic analogue to Saint-Venant's principle (DSVP) are critically reviewed. Article concentrates on isotropic homogeneous linear elastic response over a range of structural geometries including waveguides, with either free or constrained lateral surfaces, half space, wedges and cones. Nearly 200 references are examined in context of DSVP, starting with early ideas by Boley. Special attention is placed on available experimental findings on end effects and decay rate in dynamically excited structures. Current perception of possible versions of DSVP is classified into several categories, one of which, namely that of dynamic equivalence, is compatible with much of known experimental data and has been tacitly applied at various engineering situations. That observation, along with a perspective view on evolution of the traditional SVP, provides inspiring ground for renewed interest in both practical and theoretical aspects of DSVP formulation.

1 Motivation

The principle named after Saint-Venant (SVP) has been commonly accepted as a corner stone assumption, widely employed in structural engineering and theoretical analysis of solid mechanics and related fields. Traditionally, that principle pertains to phenomena localized at the ends of a structure, ends to which a self-equilibrated load is applied. Validity of the principle entails that localization.

R. Craster, J. Kaplunov (Eds.), *Dynamic Localization Phenomena in Elasticity, Acoustics and Electromagnetism*, CISM International Centre for Mechanical Sciences,
DOI 10.1007/978-3-7091-1619-7_4,

In its original version (Saint-Venant, 1856) the principle argues that "the manner of application of a given resultant force and resultant moment on the two ends of a beam little affected the stress pattern, except very near the ends, and that all the solutions of a given problem, for end conditions having the same resultants, rapidly approached one and the same solution" (Toupin, 1965b, p. 223). The underlying idea, labeled by Toupin as "the principle of vanishing end effects", has been introduced by Saint-Venant to qualify theoretical elasticity solutions for beams for use in actual engineering conditions. In a broad sense, the assumption, when valid, implies that the stress field in the interior of a body is not sensitive to spatial distribution (profile) of prescribed local boundary tractions. Applicability of SVP has been confirmed over the years for several types of structures. Authoritative accounts of available research are given in the review by Horgan and Knowles (1983) and in two subsequent updates by Horgan (1989, 1996). Static stress fields that do not conform with SVP have been exposed for thin shells and statically determinate truss structure (Hoff, 1945), laminate/composite structures (Choi and Horgan, 1977, 1978), monocoque structures (Hoff, 1945; Nerubailo et al., 2005), and prestressed plates near points of bifurcation (Durban and Stronge, 1988a; Karp, 2004).

The applicability of SVP in linear elasticity has inspired research and formulation of similar principles in other branches of mechanics of materials. Among these are non-linear materials (Roseman, 1976), pre-strained plates (Durban and Stronge, 1988b), piezoelectric solids (Ruan et al., 2000), heat transfer phenomena (Oleinik and Iosif'yan, 1976; Chirita and Quintanilla, 1996a; Ignaczak, 2002), and fluid flow (Payne and Song, 1997).

A particularly challenging quest is for possible extension of SVP to include dynamic structural response, aiming at formulation of a dynamic Saint-Venant principle (DSVP). Several progress reviews of the classical Saint-Venant principle contain, inter-alia, short comments related to DSVP which deserve recollection. The review by Horgan and Knowles (1983, p. 261) concludes with: "one would not expect to find unqualified decay estimates of the kind discussed here in problems involving elastic wave propagation". The same conclusion is repeated in the first update of that review (Horgan, 1989). In a second update a few studies, apparently supporting validity of DSVP, are mentioned (Horgan, 1996). A further review by Horgan and Simmonds (1994), on application of SVP to composites, refers to end effects in vibration problems as related to DSVP.

At least five doctoral thesisses have been dedicated to investigation of issues and questions concerning DSVP, including Grandin (1972), Binkowski (1975) (both supervised by S. Little), Karp (1996) (supervised by D. Durban), Foster (2003) (supervised by V. Berdichevski) and Babenkova (2004)

(supervised by J. Kaplunov). Needless to say, each of these studies contains a review of relevant research literature as known at the time. A related dissertation, though not directly associated with DSVP, is submitted by Meitzler (1955).

It is the purpose of the present review to agglomerate and classify available research work on elastodynamic versions of Saint-Venant principle (DSVP), both experimental and theoretical. The review, which is an outgrowth of the PhD thesis by Karp (1996), followed by a brief historical account (Karp, 2005), begins with a retrospective of early studies by Bruno Boley along with a short discussion of the notion of self-equilibrated load. Next, in Chapter 3, we review experimental work related to DSVP. Analytical and numerical studies of DSVP in waveguides with free lateral surfaces are examined in Chapter 4. Chapters 5, 6, and 7 are devoted to a few available studies on the validity of DSVP in constrained waveguides, miscellaneous structures, and composites, respectively. Dynamic decay estimates for vibrating structures and in viscous materials are reviewed in Chapter 8. Comparison between the classical SVP and DSVP is suggested in Chapter 9, and finally, concluding remarks are given in Chapter 10.

The present review concentrates on studies concerned with aspects of DSVP and dynamic end effects in linear elastic materials. It is largely based on a recently published review by Karp and Durban (2011) with several extensions and updates. Approximately 200 articles, devoted or related to the DSVP are reviewed though, in fact, only a fraction of these papers was originally intended to investigate directly the DSVP. The papers referenced here were categorized as related to DSVP from the viewpoint of our present understanding of the topic. For that reason, no attempt has been made at an exhaustive review with regard to fields which are beyond linear elastic response. However, within that context, a few neighboring fields, like evanescent waves, are covered here in part.

A few studies attempt to find a connection between range of influence of applied load and DSVP. A theorem of this kind states that a sudden excitation of a body, initially in unperturbed state, will subdivide it into two regions; the region close to the disturbance zone where the perturbation is imposed and the rest of the body which is still intact. The surface separating these two regions is propagating with a characteristic velocity determined by material properties. Self-equilibrated loads and equivalent excitations, the key ingredients of SVP, have no special importance to the essence of that theorem. Rigorous formulation of the theorem can be found in Gurtin (1972) and more recently in Maremonti and Russo (1989). That interpretation of DSVP is not addressed in the present review unless it is accompanied with an estimate of decay. Likewise, left outside the review are studies on

end effects of Saint-Venant type related to thermal response and problems governed by parabolic field equations (e.g., Sigillito, 1970), heat conduction in thermo-microstretch elastic solid (Quintanilla, 2002) and in porous solids (Iovane and Passarella, 2004), and other phenomena such as flow in ducts (e.g., Ames et al., 1993).

2 Origins of the Principle

Along the timeline, two aspects have been instrumental in assessing the causes for both stagnation and progress in studies of DSVP: the notion of self-equilibrium and its role in validation of SVP, and the original ideas suggested by Bruno Boley. Accordingly, we proceed with a brief review of both aspects followed by a short summary emphasizing the conceptual difficulty arising in treating DSVP.

2.1 Static and Dynamic Self-Equilibrium

The notion of self-equilibrated load is central to the mathematical formulation and validation of the classical SVP. Self-equilibrium of a quasi-static traction vector $\mathbf{t}$ implies zero total force and moment, generally expressed by

$$\int_{(S)} \mathbf{t} dS = \mathbf{0} \quad \int_{(S)} (\mathbf{r} \times \mathbf{t}) dS = \mathbf{0} \tag{2.1.1}$$

where S is a small portion of the surface of the body on which the self-equilibrated traction is applied and $\mathbf{r}$ is the position vector. The traction vector $\mathbf{t}$ is the projection of stress tensor , given by $\mathbf{t} = \sigma \cdot \mathbf{n}$ where $\mathbf{n}$ is the outward unit vector normal to dS. Then, SVP is stated as "...the strains that are produced in a body by the application, to a small part of its surface, of a system of forces statically equivalent to zero force and zero couple, are of negligible magnitude at distances which are large compared with the linear dimensions of the part." (Love, 1944, p. 132). Validity of SVP is considered to be established when the effect of self-equilibrated load can be shown to decay (usually exponentially) with distance resulting in a small depth of non-negligible straining. That is the localization phenomena, the focus of the present volume.

Engineering situations in which a self-equilibrated load is applied are admittedly not common. The association of self-equilibrium with SVP facilitates mathematical analysis in providing proofs or quantitative estimates of its validity. The practical usefulness of the classical SVP lies in the concept of equivalence of loads, as suggested by Saint-Venant himself: "If a certain set of external forces acting on a certain part of a surface of a body

is replaced by another system of external forces statically equivalent to the preceeding system and distributed over the same sector, the stresses corresponding to these two loads will be identical at a sufficient distance from the point of application of the forces" (Cherepanov, 1979, p. 40).

Whereas analytical proofs and estimations of validity of SVP rely mainly on the self-equilibrium formulation (Love, 1944), experimental demonstration of SVP are largely based on the equivalence definition (as stated above). A classical demonstration has been provided by Frocht (1948) using the photoelastic method (Fig. 1). The experiment shows that far from the edge on which a concentrated load is applied a uniform stress develops, as in the case of a uniformly distributed load with identical static equivalents.

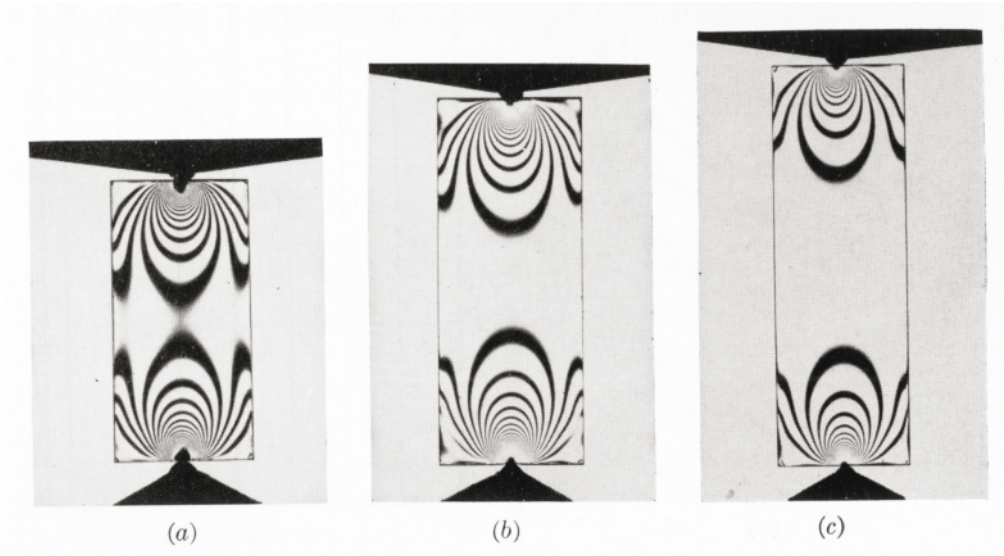

Figure 1. Photoelastic photographs of experiment with rectangular blocks loaded by a concentrated load (from Frocht, 1948, p. 30).

The notion of self-equilibrium is commonly extended to dynamic (time varying) excitation by either replacing the self-equilibrated traction with simple harmonic load fulfilling

$$\int_{(S)} (e^{-i\omega t}\mathbf{t}) dS = \mathbf{0} \quad \int_{(S)} \left(\mathbf{r} \times (e^{-i\omega t}\mathbf{t})\right) dS = \mathbf{0} \tag{2.1.2}$$

for steady state conditions (time denoted by t), or by considering any other time function $f(t)$

$$\int\limits_{(S)} f(t)\mathbf{t}dS = \mathbf{0} \quad \int\limits_{(S)} (\mathbf{r} \times f(t)\mathbf{t})\, dS = \mathbf{0} \tag{2.1.3}$$

for transients. In both cases self-equilibrium is guaranteed to hold at any instant of time.

2.2 Early Ideas by Bruno Boley

Research questions related to DSVP were already addressed in 1948 (see later in Chapter 3), yet Boley was apparently the first to examine explicitly an application of SVP to dynamic problems. His ideas on a possible extension of SVP to dynamic phenomena were expressed in two papers, dating back to 1955 and 1960, along with a wider generalization to problems governed by non-elliptic equation in 1958.

Boley investigated the possibility of extending SVP to dynamic problems by considering two idealized structures; the first consisting of three elastic semi-infinite bars interconnected by shear springs and subjected to longitudinal self-equilibrated loads (Boley, 1955). The second structure consisting of two semi-infinite bars connected by springs on which couples with zero total moment are applied (Boley, 1960a). The original sketches of the problem are recapitulated here in Fig. 2. In both cases the excitation (load or velocity) is self-equilibrated at any instant. The criterion for validity of DSVP is defined as a vanishing ratio between the maximal stresses reaching a distant portion of the beam and the initial stress at the excited end.

The dynamic response of the two structures was determined analytically, using transform method, for applied loads (or velocity) with a ramp variation in time. The time rise of the ramp (t_0) served as a parameter, with the limits of $t_0 = 0$ (representing a step function) and $t_0 \to \infty$ (corresponding to quasi-static conditions) as particular cases. Two main results were obtained, common for all three loading types; longitudinal, shear, and bending (Timoshenko beam equation was employed allowing for shear contribution to the dynamic response). For a suddenly applied load (step), stress with a magnitude of the initial value, or somewhat lower, propagates through the bars indefinitely. That result led to the conclusion: "thus the conventional principle of Saint-Venant certainly does not hold in this case" (Boley, 1955, p. 205).

The second observation made is the convergence of the dynamic solution to the static one as the excitation becomes more and more graduate (shown in Fig. 3). In the limit of the static load, the effect of the self-equilibrated

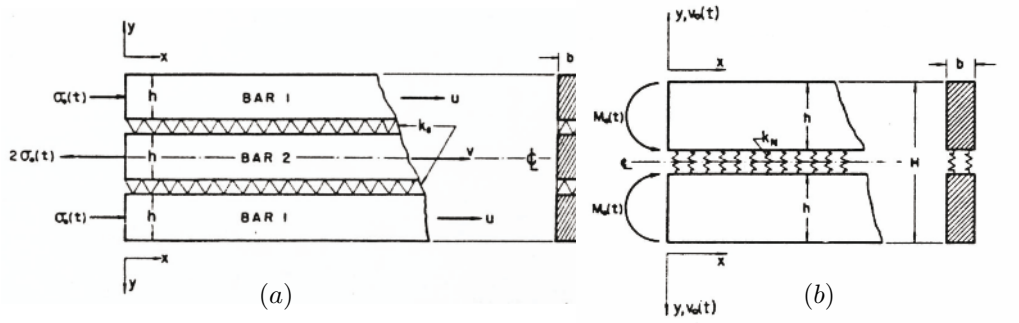

Figure 2. Axial (a) and deflective (b) beam combinations investigated by Boley (1955, 1960a).

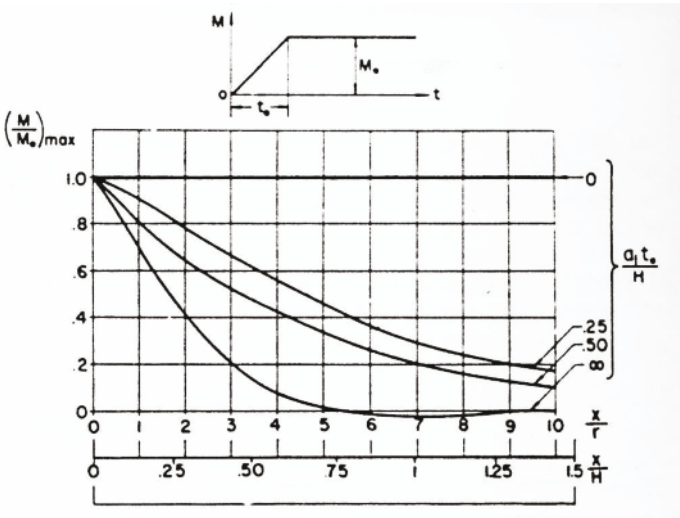

Figure 3. Attenuation patterns of the maximal stress along the axis of the combined strip imposed by moments with different rise time t_0, 0 - for step function and ∞ - for quasi-static case (from Boley, 1960a).

load practically vanishes beyond one width of the composed beam. The conclusion is then: "the conventional usage of the static Saint-Venant principle is not too greatly in error for slowly applied loads" (Boley, 1955, p. 206).

Considering the static case as asymptotic solution for the transient dy-

namic problem led Boley to suggest that the question of validity of SVP for a dynamic problem is part of the wider issue of how slowly loads must be applied before the static solution ceases to be a good approximation for the dynamic problem (Boley, 1960a). Therefore, it was suggested to redefine the quest for DSVP as a search for the rate of application of the load for which the quasi-static solution will not introduce unacceptable error. That direction of research has been followed by Grandin and Little (discussed later in Chapter 4).

In a short conference paper, which offers newly introduced ideas and terms, Boley (1958) paved the way to much of subsequent research on SVP. A question of general validity of SVP to systems governed by elliptic, parabolic or hyperbolic equations has been raised. For problems governed by elliptic equations a univocal conclusion was drawn: "The existence of the above integral formulas, involving appropriate fundamental solutions, is a general property of elliptic differential equations, which arise in such fields as steady heat conduction, electro-and magneto-statics, non-viscous fluid flow, and so forth, in addition to elasticity; to all these the principle can then be applied" (Boley, 1958, p. 259). This idea of connection between ellipticity of governing equations and SVP, together with the notion of self-equilibrated load, has been employed in many elasticity studies and led to the first genuine proofs of SVP by Knowles (1966) and Toupin (1965a). An illustration for validity of Saint-Venant's principle for a parabolic system, represented by transient heat problem, is given by Boley (1960b). In particular, a generalized notion of "principles of the Saint-Venant type" was suggested along with a recomendation to state them in terms of "upper bound" rather than by order of magnitude. Subsequent studies employing energy inequalities follow these steps.

In a recent correspondence with one of us (BK), Prof. Boley (2006) reflected on the issue from a perspective of 50 years, since he made a start on the topic of DSVP, writing that: "SVP reminds me in spirit of Pirandello's "Six Characters in Search of an Author", it is indeed a principle in search of a theorem. The proofs of SVP, for example, are really proofs of a SVP which may not necessarily be recognized by practicing engineers as the SVP they are actually using. It is probably close enough, it certainly belongs to the same species, and so they may feel confident in using it."

2.3 The Challenge

Boley (1960a, p. 74) concluded his studies on DSVP with an inspiring observation: "A discussion given elsewhere indicated that Saint-Venant's principle is a general property of elliptic boundary value problems, and

could not be expected to hold in general in problems of the hyperbolic type, such as, for example, those of the dynamical theory of elasticity. If the loading is applied sufficiently slowly, however, then it is intuitively clear that the static solution will be a good approximation to the dynamic one".

That perception that SVP is a general property of systems, whose behavior is dictated by the nature of their governing equations, has been supported by several independent studies. For example, Horgan and Wheeler (1975) wrote in the abstract: "Third order diffusive type equations, called pseudo-parabolic, are known to govern a wide variety of physical phenomena. A spatial decay estimate is derived for such an equation, similar to the known results in the parabolic case". A similar statement is expressed by Knops et al. (1990, p. 319): "Although the treatment is discussed with special reference to elasticity, it is equally applicable to general systems of elliptic differential equations, and thus reveals a relationship with the classical theorems of Phragmen-Lindelof and Liouville". That view was utilized by Oleinik and Iosif'yan (1978) several years earlier.

The interconnection between decay behavior and the type of the governing equations, together with well known non-decaying phenomena in dynamic problems, are apparently behind the wide spread rejection of SVP validity to dynamic problems in non-dissipative media. With that skepticism in mind, we attempt here to examine the idea of possible formulation of a DSVP in its classical sense, even in a restricted version. Surely, an instructive start of this review is provided by available experimental evidence on decay of dynamic end effects, discussed next.

3 Experimental Evidence

Effects of non-uniformity of dynamic excitation applied at an end of a bar attracted attention of several groups of researchers during the middle of the previous century. Research was driven by growing interest in experimental aspects of the split Hopkinson bar system (Wally and Mason, 2000; Field et al., 2001). Most of these studies were not originally associated with DSVP, yet they are reviewed below as a prelude to later work and, as will be shown, they are of significant value for at least one of the interpretations of DSVP.

Davies (1948) observed in his detailed experiments on split Hopkinson pressure bar system that the pressure distribution over the cross-section of the bar is not uniform at its free end. Two potential sources for that non-uniformity were suspected: end effects and the shape of Pochhammer-Chree modes at high frequencies. No explicit statement on the extent of "close region" near the edge is suggested in that review. In a later study it was found that the edge non-uniformity is smoothed out beyond four to five

diameters away from the excited end (Davies, 1956).

Miklowitz (1957) and Miklowitz and Nisewanger (1957) investigated numerically and experimentally the extent of validity of an approximate Mindlin-Herrmann theory for the analysis of propagation of compressive waves in a dispersive elastic rod. Strains in both near (0.75, 1, 1.24, 1.5, and 2 diameters) and far (up to 20 diameters) fields, induced by aerodynamic pressure pulse, were measured. Though limited to uniform excitation over the cross section, the findings suggest that edge effects for that particular loading are limited to several diameters off the end: "The present experiments give further support for this. They indicate that the initial disturbance, and the phenomena occurring just behind it, are of three-dimensional character and are relatively unimportant several diameters from the source" (Miklowitz and Nisewanger, 1957, p. 244).

Fox and Curtis (1958) devised an experiment aimed to confirm the asymptotic solution of step pulse excitation of a bar obtained by Folk et al. (1958) for strains far from the loaded end. Since the asymptotic solution is valid only beyond a distance of 10-20 diameters from the end, the experimental results do not include data for strains at distances smaller than 20D from the excited end. Due to different specifications of end excitations employed in the asymptotic analysis (mixed condition with no lateral extension) and imposed in the experiments (pure stress condition with no transversal tractions), an additional assumption is required to facilitate the comparison between the two, even at distances beyond 20 diameters from the excited end: "Failure to satisfy the second end condition is expected to be relatively unimportant for strains at large distances from the end. It is left to experiment to determine the extent to which this expectation is fulfilled" (p. 559). An answer to this question, provided later by several studies, does not refer to that expectation and remained unrelated to it.

Gorham and Ripperger (1959) addressed the same question of non-uniformity by measuring the difference between surface strain and average strain within the cross section of a bar, far from the excited end. The generation of various spatial forms of excitation is achieved by bullets of different size impinged at the end of the bar. They found no substantial difference between the two recordings at a distance of 26 bar diameters. No exact recording of the velocity of the bullets is given, thus preventing any attempt to estimate the frequency spectrum of the excitation (for higher velocities more energy is conveyed by modes of high frequencies). A similar investigation with bars of a square cross section has been detailed by Cunningham and Goldsmith (1959) with the important addition of surface measurement within the near zone. They found that the non-uniformity becomes unimportant at about 2 to 4 bar widths from the impact end.

A carefully conducted study on the extent of non-uniformity, made by Baker and Dove (1962), included embedded strain gauges within the bar at various distances from the impacted end, in addition to surface strain gauges. The core measurement device is shown in Fig. 4.

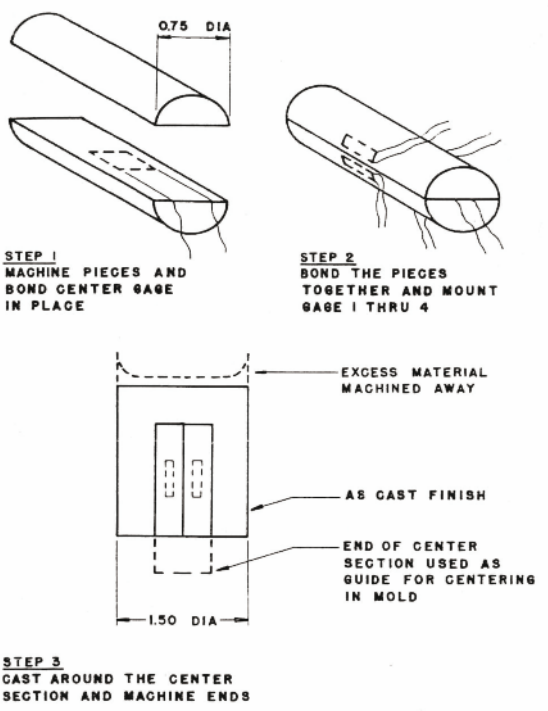

Figure 4. Configuration of the impacted bar with the attached strain gauges (from Baker and Dove, 1962).

The contact end of the impactor had a curvature of radius 3" while the diameter of the impacted bar was 1.5". The findings which resemble those of Cunningham and Goldsmith (1959) have led the authors to conclude that the results obtained earlier by Davies (1956) of 4 diameters as representative distance to which end effect are extended is an overestimation: "It was concluded that, when a pulse in longitudinal bar is initiated by central impact on a small area at one end, the change in the strain profile due to starting conditions ceases in the vicinity of 2 bar diameters from the impact end. This is not in agreement with Davies, who reported that four to five diameters were required" (p. 311). No data on the striker's velocity at the

impact is given, though from the experimental set-up it could be estimated to be of the order of one meter per second.

An additional study on the effect of excitation profile on the strain pulse, far from the excited end, is reported by Barton and Volterra (1959). The variation in profile of the excitation was achieved upon employing two strikers in a split Hopkinson bar system. One striker had a flat head and the other a rounded head. The measurement of the surface strain was taken at 24 diameters off the excited end "in order to permit the pulse to travel a sufficient distance to become uniformly distributed over the cross-section of the bar" (p. 321). A typical comparison of recordings for flat and round impacting rods is reproduced here in Fig. 5. It is evident that at such a large distance from the impact end the two strikers had practically an identical effect.

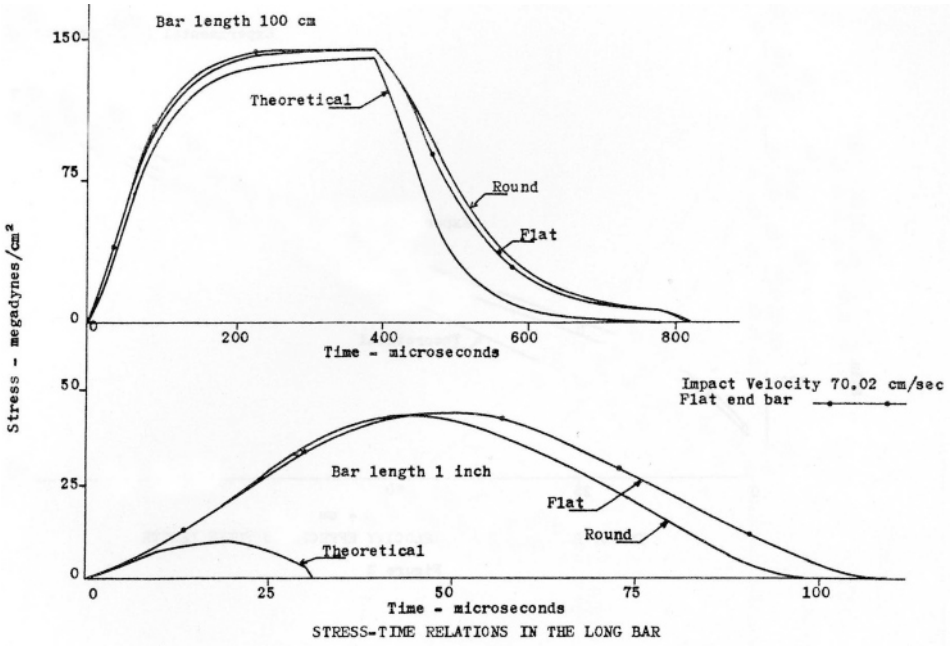

Figure 5. Surface strain for flat and round strikers of length 100 cm (upper) and 2.54 cm (lower), at impact velocity of 0.7 m/s, 24 diameters from the end (from Barton and Volterra, 1959).

Clausing (1959) examined the adequacy of the elementary, one-dimensional

theory, to predict results of impact of cylinders of different areas. The response of the impacted rod was recorded at several distances from the impinged end, starting at a distance of 2.4 diameters. The strikers were of various diameters and identical length, all with a radius larger than that of the impacted rod. Since the contact area in all experiments was identical, the results are not directly relevant to the question of the effect of the profile of the contact area.

The influence of different end conditions on the dynamic response of a strip has been examined by Dally et al. (1959) using the photoelastic method. They found that the fringe pattern is almost identical for reflection of waves from a free and a fixed end, except for the region close to the excitation or the end.

The experimental investigation by Flynn and Frocht (1961) appears to be the first experimental work specifically intended to examine possible existence of the DSVP. In this work, dynamic characteristics of near and far fields in a waveguide subjected to uniformly distributed and to concentrated loads were inspected by the photoelastic method. Two basic observations have been made in this study: identical stress distribution is obtained far from the loaded end for both types of transient loadings (uniformly distributed and concentrated); the parameter that determines the stress magnitude in the far field is the impact velocity rather than the force magnitude as in the case of classical SVP. The report was labeled by the authors as a preliminary investigation. A follow up discussion of that paper by Durelli and Dally indeed encouraged further study whereas a discussion by Borg (1961) on such demonstration doubted the possible existence of DSVP.

Borg's comment was based on comparison of the response of a semi-infinite beam, modeled by Timoshenko theory, with two different loadings of equal moments applied at the close end. In one case the moment is produced by normal stresses distributed linearly over the cross section according to the simple beam theory. In the other case the moment is induced by two identical concentrated forces separated by small distance, acting normal to beam axis. It is argued that in the second case only a shear wave is generated implying wave front propagating with shear velocity, while in the first case both shear and dilatational waves are generated, giving rise to substantial difference in wave fronts of the two cases. On this ground it was concluded that " a dynamic Saint-Venant Principle does not exist (in the form considered herein, which most closely parallels the static formulation) for the Timoshenko representation of the vibrating beam" (Borg, 1961, p. 120). To the Author's best knowledge the work by Flynn and Frocht (1961) has escaped notice in subsequent studies of DSVP, while a recent review by Field et al. (2001) refers to it as confirming the validity of DSVP.

By the end of the sixties sufficient data has accumulated to enable comparison of the spatial extent of dynamic end effects with that of static end effects. Photoelastic fringe pattern of a semi-infinite strip with concentrated static load applied at a center of a strip is given by Theocaris (1959). This pattern is very similar to that reported by Meyer (1964) for a concentrated impact load, taken from Flynn et al. (1962). In a study by Kawata and Hashimoto (1967) static and dynamic concentration factors around irregularities are compared. Fringe patterns exhibit similarity of the affected region for both static and dynamic cases. The same localized dynamic response around a hole in a strip is shown in Flynn et al. (1962) with comparison between uniform and concentrated load excitations of the strip.

Validity of DSVP as a prerequisite for suitability of an experimental set-up for acoustic emission study was recognized by Kroll and Tatro (1964). To that end the characteristics of wave propagation in a tensile specimen were examined for later use in a study of correlation between dislocation motion and acoustic emission. The authors investigated uniformity of a wave at the end of the specimen originated by a pointwise source. The results obtained (though limited to 5 diameters from the edge due to electrical interference) confirm earlier results by Bell (p. 130): "Bell has shown that, in three to five bar diameters, the stress waves have reflected many times and their resultant becomes an extensional stress wave, which is uniform across the cross section, travelling at the bar velocity v_b. This establishes a dynamic St. Venant's principle". The cited work by Bell (1960) was not available to us. The authors conclude with (p. 134): "The dynamic St. Venant's principle will insure that the stress wave becomes uniform after several diameters of travel".

Hettche and Au (1967) studied the effect of non-uniformity of the stress field across a semi-infinite plate. Theoretical considerations of that problem were supported experimentally by impacting cylindrical hollow rods. The authors state (p. 308) that " this stress is seen to be maximum at the center line and vanishes at the surface of the plate, and is critical only within the first plate thickness from the impact face".

Bertholf and Karnes (1969) investigated surface and center-line stresses in the immediate vicinity of the impact end, while the impact velocity was designed to generate stresses slightly above the yield stress. The conclusions (p. 541) reported are: "It is clear that a one-dimensional analysis is inadequate for $z < 4R$. ... For the elastic pressure bar numerical solution will determine the length at which the dilatation front becomes negligible and the uniaxial-stress approximation becomes valid. It is anticipated that this length will be between 10 and 20 dia.". That quantitative estimation is not explained, and actually is not in agreement with a comparable statement

in an earlier paper by one of the authors (Bertholf, 1967) estimating it to be 4 diameters. Moreover, the experimental results in the latter reference are in good agreement with those of Baker and Dove (1962) and others cited above, while the observation of "10 and 20 dia." is consistent with the practice to be suggested later by Follansbee (1985). No comparison to any previous analogous results is given, nor have the effects of exceeding yield stress and high impact velocity (100 m/s) been examined.

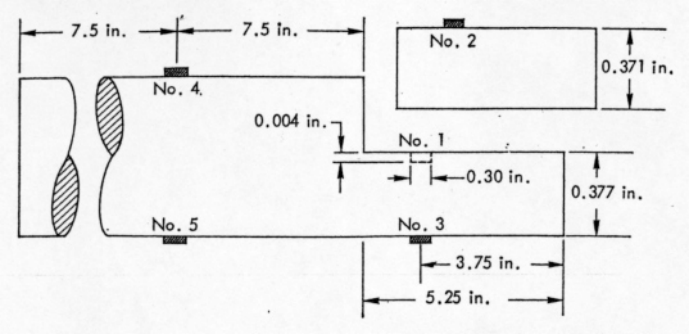

Figure 6. Configuration of the impacted bar with an embedded strain gauge No. 1 and the surface strain gauges Nos. 2-5 (from Habberstad et al., 1972).

Experimental results for the centerline strain within the near-field region are reported by Habberstad et al. (1972). The configuration of the embedded strain gauges is displayed in Fig. 6. The striker velocity was 5 m/s with a flat head in all experiments. Comparison of the center-line strain with surface strain was made for distances of 2/3, 2, and 3 diameters from the impact end. Typical result at the distance of 3 diameters is displayed in Fig. 7, showing clearly that even at that distance considerable difference exists between center-line and surface strains. By using the same bar in inverted position the authors confirmed that the recording at distances of 10 and 22 diameters, from the impact end, are identical. This makes 10 diameters the upper limit for practical uniformity of the signal.

Zemanek (1971, 1972) provided experimental and theoretical insight into the origins and nature of non-uniformity in context of reflection of a wave from a free end of a bar, raised earlier by Davies (1948). These studies are detailed in the next chapter.

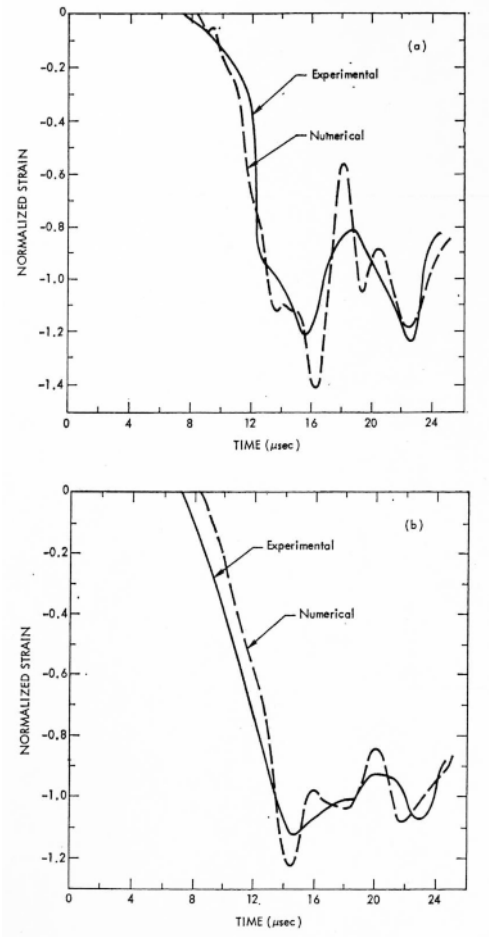

Figure 7. Experimental and numerical results for center (a) and surface (b) strain at a distance of 3 diameters from impact (from Habberstad et al., 1972).

Experimental observations of impacting rods by Bell (1973, p. 351) led the author to explicitly support the validity of DSVP (though no particular reference was given). Bell preserved the velocity of colliding rods with different distributions of the contact area while keeping the total area constant. The experiments revealed that the spatial distribution of the transient load has little effect on the surface strain of the rod at distances larger than half the diameter of the examined rod, a distance much smaller than suggested previously: " impacts of small hollow cylinders of the same area as the solid

rod demonstrated that beyond the first half-diameter the experimental results were insensitive to the major changes in the spatial distribution of loading at the impact face" (p. 351).

Though not aiming directly to investigate DSVP, two additional experimental studies using photoelasticity provide further evidence for non sensitivity of the far field to details of end excitations. Miles (1976) examined the effect of surface roughtness on the uniformity of the wave generated upon impact (Fig. 8). Here the impact velocity remains identical when a different profile of the excitation is induced by irregularities at the contact surface.

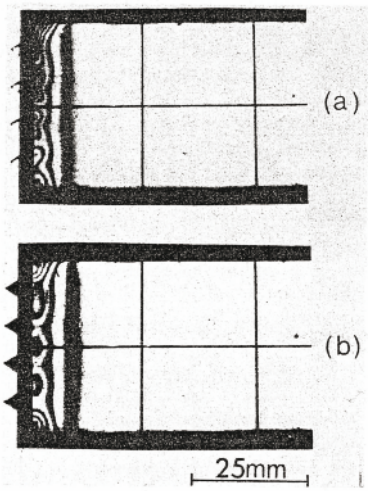

Figure 8. A fringe pattern in a plate impacted by two different materials with different surface irregularities (from Miles, 1976).

A recent study by Kawata et al. (2007) investigated dynamic stress field in a strip, generated by impact on one end, using photoelastic high speed photography. The fringe patterns obtained (Fig. 9) are identical to those generated by static loading, as shown by Frocht (1948) (Fig. 1). Both studies make it clear that the distance at which the non uniformity is preserved is nearly the same as in the static situations.

Following a gap of nearly three decades, experimental research on DSVP has been revived in recent years. Reflection of transient disturbance at a built-in end of a beam, generated by a transversal excitation at the free end, was investigated by Karp et al. (2008). The variation of end conditions was

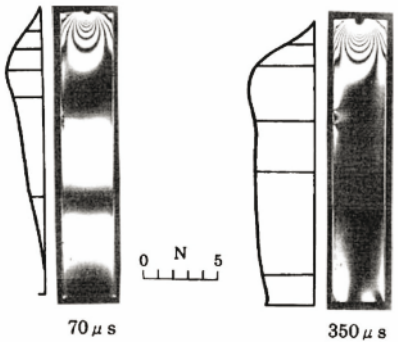

Figure 9. A fringe pattern in a plate impacted at the center of the upper end of a strip at two instants (from Kawata et al., 2007).

achieved by altering the tightness of screws used to fix the built-in end. The measurement of the surface axial strain suggested that extremely small variation in screws tightness can be detected by strain gauges located in the near field (Fig. 10), but not by strain gauges located in the far field. The extent of the near field is estimated to be approximately one width of the beam.

Symmetric excitation of a bar by striker impact in split Hopkinson bar system (SHPB) was studied by Karp et al. (2009) in the spirit of Bell's (1973) comment. The variation of end excitation was realized with various shapes of the contact surface of the striker. Experimental results, limited to surface strain measurements, were accompanied by numerical simulation confirming similarity in behavior between the core and the surface of the bar.

A similar, not yet published, study was undertaken at Nanyang Technological University, Singapore, with SHPB having much larger diameter rods, enabling direct detection of end vibration (Ma et al.). Four different strikers, having the same contact area with different shapes, used in the experiment are shown in Fig. 11.

The typical axial surface strain at a distance of x/D = 0.5 from the impacted end is displayed in Fig. 12. The difference in amplitude for each striker is evident. That difference becomes negligible beyond the distance x/D = 1 (not shown here). An interesting observation are the small oscillations, notable only at that particular distance, after the main signal has died out. That phenomenon is more pronounced for certain strikers and is associated with end vibration consisting of evanescent waves (e.g.,

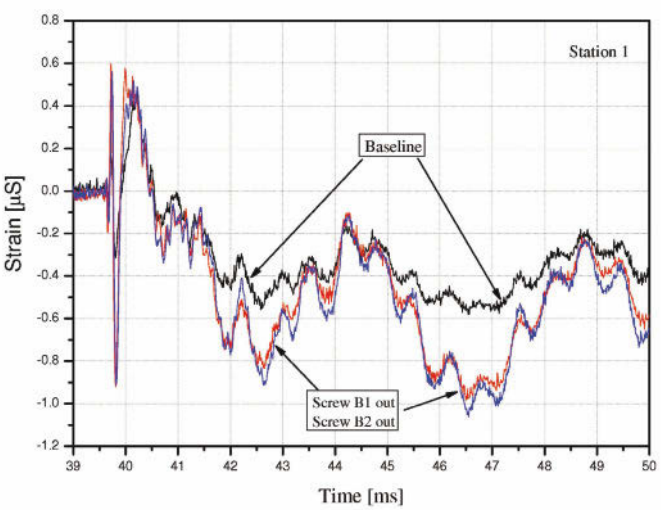

Figure 10. Surface strain recording within the near-field (station 1) for three beam fixation conditions excited by transversal excitation at the free end of a cantilever beam. Baseline is the recording of excitation when all screws are tight in. (from Karp et al., 2008).

Ratassepp et al., 2008).

In these experimental studies on SHPB system the same conclusion was reached, namely that the response of the bar is not sensitive to the form of the excitation beyond 1.5 diameters of the rod (Fig. 13).

The body of experimental research on DSVP can be summarized by the observation that most of experimental investigations aim at understanding the sensitivity of response of waveguides to spatial distribution of the load, or to the type of boundary conditions (either mixed or pure traction). The requirement of self-equilibrium of imposed excitation was not invoked, even in the few studies explicitly addressing the existence of DSVP. The induced excitations are of impact type (with Zemanek (1972) as exception). The results confirm that dynamic response of a beam or a rod excited at its end is not sensitive to the exact stress distribution of the excitation far enough from the excited end. Almost all experimentally different studies suggest that the extent of the non-uniformity of the cross-sectional properties penetrates into the bar less than 2 to 4 bar diameters (or plate thickness). Studies arguing for a larger distance do not report any contradicting results on small distance, but rather refer to an upper limit due to particular experimental limitations. Yet, the necessary conditions for equivalence be-

Figure 11. Surface strain recording (in Volts) within the near field for four strikers with identical contact area and different form (Fig. 11). Small oscillations are notable for certain strikers (from Ma et al.)

tween excitations were not identified (nor questioned). Standing out are Flynn and Frocht (1961), Bell (1973) and Miles (1976) who refer explicitly to the velocity of the impacting rod as a parameter to be kept constant for comparison of effects far from the loaded end. Nevertheless, understanding causes for far field insensitivity remains a major issue for future study. The next Chapter will provide some insight into this aspect of DSVP.

4 Unconstrained Waveguides

Waveguides with free lateral surfaces can be viewed as a dynamic analogue of beam-like and plate-like structures, for which the static version of SVP is most frequently applied. In that sense, the present chapter provides the complementary part of the previous chapter, where studies related or dedicated to the existence and validity of DSVP in such waveguides are reviewed.

The stress free condition is defined by vanishing of traction vector on lateral surfaces

$$\mathbf{t} = \sigma \cdot \mathbf{n} = \mathbf{0} \tag{4.0.1}$$

where $\mathbf{t}$ is the traction vector, σ - the stress tensor, and $\mathbf{n}$ denotes the outward unit normal to the surface.

The common features of wave propagation in cylindrical and strip waveguides (e.g., Miklowitz, 1978, p. 222) enable joint treatment of both geometries. Similarity in behavior of cylindrical and rectangular cross-sections of waveguides is also noted (e.g., Hertelendy, 1968). On these ground, no

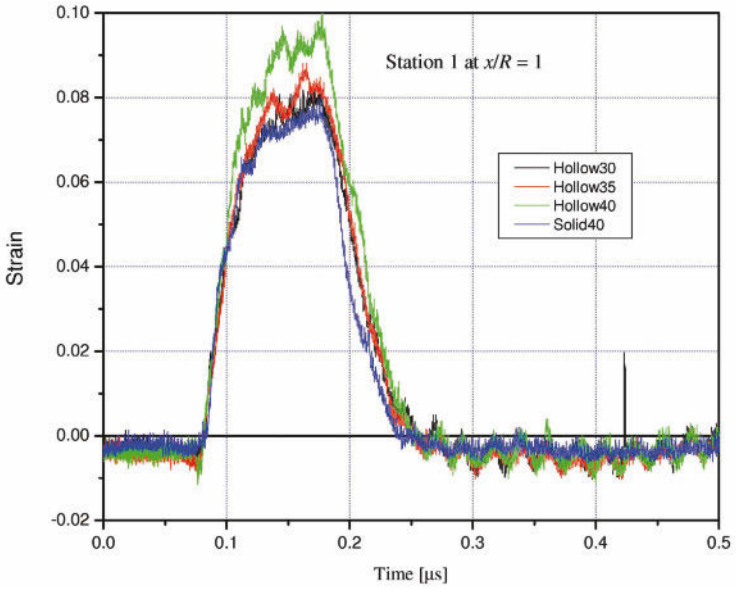

Figure 12. Surface strain recording (in Volts) within the near field for four strikers with identical contact area and different form (Fig. 11). Small oscillations are notable for certain strikers (from Ma et al.)

distinction between waveguides with different cross-sections will be made in the following review.

DeVault and Curtis (1962) examined the relevance of asymptotic solutions obtained for mixed type end data for prediction of actual results in experiments performed with pure end conditions (e.g., Miklowitz and Nisewanger, 1957). An example of the mixed data used therein for asymptotic evaluation is shown in Fig. 14. They reported (pp. 431-432): " all the main features of the observed pulse were correctly predicted despite the difference between the experimental and the assumed end conditions. if there is a real difference between predictions and experiment, it is at least small. This statement refers, of course, to a particular type of load and only to the behavior either at distances greater then a few diameters from the end of the bar or at a considerable time after the pressure is applied".

McCoy (1964) solves analytically the problem of a semi-infinite elastic rod subjected to a shear stress, with arbitrary radial variation, applied to an otherwise free end. The solution is obtained by series expansion which consists of propagating and evanescent waves. That analysis leaded to the conclusion that (p. 463): "This fact allows an evaluation of Saint Venant's

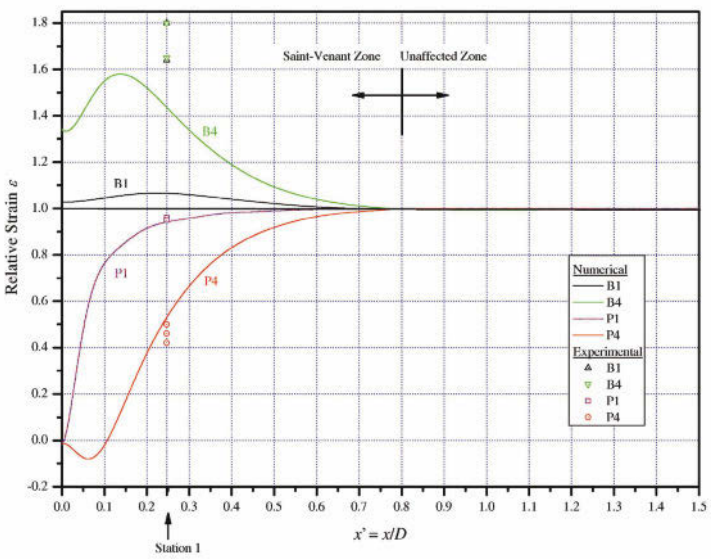

Figure 13. Surface strain recording (normalized by far field strain) in experiment and finite element calculation of a rod, versus distance from the excited end, with different strikers (P1 and P4 pin type, B1 and B4 bore type) (from Karp et al., 2009).

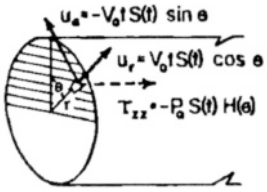

Figure 14. Mixed boundary conditions used by DeVault and Curtis (1962).

principle as applied to dynamic problems. The portion of the energy in a signal that excites a frequency above the cutoff frequency will propagate into the rod, whereas the energy which excites frequencies below the cutoff frequency will set up a vibration confined to the end of the rod. The lower the frequency the more closely confined to the end is the vibration".

Novozhilov and Slepian (1965) were apparently the first after Boley to dedicate a paper for examination of DSVP. Their interest in DSVP was motivated by practical aspects of use of Timoshenko's flexural beam equations

with non-ideal end data. For that purpose they studied decay of end effects generated in a beam by dynamic (time varying) self-equilibrated load. It was shown that a steady state (harmonic) load generates a non-zero in-flow of energy associated with propagating waves. Therefore, no dynamical counterpart of the static SVP appears to exist in dynamic steady state fields. For transients, on the other hand, by comparing self-equilibrated and non-self-equilibrated step loads it was confirmed that the static version of SVP is applicable even to rapidly changing transients due to localization of the stress near the wave front. Consequently, a restricted interpretation (Novozhilov and Slepian, 1965, p. 313) of the principle is suggested: "The Saint-Venant principle is applicable for the study of transient process in beam dynamics since deformation corresponding to suddenly applied self-equilibrating load localize themselves in the neighborhood of the wave fronts and in the neighborhood of the cross section over which the load is applied. This assertion does not extend to self-equilibrating disturbances with the continuous in-flow of energy into the beam (for example, to periodic disturbances)".

Torvik (1967) used a variational method to find the actual amplitude of reflecting modes, from a stress-free end of a plate, generated by a single-mode single-frequency incoming wave. Investigation of both propagating and evanescent waves was concluded with an interpretation of DSVP (Torvik, 1967, p. 352) stating that "Below the frequency where more than one propagating mode is possible, an extension of St. Venant's principle is possible but extremely restrictive. The energy put into the system will have to be carried away by the first mode; therefore any two dynamic loadings (at a given frequency) will give rise to the same amplitude in the first (and only) propagating mode if they do work on the same displacements of the first propagating mode at the same rate, even if the stress distribution of the loaded region differs.". The author further suggests estimating the distance beyond which such loads are equivalent by considering the decay distance of the first evanescent mode. Diligent et. al. (2003) realized experimentally the configuration calculated by Torvik. They measured directly the excitation of evanescent waves generated at a free end of a plate upon reflection of the first symmetrical mode. Research conclusion was that evanescent modes can be neglected beyond distance of five times the plate's width.

Jones and Norwood (1967) compared the stress at the wave-front generated by an end excitation of a cylindrical bar under two loadings of mixed type; step pressure with zero radial displacement and step velocity with zero shear. By using asymptotic solutions of the exact elasticity equations (valid beyond 20 diameters from the end) they found, for equivalent pressure and velocity applied at the end, that the stress distribution at distances greater

than 20 times the diameter is the same despite the different end data. This result was regarded as confirming the validity of DSVP in such problems (p. 723): "Because the lateral end conditions are markedly different, this constitutes at least an upper bound on a dynamic Saint-Venant's principle for these problems in the range of low frequencies". The equivalence of the two types of excitation was judged by the equality $P_0 = EV_0/C_0$ where P_0 is the amplitude of the step pressure, V_0 is the amplitude of the step velocity, E and C_0 are Young modulus and velocity of longitudinal waves in a bar, respectively.

Bertholf (1967) used numerical integration to evaluate the near field in a bar subjected to steady state uniform displacement with no shear at its end. The solution of Pochhammer-Chree frequency equation was considered as valid only at remote distance from the ends and was used to confirm (p. 734) correctness and accuracy of the numerical solution: "The results of applying a plane, harmonic displacement to the end of a semi-infinite bar compare satisfactory with the Pochhammer-Chree solution at points not near either the end or the wave front". The estimate for the distance at which a reasonable agreement (p. 728) is obtained was 4 bar diameters: " the Pochhammer-Chree solution is correct for distances of more than 4 dia from the end of a semi-infinite bar".

Kennedy and Jones (1969) investigated the effect of spatial distribution of a suddenly applied load on the far field in a circular bar. While the study is in the spirit of the original Saint-Venant's formulation, connection to DSVP was not discussed. The resultant of the applied loads remained constant while their distribution varied, implying self-equilibrium in a static sense obtained from the difference between these loads. The imposed excitations are given by

$$\sigma_x(0,r,t) = -P(r)H(t) \qquad u_r(0,r,t) = 0 \quad at \quad x = 0 \tag{4.0.2}$$

with

$$P(r) = P_0(p+1)\left[1 - \left(\frac{r}{a}\right)^2\right]^p \quad p \geq 0 \tag{4.0.3}$$

where P_0 is kept constant, parameter p describes the degree of the non-uniformity of the load, a is the radius of the bar and x is the axial coordinate. For $p = 0$ the load is uniformly distributed. Numerical integration results were compared to asymptotic solutions at the far field to gain confidence in the numerical prediction for the near field. The numerical evaluation was limited to distances of 5, 10, and 20 diameters from the end. In view of the findings summarized in chapter 3, the smallest distance of 5D is beyond the extent of near field. Hence, the article can be viewed as an investigation of

the effect of the profile of the excitation on the far field. It has been shown that the double transform solution for the first mode, valid in the far field, is independent of p. The conclusion is that the excitation profile has no effect on the average stress in cross sections at distances beyond 5D. The cross section peak stress is insensitive to excitation profile only beyond 20D.

Karal and Alterman (1971) examined the extent of the strain difference in the far field of a bar due to application of pure and mixed shocks at the end. They concluded that already beyond 2D from the excited end it is immaterial whether the data is pure or mixed (p. 10): "the output response for distances equal or greater than two diameters from the end of the rod exhibits the same general features whether the boundary conditions are pure or mixed".

Two numerical and experimental studies by Zemanek (1971, 1972) are instrumental in providing a possible interpretation of DSVP as related to evanescent waves. In the first study a clear distinction is made between near and far fields, along with explanation of the nature of the near field. In the second paper, results of an experimental investigation of end effects are modeled by wave reflection from a free end. A clear insight into the correlation between dynamic end effects, evanescent waves, and complex wave numbers is suggested.

Yeung Wey Kong et al. (1974) solved numerically the exact elasticity equations for impact of a rod as part of a study on the effect of mismatch of contact area between specimen and bars in a split Hopkinson bar system. Their concern was the validity of interpretation of experimental results based on one dimensional theory. Four ratios between the diameter of the contact area r0 (representing the specimen) and the bar diameter D were examined ($r_0/D = 0.18, 0.36, 0.72, 1.0$). The strains at the center and surface of the bar were extracted for stations located at $4D$ and $8D$. Comparison of the calculated surface strain at $8D$ for the four specimens discloses considerable difference, both in first order and second order response. It is not stated explicitly how the imposed boundary conditions were adjusted for the four specimens, whether it is the normal stress or the total force that was preserved for all four simulations.

Grandin and Little (1974) adopted the mathematical interpretation (p. 145) according to which the principle does not exist if a self-equilibrated oscillating load produces non-decaying waves: "The definition of what is meant by a Saint-Venant boundary region might lead to different interpretations as to whether a dynamic Saint-Venant principle exists or not. The approach taken here is to apply an edge stress distribution with null integrated force at any instant of time and determine if non-decaying waves are produced. This would indicate that beyond a certain distance the wave

fronts are independent of edge stress distribution". That interpretation led the authors to conclude that DSVP does not exist in steady state problems, as already suggested by Boley (1955, 1960a) and by Novozhilov and Slepian (1965). The authors conclude (p. 146) with: "Examination of the results at lower frequencies indicated that the stress magnitude of the non-decaying modes was greatly reduced and the results tend toward the static solution. It must, however, be noted that the frequencies must be very low before the non-decaying mode may be neglected contributing to the argument against the existence of a dynamic Saint-Venant region".

Binkowski (1975) examined the dynamic response of a circular waveguide subjected to three different end excitations, two of which were self-equilibrated and harmonic in time. Comparison of the stress field of the propagating waves generated by these two self-equilibrated loads revealed a "radically" different response. Based on that finding the author concludes (p. 60) that "A dynamic Saint-Venant region does not exist for a solid circular semi-infinite cylinder". It should be noted that the comparison is made at a frequency above the first cut-off, where two propagating modes are available.

Apparently the first formulation of Saint-Venant type energy inequality for dynamic response of a cylinder with free lateral surfaces was given by Ignaczak (1974). For the proof of spatial decay of the total cross-section energy two assumptions (p. 313) were employed: "we assume that B is a semi-infinite nonhomogeneous and isotropic elastic cylinder loaded smoothly on the end face of the cylinder, and that the stress field is to vanish in a fast way at infinity". However, in view of the results obtained by Boley (1955, 1960a) and by Novozhilov and Slepian (1965) it is not clear how the second assumption can be fulfilled for a general response of a waveguide with free surfaces.

Sinclair and Miklowitz (1975) considered a plate in plane strain with free faces excited by suddenly applied normal symmetric loads at the end. They used double transform for long time solution of two different loads, uniform and concentrated, on the centerline. It was estimated that the actual response of a plate to any other form of excitation will lie within the limits of the solution to these two forms. The authors report that if the total force is identical, the far field is practically identical as well.

Orazov (1983) investigated the validity of DSVP in an elastic semi-infinite waveguide with free or clamped surfaces subjected to displacement or stress on the near end and zero displacement at the remote end (at infinity). Under some restricting conditions on the end excitation, the author proved complete decay of the response at some distance from the end, even for a waveguide with free surfaces, thus suggesting a proof for DSVP in a

particular case. It is noted that in general, such conditions give rise also to non-evanescent waves radiating energy to infinity, resembling Sommerfeld's condition.

Kim and Steele (1989) demonstrated the advantage of stiffness matrix method over collocation method for estimation of end effects associated with time-harmonic excitation of a bar. Various forms of excitations were solved to illustrate the method, yet no explicit evaluation of the extent of the end effects is given.

Gomilko et al. (1995) compared the amplitude of waves induced by a self-equilibrated excitation to those induced by non-self-equilibrated excitations. The ratio obtained turned out to be extremely small for excitations with a low frequency, confirming a version of DSVP. Gomilko et al. (1995, p. 1153) formulated DSVP as follows: "When a self-balanced system of forces acts on the end of semi-infinite strip, stresses arise as a result of this system only near the end. At a significant distance from the point of application of the forces the effect of such a load is practically zero".

Karunasena et al. (1995) have presented an explicit verification of the amplitude and depth of penetration of evanescent waves induced by reflection of the first propagating mode at a fixed edge. The authors showed that the evanescent waves generated upon reflection from a fixed end of a composite plate are negligible at distances larger than twice the plate's width. This analysis and its results are similar to those suggested by Torvik (1967), though no connection to DSVP was noted.

Cherukuri and Shawki (1996) confirm, by using finite difference solutions, the results obtained by Fox and Curtis (1958), according to which beyond two diameters off the impacted end the type of BC (either mixed of pure) has no effect. The same conclusion, based on energy partition among propagating modes, was derived by Karp (2008) with the aid of bi-orthogonality relations for an elastic strip.

Chirita and Quintanilla (1996b) treated both transient and steady state excitations using energy inequalities. To establish decay for a transient load it was assumed that the excitations are self-equilibrated at any instant (this work appears to be among the few studies using differential inequalities where that condition is required) and allowed for lateral surfaces to remain free of traction. Under these conditions it has been proved that the cross-section energy, within the domain of influence, decays linearly with distance.

Similar energy inequalities were established by Iesan and Scalia (1997) for microstretch material, and by Borrelli and Patria (2000) for a piezoelectric beam with clamped or free surfaces. Borrelli and Patria remark (p. 74) that: "the decay result concerning the energy does not require assumptions on the boundary data on the base". Knops and Payne (2005)

derived equivalent inequalities for a nonhomogeneous, anisotropic material with constrained excitation at the base.

Karp and Durban (1997) enhanced several existing approaches, mainly similar to Torvik (1967), following Karp (1996). The central idea was to abandon the quasi-static notion of the "self-equilibrated load", and to replace it with a "system of equivalent loads". That idea is further developed in Karp (2009), where, in particular, it was shown that DSVP formulation based on "dynamic equivalents" coincides with the "static equivalents" in the limit of zero frequency. Moreover, it was demonstrated that the extent of non-uniformity associated with the end effect is the same for both static and dynamic situations, as demonstrated by the photoelastic fringes shown here in Figs. 1 and 10.

Tyas and Watson (2000) examined numerically the transient response of a bar to concentrated and arbitrary distributed loads in the context of reconstruction of the applied load out of measured strain history. Employing a finite element code they showed that for low frequency load, its magnitude can be deduced from measurements taken far enough from the edge (five times the radius). It is stated (p. 1549) that the study is not intended to postulate a dynamic version of SVP: "Unlike previous work of this type, these findings have not been used to postulate a dynamic Saint-Venant's principle for the pressure bar".

Meng and Li (2001) suggested improvements of the interpretation of data from split Hopkinson pressure bar tests by invoking DSVP. Their view of DSVP resembles a direct extension of static SVP stated as insensitivity to the spatial distribution of the applied surface load. Using finite element code the authors found that the surface response of the output bar (the second bar in SHPB system) beyond 1.5 rod diameters is insensitive to spatial distribution of the end load. For the sake of comparison, the average pressure was held constant. Application of that conclusion to the improvement of the split Hopkinson bar system is detailed in a subsequent paper (Meng and Li, 2003).

Berdichevsky and Foster (2003) considered (p. 3293) the lack of orthogonality of the eigenfunctions as a major reason for difficulties in establishing DSVP: "In dynamics, Saint-Venant's principle of exponential decay of stress resulting from a self-equilibrating load is not valid. It is not clear how to formulate the conditions that eliminate the penetrating modes". Such conditions have been derived later by Babenkova and Kaplunov (2005) and by Karp (2009). The conclusion (p. 3296) is that "An unpleasant consequence is that, in general, one cannot trust the predictions of dynamical one-dimension beam theory that takes into account only the total force and moment at the beam end".

In order to bypass that difficulty Foster and Berdichevsky (2000) and Berdichevsky and Foster (2003) suggested a novel approach to measure quantitatively, by statistical average, the degree of violation of SVP in structural dynamics. Using statistical distribution of a self-equilibrated load, they evaluated quantitatively the frequency range of a harmonic, self-equilibrated load, for which the error involved in assuming SVP is acceptable. It was shown with high probability that for a frequency region below some value, the error of classical theory is very low. In a subsequent study Foster and Berdichevsky (2004) enhanced that work to estimate (p. 2551) the effect of end effects in end vibration of a semi-infinite beam: "In the case of a dynamic load, Lamb (1916) showed that a traveling wave is also excited, so that a self-equilibrated end load will cause some level of stress to penetrate into the beam: Saint-Venant's principle is violated". Furthermore (p. 2552), "Our major conclusion is that over a wide range of frequencies, the maximum propagating stress is small compared with the maximum applied stress. Saint-Venant's principle may be said to apply in this problem, until the frequency approaches a critical high level. Below this frequency of vibration, the error involved is considerably smaller for flexural vibrations than it is for longitudinal vibrations".

This topic was further investigated by Babenkova and Kaplunov (2004) who examine conditions on a low frequency excitation for not generating propagating waves. The condition that the symmetric non-self-equilibrated excitation $\sigma_0(y)$, with y as a normalized coordinate in the transverse direction, will not induce propagating waves is given by

$$\int_0^1 \left(1 - \frac{1}{4}\nu\lambda^2 y^2\right) \sigma_0(y) dy = 0 \tag{4.0.4}$$

where ν is Poisson's ratio and λ the non-dimensional frequency. This formula involves a low-frequency corrector to the applied self-equilibrated load required to ensure validity of Saint-Venant principle and can be considered as a deviation from the self-equilibrium conditions for static decay, as the authors write (p. 2168): "The derived low-frequency decay conditions represent a starting point for an asymptotic refinement of 2D boundary conditions in dynamics of thin plates and shells. It is important that these conditions allow us to take into account deviations from the classical formulation of the Saint-Venant principle". An earlier work by these authors (Babenkova and Kaplunov, 2003) examines the application of DSVP involving similar correction to the quasi-static self equilibrated load with low frequency while applied to a finite strip. Extension for high frequency oscillating load was formulated by Babenkova and Kaplunov (2005).

A follow up study by Babenkova et al. (2005) evaluates the ratio of the power generated by self-equilibrated loads to the power generated by non-self-equilibrated loads for low frequencies; the interpretation given to DSVP resembles that of Gomilko et al. (1995). An interesting (p. 405) analogy is proposed: "In the problem of the propagation of harmonic waves in a half-strip, homogeneous (non-decaying) modes, which are determined by the real roots of the well-known dispersion equations , can serve as an analogue of the Saint-Venant solution". With that analogy the authors extend the principle (p. 1165) for high frequency excitations: "However, in contrast to statics, high-frequency behaviour is often characterized by short-wave propagating sinusoidal modes that do not decay along with polynomial terms. These propagating modes have to satisfy the Sommerfeld condition at infinity. Thus, we do not require a total decay. We require only the absence of polynomial modes that do not satisfy the radiation condition at infinity".

It is probably a telling sign, indicating that research on DSVP is still in the formative period, that none of the studies discussed in Chapter 3 were referenced in papers reviewed up to this point in Chapter 4. In particular, there is no reference to the investigations by Davies (1956), Baker and Dove (1962), and Cunningham and Goldsmith (1959), which bear direct implication to DSVP. This comment applies also to review articles by Horgan and Knowles (1983), Horgan (1989, 1996), Field et al. (2001), Karp (2005). Understanding of DSVP has evolved along more than one avenue, not in a linear pattern, with several diversities over the time line.

Karp (2008) investigated the sensitivity of far field response to the form of end excitation of an elastic, semi-infinite strip. Since, as stated by Torvik (1967), below the first cut-off frequency only one mode can be generated regardless of the form of the excitation, the study examined higher frequencies. It was found that moderately non-uniform excitations exhibit similar energy partition among the propagating modes, suggesting a degree of insensitivity to form even at high frequencies. This can explain similar far-field response detected in experiments by Barton and Voltera (1959) with rounded head strikers, albeit the high frequency spectrum of the excitation.

Adherence to the equivalence of loads required by classical SVP led Karp (2009) to formulate a DSVP based on dynamic equivalence of loads. Dynamically equivalent loads are defined as loads generating identical far-field response within the waveguide. Such formulation of DSVP, based on dynamically equivalent loads, is consistent with experimental results on insensitivity of the far field to details of end excitation and can be related directly to evanescent waves. It was also shown that the requirement on excitation for no-radiation (no far field response) is mathematically reduced to the

static requirement of self-equilibrium of load, as necessary for decay in the static case. The suggested (p. 3072) formulation of the principle reads: "If a certain set of external excitations acting on a certain part of a surface of a body is replaced by another system of external excitations dynamically equivalent to the preceeding system and distributed over the same sector, the stresses corresponding to these two excitations will be practically identical at a sufficient distance from the point of application of the excitations". Further unification of classical SVP and DSVP is proposed (p. 3075): " unification of static and dynamic formulations of SVP can be achieved by noting that in both cases the validity of the principle stems from far-field response being not sensitive to the form of the excitation".

That formulation of DSVP enables one to mitigate the objection, raised by Borg, to counter-example the validity of DSVP. Borg compared two anti-symmetric responses of a Timoshenko beam model. His argument is based on the observation that a pure bending disturbance of a beam propagates with higher velocity than a shear disturbance, and therefore two equal-magnitude moments will generate different far-field response. While this observation is correct it does not contradict the DSVP formulation suggested since the shear mode is a second anti-symmetric mode, available only above the first anti-symmetric cut-off frequency (e.g., Abramson et. al., 1958, p. 157), whereas in Karp (2009) it is suggested to restrict the validity of DSVP to frequencies below the first cut-off. In other words, these two equal-magnitude moments do not comply with the requirements for equivalent excitations (as defined in Karp, 2009).

The studies reviewed in this chapter cover analytical research of solutions relevant to experimental findings reviewed in Chapter 3. The papers reviewed in the following sections are of less direct connection to experiments, though various versions of DSVP are discussed therein.

5 Constrained Waveguides

The search for DSVP in constrained waveguides has concentrated on two types of constrains: clamped faces and energy leaking surfaces. Though the dynamic response of waveguides with constrained surfaces has been treated by several methods, those dedicated to DSVP are limited to use of energy inequality methods (with Orazov, 1983; Karp and Durban, 2005; and Karp, 2011 as exceptions). It is worth noting that elastodynamic solutions for a strip with clamped surfaces (e.g., Mindlin, 1960, Karp and Durban, 2005) suggest that any end disturbance, with frequency below the first cut-off frequency, will generate response decaying in the axial direction leaving no response at all far from the loaded end.

5.1 Clamped Lateral Surfaces

Clamped surfaces are defined by zero displacement $\mathbf{u}$ over the generators of the waveguide

$$\mathbf{u} = \mathbf{0}. \tag{5.1.1}$$

Orazov (1983) used the general formulation of elasticity equations along with eigenfunction analysis to derive decay estimates in a waveguide with general cross-section. The decay rate was associated with the wave number having the lowest imaginary part. As mentioned already, the author emphasizes that the same result is valid also for a waveguide with free lateral surfaces.

Knops (1989) determined spatial decay estimate of cross-sectional energy for a quasi-linear, semi-infinite cylinder, with anisotropy induced by finite prestress. In that study clamped faces were chosen for simplicity of the analysis (p. 193). The end excitation was taken as harmonic in time. As an intermediate result, facilitating an energy inequality, it was proven (corollary 3.1) that the cross-sectional work function Φ vanish far from the loaded end. Energy inequalities derived from that corollary lead to a somewhat complicated mathematical result, from which it follows that (p. 202): "We have demonstrated that within the disturbed region $0 < z < \beta t$ the energy is bounded above by the sum of a constant term and a term that decays exponentially with distance from the base of the beam".

A similar result has been derived by Flavin et al. (1990) for non-linear materials, by Borrelli and Patria (1995) for a mixture of two linear elastic solids, by Borrelli and Patria (1996) for a magnetoelastic cylinder, Chirita and Quintanilla (1996b) for elastic materials, Iesan and Scalia (1997) for microstretch elastic bodies and by Aron and Chirita (1997) for micropolar elastic cylinders.

Quintanilla (1999) established energy decay estimates for the spatial behavior in thermoelasticity without energy dissipation. The derivation of the inequality was made for clamped lateral surfaces with the concluding (p. 221) remark that: "The analysis presented in this section also works if we substitute the boundary conditions imposed at the beginning by $\mathbf{t} = \mathbf{0}$" (where $\mathbf{t}$ is the traction vector on the lateral surfaces). However, that statement has not been supported by other evidence and indeed contradicts the known phenomenon of propagation of non-attenuating waves under such conditions.

Borrelli and Patria (2000) derive a Saint-Venant type decay relation for piezoelectric material, similar to those obtained by Chirita and Quintanilla (1996b) for clamped surfaces excited by harmonic excitation and for a body with free surfaces excited by a transient force. Yilmaz (2007) derived sim-

ilar energy decay estimates for a system of coupled parabolic-hyperbolic equations with clamed surfaces under non-linear conditions.

Chirita and Ciarleta (2008) gave spatial decay estimate for an anisotropic homogeneous and compressible cylinder. The lateral surface and far end of the cylinder are constrained by zero displacement condition. An exponential decay result for excitation frequency below some critical frequency has been derived. Algebraic decay has been obtained for frequencies above that critical frequency though it is not explained how such decay is possible at high frequencies without exclusion of propagating waves.

Tibullo and Vaccaro (2008) derive a theorem of influence domain and decay estimation for strongly elliptic, anisotropic materials. They conclude (p. 993) that: " inside of the influence domain, a spatial estimate of Saint-Venant type has been established, which describes the exponential decay of solutions with respect to the distance from the loaded end".

A study on evanescent waves characteristics in a strip with various boundary data on the faces is undertaken by Karp and Durban (2005) in the context of incremental finite elasticity. In particular, the authors point out that the response of a strip with clamped surfaces consist of decaying fields regardless of the self-equilibrium of the excitation, provided the frequency is below the first cut-off frequency. Frequency map (Fig. 15) shows that for the symmetric fields, the first non-dimensional frequency is $\Omega = 1$. That result is in agreement with previously reviewed results for decaying fields in waveguides with clamped surfaces below a specific frequency.

5.2 Energy Leaking Surfaces

The boundary conditions for waveguides with energy leaking surfaces are expressed by the inequality

$$\mathbf{t} \cdot \mathbf{u} \neq 0 \tag{5.2.1}$$

on lateral surfaces, where $\mathbf{t}$ is surface traction and $\mathbf{u}$ is the displacement vector. Nappa (1998) establish energy decay estimates for both bounded and unbounded bodies with boundary condition of this type. The suggested interpretation of the DSVP is again a combination of domain of influence theorem and spatial energy decay relation within that domain. Extension of this interpretation of the DSVP and energy estimates was made for various domains, among them by Chirita and Nappa (1999) for incremental response of a non-linear material, by Chirita and Ciarletta (1999) for thermodynamic processes, and by Gales (2002) for swelling porous elastic solids.

In several studies it was assumed that the displacement or the load at

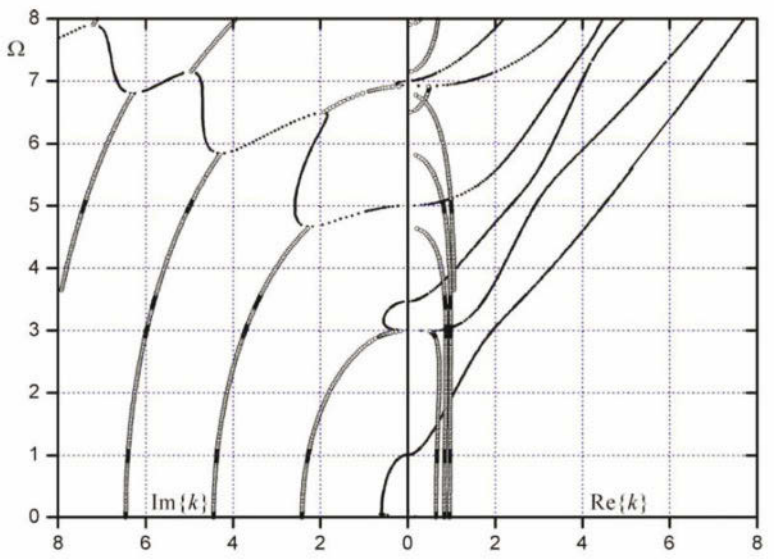

Figure 15. Frequency map (wave number k versus frequency Ω) for symmetric fields in a strip with clamped surfaces made of elastic material with Poisson's ratio $\nu = 0.25$ (Blatz-Ko material without prestretch). Thin lines (composed of black dots) indicate real and purely imaginary branches. Thick lines (composed of hollow circles) indicate complex branches (two curves for each eigenvalue). Purely real wave numbers are associated with propagating waves. (from Karp and Durban, 2005).

the surfaces are imposed, e.g.

$$\mathbf{u} = \widetilde{\mathbf{u}} \quad \text{or} \quad \mathbf{t} = \widetilde{\mathbf{t}}. \tag{5.2.2}$$

If this prescribed data is constant over time, an imposed displacement is actually sort of clamping while imposed traction represents leaking energy. If the data has time dependence, both stand for leaking energy. Such boundary condition was examined by Scalia (2001) to establish energy decay estimates for anisotropic, inhomogeneous linear material with voids. Ciarletta et al. (2002) extended that analysis for porous elastic mixtures and, in Ciarletta (2002), for a thin plate with transverse shear deformation in steady state excitation under clamped lateral conditions, and also for a transient excitation with a dictated displacement at the lateral surfaces. Additional spatial estimates in linear thermoelasto-dynamics for imposed displacement at the lateral surface were derived by Chirita and Ciarletta

(2003), and energy decay estimates for various boundary conditions are reported by Knops and Payne (2005).

Sliding and inextensional surfaces for a waveguide under plane strain (in x, y coordinates) conditions are defined by

$$\tau_{xy} = u_y = 0 \qquad \text{sliding lateral surface} \tag{5.2.3}$$

$$\sigma_y = u_x = 0 \qquad \text{inextensional lateral surface} \tag{5.2.4}$$

Dynamic response of such waveguides has a simple solution which appears in text books on elastic waves (e.g., Achenbach, 1973, Graff, 1975, Miklowitz, 1978).

The study of evanescent waves in such waveguides, within the context of incremental elasticity, is reported by Karp and Durban (2005). An interesting result which has emerged is that non-self-equilibrating excitations induce decaying fields within the strip, as has already been noted in the equivalent static case by Karp and Durban (2002). The decay rates are of the same order as for waveguides with free surfaces. Similar work has been done by Wijeyewickrema et al. (2008), with emphasis on propagating waves.

Recently, Karp (2011) combined the mathematical simplicity of waveguide analysis with sliding boundaries conditions analysis to demonstrate validity and practical aspects of DSVP. In that study the sensitivity of surface strain within the near field (Saint Venant region) to the fine details of end excitation has been confirmed. Results were interpreted with a new measure, the Saint-Venant's ratio (SVR), defined as the ratio of surface axial strain to strain amplitude in the far-field associated with propagating wave. That measure represents deviation of the near field from the far field. For example, SVR = 1 when there is no end effect at all (the profile of the excitation is identical to the profile of the propagating wave at a given frequency). The variation of SVR with non-dimensional distance x/h for various excitations is reproduced here in Fig. 16. The resemblance of these curves to those obtained for a rod subjected to a transient excitation in Fig. 13, is notable.

6 Special Geometries

Extension of SVP to half-space, wedge and a cone is not a straightforward task since these geometries lack any natural length scale, as opposed to a beam to which Saint Venant originally referred to (de Saint-Venant, 1886). Therefore, for formulation of SVP for such cases the length scale is taken from the load spatial parameters, as demonstrated in statics by von-Mises (1945) and Sternberg (1954) for a half space and by Horvay (1957),

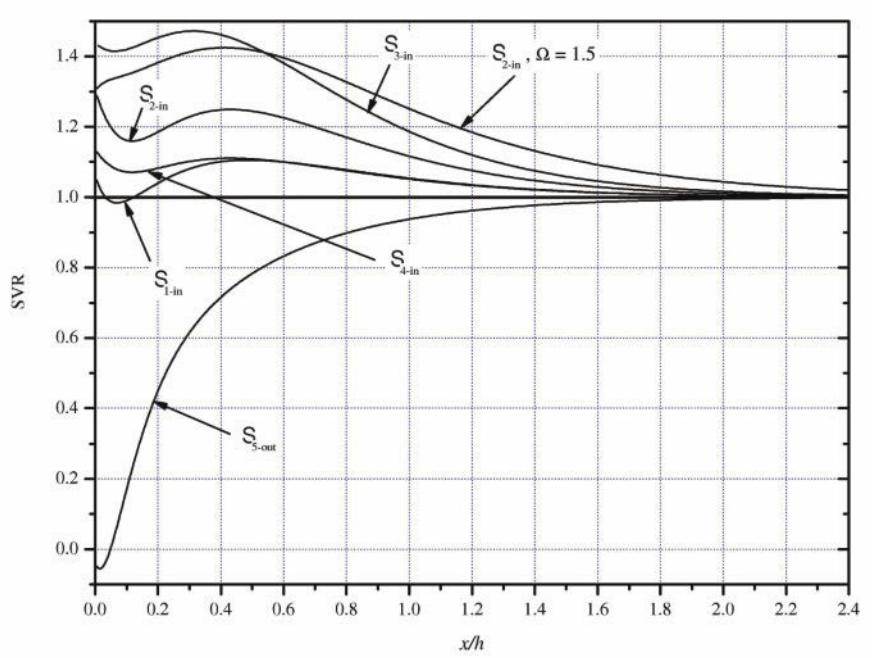

Figure 16. Variation of SVR for five excitation forms S (resembling damaged joint) with frequency $\Omega = 0.5$ (below first cut-off) and S_{2-in} excitation also with frequency $\Omega = 1.5$ (close to first cut-off). Four S_{i-in} excitations represent damaged joint at the center line of the strip while S_{5-out} excitation represents damage at the outer edges. (from Karp, 2011).

Markenscoff (1994) and Stephen (2008) for a wedge. Few studies examine the possibilities to extend findings in these geometries to the dynamic case.

6.1 Half-Space

Miyao et al. (1975) studied the application of SVP to dynamic response of a semi-infinite body subjected to an impulsive torque on the surface of a hemispherical pit. The temporal variation of the excitation applied to the body was a step load with several additional cases of gradually profiled loads. It was found that the stresses just behind the wave front are strongly influenced by the spatial distribution of shear forces on the pit. Stresses behind the wave-front, far enough from the pit, are not sensitive to such variations of load distribution. The distance at which that insensitivity manifests is smaller for excitations that gradually change with time. It is

interesting to bring the note (p. 963) stating: "Compared with the results previously obtained for the rod, the difference among stress systems produced by several systems of applied load distributions is more remarkable for the semi-infinite body".

Kim and Soedel (1988) solved the problem of dynamic response of a half-space on which a step load is applied. Emphasis of the article is on a novel method enabling a simple solution for arbitrary spatial distribution of the step load. Upon preserving the equivalent static load, the result is that far enough from the loaded area, the strains behind the wave-front are insensitive to the spatial distribution of the load. The same conclusion was obtained later by Awrejcewicz and Pyryev (2003). No explicit reference to DSVP was made.

Wang and Kim (1997), on the other hand, analyzed the effect of an impulse load with varying contact area acting on a half-space (modeling impact against a stop). Comparison of the response included the full time history of the stress at a distant point while preserving the total load. Conclusion was that at distances greater than five times the diameter of the loaded area, the size of the loaded area has a fairly small effect on the stress generated. This conclusion is directly related to DSVP, and has been used in the study to confirm the method suggested for analysis of such problems.

Awrejcewicz and Pyryev (2003) compared the response of a half-space to a step load with different spatial distributions preserving the integral intensity of the load. They conclude that Saint-Venant's principle cannot be applied to the wave front, but rather to its trail (behind the wave front) - after the lapse of time ensuring the passage of a Rayleigh wave at a point of consideration.

A more definite conclusion regarding the non-validity of SVP to dynamic excitation of a half-space has been put forward by Ziv (2002, 2003): " half-space response is hypersensitive to the type of loading, to the way it is distributed on the source rim, and to the geometry of the source rim under the load" (Ziv, 2002, p. 402). Therefore (Ziv, 2003, p. 254-255): "Saint-Venant's principle for wave propagation problems cannot be formulated. The source geometry and its load must be tackled directly as they are prescribed; i.e. two different configurations sharing the same resultant are not interchangeable".

Ignaczak (2002) considered the issue of SVP in microperiodic, layered, thermoelastic semi-space, thus formulating a time dependent energy decay estimate.

6.2 Wedge and Cone

Budaev et al. (1996) summarize two previously published studies, Budayev et al. (1994) and Morozov and Narbut (1995) on Saint-Venant's principle in a wedge and cone, both for static and dynamic excitations. Three types of end excitations, applied on the surface generators of the wedge or cone, were considered: torsion, anti-plane, and normal traction. The criterion for validity of both SVP and DSVP is whether differently distributed loads with identical moment generate the same asymptotic result far from the wedge apex. For the static normal loads they find (p. 32) that SVP is not valid since: "... it is possible to find forces $f_1(r)$ and $f_2(r)$, having the same couple M_1, for which the solutions will be quite different". For anti-plane shear excitation it is demonstrated (p. 33) that SVP does not hold, neither for the static case, nor for the dynamic case: "... so the error of substitution of one system by another is not small...". For torsion, both static and dynamic, the principle does hold (p. 36): "...then the validity of the Saint-Venant principle is deduced from previous analysis. In fact, the stresses in the cone under torsion at some large distance from the apex are mainly characterized by the moment of boundary forces".

7 Composites and Laminates

From studies on the validity of the classical SVP it is known that the decay rate in laminates and in composite materials can be much lower than in isotropic elastic materials (e.g., Horgan and Simmonds, 1994). This makes the depth of penetration of end effects to be significantly larger as is evident from studies on dynamic response of composite waveguides available in the literature. Apart from that extended depth of penetration of end effects, there is no substantial difference in analysis between elastic composite and isotropic homogeneous waveguides. The papers cited below were chosen due to specific comments related to DSVP, and for explicit association made between evanescent waves, edge vibrations and DSVP.

End effects in anisotropic cylindrical shells were discussed by Bhattacharyya and Vendhan (1991). Detailed mathematical and physical interpretation of evanescent waves was given, followed by the observation of low spatial attenuation at frequencies near cut-off frequencies. The evanescent waves (p. 71) were associated with Saint-Venant's zone: "...The effect of the attenuating modes on the dynamic stress field is localized near the end zone of the shell, the extent of the zone being dependent on the roots for a specific "end" problem. This is simply the Saint-Venant zone, so well known in static problems, and hence the end effect is essentially a dynamic Saint-Venant effect". The term "roots" refers here to wave numbers which

are the roots of the Pochhammer-Chree equation.

Dong and Huang (1985) applied the finite element method to investigate edge vibrations in laminated composite plates by considering explicitly the evanescent waves. They regard that treatment as related (p. 437) to DSVP: "The analysis procedure may be considered as the dynamic counterpart of the quantitative analysis of Saint-Venant's principle". That view is an extension of a similar static analysis made earlier by Dong and Goetschel (1982). The outcome of this work is that dynamic edge vibrations are analogous to static end effects regardless of self-equilibrium of the excitation, as suggested already by Torvik (1967). The authors derive a characteristic equation for use in finite element analysis to find (p. 435) that: "... equation (16) represents the dynamic counterpart of Saint-Venant's principle for the determination of the decay rates into the plate's interior of self-equilibrated edge vibrations". A similar study and connection with DSVP for an anisotropic composite cylinder can be found in the paper by Huang and Dong (1984). It is not clarified in what sense the "edge vibrations" are "self-equilibrated" except for these evanescent waves being a natural extension of the static eigenfunctions which are indeed self-equilibrated in a static problem.

The papers by Scalia (2001) and Chirita and Ciarleta (2008) mentioned above, in a different context, analyzed anisotropic materials and therefore belong as well to this group of studies.

8 Related Studies

In this chapter two neighboring areas in which DSVP is questioned or invoked are reviewed. Neither is a natural part of the categories detailed here, yet both could be integrated in further studies on DSVP.

8.1 Structural Vibrations

Vibration, by its nature, is not associated with spatial propagation of energy. Two distinct phenomena of structural vibration can be identified. One is the global vibration of beam, plate or shell-like structures, typical to a finite structure. The second is edge vibration associated with evanescent waves and can exist also in a semi-infinite structure (e.g., Kaul and McCoy, 1964). Since end vibration consists of evanescent waves, references to that phenomenon have been reviewed in chapter 4, including for example the work of Foster and Berdichevski (2004), albeit the vibration oriented title. Yet, to make a clear distinction between studies of finite and semi-infinite structures, this chapter reviews both types of vibration: structure vibration

and end vibration, if treated in the context of a finite structure (e.g., Gales, 2003).

Duva and Simmonds (1991, 1992) studied possible ways for obtaining accurate natural frequencies of beams, especially those weak in shear. The first order approximate frequency values were deduced from elementary beam theory. Two methods for arriving at more accurate values were examined: refined beam theories and implementing end effects. Based on analysis of two-dimensional end effects in vibration of a cantilevered beam the authors demonstrated that the contribution of end effects to correction of natural frequency of a beam (either weak in shear or not) is more meaningful in comparison with the correction obtained with higher order beam theory. Accordingly, a correction factor for the natural frequency is suggested.

A technique to bypass the need to consider end effects in analysis of vibration was suggested by Chen et al. (2003). The treatment of dynamic response of a laminated beam by conventional state space method combined with differential quadrature method shows (p. 75) that: "It also can cope with arbitrary boundary conditions without applying Saint-Venant's principle".

End effects in a rectangular plate of thickness h and dimensions axb, are considered by Kathnelson (1997). To clarify the extent and the magnitude of end effects an asymptotic analysis of the exact shear edge effect solution near a free side of a rectangular isotropic linear elastic plate is carried out. It is argued that in the dynamic case the end effects are identical.

Differential inequalities leading to energy estimates were derived by Flavin and Knops (1987) for a finite cylinder, either with clamped faces or made of viscoelastic material. That work was followed by a series of subsequent studies employing differential inequalities (cited above in the context of waveguides with free or constrained surfaces). Combining the treatment of waveguides with clamped faces with viscoelastic material response in one paper appears to reflect the common feature of spatial decay of energy (as opposed to a previous paper by Ignaczak, 1974). The authors succeeded in proving that the effect of dynamic excitation remains localized at the vicinity of the excited end for both cases.

Two remarks made by Flavin and Knops (1987) extend the validity of that result to waveguides with free lateral surfaces or without viscous dissipation. The first (Remark 2, p. 255) reads: "The results remain valid if $\eta = 0$ (no viscosity) provided that special initial conditions, appropriate to the forced oscillation are adopted.". The second (Remark 4, p. 261) states: "Theorem 2 continues to be valid in the absence of damping provided that the complementary oscillation (undumped in the ideal elastic case) which co-exists with the forced oscillation is subtracted out". It is suggested in

Karp (2009) that the "complementary oscillation" can be considered as an equivalent excitation having the same average power and frequency as the main load (and opposite phase), and that the "special initial condition" is an excitation that does not generate propagating modes.

Chirita (1995) considered spatial decay in problems governed by parabolic and hyperbolic equations. The principle derived consists of two parts: domain of influence and energy decay estimate within that domain.

Iesan and Scalia (1997) established a spatial decay estimate for a finite cylinder, made of micro stretch elastic solid, and excited at one of its ends. Both free and clamped lateral surfaces were considered, leading to exponential decay below some critical frequency. Since both formulations refer to steady state response of a finite rod, it is clear that the end excitation should have zero average power. Otherwise, energy inflow will not allow for the response to settle into a steady state. Then, the decay measures obtained reflect upon the evanescent waves.

Essentially an identical problem was studied by Gales (2003). Here, the amplitude of the steady-state vibration of a finite cylinder made of a mixture consisting of three components (an elastic solid, a viscous fluid and a gas) was investigated. An exponential decay estimate of Saint-Venant type in terms of the distance from one end of the cylinder was obtained with the decay constant depending on excitation frequency, constitutive coefficients and the first positive eigenvalue of the fixed membrane problem for the given cross-sectional geometry (as derived by Toupin, 1965a). The author concludes (p. 152) with: "To the amplitude of the steady-state vibration we associate a cross-sectional measure and, provided the exciting frequency is lower than a certain critical frequency, we derive a first-order differential inequality, which by integration leads to a spatial decay estimate of Saint-Venant type. The result proves that the above cross-sectional measure decays faster than a certain exponential function of the distance from the loaded end".

The problem of thermoelastic vibrating plate was addressed by D'Apice (2005). Saint-Venant type decay is derived for frequency of vibration below a specific value, with an exponential decay of energy contents in the cross section.

Experimental investigation of end effects on the frequency of vibration of a cantilever elastic beam was conducted by Karp et al. (2008). An aluminum beam was clamped by six screws at one end and excited by a lateral impact at its free end. The level of tightness of the screws was the controlled variable and considered as a variation of end conditions without changing the global characteristics of the structure as a cantilever beam. It was found that complete release of any of the six screws had significant

effect on near field response (Fig. 17) but not on the far field. FFT (fast Fourier transform) analysis of the far field response revealed no sensitivity to absence of one screw. Removal of two or more screws did have an effect on the vibration frequencies of the beam (not reported in the article).

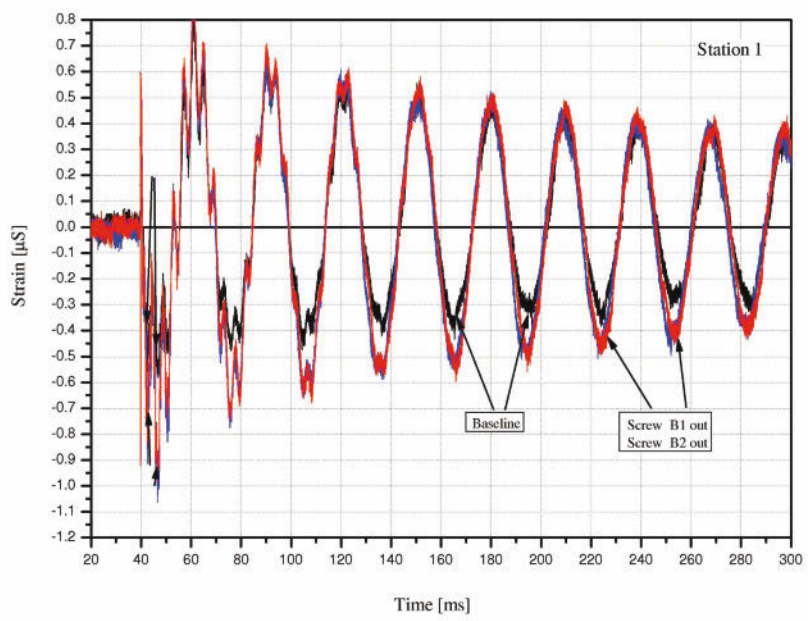

Figure 17. Axial surface strain recording in the close vicinity to clamped end of a beam, with three different "clamping" conditions subjected to transversal excitation at the far end of the beam (from Karp et al., 2008).

Evans and Porter (2008) used Green's function to demonstrate existence of edge waves for a semi-infinite plate within the context of plate theory. Specifically, the authors have shown that plane waves incident on a pinned point on the straight edge of an elastic plate can generate edge waves which radiate energy to infinity along the edge. Various aspects of edge waves are discussed in a recent volume of Mathematics and Mechanics of Solids accumulate several reports on edge vibration and resonance, including Kaplunov and Lawrie (2012), Zacharov (2012), Pichugin and Rogerson (2012), Pagneux (2006, 2012), Kaplunov and Fu (2012).

8.2 Viscoelastic Materials

Since spatial decay of energy can not be granted in elastic materials due to existence of propagating modes, even when a self-equilibrated load is applied, viscosity was introduced to provide a dissipating mechanism ensuring the required decay. That type of material is mainly studied by authors who considered the spatial decay of end effects as a criterion for a valid version of Saint-Venant's principle.

Murray (1970) looked at the question of spatial and temporal decay of discontinuities induced at a surface in a mildly nonlinear Maxwell rod with finite nonlinear viscous damping governed by a first order partial differential equation. Various degrees of spatial decay behavior were derived for different characteristics of the problem.

Rauch (1976) investigated the qualitative behavior of dissipative wave equations of a bounded domain with a general cross-section. Munoz Rivera et al. (1996) employed integral theorems to establish decay rates for viscoelastic plates with memory. The decay considered is a function of time, which formally excludes it from being of Saint-Venant's type.

In the work by Chirita (1997) energy decay estimates were obtained for transient response of a finite length bar, made of anisotropic viscoelastic material, with lateral surfaces free of traction, for both self-equilibrated and general dynamic load. An analogous asymptotic result was obtained for a semi-infinite cylinder. Existence of exponential spatial decay for both self-equilibrated and generally non-self-equilibrated loads, derived in that work, emphasize the question of relevance of self-equilibrium for a dynamic version of SVP. It also exposes the substantial difference between dissipating and non-dissipating media in the context of DSVP.

Ciarletta and Chirita (1999) establish decay estimate for a viscoelastic material with voids. De Cicco and Nappa (1999) derived an exponential decay estimate for a micropolar viscoelastic finite cylinder in a form similar to Toupin's (1965a) decay estimate for a quasi-static case.

More than ten studies on decay of dynamic disturbances in viscoelastic materials appeared in the literature (reviewed here in previous chapters). Because the damping coefficient enters implicitly into decay estimations, it is difficult to figure out mathematically the role of damping and possibly relate these works to decay estimates derived originally for elastic materials without any dissipating mechanisms. No equivalence criterion is invoked in these studies.

9 Comparing SVP with DSVP

It is a standard practice in physics to require a general formulation and solution of a dynamic problem to degenerate to its quasi-static equivalent by taking the limit of vanishing frequency $\omega \to 0$. Following that practice, it is expected that any valid version of DSVP will degenerate to the classical SVP at that limit. Successful degeneration of one the DSVP version can provide some credibility to that version.

Classification of the articles reviewed in Chapter 4 discloses five approaches to what DSVP should be (summarized in Section 10.1 below). Among these five only the dynamic equivalence approach appears to be legitimate for degeneration to SVP. Excluded are approaches denying existence of DSVP and those introducing viscosity. That comparison between SVP and DSVP and degeneration of DSVP to SVP is suggested below. The comparison is not complete due to the currently early stages of the research on that version of DSVP. Yet, it might be valuable in pointing to potentially constructive research direction on the topic.

9.1 Mathematical Formulation and Foundation

Mathematical foundation of the classical SVP is based mainly of two methods: energy inequality (e.g., Knowles, 1966, Toupin, 1965a) and eigenfunction expansion (e.g., Horvay, 1953). Let us begin the comparison with the eigenfunction expansion method.

Eigenfunction expansion method commonly regarded as an accurate quantitative estimation of validity of SVP (e.g., Goetshel and Hu, 1985; Horgan, 1989). It is commonly related to a semi-infinite strip, resembling a beam like or plate like structure, with a typical width of $2h$. The response of the strip to a self-equilibrated load is captured by eigenfunctions, decaying exponentially from the loaded end, providing the effect of localization. The complete displacement response of the strip in the (x, y) plane with x as an axial direction is given by

$$\mathbf{u}(x, y) = \sum_n A_n \mathbf{U}_n(y) e^{-\xi_n x} \tag{9.1.1}$$

where the sum is taken over the infinite set of eigenfunctions $\mathbf{U}_n(y)$ each associated with eigenvalue ξ_n. Positive real part of the eigenvalue $Re\{\xi_n\}$ dictates the rate of spatial decay of the amplitude of each mode n. The dynamic response of the same semi-infinite strip is described in a similar way by (e.g., Achenbach, 1973)

$$\mathbf{u}(x, y, t) = \sum_n A_n \mathbf{U}_n(y) e^{i(\xi_n x - \omega t)} \tag{9.1.2}$$

Except for the additional time variable and frequency parameter, there are only semantic differences between the quasi-static solution and the dynamic one. Here $\mathbf{U}_n(y)$ are wave modes and ξ_n are wave numbers. The decaying wave modes are termedevanescent, spatial decay of which is dictated now by $Im\{\xi_n\}$ due to the i factor in the exponent. By taking the limit of zero frequency, one derives the quasi-static solution from the dynamic one. The spatial decay rate of both static and dynamic fields is governed by the same variable ξ_n.

The values of the decay rates ξ_n of the static fields are obtained from the Fadle-Papkovich equation (Timoshenko and Goodier, 1972). The values of the decay rates ξ_n of the evanescent waves are obtained from the Rayleigh-Lamb equation (Mindlin, 1960; Graff, 1975). That equation is degenerated to Fadle-Papkovich equation by taking the limit of zero frequency (Miklowitz, 1978).

Let us contrast now SVP and DSVP as they are formulated using energy methods. In the static case the decay of energy contained in the body due to application of self-equilibrated load is exponential (Toupin, 1965a; Knowles, 1966). The decay rate obtained is considered to be an approximate to the exact one obtained from eigenfunction expansion ξ_n.

An equivalent examination of energy decay due to dynamic self-equilibrated load revealed non-decaying (propagating) modes that deliver energy to infinity without attenuation. Yet, since self-equilibrated loads are not a result of difference between dynamically equivalent loads, that result does not necessarily disprove DSVP. Indeed, it has been shown by Karp (2009) that under some limiting conditions a difference between any two dynamically equivalent loads result in excitation having zero average power. From waveguide analysis it is obtained that for such excitations the energy content in a waveguide will indeed decay with rate dictated by ξ_n. Such decay was obtained using energy inequalities only for waveguide with clamped lateral surfaces (as reviewed in Sec. 5.1) and a more general proof is remained to be wanted.

9.2 Practical Application

The application of SVP consists of replacing the actual system of loads by other system having identical static equivalents, namely, same total force and couple. According to the dynamic equivalence version the usage of DSVP is by replacing the original excitation by other excitation having identical dynamic equivalents, namely, total average power and frequency (below first cut-off frequency). Apparently, static and dynamic equivalences are different. Difference between two statically equivalent loads results in

self-equilibrated load whereas difference between two dynamically equivalent excitations lead to excitation with zero input power. Yet, it was shown for a simple waveguide (Karp, 2009) that any excitation having zero net power applied to a wave guide is self equilibrated in the static sense in the limit of zero frequency.

The mathematical derivation of the classical SVP out of DSVP by taking the limit of zero frequency enable one to generalize the statements of the principle, emphasizing their oneness. One common reference to SVP can now be generalized to be written as: "Principle of elastic equivalence of a *statically/dynamically* equivalent system of *loads/excitations*": Engineers customary refer to a different statement, reading now: "The far field strain produced in a body, by application of *statically/dynamically* equivalent *loads/excitations*, is the same". These two statements, combining SVP and DSVP, are in a complete agreement with the spirit of Saint-Venant's ideas as expressed by Ericksen (1979, p. 7): "St.-Venant's principle gave a rule of thumb for dividing all solutions into equivalence classes ...".

Finally, in both static and dynamic problems the meaning of the principle is that the far field response is not sensitive to the details of the applied excitation, rather to its integral properties. In the static case these integral properties are the static equivalents. In the dynamic case it is the time average input power. The unified statement of the principle is thus: "A property of a structure according to which the strain far from the loaded end has low sensitivity to the spatial distribution of *static/dynamic loads/excitations*".

10 Concluding Comments

10.1 Theoretical Formulation

Most of existing studies on DSVP look either for conditions under which spatial decay can be granted, or search for the distance beyond which the fine details of the excitation has only minor importance, if at all. Each of the two approaches has brunched into several views as to what DSVP should be. These views can be grouped roughly into five categories: DSVP is not valid even if self-equilibrated excitation is applied (Boley, 1955, 1960a; Slepiyan and Novhozilov, 1965; Grandin and Little, 1974; Ziv, 2003; Foster and Berdichevsky, 2004); DSVP is valid regardless of the self-equilibrium of the excitation provided some attenuating conditions are added, such as clamping of the lateral surfaces, energy leaking surfaces, or viscosity (Flavin and Knops, 1987; Nappa, 1998; Ciarletta and Chirita, 1999); DSVP is valid only approximately when the frequency is low enough (Boley 1955, 1960a; Grandin and Little, 1974) or when the excitation deviates slightly from self-equilibrium (Gomilko et al., 1995; Babenkova and Kaplunov, 2004); DSVP

is valid only statistically (Foster and Berdichevsky, 2004); and finally, DSVP is valid for dynamically equivalent loads, equivalence that can be defined rigorously at any frequency below the first cut-off frequency (Torvik, 1967; Karp, 2009).

At present, there is apparently no guiding idea as how to select one approach over the other. Nevertheless, it should be possible to follow the original spirit of classical SVP in considering primarily practical aspects of DSVP. As vividly described by Toupin (1965b) and by Benvenuto (1997), Saint Venant used heuristics to propose his assumption aiming at liberating engineers from dealing with beam problems associated with either unknown boundary details or intractable analytically. In Chapter 3 we have tried to provide clear experimental evidence for that quest suggesting that similar practical approach should be valid in the case of dynamic excitation as well. The comparison between the classical SVP and the dynamic equivalence interpretation of DSVP brought in Chapter 9 provide a further demonstration of the possible formulation of DSVP and probably for its potential benefit.

10.2 Application of DSVP

A review by Walley and Mason (2000) on the history of the split Hopkinson bar system for material characterization exemplifies the need for DSVP and the interpretation associated with that (p. 2): "This issue was resolved by theoretical work and experimental checks on whether the Saint Venant Principle could be extended to dynamic 'non-equilibrium' loading problems ... And from about 1953 onwards it became standard to use strain gauges bonded to the outside of Hopkinson bars to measure strain pulses propagating down them". The same view was expressed by Field et al. (2001) in summary of main developments in such systems. According to that summary (p. 112), the 50's are characterized by: "Experimental checks of the St Venant hypothesis and hence legitimation of the use of surface strain gauges to measure stress pulse propagation". Typical example for application of DSVP is found in Pope and Field (1984, p. 817): "Miniature semiconductor strain gauges are sited 10 bar diameters from the input end and by the dynamic equivalent of St Venant's principle the bar can accurately record the total force on the end face, independent of the pressure distribution".

These assertions, along with additional considerations of separation of signals, are the basis for guidance in locating strain gauges in split Hopkinson system by Follansbee (1985, p. 199) "However, these end effects quickly dampen after the wave has propagated about ten bar diameters", and in the newer version by Gray III (2000, p. 463): "The length of the pressure bars must first ensure one-dimensional wave propagation for a given pulse

length; for experimental measurements on most engineering materials, this propagation requires approximately 10 bar diameters". From experiments detailed in chapter 3 and from recent studies (e.g., Meng and Li, 2001; Karp et al., 2008, 2009) it can be safely stated that the distance at which a one-dimensional wave is attained is much smaller (2-3 diameters). From Pochhammer-Chree solution and Davies' (1948) studies it is evident that an additional restriction of low frequency should be imposed.

Another practical aspect of DSVP is detailed by Duva and Simmonds (1991). The authors examined influence of end effects on the lower natural vibration frequencies of a laminated beam and the correction to the classical prediction that should follow. A direct association of end effects with DSVP (p. 178) was made: "...It is senseless to proceed without discussing end effects. For the relatively low frequencies of vibration we are considering, these effects should be confined to end zones of width $O(H)$ as suggested by the useful discussions by Boley (1955, 1960) and Grandin and Little (1974) of a dynamic St-Venant's Principle for a semi-infinite elastic strip".

In a few additional engineering situations researchers have relied upon DSVP, either implicitly or explicitly, deliberately or tacitly. The dynamic equivalence version of DSVP is applied in the field of active noise and vibration control (without reference to DSVP). For example, the cancellation of an unwanted sound field is achieved by an array of sources activated to generate a secondary acoustic field having the same frequency and average power with an inverse polarity to the main source, resulting in a destructive interference (Rosenhouse, 2002). Kuznetsov and Stepanov (2007) used the idea of equivalence for dealing with source replacement (p. 326), stating that: "The equivalence of a model is understood in the sense that the pressure levels and interference structures of the amplitude and phase of a volume low-frequency source and of a point multipole should be sufficiently close to provide the required accuracy of measurements.". Another practical aspect of source equivalence is found in ambient noise modeling of urban landscape (e.g., Hornikx and Forssen, 2009). Kundu et al. (1991) used equivalent source replacement based on validity of SVP (p. 153): "In the proposed method unknown sources are placed not at the near field boundary but at the location of the structure. Then the Saint-Venant's principle is utilized to justify that at a distant point the effect of structure's vibration can be effectively modeled by an equivalent vibrating point force and vibrating moment at the structure's position". It is worthy to note that such application of SVP to dynamic response of a half-space was later regarded by several researches as not valid (see section 6.1).

The possible application of the concept of DSVP to the emerging field of structural health monitoring was demonstrated by Karp et al. (2008)

and Karp (2011). It was shown that by estimating the extent of end effects, along with the identification of dynamic equivalence, it is possible to expose incipient damage at joints of beam-like and plate-like structures.

It can be extrapolated from those representative examples that several engineering fields should benefit from applying the dynamic equivalence version of DSVP. It is conceivable that DSVP can be used in other engineering situations as well. This might include: source recognition in acoustics and acoustic emission (e.g., Kroll and Tatro, 1964), earthquakes analysis (e.g., Kundu et al., 1991), force reconstruction in measurement systems relying on wave guiding (e.g., Tyas and Watson, 2000), energy trapping at discontinuities associated with evanescent waves (e.g., Evans, 1992; Kaplunov and Sorokin, 1995; Aslanyan et al., 2000; McIver et al., 2002; Chamberlain, 2004), and dynamic material characterization (e.g., Waldman and Lee, 2002; Sasso et al., 2008; Gilat et al. 2009) where uniformity of the field within the cross-section is required.

10.3 Vision of DSVP

There are definite contradictions and lack of clarity related to the possible validity of DSVP in elastic problems. In particular, this is due to convincing demonstrations for non validity of DSVP (non-decaying field due to self-equilibrated excitation), and general the inherent non-decaying property of fields governed by hyperbolic partial differential equations. That unease can somewhat be mitigated by appreciating that even the study of the classical SVP is not yet complete. A brief review of the history of the ideas related to the classical SVP expose parallel counter examples and mixed attitudes to the essence of SVP.

Examples for structures for which the classical SVP is not valid were discussed years before, and also after, proofs for validity of SVP were derived. Four such structures are shown here in Figures 18 and 19. Additional counter examples for SVP are given by Horvay (1957), Toupin (1965b) and more recently by Huang (1989) and by Markenscoff (1994). It appears that these counter examples for validity of the classical SVP did not lead the community to doubt its existence, nor its usefulness.

It is instructive to quote several prominent scientists referring to the meaning of the classical SVP. von-Mises (1945) wrote a century after Saint-Venant introduced his assumption (p. 562): "What Saint Venant originally had in mind was doubtlessly the case of a long cylinder with infinite ratio of length to diameter. The purpose of the present paper was to show that an extension of the principle to bodies of finite dimensions is not legitimate". In a similar spirit, Sternberg (1954, p. 401) wrote: "For Saint-Venant's prin-

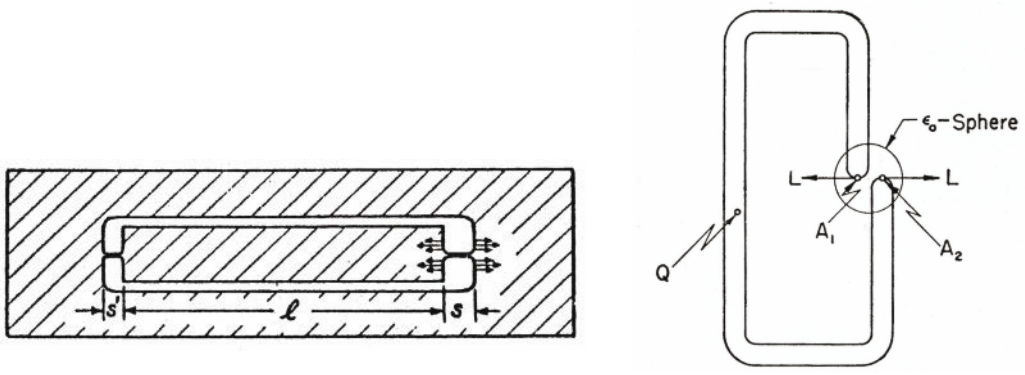

(*a*) (*b*)

Figure 18. Two structures for which the classical SVP is not valid: (a) from Donnell (1962), (b) from Sternberg (1954).

ciple is a statement about relative orders of magnitude and does not tell us anything about the extent of the region within which a self-equilibrated system of tractions, applied to a portion of the surface of an elastic body, "materially" influences the stress distribution in the body". The non univocal meaning of SVP is also evidenced from discussion brought by Naghdi (1960). Even three decades later Levine and Quintanilla (1989, p., 71) noted that: "we believe that the study of the principle and problem is not finished even in the simple case of cylinders".

These citations, along with several counter examples, related to the classical SVP may suggest that existence of clear examples for non-validity of DSVP and some disagreement concerning its very essence, does not necessarily mean the search for DSVP in linearly elastic material is hopeless. Moreover, the wide range of experimental situations in which one of the versions of DSVP appears to be valid, might motivate one to search for ways to relax the apparent contradictions, made explicit in Section 2.3. The use of energy inequalities is one of avenues to be followed in providing a rigorous proof for decaying fields generated by excitations having zero net power. Such a research is expected to provide clearer definitions of the conditions under which DSVP is expected to be valid, and when it does not.

Unification of the classical SVP with the equivalence version of DSVP raises an additional question on whether that version can also be generalized to other Saint-Venant type decay estimates (not reviewed here) such as in quasi-linear or non-linear elasticity, non-mechanical waveguides (op-

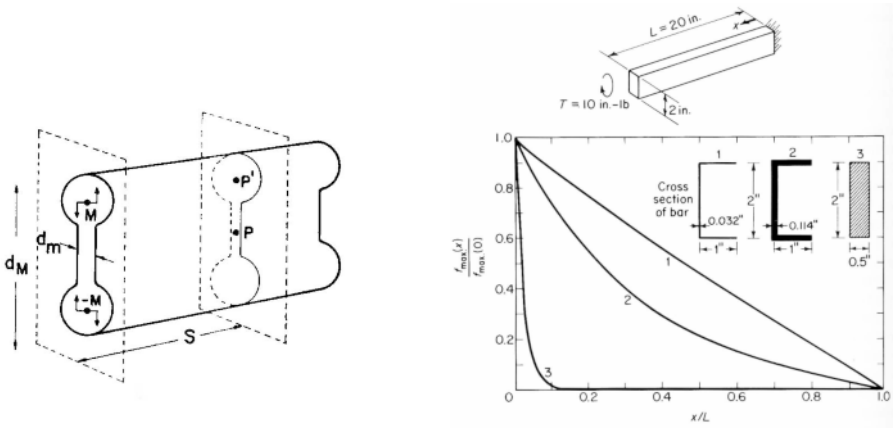

(*a*) (*b*)

Figure 19. Two structures for which the classical SVP is not valid: (a) from Toupin, (1965a), (b) from Hoff (1945).

tical), and to heat problems. For example, in the proof of the static SVP, correspondence between the energy inequalities (Toupin, 1965a; Knowles 1966) and direct elasticity solutions with eigenfunctions (Timoshenko and Goodier, 1972) has been established. Can such correspondence be shown to hold for dynamic or heat problems? In that context, it is an open question how to settle the apparent contradiction between established energy decay, obtained by several authors, and the non-decaying propagating modes in a non-dissipating structure with free surfaces.

Since DSVP is related to localizied phenomena, it is natural to expect existence of connections with the various topics covered in this volume. Such possible connections are ought to be pursued, both in continuum mechanics and electromagnetic fields.

Apparent inconsistencies, between several views of DSVP and engineering practice, define clear objectives for additional future research. Since dynamic phenomena encompass a richer spectrum in comparison with static cases, it is expected that applications will exceed the well established limits of the classical SVP. Applying the principle should be supported by firm experimental evidence, both in validity and in quantitative estimation. The work reviewed in chapter 3 provides a promising start for fruitful research

to come. Engineers in particular are expected to recognize the validity of the DSVP (at least in one of its versions) and to assimilate its use.

Both theory and engineering practice call for such an undertaking, with research program including related issues like stability of solutions and well posedness. The theoretical basis of the DSVP should be widened and it is hoped that the present review will contribute towards formulating a unified theory, compatible with the body of knowledge already available, on a dynamic analogue of Saint-Venant's principle. Note: This article is an extended and updated version of a review published few years ago in Applied Mechanics Reviews (Karp and Durban, 2011).

Bibliography

[1] Abramson H.N., Plass H.J., Ripperger E.A., 1958, Stress waves in rods and beams, *Advances in Applied Mechanics* 5 111–194

[2] Achenbach J.D., 1973, *Wave propagation in elastic solids*, North-Holland, Amsterdam

[3] Ames K.A., Payne L.E., Schaefer P.W., 1993, Spatial decay estimates in time-dependent stokes flow, *SIAM J. Math. Anal.* 24(6) 1395–1413

[4] Aron M., Chirita S., 1997, Decay and continuous dependence estimates for harmonic vibrations of micropolar elastic cylinder, *Arch. Mech.* 49 665–675

[5] Aslanyan A., Parnovski L, Vassiliev D., 2000, Complex resonances in acoustic waveguides, *Q. J. Mech. Appl. Math.* 53(3) 429–447

[6] Awrejcewicz J., Pyryev Y., 2003, The Saint-Venant's principle and an impact load acting on an elastic half-space, *J. Sound Vib.* 264 245–251

[7] Babenkova E., 2004, *A dynamic analog of the Saint–Venant principle and boundary conditions for vibrating plates*, Ph.D. dissertation, University of Manchester

[8] Babenkova E., Kaplunov J., 2003, The two-term interior asymptotic expansion in the case of low-frequency longitudinal vibrations of an elongated elastic rectangle, A.B. Movchan (ed.), *IUTAM Symposium on Asymptotics, Singularities and Homogenisation in Problems of Mechanics*, Book Series - Solid Mechanics and its Applications, Vol. 113, Kluwer, 137–145

[9] Babenkova E., Kaplunov J., 2004, Low-frequency decay conditions for a semi-infinite elastic strip, *Proceedings of the Royal Society of London A* 460 2153–2169

[10] Babenkova E., Kaplunov J., 2005, Radiation conditions for a semi-infinite elastic strip, *Proceedings of the Royal Society of London A* 461 1163–1179

[11] Babenkova E., Kaplunov J., Ustinov Y.A., 2005, Saint-Venant's principle in the case of the low-frequency oscillations of a half-strip, *PMM Journal of Applied Mathematics and Mechanics* 69 405–416

[12] Baker W.E., Dove R.C., 1962, Measurement of internal strains in a bar subjected to longitudinal impact, *Experimental Mechanics* 2 307–311

[13] Barton C.S., Volterra E.G., 1959, On the elastic impact of short cylindrical rods on long cylindrical rods, *Proc. 4th Midwestern Conference on Solid Mechanics*, Austin, Texas, 318–330

[14] Bell J.F., 1960, The initial development of an elastic strain pulse propagating in a semi-infinite bar, *Johns Hopkins University*, November 1960, 1–31

[15] Bell J.F., 1973, The experimental foundations of solid mechanics, in *Mechanics of solids*, Vol. VIa/1, in *HNBK der Phys.*, S. Flugge ed., Springer-Verlag, New-York

[16] Benvenuto E., 1997, Engineering, Mathematics and Natural Philosophy in the Work of Barre de Saint Venant, Plenary lecture in *3rd EUROMECH Solid Mechanics Conference*, KTH, Royal Institute of Technology, Stockholm, Sweden, August 18–22

[17] Berdichevsky V., Foster D.J., 2003, On Saint-Venant's principle in the dynamics of elastic beams, *Int. J. Solids Struct.*, 40, 3293–3310

[18] Bertholf L.D., 1967, Numerical solution for two-dimensional elastic wave propagation in finite bars, *J. Appl. Mech. (Trans. ASME)*, 34, 725–734

[19] Bertholf L.D., Karnes C.H., 1969, Axisymmetric elastic-plastic wave propagation in 6061-T6 Aluminum bars of finite length, *J. Appl. Mech. (Trans. ASME)*, 36, 533–541

[20] Bhattacharyya, S.K., Vendhan, C.P., 1991, Wave propagation in semi-infinite plane anisotropic thin circular shells, *J. Sound Vib.*, 149, 71–82

[21] Binkowski J.F., 1975, *Analysis of a dynamic Saint-Venant region in a semi-infinite circular cylinder*, Ph.D. Thesis, Michigan State Univ., East Lansing

[22] Boley B.A., 1955, Application of Saint-Venant's principle in dynamical problems, *J. Appl. Mech. (Trans. ASME)*, 22, 204–206

[23] Boley B.A., 1958, Some observations on Saint-Venant's principle, in *Proc. of the third U.S. national congress of Applied Mechanics*, ASME, 259–64

[24] Boley B.A., 1960a, On a dynamical Saint Venant principle, *J. Appl. Mech. (Trans. ASME)*, 27, 74–78

[25] Boley B.A., 1960b, Upper bounds and Saint Venant's principle in transient heat conduction, *Quart. Appl. Math.*, 18, 205–207

[26] Boley B.A., 2006, Private communication

[27] Borg S.F., 1961, On Saint-Venant's principle under dynamic conditions; Discussion, *Experimental Mechanics*, 1(9), 119–120
[28] Borrelli A., Patria M.C., 1995, Energy bounds for mixture of two linear elastic solids occupying a semi-infinite cylinder, *Acta Mech.*, 109, 191–206
[29] Borrelli A., Patria M.C., 1996, Energy bounds in dynamical problems for a semi-infinite magnetoelastic beam, *ZAMP*, 47, 880–893
[30] Borrelli A., Patria M.C., 2000, Spatial decay estimates in dynamical problems for a semi-infinite piezoelectric beam, *IMA J. Appl. Math.*, 64, 73–93
[31] Budaev B.V., Morozov N.F., Narbut M.A., 1994, Torsion of a circular cone with static and dynamic loading, *J. Appl. Maths Mechs*, 58(6), 1097–1100
[32] Budaev B.V., Morozov N.F., Narbut M.A., 1996, Saint Venant's principle in statical and dynamical problems for an elastic wedge and a cone, *Mathematische Nachrichten*, 177, 31–39
[33] Chamberlain P.G., 2004, The effect of evanescent wave modes on scattering and near-trapping, *IMA Journal of Applied Mathematics* 69, 205–218
[34] Chen W.Q., Lv C.F., Bian Z.G., 2003, Elasticity solution for free vibration of laminated beams, *Composite Structures* 62, 75–82
[35] Cherepanov G.P., 1979, *Mechanics of Brittle Fracture*, McGRAW-Hill International Book Company
[36] Cherukuri H. P., Shawki T. G., 1996, A finite-difference scheme for elastic wave propagation in a circular disk, *J. Acoust. Soc. Am.* 100(4), 2139–2155
[37] Chirita S., 1995, On the spatial decay estimates in certain time-dependent problems of continuum mechanics, *Arch. Mech.*, 47, 755–771
[38] Chirita S., 1997, On Saint-Venant's principle in dynamic linear viscoelasticity, *Q. Appl. Math.*, LV, 139–149
[39] Chirita S., Ciarletta M., 1999, Time-weighted surface power function method for the study of spatial behaviour in dynamics of continua, *Eur. J. Mech. A/Solids*, 18, 915–933
[40] Chirita S., Ciarletta M., 2003, Some further growth and decay results in linear thermoelastodynamics, *Journal of Thermal Stresses*, 26, 889–903
[41] Chirita S., Ciarletta M., 2008, Spatial evolution of harmonic vibrations in linear elasticity, *Journal of Mechanics of Materials and Structures*, 3(9), 1675–1693
[42] Chirita S., Nappa L., 1999, Effects of Saint-Venant type and uniqueness and continuous dependence results for incremental elastodynamics, *Int. J. Non-Linear. Mech.*, 34, 159–167

[43] Chirita S., Quintanilla R., 1996a, Spatial decay estimates of Saint-Venant type in generalized thermoelasticity, *Int. J. Engng. Sci.*, 34, 299–311

[44] Chirita S., Quintanilla R., 1996b, On Saint-Venant's principle in linear elastodynamics, *J. Elasticity*, 42, 201–215

[45] Ciarletta M., 2002, On the spatial behaviour of the transient and steady-state solutions in thin plates with transverse shear deformation, *International Journal of Engineering Science* 40, 485–498

[46] Ciarletta M., Chirita S., 1999, Thermodynamic restrictions, free energies and Saint-Venant's principle in the linear theory of viscoelastic materials with voids, *Int. J. Solids Srtuct.* 36, 1949–1964

[47] Ciarletta M., Iovane G., Passarella F., 2002, On the spatial and temporal behavior in dynamics of porous elastic mixtures, *Ukrainian Mathematical Journal* 54(4) 647–670

[48] Choi I., Horgan C.O., 1977, Saint-Venant principle and end effects in anisotropic elasticity, *J. Appl. Mech. (Trans. ASME)*, 44, 424–430

[49] Choi I., Horgan C.O., 1978, Saint-Venant end effects for deformation of sandwich strips, *Int. J. Solids. Struct.*, 14, 187–95

[50] Clausing D.P., 1959, Impact of cylinders of different areas. In *Proc. 4th Midwestern Conference on Solid Mechanics*, Austin, Texas, 349–357

[51] Cunningham D.M., Goldsmith W., 1959, Short-time impulse produced by longitudinal impact, *Proc. Soc. Exp. Stress Anal.* XVI (2), 153–162

[52] D'Apice C., 2005, Convexity considerations and spatial behavior for the harmonic vibrations in thermoelastic plates, *J. Math. Anal. Appl.*, 312(1) 44–60

[53] Dally J.E., Rilet W.F., Durelli A.J., 1959, A photoelastic approach to transient stress problems employing low-modulus materials, *J. Appl. Mech. (Trans. ASME)*, 26, 613–620

[54] Davies R.M., 1948, A critical study of the Hopkinson pressure bar. *Philosophical Transactions of the Royal Society of London A*, 240, 375–457

[55] Davies R.M., 1956, Stress waves in solids, *Brit. J. Appl. Phys.*, 7, 203–209

[56] De Cicco S., Nappa L., 1999, On Saint-Venant's principle for micropolar viscoelastic bodies, *Int. Journal of Engineering Science* 37, 883–893

[57] DeVault G.P., Curtis C.W., 1962, Elastic cylinder with free lateral surface and mixed time-dependent end conditions. *J. Acoust. Soc. Am.*, 34(4), 421–432

[58] Diligent O., Lowe M.J.S., Le Clezio E., Castaings M., Hosten B., 2003, Prediction and measurement of nonpropagating Lamb modes at the free end of a plate when the fundamental antisymmetric mode A[0] is incident, *J. Acoust. Soc. Am.*, 113, 3032–3042

[59] Dong S.B., Goetschel D.B., 1982, Edge effects in laminated composite plates, *J. Appl. Mech. (Trans. ASME)*, 49, 129–135
[60] Dong S.B., Huang K.H., 1985, Edge vibrations in laminated composite plates, *J. Appl. Mech. (Trans. ASME)*, 52, 433–438
[61] Donnell L.H., 1962, About Saint-Venant's principle, *J. Appl. Mech. (Trans. ASME)*, 29, 753
[62] Durban D., Stronge W.S., 1988a, Diffusion of self-equilibrating end loads in plane strain plasticity, *J. Mech. Phys. Solids*, 36, 459–476
[63] Durban D., Stronge W.J., 1988b, Diffusion of self-equilibrating end loads in elastic solids, *J. Appl. Mech. (Trans. ASME)*, 55, 492–495
[64] Duva J.M. and Simmonds J.G., 1991, The usefulness of elementary theory of the linear vibrations of layered, orthotropic elastic beams and corrections due to two-dimensional end effects, *J. Appl. Mech. (Trans. ASME)*, 58, 175–180
[65] Duva J.M. and Simmonds J.G., 1992, The influence of two-dimensional end effects on the natural frequencies of cantilevered beams weak in shear, *J. Appl. Mech. (Trans. ASME)*, 59, 230–232
[66] Ericksen J.L., 1979, On St.-Venant's problem for thin-walled tubes, *Arch. Rational Mech. Anal.* 70, 7–12
[67] Evans D.V., 1992, Trapped acoustic modes, *IMA Journal of Applied Mathematics*, 49, 45–60
[68] Evans D.V., Porter R., 2008, Flexural waves on a pinned semi-infinite thin elastic plate, *Wave Motion* 45, 745–757
[69] Field J.E., Proud W.G., Walley S.M., Goldrein H.T., 2001, Review of experimental techniques for high rate deformation and shock studies, In: *New Experimental Methods in Material Dynamics and Impact.* Eds. W.K. Nowacki and J.R. Klepaczko, pp. 109-177, Institute of Fundamental Technological Research, Warsaw, Poland
[70] Flavin J.N., Knops R.J., 1987, Some spatial decay estimates in continuum dynamics, *J. Elasticity*, 17, 249–64
[71] Flavin J.N., Knops R.J., Payne L.E., 1990, Energy bounds in dynamical problems for a semi-infinite elastic beam, in *Elasticity. Mathematical Methods and Applications.* The Ian N. Sneddon 70th Birthday volume. Eason G and Ogden R.W. Eds., Ellis Horwood, 101–112
[72] Flynn P.D., Feder J.C., Gilbert J.T., Roll A.A., 1962. Stress waves due to explosive and mechanical loading of low modulus photoelastic materials, Frankford Arsenal Report No. A 62–4
[73] Flynn P.D., Frocht M.M., 1961. On Saint-Venant's principle under dynamic conditions. *Experimental Mechanics* 1, 16–20
[74] Folk R., Fox G., Shook C.A., Curtis C.W., 1958, Elastic strain produced by sudden application of pressure to one end of a Cylindrical bar. I. Theory, *J. Acoust. Soc. Am.*, 30(6), 552–58

[75] Follansbee P.S., 1985, The Hopkinson bar, *Mechanical Testing*, Vol. 8, ASM Handbook, American Society for Metals, 198–203
[76] Foster D.J., 2003, *On Saint-Venant's principle in the dynamics of elastic beams*, Ph.D dissertation, Wayne State University
[77] Foster D.J., Berdichevsky V., 2000, Probabilistic characterization of dynamical Saint-Venant effects, *8th ASCE Specialty Conferebceon on Probabilistic Mechanics and Structural Reliability*, PMC 2000-134
[78] Foster D.J., Berdichevsky V., 2004, On Saint-Venant's principle in the two-dimensional flexural vibrations of elastic beams, *Int. J. Solids Struct.*, 41, 2551–2562
[79] Fox G., Curtis C.W., 1958, Elastic strain produced by sudden application of pressure to one end of a cylindrical bar. II. Experimental observations. *The Journal of the Acoustical Society of America* 30(6), 559–563
[80] Frocht M.M., 1948, *Photoelasticity*, Vol. II, John Wiley and Sons, Inc. London
[81] Gales C., 2002, On the spatial behavior in the theory of swelling porous elastic soils, *International Journal of Solids and Structures* 39, 4151–4165
[82] Gales C., 2003, Spatial decay estimates for solutions describing harmonic vibrations in the theory of swelling porous elastic soils, *Acta Mechanica* 161, 151–163
[83] Gilat A., Schmidt T.E., Walker A.L., 2009. Full field strain measurement in compression and tensile split Hopkinson bar experiments. *Experimental Mechanics* 49, 291–306
[84] Goetschel D.B., Hu T.H., 1985, Quantification of Saint-Venant's principle for a general prismatic member, *Comp. Struct.*, 21, 869–874
[85] Gomilko A.M., Gorodetskaya N.S., Meleshko V.V., 1995, A dynamic Saint-Venant principle for an elastic semi-infinite strip, *Journal of a Mathematical Sciences*, 74(4), 1150–1153
[86] Gorham R.A., Ripperger E.A., 1959, A comparison of surface strains to average strains in longitudinal elastic wave propagation. In: *Proc. 4th Midwestern Conference on Solid Mechanics*, Austin, Texas, pp. 382–395
[87] Graff K.F., 1975, *Wave motion in elastic solids*, Clarendon Pr., Oxford
[88] Grandin H.T. Jr., 1972, *Investigation of a dynamic Saint-Venant region in a semi-infinite strip*, Ph.D. Thesis, Michigan State University
[89] Grandin H.T., Little R.W., 1974, Dynamic Saint-Venant's region in a semi-infinite elastic strip, *J. Elasticity*, 4, 131–46
[90] Gray III G.T., 2000, Classic Split-Hopkinson pressure bar testing, *Mechanical Testing*, Vol. 8, ASM Handbook, American Society for Metals, pp. 462–476

[91] Gurtin M.E., 1972, The linear theory of elasticity, *Mechanics of solids II*, Vol. VIa/2, in *HNBK der Phys.*, S. Flugge ed., Springer-Verlag, New-York
[92] Habberstad J.L., Hoge K.G., Foster J.E., 1972, An experimental and numerical study of elastic strain waves on the center line of a 6061-T6 Aluminum bar. *J. Appl. Mech. (Trans. ASME)*, 39, 367–371
[93] Hertelendy P., 1968, An approximate theory governing symmetric motions of elastic rods of rectangular or square cross section, *J. Appl. Mech. (Trans. ASME)* 35, 333–341
[94] Hettche L.R., Au T., 1967, Edge impact of an elastic-plastic semi-infinite plate, *Experimental Mechanics*, 7, 302–308
[95] Hoff N.J., 1945, The applicability of Saint-Venant's principle to airplane structures, *Journal of the Aeronautical Sciences*, 12, 455–460
[96] Horgan C.O., 1989, Recent developments concerning Saint-Venant's principle: An update, *Appl. Mech. Rev.*, 42, 295–303
[97] Horgan C.O., 1996, Recent developments concerning Saint-Venant's principle: A second update, *Appl. Mech. Rev.*, 48, 101–111
[98] Horgan C.O., Knowles J.K., 1983, Recent developments concerning Saint-Venant's principle, *Adv. Appl. Mech.*, 23, 179–269
[99] Horgan C.O., Simmonds J.G., 1994, Saint-Venant's end effects in composite structures, *Comp. Engng.*, 4, 279–286
[100] Horgan C.O., Quintanilla R., 2001, Spatial decay of transient end effects in functionally graded heat conducting materials, *Q. Appl. Math.*, LIX, 529–542
[101] Horgan C.O., Wheeler L.T., 1975, A spatial decay estimate for pseudoparabolic equations. *Letters in Applied and Engineering Sciences* 3, 237–243
[102] Hornikx M., Forssen J., 2009, Noise abatement schemes for shielded canyons, *Applied Acoustics* 70, 267–283
[103] Horvay G., 1953, The end problem of rectangular strips, *J. Appl. Mech. (Trans. ASME)*, 20, 87–94
[104] Horvay G., 1957, Saint-Venant's principle: a biharmonic eigenvalue problem, *J. Appl. Mech. (Trans. ASME)*, 24, 381–386
[105] Huang C.G., 1989, Several rigorous counterexamples about Saint-Venant's principle, *Computers Math. Appl.* 18(8), 729–738
[106] Huang K.H., Dong S. B., 1984, Propagating waves and edge vibrations in anisotropic composite cylinders, *J. Sound and Vibration*, 96, 363–379
[107] Iesan D., Scalia A., 1997, On Saint-Venant's principle for microstretch elastic bodies, *Int. J. Engng Sci.* 35(14), 1277–1290
[108] Ignaczak J., 1974, A dynamic version of Saint-Venant's principle in the linear theory of elasticity, *Academie Polonaise des Sciences, Bulletin, Serie des Sciences Techniques* 22(6) 483–489, (313–319)

[109] Ignaczak J., 2002, Saint-Venant's principle for a microperiodic composite thermoelastic semispace: the dynamical refined average theory. *J. Therm. Stresses*, 25, 1065–1079

[110] Iovane G., Passarella F., 2004, Saint-Venant's principle in dynamic porous thermoelastic media with memory for heat flux, *Journal of Thermal Stresses*, 27, 983–999

[111] Jones O.E., Norwood F.R., 1967, Axially symmetric cross-sectional strain and stress distributions in suddenly loaded cylindrical elastic bars, *J. Appl. Mech. (Trans. ASME)*, 34, 718–724

[112] Kaplunov J., Fu Y.B., 2012, Analysis of localized edge vibrations of cylindrical shells using the Stroh formalism, *Mathematics and Mechanics of Solids*, 17(1), 59–66

[113] Kaplunov J., Lawrie J.B., 2012, Edge waves and resonance on elastic structures: An overview, *Mathematics and Mechanics of Solids*, 17(1), 4–16

[114] Kaplunov J.D., Sorokin S.V., 1995, A simple example of a trapped mode in an unbounded waveguide, *The Journal of the Acoustical Society of America* 97(6), 3898–3899

[115] Karal F., Alterman Z., 1971, Far-field dependence on the end conditions in a semi-infinite elastic rod of circular cross-section, *J. Sound and Vibration*, 17, 5–11

[116] Karp, B., 1996. *On Saint-Venant's principle in Elastostatics and Elastodynamics*, D.Sc. Thesis, Technion, Haifa. (Full text in Hebrew, Abstract in English)

[117] Karp B., 2004, End effects in prestrained plates under compression, *Journal of Applied Mechanics* 71, 816–824

[118] Karp B., 2005, Dynamic version of Saint-Venant's principle - Historical account and recent results. *Nonlinear Analysis*, 63, e931–e942

[119] Karp B., 2008, Generation of symmetric Lamb waves by non-uniform excitations, *Journal of Sound and Vibration*, 312 (1-2), 195–209

[120] Karp B., 2009, Dynamic equivalence, self-equilibrated excitation and Saint-Venant's principle for an elastic strip. *Int. J. Solids Struct.* 46, 3068–3077

[121] Karp B., 2011, Study of dynamic end effects in an elastic strip with sliding boundary conditions, *Int. J. Solids Struct.* 48, 126–136

[122] Karp B. and Durban D., 1997, Towards a dynamic version of Saint-Venant's principle, In *Modern practice in stress and vibration analysis*, Gilchrist M.D. Ed., A.A. Balkema, ISBN 90 5410 896 7. 3rd international conference, Dublin, Ireland, 3-5 September 1997

[123] Karp, B., Durban, D., 2002. Influence of Boundary Conditions on Decay Rates in a Prestrained Plate. *J. Appl. Mech. - Trans of ASME* 69, 515–520

[124] Karp B., Durban D., 2005, Evanescent and Propagating Waves in Prestretched Hyperelastic Plates, *Int. J. Solids Struct.*, 42, 1613–1647

[125] Karp B., Durban D., 2011, Saint-Venant's Principle in dynamics of structures - A Review. *Applied Mechanics Reviews.* 64, 020801:1-20

[126] Karp B., Rittel D., Durban D., 2008, Health monitoring of joints using dynamic end effects, *Journal of Sound and Vibration*, 312 (1-2), 257–272

[127] Karp B., Dorogoy A., Wang Z., 2009, Non-uniform impact excitation of a cylindrical bar, *Journal of Sound and Vibration* 323, 757–771

[128] Karunasena W., Liew K.M., Kitipornchai S., 1995, Reflection of plate waves at the fixed edge of a composite plate, *J. Acoust. Soc. Am.*, 98, 644–651

[129] Kathnelson A.N., 1997, An asymptotic edge effect in thin rectangular vibrating plates, *Journal of Sound and Vibration* 207(2), 271–275

[130] Kaul R.K., McCoy J.J., 1964, Propagation of axisymmetric waves in a circular semiinfinite elastic rod. *Acoust. Soc. of Am.* 26(4), 653–660

[131] Kawata K., Hashimoto S., 1967. On some differences between dynamic- and static-stress distributions. *Experimental Mechanics* 7, 91–96

[132] Kawata K., Hashimoto S., Masuda Y., Hayasi R., 2007. High-speed photoelastic analysis of axially-impacted finite column. *Experimental Mechanics* 47, 465–471

[133] Kennedy L.W., Jones O.E., 1969, Longitudinal wave propagation in a circular bar loaded suddenly by a radially distributed end stress, *J. Appl. Mech. (Trans. ASME)*, 36, 470–8

[134] Kim J.S., Soedel W., 1988. On the response of three-dimensional elastic bodies to disturbed dynamic pressures, Part I: Half-space, *J. Sound and Vibrations*, 126, 279–295

[135] Kim Y.Y., Steele C.R., 1989. End effects and time-harmonic longitudinal wave propagation in semi-infinite solid cylinder. *J. Appl. Mech. (Trans. ASME)*, 56, 334–346

[136] Knops R.J., 1989, Spatial decay estimates in the vibrating anisotropic elastic beam, in *Waves and stability in continuous media*, ed. Rionero S., Series on Advances in Mathematics for Applied Sciences - Vol. 4, World Scientific, pp. 192–203

[137] Knops R.J., Payne L.E., 2005, Alternative spatial growth and decay for constrained motion in an elastic cylinder. *Mathematics and Mechanics of Solids* 10, 281–310

[138] Knops R.J., Rionero S., Payne L.E., 1990, Saint-Venant's principle on unbounded regions. *Proceedings of the Royal Society of Edinburgh* 115A, 319–336

[139] Knowles J.K., 1966, On Saint-Venant's principle in linear theory of elasticity, *Arch. Ratio. Mech. Anal.*, 21, 1–22

[140] Kroll R.J., Tatro C.A., 1964, Stress-wave propagation in axially symmetric test specimen, *Experimental Mechanics*, 4(5), 129–134

[141] Kundu T., Mathur R.P., Desai C.S., 1991, Three dimensional soil-structure interaction analysis: Deformable structures in multilayered soil mass. *Engineering Computations* 8, 153–180

[142] Kuznetsov G.N., Stepanov A. N., 2007, The Field of an equivalent multipole composite radiator in a waveguide, *Acoustical Physics*, 53(3), 326–334

[143] Levine H.A., Quintanilla R., 1989, Some remarks on Saint-Venant's principle. *Math. Methods in the Applied Sciences* 11, 71–77

[144] Love A.E.H., 1944, *A Treatise on the mathematical theory of elasticity*, Dover Pub. New York

[145] Ma G.W., He L., Karp B., Li Q.M., Investigation of Dynamic Saint-Venant's Principle in a Cylindrical Waveguide Part I: Experimental and numerical approaches. In preperation

[146] Maremonti P. Russo R., 1989, A domain of influence theorem in finite elasticity, in *Waves and stability in continuous media*, ed. Rionero S., Series on Advances in Mathematics for Applied Sciences - Vol. 4, World Scientific. pp. 237–242

[147] Markenscoff X., 1994, Some remarks on the wedge paradox and Saint-Venant's principle, *J. Appl. Mech. (Trans. ASME)*, 61, 519–523

[148] McCoy J.J., 1964, Propagation of Torsional Waves in a Circular Elastic Rod, *ZAMP*, 15, 456–465

[149] McIver M., Linton C.M., Zhang J., 2002, The branch structure of embedded trapped modes in two-dimensional waveguides, *Q. J. Mech Appl. Math.* 55(2), 313–326

[150] Mei C., 2005, Effect of material coupling on wave vibration of composite Euler-Bernoulli beam structures, *Journal of Sound and Vibration* 288, 177–193

[151] Meitzler A.H., 1955, *Propagation of elastic pulses near the stressed end of a cylindrical bar*, Dissertation, Lehigh University

[152] Meng H., Li Q.M., 2001, Modification of SHPB set-up based on wave separation technique and dynamic Saint-Venant's principle, Second International Conference on Experimental Mechanics, F. S. Chau, and C. Quan Eds., *Proceedings of the SPIE - The international Society for Optical Engineering*, 4317, 85–93

[153] Meng H., Li Q.M., 2003, An SHPB set-up with reduced time-shift and pressure bar length, *Int. J. Impact Eng.*, 28, 677–696

[154] Meyer M.L., 1964. On spherical near fields and far fields in elastic and visco-elastic solids. *Journal of Mechanics and Physics of Solids* 12, 77–111

[155] Miklowitz J., 1957, The propagation of compressional waves in a dispersive elastic rod; Part I - Results from the theory, *J. Appl. Mech.*, 24, 231–239

[156] Miklowitz J., 1978, *The Theory of Elastic Waves and Waveguides*, North-Holand Pub. Comp., Amsterdam

[157] Miklowitz J., Nisewanger C.R., 1957, The propagation of compressional waves in a dispersive elastic rod; Part II - Experimental results and comparison with theory, *J.Appl.Mech.*, 24 (1957), 240–244

[158] Miles A.W., 1976, Shock-front loading method for studies in dynamic photoelasticity, *Exp.Mech.*, 11, 349–355

[159] Mindlin R.D., 1960. Waves and vibrations in isotropic, elastic plates. In: *Structural Mechanics*, Ed. Goodier J.N. and Hoff N.J., Pergamon, New York

[160] Miyao S., Tsuchida E., Matsumoto H., Nakahara I., 1975, A semi-infinite body subjected to an impulsive torque on a hemispherical pit of a free surface. *Bulletin of the JSME*, 18 (123), 959–964

[161] Morozov N.F., Narbut M.A., 1995, Antiplane deformation of an elastic wedge under action concentrated near the corner point, *J Appl Maths Mechs*, 59(2), 307–309

[162] Munoz Rivera J.E., Lapa E.C., Barreto R., 1996, Decay rates for viscoelastic plates with memory, *Journal of Elasticity*, 44, 61–87

[163] Murray J.D., 1970, Perturbation effects on the decay of discontinuous solutions of nonlinear first order wave equations, *SIAM J. Appl. Math.*, 19(2), 273–298

[164] Naghdi P.M., 1960, On Saint Venant's principle: elastic shells and plates, *J. Appl. Mech. (Trans. ASME)*, 27, 417–422

[165] Nappa L., 1998, Spatial decay estimates for the evolution equations of linear thermoelasticity without energy dissipation, *J. Therm. Stresses*, 21, 581–592

[166] Nerubailo B. V., Zotova N. V., Orlov R. Kh., Sukhorukova S. V., 2005, The applicability of Saint-Venant's principle to monocoque structures, *Journal of Engineering Physics and Thermophysics*, 78(3), 586–589

[167] Novozhilov V.V., Slepian L.I., 1965, On Saint-Venant's principle in the dynamics of beams, *PMM*, 29, 261–81

[168] Oleinik O.A., Iosif'yan G.A., 1976, An analogue of Saint-Venant's principle and the uniquiness of solutions of boundary value problems for parabolic equations in unbounded domains. *Russian Math. Surveys* 31(6), 153–178

[169] Oleinik O.A., Iosif'yan G.A., 1978, The Saint-Venant principle in the two-dimensional theory of elasticity and boundary problems for a biharmonic equation in unbounded domains. *Siberian Mathematical Journal* 19(5), 813–822

[170] Orazov M.B., 1983, The Saint-Venant principle for equations of steady-state vibrations in an elastic semi-cylinder, Akademiia Nauk Turkmenskoi SSR, Izvestiia, Seriia Fiziko-Tekhnicheskikh, Khimicheskikh i Geologicheskikh Nauk , 5, 3-8. (In Russian)

[171] Pagneux V., 2006, Revisiting the edge resonance for Lamb waves in a semi-infinite plate, *J. Acoust. Soc. Am.*, 120(2), 649–656

[172] Pagneux V., 2012, Complex resonance and localized vibrations at the edge of a semi-infinite elastic cylinder, *Mathematics and Mechanics of Solids*, 17(1), 17–26

[173] Payne L.E., Song J.C., 1997, Spatial decay estimates for the Brinkman and Darcy flows in a semi-infinite cylinder. *Continuum Mechanics and Thermodynamics*, 9, 175–190

[174] Pichugin A.V., Rogerson G.A., 2012, Extensional edge waves in prestressed incompressible plates, *Mathematics and Mechanics of Solids*, 17(1), 27–42

[175] Pope P.H., Field J.E., 1984, Determination of strain in a dynamic compression test, *J. Phys. E: Sci. Instrum.*, 17, 817–820

[176] Quintanilla R., 1999, On the spatial behavior in thermoelasticity without energy dissipation, *J. Thermal Stresses*, 22, 213–224

[177] Quintanilla R., 2002, On the spatial decay for the dynamical problem of thermo-mictostretch elastic solids, *Int. J. Engng. Sci.*, 40, 109–121

[178] Rauch J., 1976, Qualitative behavior of dissipative wave equations on bounded domains, *Arch. Ratio. Mech. Anal.* 62, 77–85

[179] Ratassepp M., Klauson A., Chati F., Leon F., Maze G., 2008, Edge resonance in semi-infinite thick pipe: numerical predictions and measurements, *J. Acoust. Soc. Am.*, 124, 875–885

[180] Roseman J.J., 1976, Principle of Saint-Venant in linear and non-linear plane elasticity, *Arch. Rational Mech. Anal.* 26, 142–162

[181] Rosenhouse G., 2002. Physical aspects in active noise and vibration control. In: *Theoretical and Computational Acoustics.* Eds. Shang E.-C., Qihu Li, Gao T.F., World Scientific

[182] Ruan X, Danforth S.C., Safari A., Chou T-W., 2000, Saint-Venant end effects in piezoceramic materials, *International Journal of Solids and Structures* 37, 2625–2637

[183] Sasso M., Newaz G., Amodio D. , 2008, Material characterization at high strain rate by Hopkinson bar tests and finite element optimization, *Materials Science and Engineering A* 487, 289–300

[184] de Saint-Venant A.-J.-C.B., 1856, Memoire sur la Flexion des Prismes, *J. de Mathematiques Pures et Appliquees* (Liouville), Deuxieme Serie, Tome I., 89–189

[185] Scalia A., 2001, Spatial and temporal behavior in elastic materials with voids, *Acta Mechanica* 151, 47–60

[186] Sigillito V.G., 1970, On the spatial decay solutions of parabolic equations, *ZAMP*, 21, 1078–1081

[187] Sinclair G.B., Miklowitz J., 1975, Two nonmixed symmetric end-loadings of an elastic waveguide, *Int. J. Solids Struct.*, 11, 275–294

[188] Stephen N.G., 2008, On state-space elastostatics within a plane stress sectorial domain - the wedge and the curved beam, *International Journal of Solids and Structures* 45(20), 5437–5463

[189] Sternberg E., 1954, On Saint-Venant's principle, *Quart. of Applied Math.* XI(4), 393–402

[190] Theocaris P.S., 1959. The stress distribution in a semi-infinite strip subjected to a concentrated load. *ASME Journal of the Applied Mechanics* 26, 401–406

[191] Tibullo V., Vaccaro M., 2008, Spatial behaviour for constrained motion of a cylinder made of a strongly elliptic anisotropic material, *Journal of Mechanics of Materials and Structures*, 3(5), 983–993

[192] Timoshenko S.P., Goodier J.N., 1972, *Theory of Elasticity*, 3rd Ed., McGraw Hill Int.

[193] Torvik P.J., 1967, Reflection of wave trains in semi-infinite plates, *J. Acoust. Soc. Am.*, 41, 346–53

[194] Toupin R.A, 1965a, Saint-Venant's principle, *Arch. Rational Mech. Anal.*, 18, 83–96

[195] Toupin R.A, 1965b, Saint-Venant and a matter of principle, *Transactions of The New York Academy of Sciences* 28(2), 221–232

[196] Tyas A., Watson A.J., 2000, A study of the effect of spatial variation of load in the pressure bar, *Meas. Sci. Technol.*, 11, 1539–1551

[197] von-Mises R., 1945, On Saint-Venant's principle, *Bull. Amer. Math. Soc.*, 51, 555–562

[198] Waldman S.D., Lee J., 2002, Boundary conditions during bi-axial testing of planar connective tissues. Part 1: Dynamic behavior. *Journal of Material Sciences: Material in Medicine*, 13, 933–938

[199] Walley S.M., Mason T.A., 2000, *Waves in rods*, Presented at a website of DYMAT 2000

[200] Wang, C., Kim, J., 1997. The dynamic analysis of a thin beam impacting against a stop of general three-dimensional geometry, *J. Sound and Vibrations*, 203, 237–249

[201] Wijeyewickrema A.C., Ushida Y., Kayestha P., 2008, Wave propagation in a prestressed compressible elastic layer with constrained boundaries, *Journal of Mechanics of Materials and Structures*, 3(10), 1963–1976

[202] Yeung Wey Kong Y.C.T., Parsons B., Cole B.N., 1974, The dispersive behaviour of a Hopkinson pressure bar in material property test. pp. 33–47. In: *Mechanical Properties at High Rates of Strain*, Proceedings of the Conference on Mechanical Properties of Metals at High Rates of Strain, Oxford, 2–4 April. The Institute of Physics, London and Bristol

[203] Yilmaz Y., 2007, Spatial estimates for a system of coupled parabolic-hyperbolic equations under nonlinear boundary condition. *Journal of the Franklin Institute* 344, 489–494

[204] Zakharov D.D., 2012, Surface and edge waves in solids with nematic coating, *Mathematics and Mechanics of Solids*, 17(1), 67–80

[205] Zemanek J. Jr., 1971, Beam behavior within the nearfield of a vibrating, *J. Acoust. Soc. Am.*, 49, 181–191

[206] Zemanek J. Jr., 1972, An experimental and theoretical investigation of elastic wave propagation in a cylinder, *J. Acoust. Soc. Am.*, 51, 265–283

[207] Ziv M., 2002, Source signature and elastic waves in half-space under a sustainable line-concentrated impulsive normal force, *Int. J. Numer. Anal. Meth. Geomech.*, 26, 373–406

[208] Ziv M., 2003, Source signature and elastic waves in half-space under a momentary shear line impulse, *Int. J. Numer. Anal. Meth. Geomech.*, 27, 233–258

Trapped Modes and Edge Resonances in Acoustics and Elasticity

Vincent Pagneux
Laboratoire d'Acoustique de l'Université du Maine, LAUM UMR CNRS 6613, Le Mans, France

Abstract This chapter considers localized modes for acoustic and elastic waves. We first discuss trapped modes for acoustic scalar waves that are perfectly localized solutions near defects in waveguides with a real resonance frequency. Emphasis is given on the trapping mechanism coming from the evanescent nature of transverse modes in waveguides. We then study the case of quasi-trapped modes where the wave is strongly localized but can radiate energy. Complex resonance frequencies are shown to appear through approximate models and general principles. Eventually, we focus on elastic wave localization near traction free edges in plates and rods. The complicated polarization of the wave in elasticity is shown to increase the ability for trapping with very simple geometries.

1 Introduction

Modes are solutions of the wave equation without sources. They provide a very powerful tool to understand the response of wave systems when excited by a source because they represent an intrinsic basis corresponding to various kind of resonances. When the frequency is close to a resonance frequency the solution is dominantly given by the corresponding mode. The more often, modes are defined for closed cavity where the boundaries are able to quantify the frequencies. Here, we are concerned with trapped modes and localized solutions that exist for open geometry with confinement in at least one direction. These waveguide structures support evanescent waves that facilitate the trapping. Trapped modes were introduced more than fifty years ago (see for instance Jones (1953)) and since then have induced an important amount of works (Callan et al., 1991; Evans et al., 1994; Kaplunov and Sorokin, 1995; Granot, 2002; Bonnet-BenDhia and Mercier, 2007). Recent comprehensive reviews can be found in Linton and McIver (2007) and Postnova and Craster (2008).

R. Craster, J. Kaplunov (Eds.), *Dynamic Localization Phenomena in Elasticity, Acoustics and Electromagnetism*, CISM International Centre for Mechanical Sciences,
DOI 10.1007/978-3-7091-1619-7_5,

In these notes, in section 2, a reminder on the usual modes in a closed cavity is presented, followed by a brief introduction to trapped modes in open geometries. Section 3 is dedicated to trapped modes for scalar waves. The basic mechanism of trapping is illustrated with the simple model of the potential well. Then, the case of waveguides with Dirichlet boundary conditions is dealt with. Acoustic waveguides with Neumann boundary conditions give a more subtle situation where trapping occurs owing to symmetries that allow to localize the solution. Waves localized but radiating energy are discussed in section 4. A simple model permits to introduce the complex resonance frequencies corresponding to these quasi-trapped modes and basic analytical properties in the complex frequency plane are presented. In section 5, we look at elastic waveguides and their particularity. It is shown that the vectorial nature of the elastic waves, with longitudinal and transversal polarizations, offers the ability to trap the solution near traction free edge, either in plates or in rods.

2 Different kinds of modes

In the first four sections of these notes we will consider scalar waves. In the harmonic regime, with the time dependence chosen as $e^{-i\omega t}$, they are governed the Helmholtz equation

$$\triangle\phi + k^2\phi = 0, \tag{1}$$

where $k = \omega/c$. If c does not depend on ω the scalar wave is dispersionless: typically it corresponds to acoustic waves (Morse and Ingard, 1968). If $dc/d\omega \neq 0$ the wave is dispersive as is the case for instance for water waves (Cobelli et al., 2011). The Helmholtz equation (1) has to be supplemented by boundary conditions. The more often[1] they are of the Dirichlet or Neumann type: $\phi = 0$ at the wall for Dirichlet and $\partial_n\phi = 0$ for Neumann. Depending on the physical problem, Dirichlet or Neumann boundary conditions (BC) are applied as summarized below:

- Acoustics (Neumann BC at hard wall)
- Electromagnetism 2D (Neumann or Dirichlet BC for perfect metal)
- Elasticity with SH polarization (Neumann BC for stress free interface)
- Quantum mechanics (Dirichlet BC at hard wall)
- Water waves (Neumann BC at vertical hard wall)

In all these cases we have to deal with a scalar wave represented by a single scalar function ϕ. In the following, a heuristic introduction to the notion

[1] Note that mixed boundary conditions exist also: they correspond to a local impedance or a local admittance.

of modes for the usual case of a closed cavity and the unusual case of open geometry is given.

2.1 Modes in cavity (usual)

The usual modes are solutions of the homogeneous Helmholtz equation (1) in a closed cavity. Figure 1 displays the example of a mode in an acoustic cavity with hard wall. The wave cannot escape the cavity and the boundary conditions are able to select a particular set of discrete frequencies k_n and eigenmodes ϕ_n that satisfy

$$\triangle\phi_n + k_n^2\phi_n = 0, \tag{2}$$

with $\partial_n\phi_n = 0$ on the boundary, and where n is the index of the mode. The

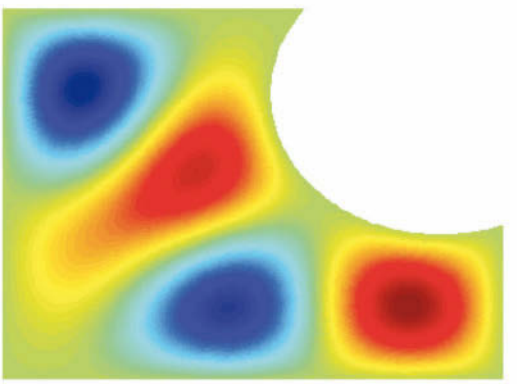

Figure 1. A mode in an acoustic cavity.

set of modes ϕ_n provides an orthonormal basis[2] with the property:

$$(\phi_m|\phi_n) = \delta_{nm}, \tag{3}$$

where the scalar product is defined as $(\phi|\psi) = \int \overline{\phi(\boldsymbol{x})}\psi(\boldsymbol{x})d\boldsymbol{x}$. The usefulness of the modes can now be illustrated when we want to solve the wave equation in the same cavity with a source s:

$$\triangle\phi + k^2\phi = s(\boldsymbol{x}). \tag{4}$$

[2]It comes from the self-adjointness of the problem, for details on the mathematical aspects see for instance Stakgold (1998).

The sought ϕ can be expanded on the mode basis as

$$\phi(\boldsymbol{x}) = \sum_n c_n \phi_n(\boldsymbol{x}). \tag{5}$$

Inserting this expansion in the wave equation and using the orthonormality (3), the coefficients c_n are found to be

$$c_n = \frac{(s|\phi_n)}{k^2 - k_n^2}. \tag{6}$$

When $k \simeq k_n$, the solution is dominantly given[3] by the mode ϕ_n. We see here the intrinsic character of the modes: they provide a set of functions independent of sources and they govern the wave with source when the imposed frequency is close to a resonance frequency.

2.2 Modes in open geometry (unusual)

We have seen that a closed cavity sustains an infinite of modes. In open geometry the wave has the ability to radiate towards infinity so that in general there is no homogeneous solution of the Helmholtz equation with finite energy. Nevertheless, for open geometry where the wave can be evanescent towards infinity, we will see that it is possible to obtain trapped mode. A

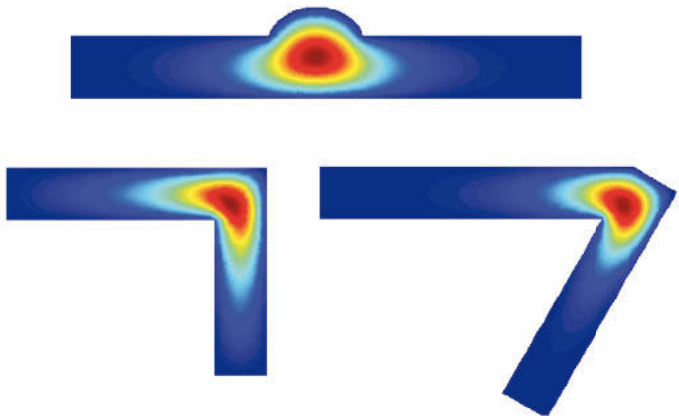

Figure 2. Trapped modes in three different waveguides with Dirichlet boundary conditions. (top) bump, (bottom) bends.

[3]Assuming that the projection of the source term $(s|\phi_n)$ is not zero.

trapped mode is defined as an homogeneous solution of the wave equation ($\triangle\phi + k^2\phi = 0$) with finite energy,

$$\int |\phi|^2 d\boldsymbol{x} \text{ finite.}$$

It is associated with a real resonance frequency k and the set of resonance frequencies of trapped modes for a given geometry is discrete. Waveguides are the typical geometries where trapped modes may exist because in such geometries the wave propagates towards infinity through a finite number of propagating transverse modes and an infinite number of evanescent waves. For instance, for waveguides with Dirichlet boundary conditions, there is a frequency threshold below which the wave is purely evanescent in the leads towards infinity. Below this threshold, the wave cannot escape from a defect in the waveguide and a trapped mode can be easily found. Figure 2

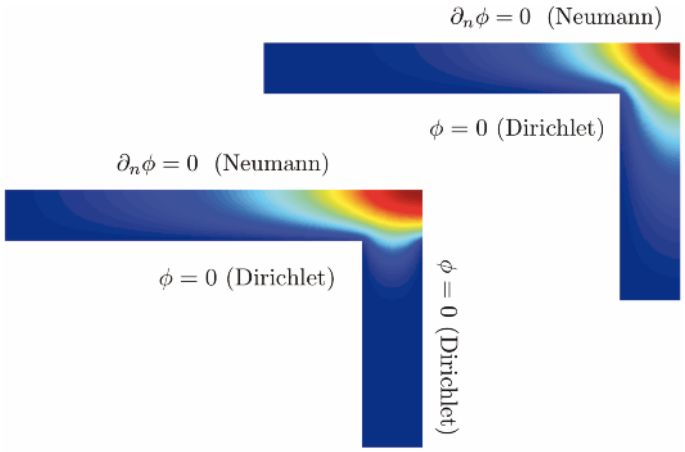

Figure 3. Trapped modes in bent waveguides with a mixing of Dirichlet and Neumann boundary conditions in the leads.

shows three examples of trapped mode for waveguides with Dirichlet boundary conditions[4]. Boundary conditions of different types can also support trapped modes. Figure 3 correspond to trapped modes in bent waveguides with a mixing of Dirichlet and Neumann boundary conditions. The trapping is still rather "easy" since a waveguide with Neumann BC on one side

[4]This situation is common in quantum mechanics where these modes are called bound states.

and Dirichlet BC on the other side still has a non-zero frequency threshold where the wave cannot propagate. The case of waveguides with Neumann boundary conditions (as in acoustics) needs a little more of subtlety. The plane is always propagating with no cut-on frequencies and the wave is able to radiate towards infinity even for low frequencies. Nevertheless, as will be described with more details in the next section, by using symmetry of the geometry it is possible to recover the same situation as for Dirichlet waveguides where the antisymmetric part of the wave is evanescent below a threshold frequency. Examples of trapped modes for symmetric acoustic waveguides are shown in Figure 4.

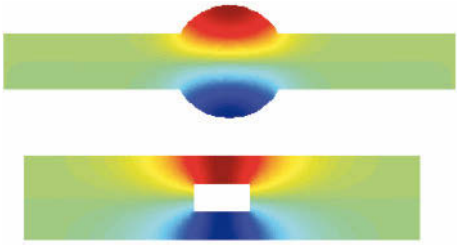

Figure 4. Trapped modes for symmetric waveguides with Neumann boundary conditions (acoustic case).

3 Trapped modes for scalar waves

Trapped modes can exist in waveguides, i.e. system confined in at least one direction, where evanescent waves are able to localize the energy around a defect. The basic mechanism of trapping is well described by the simple model of the potential well.

3.1 Trapping mechanism: the potential well

The potential well is illustrated in Figure 5. In this model, the wave is governed by the Schrodinger equation

$$\phi'' + (k^2 - V(x))\phi = 0, \tag{7}$$

where V is the potential (further details on the physical context can be found for instance in Landau and Lifshitz (1977)). For this model, V is constant ($V = V_0$) except in a the central region $|x| < a$ where it is zero (see Fig. 5). The equations inside the well and outside the well are respectively

$$|x| < a : \quad \phi'' + k^2\phi = 0 \tag{8}$$

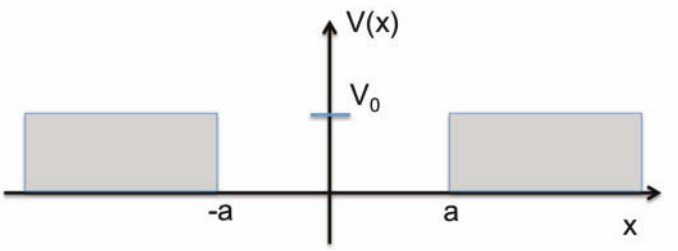

Figure 5. The potential well.

and

$$|x| > a : \quad \phi" + (k^2 - V_0)\phi = 0. \tag{9}$$

Inside the well, for $|x| < a$, the wave can always propagate, but the propagation of the wave outside the well, for $|x| > a$, is controlled by the sign of $k^2 - V_0$. If $k^2 < V_0$, the wave is evanescent and the it will be seen that a trapped mode exists.

Trapping case: $k^2 < V_0$**.** In this case, the wave is evanescent outside the well. A trapped mode is a solution of the homogeneous wave equation (7) with outgoing radiation condition outside the well. Benefiting from the symmetry of the problem with respect to $x = 0$, we are looking for a trapped mode even in x. Inside the well, $|x| < a$, the solution is

$$\phi = A \cos kx \tag{10}$$

and for $|x| > a$ the outgoing radiation condition selects a solution of the form

$$\phi = Be^{-\alpha|x|}. \tag{11}$$

The continuity of ϕ and ϕ' at $x = a$ yields an implicit equation on k:

$$k \tan ka = \alpha, \tag{12}$$

where $\alpha = \sqrt{V_0 - k^2}$. This implicit equation can solved graphically as shown in Figure 6. Whatever the value of V_0, it is obvious that it posses at least one solution k_R that corresponds to the resonance frequency of a trapped mode. When V_0 goes to zero, it is possible to obtain an approximate explicit resonance frequency:

$$k_R^2 \simeq V_0 - V_0^2 a^2.$$

It is typical of a trapped mode with a weak defect: the resonance frequency is asymptotically close to (and below) the threshold (or the cut-on frequency,

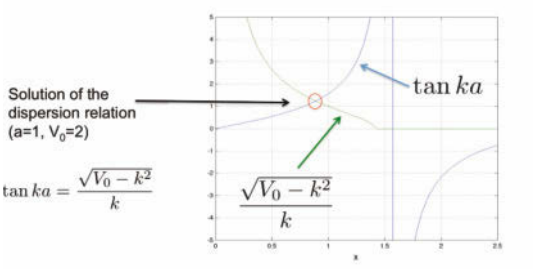

Figure 6. Resolution of the implicit equation of the trapped mode.

here represented by $\sqrt{V_0}$) where the wave becomes propagative. This kind of results are also found for trapped in waveguides with small defect (Nazarov, 2011). The shape of the trapped mode calculated for $a = 1$ and $V_0 = 2$ is shown in Figure 7. The corresponding resonance frequency solution of the implicit equation (12) is numerically found to be $k_R = 0.89$. The

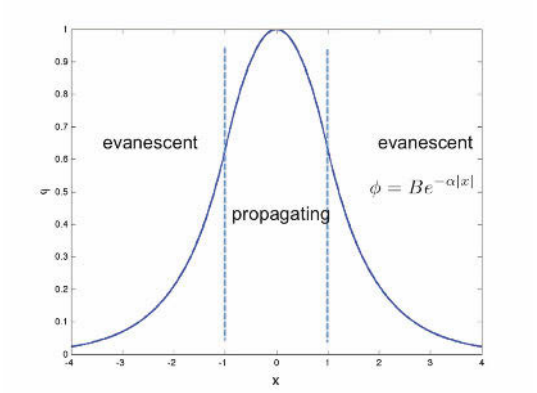

Figure 7. Shape of the trapped mode for $a = 1$ and $V_0 = 2$. The resonance frequency is $k_R = 0.89$.

structure of trapping appears. Inside the well, playing the role of a defect, the wave is propagating and it cannot radiate towards infinity since the wave is evanescent outside. Actually, we have the same situation as in a closed cavity with the evanescent region playing the role of effective walls.

Scattering case: $k^2 > V_0$**.** When the frequency is above the threshold ($k^2 > V_0$) the wave is propagating everywhere. The trapping is not possible and the solution to the wave equation is in the form of a scattering state (Landau and Lifshitz, 1977). For $x < -a$

$$\phi = e^{i\beta x} + Re^{-i\beta x}, \tag{13}$$

and for $x > a$

$$\phi = Te^{i\beta x}, \tag{14}$$

where $\beta = \sqrt{k^2 - V_0}$. The scattering coefficients can be found (Landau and Lifshitz, 1977) from the linear system of four equations with four unknowns obtained by applying the continuity of ϕ and ϕ' at $x = \pm a$ with the solution inside the well ($|x| < a$) given by

$$\phi = A\cos kx + B\sin kx. \tag{15}$$

It appears that no trapping is possible in this case because as soon as

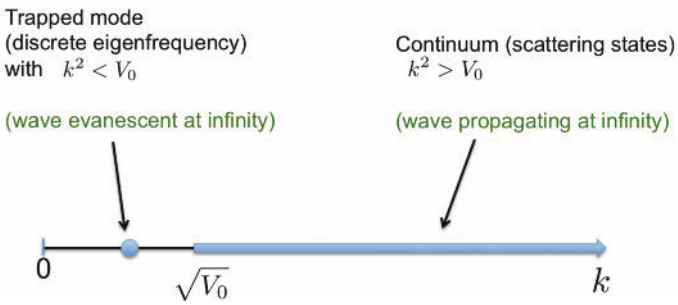

Figure 8. Spectrum of the potential well.

the wave is nonzero it has to radiate energy towards infinity. A sketch of the spectrum along the frequency axis k is shown in Figure 8. Above the threshold, we have the scattering states for the continuous set of k such that $k > \sqrt{V_0}$. Below the threshold, no wave can propagate towards infinity and the trapping is possible for some discrete values of k. These resonance frequencies are selected by interference effect in the propagating well with the effective wall effects of the evanescence regions. In this particular model of the potential well there is at least one trapped mode, but in other situations with a similar threshold frequency it is possible that no trapping occurs (Nazarov, 2011).

The simple mechanism of trapping that has been described is the typical one in other wave system for open geometries in 1D, 2D and 3D. The

important property is the existence of a frequency gap for which the wave is evanescent towards infinity. Then, for frequencies inside the gap, the evanescence environment is able to play the role of an effective wall for a defect and we recover the situation of a closed cavity. In the following, we focus on waveguides in 2D that naturally present cut-on frequencies creating the frequency gap.

3.2 Dirichlet waveguide

Trapped modes are solutions of the homogeneous wave equation with outgoing radiation conditions. We have seen that evanescence is the way to be trapped and the perfect candidates are thus waveguide geometries. We begin with Dirichlet waveguides where previously discussed frequency gap appears more simply than for Neumann waveguides. The transverse modes

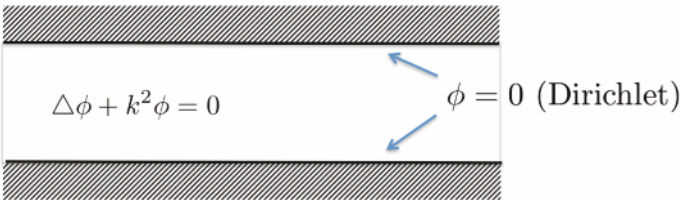

Figure 9. Dirichlet waveguide of width h.

of the waveguide are necessary to make to appear the evanescent character of the propagation. They are defined as solution of the wave equation in a straight waveguide (Figure 9) sought in the separable form:

$$\phi(x, y) = e^{i\alpha x} g(y). \tag{16}$$

Inserting this form into the wave equation gives the ordinary differential equation on the function g:

$$\frac{d^2 g}{dy^2} + (k^2 - \alpha^2) g = 0. \tag{17}$$

On the other hand, the Dirichlet boundary conditions on the wall, $\phi = 0$ for $y = 0 = h$, implies that

$$g(0) = g(h) = 0. \tag{18}$$

Equations (17) with (18) have an infinite discrete set of solutions

$$g_n(y) = \sqrt{\frac{2}{h}}\ \sin(\frac{n\pi y}{h}) \tag{19}$$

indexed by the integer $n \geq 1$. The pre-factor $\sqrt{2/h}$ is chosen so as to ensure the orthonormality of the transverse modes

$$\int_0^h g_n(y) g_m(y) dy = \delta_{nm}.$$

Each transverse mode is associated to an axial wavenumber α indexed by $n \geq 1$:

$$\alpha_n^2 = k^2 - \left(\frac{n\pi}{h}\right)^2. \tag{20}$$

Here comes the propagating or evanescent waves. For a given frequency k, a transverse mode is either propagating (real α_n) or evanescent (imaginary α_n) depending on the sign of α_n^2. Thus for $k > n\pi/h$ the wave is propagating and for $k < n\pi/h$ the wave is evanescent. Since $n \geq 1$ there appears that all the transverse modes are evanescent for $k < \pi/h$. The

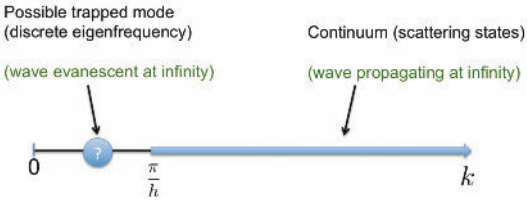

Figure 10. Spectrum of the Dirichlet waveguide with lead width h.

general solution of the wave equation can be expanded[5] on the infinite set of transverse modes[6] as

$$\phi = \sum_0^\infty (c_n e^{i\alpha_n x} + d_n e^{-i\alpha_n x}) g_n(y), \tag{21}$$

which means that for $k < \pi/h$ any wave solution is only composed of evanescent waves. For $k > \pi/h$, at least the mode with $n = 1$ is propagating and when the frequency increases more and more transverse modes are propagating with the cut-on frequencies at $k_{c,n} = n\pi/h$. In the presence of a defect, similarly to the model of the potential well, a sketch of the spectrum along the frequency axis k can be given (Figure 10). For a Dirichlet

[5]The terms $e^{\pm i\alpha_n x}$ correspond respectively to right/left going waves.

[6]These transverse modes play the role of generalized Fourier series modes and form a complete basis on $0 \leq y \leq h$ (Stakgold, 1998).

waveguide, with leads towards infinity of width h, the wave cannot propagate in a gap $0 < k < \pi/h$. Thus a the existence of a trapped mode is possible in this gap, depending of the shape of the defect between the leads. For a local perturbation of the width of the waveguide corresponding to an increase of the volume it can be proven that a trapped mode exists and asymptotic approximations of the resonance frequencies can be obtained (Nazarov, 2011). Figure 11 displays the pattern of such a trapped mode. For the case of bent quantum waveguides, there is an important literature discussing the existence of trapped modes often called bound states in this quantum mechanics community (Duclos and Exner, 1995).

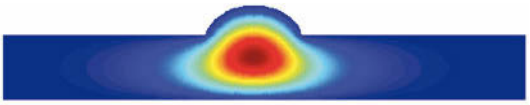

Figure 11. Trapped mode for a defect in Dirichlet waveguide.

3.3 Neumann waveguide

The question of trapped modes in waveguides with Neumann boundary conditions is more involved because the plane transverse mode can always propagate. Indeed, when seeking a separable solution of the form $\phi = e^{i\alpha x} g(y)$ in the geometry shown in Figure 12, the ODE for g is the same as for Dirichlet waveguides,

$$g" + (k^2 - \alpha^2)g = 0, \tag{22}$$

but the Neumann boundary conditions imply that

$$g'(0) = g'(h) = 0. \tag{23}$$

The transverse modes are thus of the form

$$g_n(y) = \sqrt{\frac{2-\delta_0}{h}}\ \cos(\frac{n\pi y}{h}), \tag{24}$$

where $n \geq 0$ and with the pre-factor permitting the orthonormality

$$\int_0^h g_n(y) g_m(y)\ dy = \delta_{nm}.$$

Following the same reasoning as in the previous section, the transverse

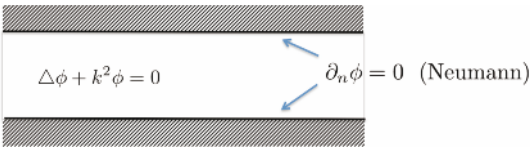

Figure 12. Neumann waveguide of width h.

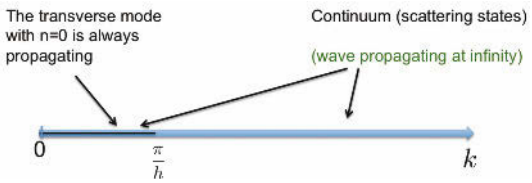

Figure 13. Structure of the spectrum for a Neumann waveguide with lead width h.

mode indexed by n is propagating if $k > n\pi/h$. The novelty here is that the plane transverse mode (with $n = 0$) has no cut-on frequency and can propagate for any frequency. The spectrum is shown in Figure 13.

Thus, the wave can radiate towards infinity whatever the frequency. To create a gap we need to decouple the plane wave mode from the other ones. The "trick" is then to use the symmetry of the geometry in order to get the decoupling. Indeed, for a waveguide symmetric with respect with the axis x (Figure 14), the symmetric part (even w.r.t. y) of the solution ϕ_s and the antisymmetric part (odd w.r.t. y) ϕ_a of the solution are defined as

$$\phi_s(x,y) = \frac{1}{2}\left(\phi(x,y) + \phi(x,-y)\right) \tag{25}$$

and

$$\phi_a(x,y) = \frac{1}{2}\left(\phi(x,y) - \phi(x,-y)\right). \tag{26}$$

These two parts of the wave are decoupled owing to the symmetry of the

Figure 14. A symmetric waveguide.

geometry. Consequently, we have in fact two decoupled problem for wave

propagation in this case: the symmetric part of the wave associated with the even transverse modes indexed by even integers (n=0,2,4,...) and the antisymmetric part of the wave associated with odd transverse modes indexed by odd integers (n=1,3,5,...). Since the plane mode with $n = 0$ belongs to the first part, the decoupling due to the symmetry allows to recover the same threshold (cut-on frequency) as for the waveguide with Neumann boundary conditions. The gap exists for the antisymmetric part of the wave (Figure 15). The existence of trapped modes for Neumann waveguides using this

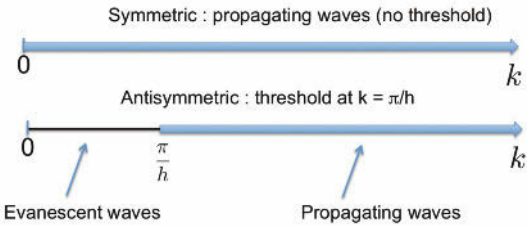

Figure 15. Spectrum for a symmetric waveguide with lead width h.

symmetry argument is the classical one in the literature (Evans et al., 1994). In Figure 16 the example of such a trapped mode is shown for the geometry of an acoustic expansion chamber.

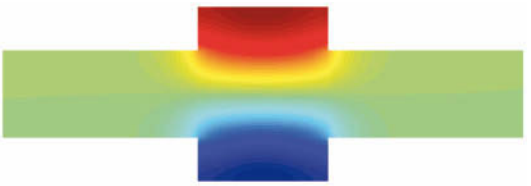

Figure 16. A trapped mode in symmetric Neumann waveguide.

3.4 Approximate mode matching

The determination of trapped modes is difficult and needs usually full numerical computations, but, for some geometries, it is possible to find simple approximations. In the case of a rectangular obstacle (Fig 17), mode matching techniques can be applied and useful simple analytical approximations can be found. Consider the geometry shown in Figure 17: it is symmetric with Neumann boundary conditions and as such can accept a trapped mode solution (remind that it is a solution of the homogeneous

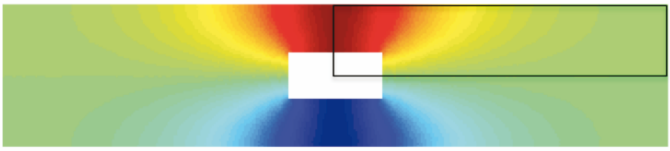

Figure 17. Trapped mode for a symmetric rectangular obstacle in a Neumann waveguide.

Helmholtz equation (1) with outgoing radiation condition). The trapped mode has to be an antisymmetric solution as discussed in the previous section, and by symmetry the domain can be reduced to the rectangle drawn in Figure 17 and reproduced in Figure 18. To apply an approximate mode matching technique we choose to keep just the plane mode in the central region of Figure 18 but to take into account the full set of evanescent waves outside the obstacle. Thus the solution for $0 < x < a$ is approximated by

$$\phi(x, y) = A \cos(kx) \tag{27}$$

and outside the obstacle ($x > a$) the solution is expanded on the full series of evanescent modes,

$$\phi(x, y) = \sum_{n \geq 0} c_n e^{-K_n} g_n(y), \tag{28}$$

where $K_n = \sqrt{\gamma_n^2 - k^2}$, $\gamma_n = (2n + 1)\pi/h$ and $g_n(y) = 2/\sqrt{h} \sin \gamma_n y$. Note that, since we are in the frequency gap $k < \pi/h$ (see previous section), $\gamma_n > k$ for all n. The following interface boundary conditions have to be

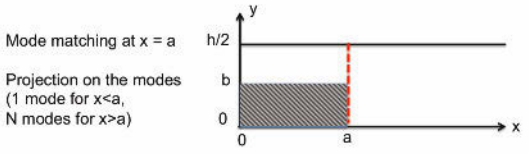

Figure 18. Partition of the problem.

satisfied at $x = a$:

$$\phi(a^+, y) = \phi(a^-, y) \quad \text{for} \quad b < y < h/2 \tag{29}$$

and

$$\partial_x\phi(a^+,y) = \partial_x\phi(a^-,y) \quad \text{for} \quad b < y < h/2, \tag{30}$$

$$\partial_x\phi(a^+,y) = 0 \quad \text{for} \quad 0 < y < b. \tag{31}$$

Mode matching consists in projecting equations (29–31) on the transverse modes that have been taken into account in the solution expansion in (27–28). Projection of the continuity of ϕ on the plane mode,

$$\int_b^{h/2} \phi(a^+,y)\, dy = \int_b^{h/2} \phi(a^-,y)\, dy, \tag{32}$$

yields a first relation between the unknown coefficients A and c_n:

$$\sum_{n\geq 0} c_n \int_b^{h/2} g_n(y)\, dy = A(h/2-b)\cos(ka). \tag{33}$$

On the other hand projection of equations (30-31) on each of the outside transverse modes is done through

$$\int_0^{h/2} \partial_x\phi(a^+,y) g_n(y)\, dy = \int_b^{h/2} \partial_x\phi(a^+,y) g_n(y)\, dy \tag{34}$$

$$= \int_b^{h/2} \partial_x\phi(a^-,y) g_n(y)\, dy, \tag{35}$$

and it gives for each $n \geq 0$:

$$K_n c_n = Ak\sin(ka) \int_b^{h/2} g_n(y)\, dy. \tag{36}$$

Eventually, by eliminating c_n between (33) and (36), we obtain

$$\tan(ka) = \frac{h}{8}(h-2b) \frac{1}{\displaystyle\sum_{n\geq 0} \frac{\cos(\gamma_n b)}{\gamma_n} \frac{k}{\sqrt{\gamma_n^2 - k^2}}} \tag{37}$$

where k is the unknown. This determines implicitly the resonance frequency. The $k = k_R$ solution is a good approximation when the rectangular obstacle is long enough because it neglects the higher order modes for $x < a$.

3.5 Mathematical proof: variational technique

These notes are not really mathematically oriented and the rigorous approach to trapped modes can be found in the functional analysis literature (Duclos and Exner, 1995; A.S. Bonnet-BenDhia and Mahé, 1997; Bonnet-BenDhia and Mercier, 2007; Nazarov, 2011). Nevertheless we briefly present here the popular variational technique often used to prove the existence of trapped mode.

The idea comes from the min-max principle for an hermitian matrix of finite size ($M = \overline{M}^T$). It states that the eigenvalues λ_n of M verify

$$\min(\lambda_n) \leq \frac{(x|Mx)}{(x|x)}$$

$\forall x \neq 0$. We recognize here the Rayleigh quotient. This latter can be also defined for the eigenvalue problem corresponding to trapped mode under the form

$$Q(\psi) = \frac{\int |\nabla\psi|^2 d\mathbf{x}}{\int |\psi|^2 d\mathbf{x}}.$$

Here ψ is a square integrable[7] test function respecting the imposed boundary conditions (i.e. ψ must be in the domain of the operator). Then, the variational min-max principle (Bonnet-BenDhia and Mercier, 2007) states that if

$$Q(\psi_0) < \frac{\pi^2}{h^2}$$

for some test function ψ_0 then there exists a trapped mode with resonance frequency k_R such that

$$k_R \leq \sqrt{Q(\psi_0)}.$$

What is nice here is that it is sufficient to cleverly choose a test function which is not a solution of the wave equation to prove the existence of a trapped mode. Let us take the simple example of the trapped mode for the Neumann waveguide with a rectangular obstacle (Figure 19). We can choose the test function defined by

$$\psi_0 = \text{sign}(y)\cos(\frac{\pi x}{2a})$$

for $|x| < a$ and

$$\psi_0 = 0$$

[7] In the sense that the function and its gradient are square integrable so that the Rayleigh quotient is well defined.

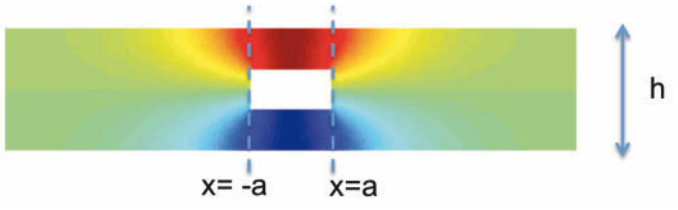

Figure 19. Trapped mode in the Neumann waveguide with rectangular obstacle.

for $|x| > a$.

Of course this test function is not a solution of the Helmholtz equation but it is square integrable (as is its gradient) and it verifies the Neumann boundary condition at the wall. A simple computation shows that

$$Q(\psi_0) = \frac{\int |\nabla \psi_0|^2 d\mathbf{x}}{\int |\psi_0|^2 d\mathbf{x}} = \frac{\pi^2}{4a^2}.$$

From the variational principle min-max principle, we know that a trapped mode exists if

$$Q(\psi_0) = \frac{\pi^2}{4a^2} \leq \frac{\pi^2}{h^2}. \tag{38}$$

Hence, from the variational principle and (38), we can conclude that a

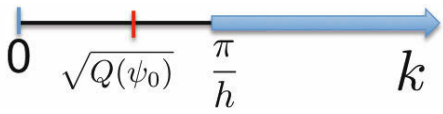

Figure 20. Spectrum of the Neumann waveguide with rectangular obstacle.

trapped mode exists if

$$a > h/2$$

and that the corresponding resonance frequency will satisfy

$$k_R < \frac{\pi}{2a}.$$

The corresponding scheme of the spectrum is shown in Figure 20.

By this example, we see how powerful is this variational technique: with the very simple choice of the test function ψ_0 it has been possible to rigorously prove the existence of the trapped mode and to find an upper bound for the resonance frequency.

3.6 Higher frequencies

So far, we have focused on trapped modes at low frequencies. Their existence can be understood from the existence of a frequency gap $0 < k < \pi/h$ where the waves are evanescent in outgoing leads of the waveguide. For higher frequencies, trapped modes can also exist but their existence is more difficult to show. Heuristically, it can be argued there that for higher cut-on frequencies there exists "gaps" with a finite number of transverse mode that can radiate. A trapped mode has to be in "good interferences" in order to annihilate the component on this finite number of modes. In such a situation, McIver et al. (2001) have chosen the term embedded trapped modes to stress that no symmetry is able to decouple the modes from the continuous spectrum of scattering states[8]. By taking an obstacle with several parameters they have shown that is possible to construct trapped mode above the threshold of evanescence given by symmetries of the geometry.

Figure 21 displays the example of a trapped mode with a resonance frequency above the threshold of evanescence ($k > \pi/h$) for a Dirichlet waveguide. In this case two propagating transverse modes might radiate towards infinity.

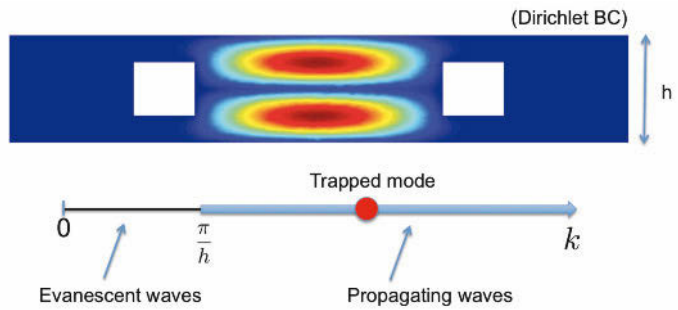

Figure 21. Trapped mode for a Dirichlet waveguide at higher frequencies.

4 Quasi-trapped modes and edge waves

4.1 Quasi-trapped modes and complex resonance

The trapped modes previously discussed are very particular object that are perfectly localized in infinite waveguide. But waves can also be localized

[8]These modes are often called BIC (Bound States in the Continuum) in quantum mechanics.

with a small leakage. This corresponds to quasi-trapped modes (or complex resonance as we shall see).

Figure 22. Localized wave in a thin slot.

As an example, consider the geometry shown in Figure 22: a semi-infinite acoustic waveguide (Neumann) with a thin slot at the edge. It can be thought as a system coupling the closed thin slot with the trivial semi-infinite waveguide, and, intuitively, it is not surprising that this geometry can posses solution with the wave strongly localized in the slot when the frequency is close to the resonance frequency of the closed slot. The solution plotted in Figure 22 corresponds to such a quasi-trapped wave close to the $\lambda/4$ resonance ($kL \simeq \pi/2$) of the slot. Here, by energy conservation, the reflected power flux is equal to the incident one (and so the wave is leaking towards infinity), but the amplitude in the slot is much larger than in the principal waveguide.

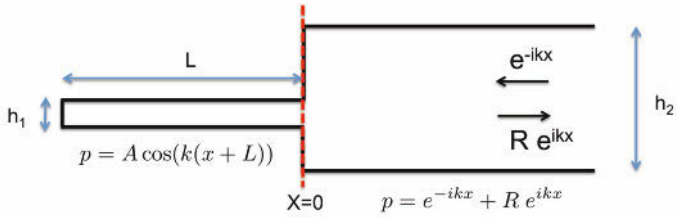

Figure 23. Approximate model for the thin slot quasi-trapping.

To gain further insight, it is useful to look at an approximate solution to this problem. We are at low frequencies so that we can just take the plane wave transverse mode in each part of the waveguide ($kh_2 < \pi$). For $x < 0$, the wave in the slot is given by

$$p = A \cos k(x + L), \tag{39}$$

and in the principal waveguide ($x > 0$):

$$p = e^{-ikx} + Re^{ikx}. \tag{40}$$

The approximate model is summarized in Figure 23. It remains to apply the matching at the interface $x = 0$ that consists in the continuity of p and hp'. These yield the two equations:

$$A\cos(kL) = 1 + R \tag{41}$$

and

$$-Akh_1 \sin(kL) = -ikh_2(1 - R). \tag{42}$$

Eliminating the coefficient A, we find the reflection coefficient R to be

$$R = \frac{1 + i\dfrac{h_1}{h_2}\tan(kL)}{1 - i\dfrac{h_1}{h_2}\tan(kL)}. \tag{43}$$

This simple result is interesting because it illustrates the behavior of a quasi-trapped mode. First, note that $|R| = 1$ for real frequency due to energy conservation. Next, by inspecting what happens for complex k, from (43), it appears that R has pole for k solution of

$$1 - i\frac{h_1}{h_2}\tan(kL) = 0. \tag{44}$$

This complex value of k is the complex resonance frequency (Flax et al., 1981; Aslanyan et al., 2000) corresponding to a quasi-trapped mode. For very thin slot the asymptotic solution of (44) is given by

$$k_R L \simeq \frac{\pi}{2} - i\epsilon \quad (n\pi) \tag{45}$$

where $\epsilon = h_1/h_2 \ll 1$. Hence, we recover the intuitive $\lambda/4$ resonance foreseen in Figure 22, but with an imaginary part due to the leakage of the wave towards infinity.

More generally (independently of the approximate solution presented above), a complex resonance is associated to a mode with complex resonance frequency. It is mode since it is a solution of the homogeneous wave equation with outgoing radiation towards infinity (it can radiate because k has an imaginary part[9]). Thus a complex resonance frequency is both (Aslanyan et al., 2000):

- a complex k for which there is a solution to the homogeneous Helmholtz equation with outgoing radiation condition

[9] This imaginary part has to be negative as will be seen in the next section.

- a complex k that is a pole of the reflection coefficient (or more generally the scattering matrix)

Both definitions are valid because a pole of the reflection coefficient gives a solution to the wave equation without incident wave.

In the time domain, the negative imaginary part of the frequency gives the ringing time of the mode (similar to the radioactive half-life) since with the chosen convention of time dependence $e^{-i\omega t}$ the wave decreases as $e^{\omega_i t}$ where $\omega_i = c\,\mathrm{Imag}(k_R)$. Besides, a complex resonance has a quality factor measuring (as for the harmonic oscillator) how sharp is the resonance. Figure 24 displays a quasi trapped mode for a complex resonance with a very large quality factor. This huge quality factor is due to the weak coupling between the mode of the rectangular cavity and the lead of the waveguide where the the wave can leak.

Figure 24. Example of long lived state with quality factor $Q \simeq 10^5$.

4.2 Some properties for complex resonance

It is possible to show that the imaginary part of the complex resonance frequency is positive due to outgoing radiation condition. Let us consider the geometry depicted in Figure 25. A quasi-trapped mode is solution to the wave equation

$$\triangle p + k^2 p = 0, \tag{46}$$

with Neumann boundary condition on the walls and outgoing radiation condition on S_{out}. Multiplying this equation by $\overline{p}$ and integrating on the

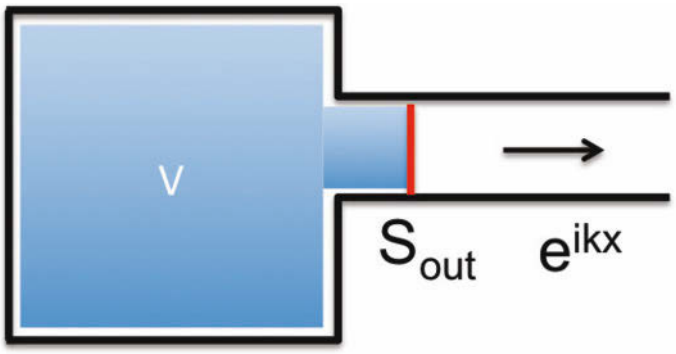

Figure 25. Cavity coupled to a a waveguide.

volume V gives

$$\int_{Sout} \overline{p}\, \partial_n p - \int\int_V |\nabla p|^2 + k^2 \int\int_V |p|^2 = 0. \tag{47}$$

The outgoing radiation condition is translated[10] into $\partial_n p = ikp$ on S_{out} so that we obtain

$$ik \int_{Sout} |p|^2 - \int\int_V |\nabla p|^2 + k^2 \int\int_V |p|^2 = 0. \tag{48}$$

Taking the imaginary part of this equation yields

$$ik_r \int_{Sout} |p|^2 + 2k_i k_r \int\int_V |p|^2 = 0 \tag{49}$$

where k_r and k_i are the real and imaginary part of k. Eventually, it comes that

$$k_i = -\frac{\displaystyle\int_{Sout} |p|^2}{2\displaystyle\int\int_V |p|^2}. \tag{50}$$

Equation (50) demonstrates that the imaginary part of the complex resonance frequency has to be negative. With[11] $k = \omega/c$, we conclude that the

[10] Here, for the sake of simplicity, we assume that only the plane transverse mode has to be taken into account but the exact outgoing radiation condition using the Dirichlet to Neumann operator works similarly.

[11] In this section we are in the dispersionless case where c does not depend on ω so that k and ω are interchangeable.

complex resonance frequency can only be located in the lower half plane $\mathrm{Im}(\omega) < 0$.

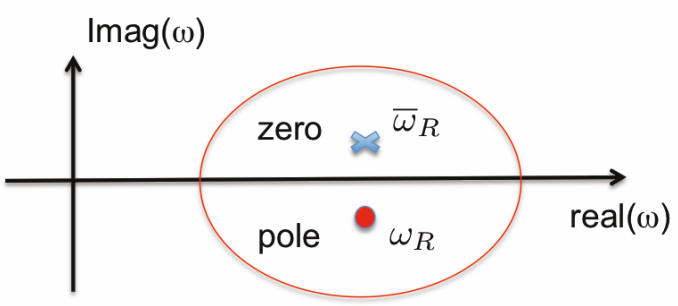

Figure 26. Analytical structure of R in the complex frequency plane.

Besides, by time reversal symmetry (complex conjugation) it appears that[12]

$$\overline{R(\omega)} = \frac{1}{R(\overline{\omega})}. \tag{51}$$

It means that a pole ω_R of the reflection coefficient (complex resonance frequency) is associated to a zero of R at $\overline{\omega}_R$. Locally, near the complex resonance frequency, the reflection coefficient can thus be expressed as

$$R(\omega) = e^{i\theta} \frac{\omega - \overline{\omega}_R}{\omega - \omega_R}. \tag{52}$$

The phase θ is slowly varying for ω in the neighborhood of ω_R and it is real for real ω because then $|R| = 1$ by energy conservation. It is termed a background phase term for it represents the slow variation in the scattering compared to the rapid variation due the close resonance frequency ω_R. This local expression for R is very useful: it encodes very simply the local behavior of the quasi-resonance and it explains the universal 2π shift observed for the phase of the scattering. Figure 26 summarizes the analytical structure of the reflection coefficient. Poles (or complex resonance frequency) of R are in the lower half plane and they are mirrored by zeros in the upper half plane.

Figure 27. 2D edge resonance in an acoustic waveguide, obtained by symmetry from the trapped mode with a rectangular obstacle.

4.3 Edge waves

A 2D trapped mode in an acoustic waveguide (with Neumann boundary conditions) is solution of the Helmholtz equation

$$(\partial_{xx} + \partial_{yy})\, p + k_R^2 p = 0, \tag{53}$$

with the outgoing boundary condition

$$p(x, y) \to 0 \tag{54}$$

when $x \to 0$. By symmetry w.r.t. the vertical axis, the trapped mode examined in Figure 19 can be converted to a trapped mode in the semi-infinite waveguide shown in Figure 27. This solution is essentially 2D, but what does it imply in 3D?

We consider the extension of the previous geometry to 3D as displayed in Figure 28. An edge wave for the 3D geometry is sought as a solution of the 3D Helmholtz equation

$$(\partial_{xx} + \partial_{yy} + \partial_{zz})\, p + k^2 p = 0 \tag{55}$$

with Neumann boundary conditions at the walls and the outgoing radiation

$$\phi(x, y, z) \to 0 \tag{56}$$

when $x \to 0$. The edge wave propagating along the z axis is written as

$$p(x, y, z) = e^{i\beta z} \phi(x, y). \tag{57}$$

[12] This property is also valid for the scattering matrix (Flax et al., 1981; Aslanyan et al., 2000).

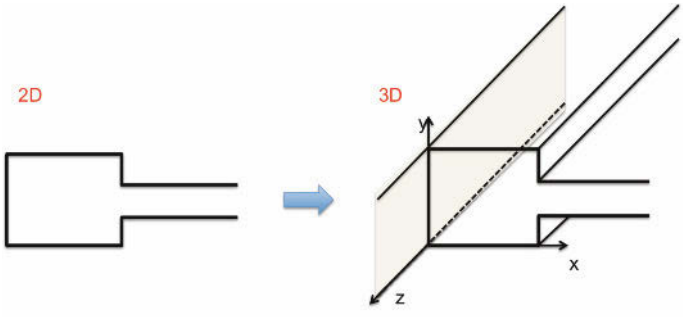

Figure 28. From 2D to 3D.

Inserting Equation (57) into the 3D Helmholtz equation yields the equation for ϕ:

$$(\partial_{xx} + \partial_{yy})\,\phi + (k^2 - \beta^2)\,\phi = 0, \tag{58}$$

with Neumann boundary condition and the condition that $\phi(x, y) \to 0$ when $x \to 0$. The equations and the boundary conditions for ϕ of the 3D edge wave are exactly the same as those of the 2D trapped mode. It means that ϕ is a 2D trapped mode and by comparing Equations (53) and (58):

$$k^2 - \beta^2 = k_R^2. \tag{59}$$

This gives immediately the dispersion relation of the 3D edge wave

$$\frac{\omega^2}{c^2} = \beta^2 + k_R^2. \tag{60}$$

Hence a 2D trapped mode can be converted into a 3D edge wave and the 2D resonance frequency becomes the cut-on frequency in 3D. The corresponding dispersion relation is plotted in Figure 29.

A 2D quasi trapped mode can also be extended to 3D. It is then converted into a 3D leaky edge mode. It is damped (leaky) as it propagates along the z axis since the wave is not perfectly localized at the edge and it radiates continuously some energy. Mathematically, the leakage $\mathrm{Im}(\beta) > 0$ comes from the differentiation of the dispersion relation,

$$\mathrm{Im}(k_R)\mathrm{Re}(k_R) + \mathrm{Im}(\beta)\mathrm{Re}(\beta) = 0,$$

that implies

$$\mathrm{Im}(k_R) < 0 \Rightarrow \mathrm{Im}(\beta) > 0.$$

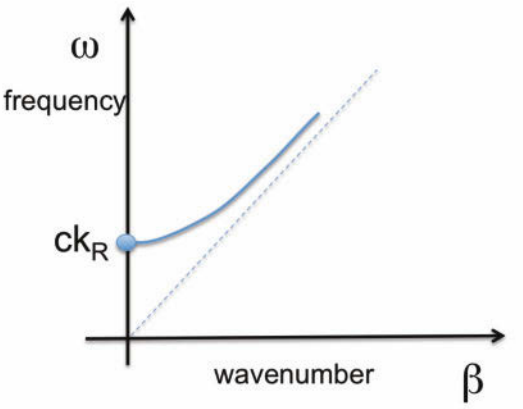

Figure 29. Dispersion relation of the 3D edge wave.

4.4 The simplest edge

Let us examine the simplest case of edge: the semi-infinite strip with a cut at $x = 0$ (Figure 30). Is a trapping of the scalar acoustic wave possible near the edge with a simple boundary condition?

For Dirichlet boundary conditions at the edge $x = 0$,

$$\phi(0, y) = 0$$

automatically results in

$$\phi(x, y) = \sum_n c_n (e^{ik_n x} - e^{-ik_n x}) g_n(y).$$

For Neumann boundary conditions, $\partial_x \phi(0, y) = 0$ imposes

$$\phi(x, y) = \sum_n c_n (e^{ik_n x} + e^{-ik_n x}) g_n(y).$$

We conclude that neither Dirichlet nor Neumann boundary conditions at the edge is able to support an acoustic solution with outgoing boundary conditions towards $x \to \infty$. A richer boundary condition is needed to trap the wave. For scalar waves, impedance at the edge can sustain trapping (but they add a parameter in the problem). In the next section, we will see that elastic waves (vectorial waves) have the ability to trap the wave near the simplest edge with a traction free surface.

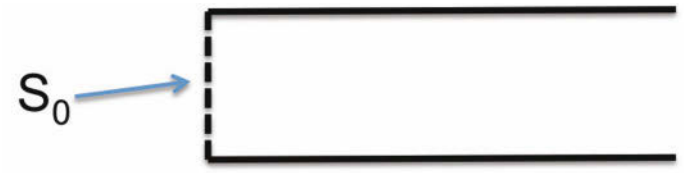

Figure 30. The simplest edge: the semi-infinite strip.

5 Edge resonance in elastic waveguides

5.1 Elastic waveguides

The considered geometry is depicted in Figure 31. The equations of linear elastodynamics for isotropic solid are

$$-\rho\omega^2\mathbf{w} = \nabla.\sigma, \tag{61}$$

where ρ is the mass density, $\mathbf{w} = (u_x, u_y, u_z)^T$ is the elastic displacement and σ is the stress tensor. Owing to the elastic Lamé parameters λ and μ, the Hooke law links the strain tensor to the stress tensor through

$$\sigma = \lambda \,\mathrm{div}\boldsymbol{w}\,\mathrm{Id} + \mu(\nabla\boldsymbol{w} + \nabla\boldsymbol{w}^T). \tag{62}$$

Equation (61) can be be rewritten in term of displacement only:

$$-\rho\omega^2\mathbf{w} = (\lambda + 2\mu)\nabla(\nabla.\mathbf{w}) - \mu\nabla\wedge\nabla\wedge\mathbf{w}. \tag{63}$$

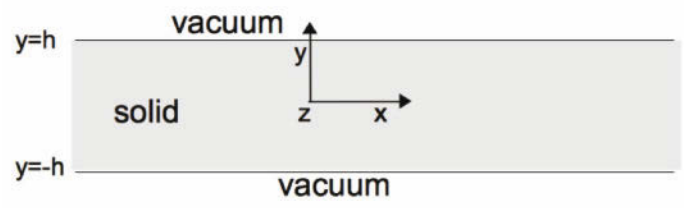

Figure 31. Elastic waveguide.

In free space plane wave solutions can be sought in the form

$$\mathbf{w} = \mathbf{w}_0\, e^{i\mathbf{kx}}, \tag{64}$$

that makes to appear two different polarizations. The longitudinal wave is such that

$$\mathbf{k} \wedge \mathbf{w}_0 = 0 \tag{65}$$

with a dispersion relation given by

$$k^2 = \frac{\omega^2}{c_L^2} \tag{66}$$

with $c_L^2 \equiv (\lambda + 2\mu)/\rho$. The transversal waves are such that

$$\mathbf{k}.\mathbf{w}_0 = 0 \tag{67}$$

with the dispersion relation

$$k^2 = \frac{\omega^2}{c_T^2} \tag{68}$$

with $c_T^2 = \mu/\rho$. In contrast with acoustic waves (scalar waves), the elastic waves can be called vectorial waves since they have different kinds of polarizations.

In waveguides (Figure 31), the transverse modes are of the form

$$\mathbf{w} = \mathbf{w}_0(y)\ e^{i\mathbf{kx}}, \tag{69}$$

with $\mathbf{k} = q\ \mathbf{e}_x$ and $\partial_z = 0$. Because of the different kinds of polarizations, two families of transverse modes exist:

- SH transverse modes (anti-plane strain). Their non zero components are u_z and $(\sigma_{xz}\ ,\ \sigma_{yz})$. It corresponds to a scalar wave equivalent to acoustic problem with u_z replacing the pressure and with Neumann boundary conditions at the free stress interface.
- Lamb modes (plane strain). Their non-zero components are $(u_x\ ,\ u_y)$ and $(\sigma_{xx}\ ,\ \sigma_{xy}\ ,\ \sigma_{yy}\ ,\ \sigma_{zz})$. It corresponds to a vectorial wave that is composed of one longitudinal polarization and one transversal polarization.

Having discussed the acoustic case in the previous sections, we now focus on Lamb modes that are vectorial waves. To find the transverse modes it is convenient to write the displacement with two potentials

$$\mathbf{w} = \nabla\phi + \nabla\psi \times e_z, \tag{70}$$

and each of the potentials ϕ and ψ obeys a scalar wave equation

$$(\Delta + k_l^2)\phi = 0 \tag{71}$$

and

$$(\Delta + k_t^2)\psi = 0. \tag{72}$$

The complexity comes from the stress free boundary conditions $\sigma.\mathbf{n} = 0$ with $\mathbf{n} = \pm\mathbf{e}_y$ at $y = \pm h$. They are

$$\sigma_{xy} = (\lambda + 2\mu)\phi_{yy} + \lambda\phi_{xx} - 2\mu\psi_{xy} = 0 \quad \text{at} \quad y = \pm h$$

and

$$\sigma_{yy} = \mu(\psi_{yy} - \psi_{xx} + 2\phi_{xy}) = 0 \quad \text{at} \quad y = \pm h.$$

For transverse modes, the x-dependancies are of the form $f(x, y) = F(y)e^{iqx}$. By using ϕ and ψ that verify (71) and (72) and the boundary conditions, some algebra show that the global dispersion relation can be factorized in two simpler dispersion relations:

$$\frac{\tanh \alpha h}{\tanh \beta h} = \frac{4q^2\alpha\beta}{(q^2 + \alpha^2)^2} \quad \text{for symmetric modes} \tag{73}$$

$$\frac{\tanh \alpha h}{\tanh \beta h} = \frac{(q^2 + \alpha^2)^2}{4q^2\alpha\beta} \quad \text{for antisymmetric modes} \tag{74}$$

with $\alpha = (q^2 - k_t^2)^{1/2}$ and $\beta = (q^2 - k_l^2)^{1/2}$. Symmetric modes have an axial displacement u_x even w.r.t. y whilst antisymmetric modes have u_x odd w.r.t. y.

Each of the dispersion relation 73 and 74 can be written as $D(\Omega, K) = 0$ where $\Omega = k_t h$ is the dimensionless frequency and $K = qh$ is the dimensionless wavenumber. An example of the behavior of the dispersion behavior of Lamb modes is shown in Figures 32 and 33 for an elastic material with Poisson ratio $\nu = 0.3$ ($c_L/c_T \simeq 1.87$). At low frequencies, only modes S_0 and A_0 are propagating; the slope of the curve for S_0 gives the wave speed of longitudinal vibrations in thin plate under the plane stress approximation whilst the parabolic behavior of mode A_0 corresponds to the Kirchhoff equation for thin plate with flexural vibrations. For a given frequency Ω, there is a finite number of propagating modes and an infinity of evanescent modes (with an non-zero imaginary part of the wavenumber, not shown in the Figures). Note the atypical behavior near the cut-on frequency of modes S_1 and S_2 in Figure 32: this pair of modes becomes propagating at points C_1 and C_2 with a non-zero wavenumber K. Moreover, the mode S_2 has a negative phase velocity ($K < 0$) on a narrow band of frequencies.

5.2 Multimodal method in elastic waveguides

It has been remarked that the structure of the Lamb mode spectra is much more complicated than the one of transverse acoustic modes presented

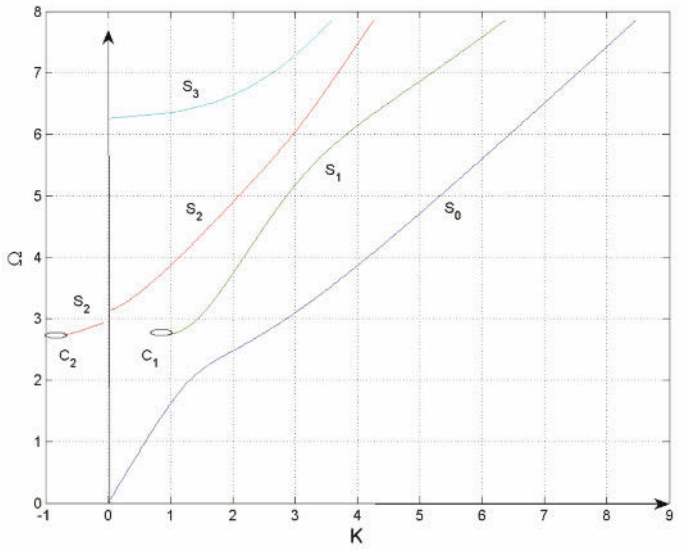

Figure 32. Dispersion diagram of the symmetric Lamb modes.

earlier. In this section, we examine a formalism (Pagneux and Maurel, 2002, 2004, 2006) that facilitates the use of these modes; it make to appear a structure where the projection on the transverse Lamb modes is done using a bi-orthogonality relation.

Elasticity equation can be re-written as

$$\partial_x \begin{pmatrix} \mathbf{X} \\ \mathbf{Y} \end{pmatrix} = \begin{pmatrix} 0 & \mathsf{F} \\ \mathsf{G} & 0 \end{pmatrix} \begin{pmatrix} \mathbf{X} \\ \mathbf{Y} \end{pmatrix}, \tag{75}$$

where vectors $\mathbf{X}$ and $\mathbf{Y}$ are

$$\mathbf{X} = \begin{pmatrix} u_x \\ \sigma_{xy} \end{pmatrix} \quad \text{and} \quad \mathbf{Y} = \begin{pmatrix} -\sigma_{xx} \\ u_y \end{pmatrix},$$

and where F and G are the matrices of differential operators

$$\mathsf{F} = \begin{pmatrix} -\dfrac{f_1}{\lambda} & -f_1\partial_y \\ f_1\partial_y & -\rho\omega^2 - f_2\partial_{y^2} \end{pmatrix}, \quad \text{and} \quad \mathsf{G} = \begin{pmatrix} \rho\omega^2 & \partial_y \\ -\partial_y & \dfrac{1}{\mu} \end{pmatrix}, \tag{76}$$

with $f_1 = \lambda/(\lambda+2\mu)$ and $f_2 = 4\mu(\lambda+\mu)/(\lambda+2\mu)$. The boundary conditions at the stress surfaces, $\sigma.n = 0$ (i.e. $\sigma_{xy} = \sigma_{yy} = 0$ at $y = \pm h$), can be

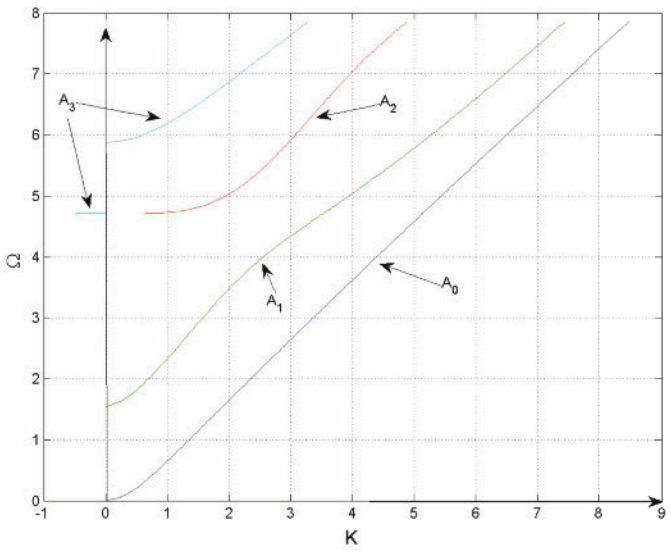

Figure 33. Dispersion diagram of the antisymmetric Lamb modes.

expressed directly on components $\mathbf{X}$ and $\mathbf{Y}$ for σ_{xy} is the second component of $\mathbf{X}$ and $\sigma_{yy} : \mathbf{Y} \to \sigma_{yy}(\mathbf{Y}) = f_1\sigma_{xx} + f_2\partial_y u_y$.

The equation to find the transverse Lamb modes takes the explicit form (the x dependance e^{iqx} implies that ∂_x becomes iq) of an eigenvalue problem

$$iq \begin{pmatrix} \mathbf{X} \\ \mathbf{Y} \end{pmatrix} = \begin{pmatrix} 0 & \mathsf{F} \\ \mathsf{G} & 0 \end{pmatrix} \begin{pmatrix} \mathbf{X} \\ \mathbf{Y} \end{pmatrix}, \tag{77}$$

and the boundary conditions (i.e. $\sigma_{xy} = \sigma_{yy} = 0$ at $y = \pm h$) does not involve the eigenvalue q. Lamb modes are thus eigenvectors of this eigenproblem with eigenvalues q. There is an infinity of modes: right-going transverse modes have eigenvalues q_n and eigenvectors $[\mathbf{X}_n, \mathbf{Y}_n]^T$ and left-going transverse modes have eigenvalues $-q_n$ and eigenvectors $[-\mathbf{X}_n, \mathbf{Y}_n]^T$. Assuming the completeness of Lamb modes, any solution can be expanded as

$$\begin{pmatrix} \mathbf{X} \\ \mathbf{Y} \end{pmatrix} = \sum_{n\geq 0} a_n^+ \begin{pmatrix} \mathbf{X}_n \\ \mathbf{Y}_n \end{pmatrix} + \sum_{n\geq 0} a_n^- \begin{pmatrix} -\mathbf{X}_n \\ \mathbf{Y}_n \end{pmatrix}. \tag{78}$$

The terms of the series can be rearranged to give

$$\mathbf{X} = \sum_{n\geq 0} a_n \mathbf{X}_n \tag{79}$$

and

$$\mathbf{Y} = \sum_{n\geq 0} b_n \mathbf{Y}_n \tag{80}$$

with

$$a_n = a_n^+ - a_n^-$$

and

$$b_n = a_n^+ + a_n^-.$$

Note that the sum are restricted to positive index numbers.

The operators F and G have a very nice property:

$$\begin{array}{ll} (\mathsf{F}\tilde{\mathbf{Y}}|\mathbf{Y}) & = (\tilde{\mathbf{Y}}|\mathsf{F}\mathbf{Y}) + [\sigma_{yy}\tilde{u}_y - \tilde{\sigma}_{yy}u_y]_{-h}^{h} \\ (\mathsf{G}\tilde{\mathbf{X}}|\mathbf{X}) & = (\tilde{\mathbf{X}}|\mathsf{G}\mathbf{X}) + [u_x\tilde{\sigma}_{xy} - \tilde{u}_x\sigma_{xy}]_{-h}^{h}. \end{array} \tag{81}$$

Hence, F and G are symmetric with the inner product defined by[13]

$$\left(\begin{pmatrix} u_1 \\ v_1 \end{pmatrix} | \begin{pmatrix} u_2 \\ v_2 \end{pmatrix}\right) = \int_{-h}^{h} (u_1u_2 + v_1v_2)dy$$

for the elastic waves with stress free boundary conditions at $y = \pm h$ since $\sigma_{xy}(\pm h) = 0$ and $\sigma_{yy}(\pm h) = 0$, see (81). It is then easy to show that $(k_m^2 - k_n^2)(\mathbf{X}_m|\mathbf{Y}_n) = 0$ for two Lamb modes with indices m and n. The chosen formalism and the properties of F and G allow to directly prove the bi-orthogonality condition:

$$(\mathbf{X}_n|\mathbf{Y}_m) = J_n\delta_{mn}. \tag{82}$$

Eventually, the projections on the Lamb modes are made easy: from the equations (79) and (80), the components a_n and b_n are given by

$$(\mathbf{Y}_n|\mathbf{X}) = J_n a_n$$

and

$$(\mathbf{X}_n|\mathbf{Y}) = J_n b_n.$$

5.3 2D edge resonance

Let us consider a very simple configuration: a 2D semi infinite elastic waveguide of width h embedded in vacuum. The edge is at $x = 0$ and the guide is in the $(x > 0, -h < y < h)$ region (geometry of Figure 34). If the

[13]This inner product is not a scalar product because the vectors $\mathbf{X}$ and $\mathbf{Y}$ are complex.

wave is excited at $x = 0$ by a source imposing $\mathbf{X}(x = 0, y)$ or $\mathbf{Y}(x = 0, y)$, the solution has only right-going wave and can be expressed as

$$\begin{cases} \mathbf{X} = \sum_{n\geq 0} \alpha_n e^{iq_n x} \mathbf{X}_n(y), \\ \mathbf{Y} = \sum_{n\geq 0} \alpha_n e^{iq_n x} \mathbf{Y}_n(y), \end{cases} \tag{83}$$

because $a_n^- = 0$. The coefficients α_n are uniquely determined by the bi-orthogonality relation (82)

$$(\mathbf{X}(x = 0, y)|\mathbf{Y}_n) = J_n \alpha_n \quad \text{or} \quad (\mathbf{Y}(x = 0, y)|\mathbf{X}_n) = J_n \alpha_n.$$

That means that, for this problem posed with an initial condition on $\mathbf{X}$ or $\mathbf{Y}$ (a mixed condition since it is concerned with one component of displacement and one component of the stress tensor), we have the uniqueness of the solution: the solution is zero for $\mathbf{X}(x = 0, y) = 0$ or $\mathbf{Y}(x = 0, y) = 0$.

What happens now if the the constraint $\sigma.n$ is imposed as a source at $x = 0$? It gives the values of σ_{xx} and σ_{xy} which corresponds to one component of $\mathbf{X}$ and one component of $\mathbf{Y}$. Thus, to impose the constraint $\sigma.n$ at $x = 0$ is a mixed condition in the $\mathbf{XY}$ formalism, and the bi-orthogonality relation does not allow the projection of the solution on the Lamb modes: it seems that uniqueness is not ensured. Said differently, if $\sigma_{xx} = 0$ and $\sigma_{xy} = 0$ are imposed at $x = 0$, it is possible to have a non-zero solution with outgoing radiation condition in the very simple problem of the semi-infinite elastic waveguide. This solution corresponds to a localized mode of vibration, trapped on the free edge at $x = 0$.

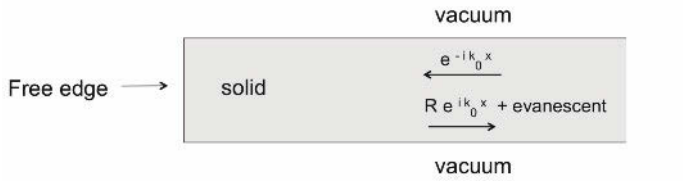

Figure 34. Reflection of the S_0 Lamb mode by a free edge.

The linear elastic equation can be written in a dimensionless from by normalizing all the lengths by the semi-width h and the stress by the Lamé coefficient μ:

$$\partial_x \begin{pmatrix} \mathbf{X} \\ \mathbf{Y} \end{pmatrix} = \begin{pmatrix} 0 & F \\ G & 0 \end{pmatrix} \begin{pmatrix} \mathbf{X} \\ \mathbf{Y} \end{pmatrix}, \tag{84}$$

with

$$F = \frac{1}{\gamma}\begin{pmatrix} -1 & -(\gamma-2)\partial_y \\ (\gamma-2)\partial_y & -\gamma\Omega^2 - 4(\gamma-1)\partial_{y^2} \end{pmatrix} \tag{85}$$

and

$$G = \begin{pmatrix} \Omega^2 & \partial_y \\ -\partial_y & 1 \end{pmatrix}, \tag{86}$$

with $\gamma = (\lambda + 2\mu)/\mu = c_L^2/c_T^2$. The boundary conditions $\sigma.n = 0$ at the traction free surfaces are

$$\begin{cases} \sigma_{xy} = 0 \\ \sigma_{yy} = 1/\gamma((\gamma-2)\sigma_{xx} + 4(\gamma-1)\partial_y u_y) = 0 \end{cases} \quad \text{at} \quad y = \pm 1, \tag{87}$$

on the horizontal faces and

$$\begin{cases} \sigma_{xy} = 0 \\ \sigma_{xx} = 0 \end{cases} \quad \text{at} \quad x = 0. \tag{88}$$

Since $\gamma = 2(1-\nu)/(1-2\nu)$ ($0 < \nu < 1/2$ is the Poisson ratio) and $\Omega = k_T h$, when made dimensionless, the problem of vibrations of the semi-infinite elastic waveguide *depends only on two parameters*: the frequency Ω and the Poisson ratio ν.

In the following we will consider only symmetric waves (with Lamb modes S_n) for frequency below the cut-on frequency of the mode S_1 (see points C_1 and C_2 in Figure 32): only the mode S_0 is propagating. To study the edge resonance it is convenient to pose the problem as a reflection problem. The situation is described in Figure 34 with a left-going S_0 incident wave and a reflected right-going field composed of the propagating S_0 (with reflection coefficient R) and the remaining evanescent Lamb modes $(S_1, S_2, S_3, ...)$. The solution can be written as[14]

$$\begin{pmatrix} \mathbf{X} \\ \mathbf{Y} \end{pmatrix} = e^{-ik_0 x}\begin{pmatrix} \mathbf{X}_0 \\ -\mathbf{Y}_0 \end{pmatrix} + Re^{ik_0 x}\begin{pmatrix} \mathbf{X}_0 \\ \mathbf{Y}_0 \end{pmatrix} + \sum_{n=1}^{+\infty} a_n e^{ik_n x}\begin{pmatrix} \mathbf{X}_n \\ \mathbf{Y}_n \end{pmatrix}. \tag{89}$$

For real frequency Ω, the conservation of energy imposes that $|R| = 1$. Several authors have studied that reflection coefficient (Shaw, 1956; Torvik, 1967; Auld and Tsao, 1977; M. Koshiba et al., 1983; Gregory and Gladwell, 1983; Le Clezio et al., 2003) and they all showed the same behavior of R as a function of the real frequency. Figure 35 displays this behavior for a

[14] In contrast to the previous section, the convention here is $\mathbf{X}_0^- = \mathbf{X}_0^+$ and $\mathbf{Y}_0^- = -\mathbf{Y}_0^+$ in order to have a reflection coefficient R tending to 1 at low frequencies.

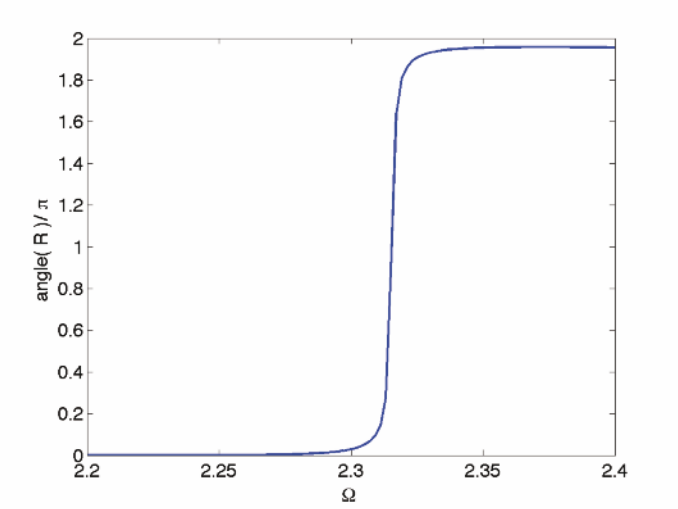

Figure 35. Phase of the reflection coefficient R as a function of frequency for $\nu = 0.3$.

Poisson ratio $\nu = 0.3$: the phase of R has a rapid variation of the phase near a particular frequency. This is the typical behavior of a quasi-trapped mode, i.e. a complex resonance frequency that has a finite quality factor in the harmonic regime (Ω real). By using the variational tools of functional analysis, Roitberg et al. (1998) have proved that a trapped mode exists for this free edge. The works in Zernov et al. (2006) and Pagneux (2006) have shown that, in fact, there is one complex resonance frequency Ω_R for each value of the Poisson ratio ν.

The complex resonance frequency Ω_R is written as

$$\Omega_R(\nu) = \Omega'_R(\nu) + i\Omega"_R(\nu)$$

which corresponds to a quality factor $Q = \Omega'_R/(2|\Omega"_R|)$. As seen in section 4, a complex resonance frequency is associated to a quasi-trapping without incident mode and it is also a pole of the reflection coefficient R with $\mathrm{Im}(\Omega) < 0$. The edge resonance frequency $\Omega_R(\nu)$ corresponds to a pole of $R(\Omega, \nu)$.

Figures 36 and 37 show the behavior of Ω_R as a function of the Poisson ratio. The real part is monotone and it corresponds to the value of the frequency of quasi-resonance in the harmonic regime (cf. Figure 36). A

very accurate empirical expression (Pagneux, 2006) for this real part is

$$\mathrm{Re}(\Omega_R) = 0.652\nu^2 + 0.898\nu + 1.9866$$

whose error is less than 10^{-3}.

The imaginary part of the complex resonance frequency has a more complicated behavior: Figure 28, which shows $-\Omega"_R$ on a logarithmic scale, demonstrates that there are two values of the Poisson ratio where the quasi-trapped mode becomes a perfectly trapped mode with a real resonance frequency. The perfect resonance at $\nu = 0$ is due to a particular symmetry of the elasticity equation discovered by Roitberg et al. (1998). They showed that, for $\nu = 0$ (i.e. $\lambda = 0$), the elastic field can be decomposed into two parts that are decoupled:

$$\begin{pmatrix} u_x \\ u_y \end{pmatrix} = \begin{pmatrix} \frac{1}{2h}\int_{-h}^{h} u_x dy \\ 0 \end{pmatrix} + \begin{pmatrix} u_x - \frac{1}{2h}\int_{-h}^{h} u_x dy \\ u_y \end{pmatrix}. \tag{90}$$

The first part contains the propagating S_0 mode and the second part all the remaining evanescent waves. This subtle decoupling is similar to the simpler one that was presented for trapped modes in Neumann waveguides in section 3, and it allows the trapped mode at the real Ω_R that does not radiate through the propagating S_0 Lamb mode. The other perfect resonance at $\nu = 0.2248$ can be explained by the uncoupled reflection of the Lamé mode (Pagneux, 2006). Note the low values of $\mathrm{Im}(\Omega_R)$ that imply that the edge resonance has a large quality factor.

5.4 Edge resonance for cylinders

The edge resonance exists also for semi-infinite cylinders with traction free boundary conditions (Gregory and Gladwell, 1989; Holst and Vassiliev, 2000; Pagneux, 2012). The problem under study corresponds to the semi-infinite circular rod geometry with the vertical edge at $z = 0$ and the horizontal surfaces at $r = a$, where (r, θ, z) are the cylindrical coordinates. The domain of the solid rod is defined by $r < a$ and $z > 0$.

We consider elastic waves that are axially symmetric with displacement components in the radial and axial directions (Zemanek, 1972; Graff, 1991): $\mathbf{w} = (u_r(r,z), 0, u_z(r,z))^T$. By taking into account these symmetries and by making dimensionless the equations (renormalizing all the lengths by a and the stress tensor by μ), the equations become

$$\begin{aligned} -\Omega^2 u_r &= \partial_r \sigma_{rr} + \partial_z \sigma_{rz} + \frac{\sigma_{rr} - \sigma_{\theta\theta}}{r}, \\ -\Omega^2 u_z &= \partial_r \sigma_{rz} + \partial_z \sigma_{zz} + \frac{\sigma_{rz}}{r}, \end{aligned} \tag{91}$$

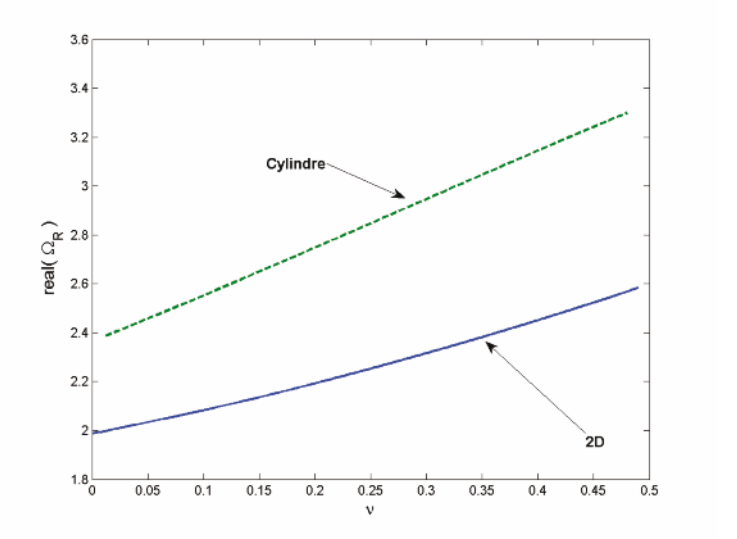

Figure 36. Real part of the complex resonance frequency.

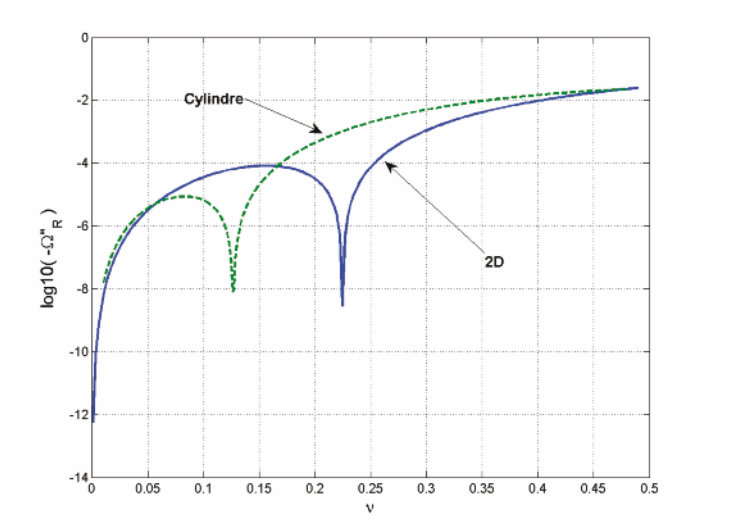

Figure 37. Imaginary part of the complex resonance frequency.

$$\begin{aligned}
\sigma_{rr} &= 2\partial_r u_r + (\gamma-2)(\frac{1}{r}\partial_r(ru_r) + \partial_z u_z),\\
\sigma_{\theta\theta} &= 2\frac{u_r}{r} + (\gamma-2)(\frac{1}{r}\partial_r(ru_r) + \partial_z u_z),\\
\sigma_{zz} &= 2\partial_z u_z + (\gamma-2)(\frac{1}{r}\partial_r(ru_r) + \partial_z u_z),\\
\sigma_{rz} &= \partial_z u_r + \partial_r u_z,
\end{aligned} \tag{92}$$

with the frequency $\Omega = \omega a/c_T$. It is similar to the one defined in 2D with the 2D semi-height h replaced by the radius a.

The stress free boundary conditions at the horizontal surface ($r = 1$) and at the free edge ($z = 0$) are

$$\begin{aligned}
&\sigma_{rr} = \sigma_{rz} = 0 \quad \text{at } r = 1,\\
&\sigma_{zz} = \sigma_{rz} = 0 \quad \text{at } z = 0.
\end{aligned} \tag{93}$$

Note that, as in 2D, there are only two parameters: the frequency Ω and the Poisson ratio ν.

In this axisymmetric geometry the Lamb modes are replaced by the Pochhammer modes (Graff, 1991) whose dispersion relation is

$$(-k^2+b^2)^2 J_0(d)J_1(b) + 4bdk^2 J_0(b)J_1(d) - 2d\Omega^2 J_1(d)J_1(b) = 0$$

with $b = \sqrt{\Omega^2 - k^2}$ and $d = \sqrt{\Omega^2/\gamma - k^2}$. We will consider frequency Ω such that only the first mode, $n = 0$, is a propagating mode and it will be called the L_0 mode. All the other modes, L_n with $n \geq 1$, are evanescent with $\mathrm{Im}(k_n) > 0$.

As in 2D, there is one complex resonance frequency Ω_R for each value of the Poisson ratio ν. The real value of Ω_R is displayed in Figure 36. The quasi-linear behavior as a function of ν is very well approximated (Pagneux, 2012) by the empirical formula

$$\mathrm{Re}(\Omega_R) = 1.9624\nu + 2.3573,$$

accurate up to 0.3%. Figure 37 shows the behavior of the imaginary part of Ω_R. Once again, as in 2D, there are two values of the Poisson ratio where the trapping is perfect with a zero imaginary part of Ω_R and no radiation from the edge. The first value ($\nu = 0$) was discovered by Holst and Vassiliev (2000) by the use of a symmetry similar the one of equation (90) and the second value ($\nu = 0.1267$) was found in Pagneux (2012) and it is linked to the Lamé mode. The shape of the localized vibration is shown if FIgure 38.

5.5 Edge resonance in 3D plate

The study of the 2D elastic edge resonance has been extended to 3D in Zernov and Kaplunov (2008). These authors have shown that along the

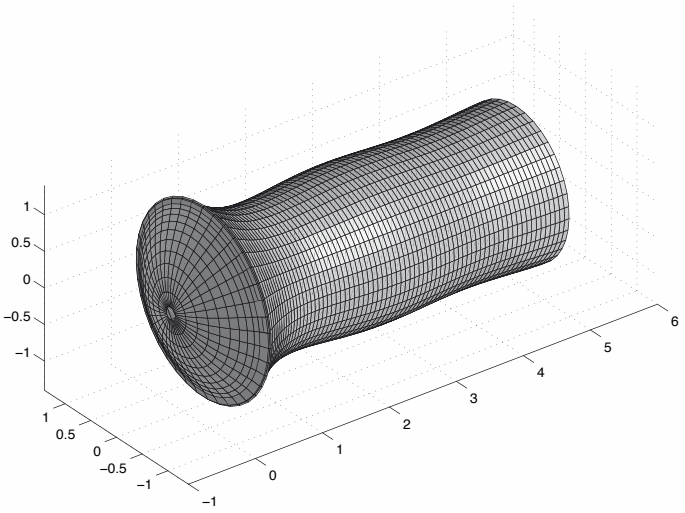

Figure 38. Shape of the localized vibration at edge resonance for $\nu = 0.3$.

stress free straight edge there are two edge waves: the first one has no cut-on frequency and is similar to a generalized Rayleigh wave, the second one is the 3D counterpart of the 2D edge resonance we have considered before with Ω_R playing the role of the cut-on frequency.

Another 3D plate configuration is the one depicted in Figure 39. In this case, it can be shown (Pagneux and Clorennec, 2012) that there exists also a edge resonance for axisymmetric vibration around the hole.

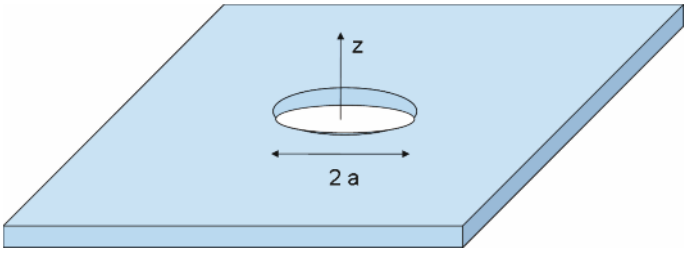

Figure 39. Hole in a 3D plate.

5.6 Concluding remarks

In these notes, we looked at the perfectly localized trapped modes and the ubiquitous slightly radiating quasi-trapped modes. In practice, the difference between these two families of modes is not so clear since, in an experiment, the inevitable attenuation prevents an infinite quality factor (i.e. a perfect resonance). It remains that the study of trapped modes provides clues to efficient resonance mechanisms. The specific ability of trapping for elastic waves near surface with traction-free boundary condition has also been discussed. The well known Rayleigh surface wave already testifies to this ability. Few examples in elastic waveguides have been examined in this chapter and the conclusion might be that we have to mind the edge effects in elastodynamics.

Bibliography

A. Aslanyan, L. Parnovski and D. Vassiliev. Complex Resonances In Acoustic Waveguides. *Quarterly J. Mechanics Applied Mathematics*, 53: 429–447, 2000.

A. Auld and E. M. Tsao. A variational analysis of edge resonance in a semi-infinite plate. *IEEE Trans. Sonics Ultrason.*, 24: 317–326, 1977.

A.S. Bonnet-BenDhia and F. Mahé. A guided mode in the range of the radiation modes for a rib waveguide. *J. Optics*, 28: 4143, 1997.

A.S. Bonnet-BenDhia and J.F. Mercier. Resonances of an elastic plate in a compressible confined fluid. *Quarterly Journal of Mechanics and Applied Mathematics*, 60: 397–421, 2007.

M. Callan, C. M. Linton and D. V. Evans. Trapped modes in two-dimensional waveguides. *J. Fluid Mech.*, 229: 51-64, 1991.

P. Cobelli, V. Pagneux, A. Maurel and P. Petitjeans. Experimental study on water wave trapped modes. *J. Fluid Mech.*, 666: 445–476, 2011.

P. Duclos and P. Exner. Curvature-induced bound states in quantum waveguides in two and three dimensions. *Rev. Math. Phys.*, 7: 73–102, 1995.

D.V. Evans, M. Levitin, and D. Vassiliev. Existence theorems for trapped modes. *J. Fluid Mech.*. 26: 21-31, 1994.

L. Flax, G.C. Gaunaurd and H. berall. Theory of resonance scattering. *Physical Acoustics*, Volume 15, pages 191-294, 1981.

K.F. Graff. *Wave Motion in Elastic Solids*, Dover, 1991.

E. Granot. Emergence of a confined state in a weakly bent wire. *Phys. Rev. B*, 65: 233101, 2002.

R. D. Gregory and I. Gladwell. The reflection of a symmetric Rayleigh-Lamb wave at the fixed or free edge of a plate. *J. Elast.*, 13: 185–206, 1983.

R.D. Gregory and I. Gladwell. Axisymmetric waves in a semi-infinite elastic rod. *Q. J. Mech. Appl. Math.*, 42: 327–337, 1989.

A. Holst and D. Vassiliev. Edge resonance in an elastic semi-infinite cylinder. *Applicable Anal.*, 74: 479–495, 2000.

D. S. Jones. The eigenvalues of $\nabla^2 u + \lambda u = 0$ when the boundary conditions are given in semi-infinite domains. *Proc. Camb. Phil. Soc.*, 49: 668–684, 1953.

J. D. Kaplunov and S.V. Sorokin. A simple example of a trapped mode in an unbounded waveguide. *J. Acoust. Soc. Am.*, 97: 3898, 1995.

M. Koshiba, S. Karakida, and M. Suzuki. Finite-element analysis of edge resonance in a semi-infinite plate. *Electron. Lett.*, 19: 256–257, 1983.

L. D. Landau and E. M. Lifshitz. *Quantum Mechanics: Nonrelativistic Theory*, Pergamon Press, 1977

E. Le Clezio, M. V. Predoi, M. Castaings, B. Hosten, and M. Rousseau. Numerical predictions and experiments on the free-plate edge mode, *Ultrasonics*, 41: 25–40, 2003.

C.M. Linton and P. McIver. Embedded trapped modes in water waves and acoustics. *Wave Motion*, 45: 16-29, 2007.

M. McIver, C.M. Linton, P. McIver, J. Zhang and R. Porter. Embedded trapped modes for obstacles in two-dimensional waveguides. *Quarterly J. Mechanics Applied Mathematics*, 54: 273–293, 2001.

P. M. Morse and K, U. Ingard. *Theoretical Acoustics*, McGraw Hill, New York, 1968.

S.A. Nazarov. Asymptotic expansions of eigenvalues in the continuous spectrum of a regularly perturbed quantum waveguide *Theoretical and mathematical physics*, 167: 606–627, 2011.

V. Pagneux and A. Maurel. Lamb wave propagation in inhomogeneous elastic waveguides. *Proc. R. Soc. London, Ser. A*, 458: 19131930, 2002.

V. Pagneux and A. Maurel. Scattering matrix properties with evanescent modes for waveguides in fluids and solids. *J. Acoust. Soc. Am.*, 116: 1913–1920, 2004.

V. Pagneux and A. Maurel. Lamb wave propagation in elastic waveguides with variable thickness. *Proc R Soc Lond A*, 462: 1315–1339, 2006.

V. Pagneux. Revisiting the edge resonance for Lamb waves in a semi-infinite plate. *J. Acoust. Soc. Am.*,120: 649–656, 2006.

V. Pagneux. Complex resonance and localized vibrations at the edge of a semi-infinite elastic cylinder. *Mathematics and Mechanics of Solids*, 17: 17–26, 2012.

V. Pagneux and D. Clorennec. Complex edge resonance around a hole in a 3D plate. *to be submitted*, 2012.

J. Postnova and R.V. Craster. Trapped modes in elastic plates, ocean and quantum waveguides. *Wave Motion*, 45: 565-579, 2008.

I. Roitberg, D. Vassiliev, and T. Weidl. Edge resonance in an elastic semi-strip. *Q. J. Mech. Appl. Math.*, 51: 1–13, 1998.

E. A. G. Shaw. On the resonant vibrations of thick barium titanate disks. *J. Acoust. Soc. Am.*, 28: 38–50, 1956.

I. Stakgold. *Green's Functions and Boundary Value Problems*, Wiley Interscience, 1998.

P. J. Torvik. Reflection of wave trains in semi-infinite plates. *J. Acoust. Soc. Am.*, 41: 346–353,1967.

J. Zemanek. An experimental and theoretical investigation of elastic wave propagation in a cylinder. *J. Acoust. Soc. Am.*, 51: 265–283, 1972.

V. Zernov, A.V. Pichugin and J. Kaplunov. Eigenvalue of a semi-infinite elastic strip. *Proc. R. Soc. Lond. A*, 462: 1255–1270, 2006.

V. Zernov and J. Kaplunov. Three-dimensional edge waves in plates. *Proc. R. Soc. Lond. A*, 464: 301–318, 2008.

Surface waves in elastic half spaces coated with crystalline films

David J. Steigmann
Department of Mechanical Engineering, University of California, Berkeley, CA. 94720, USA

Abstract A two-dimensional model of thin-film substrate interactions is obtained from three-dimensional elasticity theory for films having various kinds of crystalline symmetry. Extensions to electroelastic behaviour are also discussed.

1 Introduction

Considered here is the general theory of surface wave propagation in elastic thin-film/substrate systems. Elasticity is of course an inherently nonlinear subject, although a great many applications are amenable to analysis using the linear theory, including those developed here. Thus for the sake of completeness and to establish the logical progression of our work we present a brief tutorial on the general nonlinear purely mechanical theory as a prelude to linearization.

The main contribution of the present work is the derivation of and solution to an asymptotic *two*-dimensional theory for the dynamics of a thin film bonded to a substrate, as distinct from the asymptotic treatment of the underlying three-dimensional equations [6]. Here the small parameter is the film thickness, and the considered model furnishes the rigorous leading-order system when this is small against the wavelength of a propagating surface wave.

The purely elastic theory is developed first, followed by an extension to electroelasticity. We draw particular attention to some non-standard effects associated with the propagation of Love waves in conventional isotropic elastic half spaces coated with thin films having various kinds of crystalline symmetry.

Standard notation is used throughout. Thus we use bold face for vectors and tensors and indices to denote their components. Latin indices take values in $\{1, 2, 3\}$; Greek in $\{1, 2\}$. The latter are associated with surface coordinates and associated vector and tensor components. A dot between

R. Craster, J. Kaplunov (Eds.), *Dynamic Localization Phenomena in Elasticity, Acoustics and Electromagnetism*, CISM International Centre for Mechanical Sciences,
DOI 10.1007/978-3-7091-1619-7_6,

bold symbols is used to denote the standard inner product. Thus, if $\mathbf{A}_1$ and $\mathbf{A}_2$ are second-order tensors, then $\mathbf{A}_1 \cdot \mathbf{A}_2 = tr(\mathbf{A}_1\mathbf{A}_2^t)$, where $tr(\cdot)$ is the trace and the superscript ^{t} is used to denote the transpose. The norm of a tensor $\mathbf{A}$ is $|\mathbf{A}| = \sqrt{\mathbf{A}\cdot\mathbf{A}}$. The linear operator $Sym(\cdot)$ delivers the symmetric part of its second-order tensor argument. The notation $\otimes$ identifies the standard tensor product of vectors. If $\mathcal{C}$ is a fourth-order tensor, then $\mathcal{C}[\mathbf{A}]$ is the second-order tensor with orthogonal components $\mathcal{C}_{ijkl}A_{kl}$. The transpose $\mathcal{C}^t$ is defined by $\mathbf{B}\cdot\mathcal{C}^t[\mathbf{A}] = \mathbf{A}\cdot\mathcal{C}[\mathbf{B}]$, and $\mathcal{C}$ is said to possess major symmetry if $\mathcal{C}^t = \mathcal{C}$. If $\mathbf{A}\cdot\mathcal{C}[\mathbf{B}] = \mathbf{A}^t\cdot\mathcal{C}[\mathbf{B}]$ and $\mathbf{A}\cdot\mathcal{C}[\mathbf{B}] = \mathbf{A}\cdot\mathcal{C}[\mathbf{B}^t]$ then $\mathcal{C}$ is said to possess minor symmetry. We use symbols such as Div and $Grad$ to denote the three-dimensional divergence and gradient operators, while div and ∇ are reserved, after Section 2, for their two-dimensional counterparts. Thus, for example, $Div\mathbf{A} = A_{ij,j}\mathbf{e}_i$ and $div\mathbf{A} = A_{i\alpha,\alpha}\mathbf{e}_i$, where $\{\mathbf{e}_i\}$ is an orthonormal basis and subscripts preceded by commas are used to denote partial derivatives with respect to Cartesian coordinates. Finally, the notation $F_{\mathbf{A}}$ stands for the tensor-valued derivative of a scalar-valued function $F(\mathbf{A})$.

2 Brief resumé of nonlinear elasticity theory

Background material on nonlinear elasticity theory is given in [3; 9; 1]. The basic problem in this theory is to find a deformation function mapping the position $\mathbf{x}$ of a material point of a body, in some reference configuration κ, to the position $\mathbf{y}$ of the same material point of the body in its current configuration at time t. Thus we seek a function $\boldsymbol{\chi}(\boldsymbol{\cdot}, t)$ such that $\mathbf{y} = \boldsymbol{\chi}(\boldsymbol{x}, t)$. This is presumed to be invertible at each fixed t, to reflect the notion that any given position may be occupied by one, and only one, material point at any instant. The inverse function theorem then requires that the deformation gradient,

$$\mathbf{F} = Grad\boldsymbol{\chi}, \tag{1}$$

the gradient of $\boldsymbol{\chi}(\boldsymbol{\cdot}, t)$ with respect to $\mathbf{x}$, be invertible.

The motion χ must be such as to satisfy the linear momentum balance

$$div\mathbf{T} + \rho\mathbf{b} = \rho\mathbf{y}_{tt}, \tag{2}$$

where $\mathbf{y}_t = \partial\boldsymbol{\chi}(\boldsymbol{x}, t)/\partial t$, etc., ρ is the mass density in the current configuration, $\mathbf{b}$ is the body force per unit mass, $\mathbf{T}$ is the Cauchy stress, and div is the divergence operator with respect to position $\mathbf{y}$. Granted (2), the moment-of-momentum balance is simply the requirement that the Cauchy stress be symmetric, i.e.

$$\mathbf{T} = \mathbf{T}^t. \tag{3}$$

Standard boundary data consist in the specification of $\mathbf{y}$ and the traction

$$\mathbf{t} = \mathbf{T}\mathbf{n} \tag{4}$$

on complementary parts of the boundary, where $\mathbf{n}$ is the exterior unit normal to the bounding surface of the body in its current configuration.

For purposes of analysis it is convenient to recast (2) as a differential equation defined on the specified reference configuration κ. The relevant equation is

$$Div\mathbf{P} + \rho_\kappa \mathbf{b} = \rho_\kappa \mathbf{y}_{tt}, \tag{5}$$

where ρ_κ is the mass density in κ, and

$$\mathbf{P} = \mathbf{T}\mathbf{F}^* \tag{6}$$

is the Piola stress, in which

$$\mathbf{F}^* = J\mathbf{F}^{-t} \tag{7}$$

is the cofactor of the deformation gradient, with

$$J = \det \mathbf{F}. \tag{8}$$

Normally we denote the inverse by appending a superscript -1; here $-t$ is the transposed inverse, or inverted transpose, the two being equivalent by virtue of the commutativity of the inverse and transpose operations. If κ is a configuration that could in principle be occupied by the material (e.g., an initial configuration), then the requirement

$$J > 0 \tag{9}$$

is imposed to reflect the physical requirement that matter deforms without self penetration.

The referential and current mass densities are connected by

$$\rho_\kappa = \rho J \tag{10}$$

and conservation of mass requires that ρ_κ be independent of t when expressed as a function of $\mathbf{x}$ and t. Accordingly it is regarded as an assigned function of $\mathbf{x}$.

The connection between the Cauchy and Piola stresses is most readily understood by expressing the force acting on an arbitrary material surface $S \subset \kappa$ in the alternative forms

$$\int_s \mathbf{t} da = \int_S \mathbf{p} dA, \tag{11}$$

where $s = \chi(S,t)$ is the image of the material surface in the current configuration, consisting of the same set of material points. Using Nanson's formula

$$\alpha \mathbf{n} = \mathbf{F}^* \mathbf{N}, \tag{12}$$

in which $\mathbf{N}$ is the exterior unit normal to S and $\alpha = |\mathbf{F}^*\mathbf{N}|$ is the areal stretch of S, we then use (4) to obtain

$$\int_S \mathbf{p} dA = \int_s \mathbf{T}\mathbf{n} da = \int_S \mathbf{T}\mathbf{F}^*\mathbf{N} dA, \tag{13}$$

and hence

$$\mathbf{p} = \mathbf{P}\mathbf{N}. \tag{14}$$

Thus the Piola stress operates on the referential unit normal to furnish the force per unit reference area.

To model elastic bodies we assume the stress $\mathbf{T}$ (or $\mathbf{P}$) to be given by an empirical function of $\mathbf{F}$, which may depend parametrically on $\mathbf{x}$ if the material properties are non-uniform, as in a functionally graded material. Thermodynamic considerations pertaining to the non-existence of perpetual motion machines imply that the stress is determined via an empirical *strain-energy* function $W(\mathbf{F})$, i.e. [9]

$$\mathbf{P} = W_{\mathbf{F}}, \tag{15}$$

the gradient of W with respect to $\mathbf{F}$. This too depends parametrically on $\mathbf{x}$ in non-uniform materials. Here, however, we are concerned exclusively with uniform materials, for which there is no such dependence.

Combining (6) with (15) we conclude that the function W must be such that $(W_{\mathbf{F}})\mathbf{F}^t$ is symmetric; that is, equal to its own transpose. This in turn is equivalent to

$$(W_{\mathbf{F}})\mathbf{F}^t \cdot \mathbf{\Omega} = 0 \tag{16}$$

for *all* skew tensors $\mathbf{\Omega}$ ($\mathbf{\Omega}^t = -\mathbf{\Omega}$). The symmetries inherent in the dot product imply that (16) is equivalent to

$$W_{\mathbf{F}} \cdot \mathbf{\Omega}\mathbf{F} = 0. \tag{17}$$

Fix $\mathbf{\Omega}$ and consider the one-parameter family of tensors $\mathbf{Q}(u)$ defined by the initial-value problem

$$\dot{\mathbf{Q}} = \mathbf{\Omega}\mathbf{Q} \quad \text{with} \quad \mathbf{Q}(0) = \mathbf{I}, \tag{18}$$

where $\mathbf{I}$ is the identity tensor and the superposed dot is the derivative with respect to u. The components of the identity are simply the Kronecker deltas

δ_{ij}. It is well known that the set of such $\mathbf{Q}'s$ coincides precisely the group of rotation tensors, i.e.

$$\mathbf{Q}^{-1} = \mathbf{Q}^t; \quad \det \mathbf{Q} = 1. \tag{19}$$

Consider an associated one-parameter family of deformation gradients defined by

$$\mathbf{F}(u) = \mathbf{Q}(u)\mathbf{F}_0, \quad \text{with} \quad \mathbf{F}_0 = \mathbf{F}(0). \tag{20}$$

This is a rotation superposed on a deformation with gradient $\mathbf{F}_0$. Then,

$$\dot{\mathbf{F}} = \dot{\mathbf{Q}}\mathbf{F}_0 = \dot{\mathbf{Q}}\mathbf{Q}^t\mathbf{F} = \mathbf{\Omega}\mathbf{F}, \tag{21}$$

and for this family of deformations we find, using (17) and the chain rule, that

$$\dot{W} = W_{\mathbf{F}} \cdot \dot{\mathbf{F}} = 0, \tag{22}$$

so that $W(\mathbf{F}(u))$ is independent of u, i.e.

$$W(\mathbf{Q}\mathbf{F}_0) = W(\mathbf{F}_0), \tag{23}$$

in which the rotation $\mathbf{Q}$ is arbitrary.

A necessary condition follows on identifying $\mathbf{Q}$ with the transpose of the rotation factor $\mathbf{R}_0$ in the polar decomposition

$$\mathbf{F} = \mathbf{R}\mathbf{U} \tag{24}$$

of the deformation gradient, where $\mathbf{U}$ is the positive definite, symmetric right-stretch tensor. This yields the conclusion that W is determined by the stretch, i.e. $W(\mathbf{F}_0) = W(\mathbf{U}_0)$. However, this is inconvenient in practice because $\mathbf{U}$ is not easily obtained from $\mathbf{F}$. To circumvent this we note that there is a one-to-one relation between the right stretch and the symmetric Cauchy-Green deformation tensor $\mathbf{C} = \mathbf{U}^2 = \mathbf{F}^t\mathbf{F}$; the former is the unique positive definite symmetric square root of the latter. We conclude that $\mathbf{U}$ is determined by $\mathbf{C}$ and hence (dropping subscripts in (23)) that $W(\mathbf{F}) = \hat{W}(\mathbf{C})$ for some function $\hat{W}$. In turn, the Cauchy-Green tensor stands in one-to-one relation to the symmetric Lagrange strain

$$\boldsymbol{\epsilon} = \tfrac{1}{2}(\mathbf{F}^t\mathbf{F} - \mathbf{I}) \tag{25}$$

and so we may write $W(\mathbf{F}) = \bar{W}(\boldsymbol{\epsilon})$ for some function $\bar{W}$. An elementary application of the chain rule then furnishes

$$W_{\mathbf{F}} = \mathbf{F}\bar{W}_{\boldsymbol{\epsilon}}, \tag{26}$$

where, on the right-hand side, $\bar{W}_{\boldsymbol{\epsilon}}$ is the symmetric tensor-valued gradient with respect to strain. Accordingly, the 2nd Piola-Kirchhoff stress $\mathbf{S}$, defined by

$$\mathbf{P} = \mathbf{FS}, \tag{27}$$

is given by

$$\mathbf{S} = \bar{W}_{\boldsymbol{\epsilon}}. \tag{28}$$

Comparison of (6) and (27) yields $J\mathbf{T} = \mathbf{FSF}^t$, and so the symmetry of $\mathbf{S}$, implied by (23), yields the symmetry of $\mathbf{T}$. It follows that (23) is both necessary and sufficient for the symmetry of the Cauchy stress.

We neglect body forces, and thus reduce (5) and (15) to the system

$$Div(W_{\mathbf{F}}) = \rho_\kappa \boldsymbol{\chi}_{tt} \tag{29}$$

for the determination of the motion $\boldsymbol{\chi}(\boldsymbol{x}, t)$, in which ρ_κ is an assigned constant if, as we assume, the material properties are uniform.

In this work we restrict attention to deformations for which the strong ellipticity condition is satisfied, i.e.

$$\mathbf{a} \otimes \mathbf{b} \cdot W_{\mathbf{FF}}[\mathbf{a} \otimes \mathbf{b}] > 0 \quad \text{for all} \quad \mathbf{a} \otimes \mathbf{b} \neq \mathbf{0}. \tag{30}$$

3 Leading order model for a thin, nonlinearly elastic film in the long-wave limit

We seek equations of motion for a thin film bonded to a substrate that are valid to leading order in the film thickness, presumed to be small against the length scale afforded by the wavelength of a propagating surface wave. Thus the model to be derived and studied is valid in the long-wave limit.

Consider a planar film of thickness h, bonded to an elastic half space. The interface between film and substrate, denoted by Ω, is an unbounded plane with unit normal $\mathbf{k}$ directed away from the substrate. It proves advantageous to decompose three-dimensional position $\mathbf{x}$ in the film in terms of position $\mathbf{r}$ to a projected point on Ω and a linear coordinate ς in the direction of the normal. Thus,

$$\mathbf{x} = \mathbf{r} + \varsigma \mathbf{k}, \quad \text{with} \quad \mathbf{r} \in \Omega \quad \text{and} \quad \varsigma \in [0, h]. \tag{31}$$

The motion of the film may then be regarded as a function of $\mathbf{r}$ and ς, i.e. $\mathbf{y} = \boldsymbol{\chi}(\mathbf{x}, t) = \hat{\boldsymbol{\chi}}(\boldsymbol{r}, \varsigma, t)$; we also write $\mathbf{F}(\mathbf{x}, t) = \hat{\mathbf{F}}(\mathbf{r}, \varsigma, t)$. It then follows from the definition of the gradient that

$$(\nabla \mathbf{y}) d\mathbf{r} + \mathbf{y}' d\varsigma = d\mathbf{y} = \hat{\mathbf{F}} d\mathbf{x} = \hat{\mathbf{F}} \mathbf{1} d\mathbf{r} + \hat{\mathbf{F}} \mathbf{k} \otimes \mathbf{k} d\varsigma, \tag{32}$$

where $(\cdot)' = \partial(\cdot)/\partial\varsigma$, $\nabla(\cdot)$ is the (two-dimensional) gradient with respect to $\mathbf{r}$ and

$$\mathbf{1} = \mathbf{I} - \mathbf{k} \otimes \mathbf{k} \tag{33}$$

is the projection onto the plane Ω. This yields

$$\nabla \mathbf{y} = \hat{\mathbf{F}}\mathbf{1} \quad \text{and} \quad \mathbf{y}' = \hat{\mathbf{F}}\mathbf{k}. \tag{34}$$

Using a similar notation for the Piola stress, we write $\mathbf{P} = \hat{\mathbf{P}}\mathbf{1} + \hat{\mathbf{P}}\mathbf{k} \otimes \mathbf{k}$ and find that

$$Div\mathbf{P} = div(\hat{\mathbf{P}}\mathbf{1}) + \hat{\mathbf{P}}'\mathbf{k}, \tag{35}$$

where, in contrast to its use in (2), *div* is now the (two-dimensional) referential divergence operator on Ω. Thus (5) may be recast in the convenient form

$$div(\hat{\mathbf{P}}\mathbf{1}) + \hat{\mathbf{P}}'\mathbf{k} = \rho_\kappa \hat{\boldsymbol{\chi}}_{tt}. \tag{36}$$

We seek a *two-dimensional* model of the thin film, in terms of differential operators defined entirely on Ω. To effect the dimension reduction, we adopt the weak form of the equations of motion in which the film thickness is made explicit. We then estimate this for small thickness and extract the leading-order local equations.

To this end let $\mathbf{y}(\mathbf{x}, t, \mu)$ be a one-parameter (μ) family of motions, let the actual motion $\mathbf{y} = \boldsymbol{\chi}(\mathbf{x}, t)$ be its value at $\mu = 0$, and let

$$\dot{\mathbf{y}} = \frac{\partial}{\partial \mu}\mathbf{y}(\mathbf{x}, t, \mu)_{|\mu=0}. \tag{37}$$

Then the weak form of (5), holding in an arbitrary subvolume π of the film, is

$$\int_\pi \mathbf{P} \cdot \dot{\mathbf{F}} dV = \int_{\partial\pi} \mathbf{P}\mathbf{N} \cdot \dot{\mathbf{y}} dA - \int_\pi \rho_\kappa \dot{\mathbf{y}} \cdot \mathbf{y}_{tt} dV, \tag{38}$$

in which

$$\dot{\mathbf{F}} = \nabla \dot{\mathbf{y}} + \dot{\mathbf{y}}' \otimes \mathbf{k}, \tag{39}$$

where $\dot{\mathbf{y}}' = (\mathbf{y}')^{\cdot} = (\dot{\mathbf{y}})'$. We remark that, on the film/substrate interface Ω, the deformation gradient is

$$\mathbf{F}_0 = \nabla \mathbf{y}_0 + \mathbf{d} \otimes \mathbf{k}, \tag{40}$$

where, here and henceforth, the notation $(\cdot)_0$ stands for the restriction $(\cdot)_{|\Omega}$ of a variable defined in the film. This is the interior limit of the considered quantity as $\varsigma \to 0$. In particular,

$$\mathbf{y}_0(\mathbf{r}, t) = \hat{\mathbf{y}}(\mathbf{r}, 0, t) \quad \text{and} \quad \mathbf{d}(\mathbf{r}, t) = \hat{\mathbf{y}}'(\mathbf{r}, 0, t), \tag{41}$$

and these are *independent* vector fields on Ω.

Proceeding from (38) and (39), we have

$$\int_\pi \mathbf{P}\cdot\dot{\mathbf{F}}dV = \int_\pi (\mathbf{P1}\cdot\nabla\dot{\mathbf{y}}+\mathbf{Pk}\cdot\dot{\mathbf{y}}')dV = \int_\omega\int_0^h (\mathbf{P1}\cdot\nabla\dot{\mathbf{y}}+\mathbf{Pk}\cdot\dot{\mathbf{y}}')d\varsigma dA, \quad (42)$$

where $\omega\subset\Omega$ is an arbitrary part of Ω and we have selected $\pi=\omega\times[0,h]$. For an arbitrary function $g(\mathbf{r},\varsigma)$ we use the Taylor expansion

$$\int_0^h g d\varsigma := I(\mathbf{r},h) = hI'(\mathbf{r},0)+o(h), \quad \text{with} \quad I'(\mathbf{r},h)=g(\mathbf{r},h), \qquad (43)$$

to derive the estimate

$$I(\mathbf{r},h) = hg_0+o(h), \qquad (44)$$

and thus estimate (42) as

$$\int_\pi \mathbf{P}\cdot\dot{\mathbf{F}}dV = h\int_\omega(\mathbf{P}_0\mathbf{1}\cdot\nabla\dot{\mathbf{y}}_0+\mathbf{P}_0\mathbf{k}\cdot\dot{\mathbf{d}})dA+o(h). \qquad (45)$$

Similarly,

$$\int_\pi \rho_\kappa\dot{\mathbf{y}}\cdot\mathbf{y}_{tt}dV = h\int_\omega \rho_\kappa\dot{\mathbf{y}}_0\cdot\mathbf{y}_{0tt}dA+o(h). \qquad (46)$$

The remaining integral in (38) may be decomposed as

$$\int_{\partial\pi}\mathbf{PN}\cdot\dot{\mathbf{y}}dA = \int_{\partial\omega}\int_0^h \mathbf{P1}\boldsymbol{\nu}\cdot\dot{\mathbf{y}}d\varsigma dS+\int_{\omega^+}\mathbf{P}^+\mathbf{k}\cdot\dot{\mathbf{y}}^+dA-\int_\omega\mathbf{P}_0\mathbf{k}\cdot\dot{\mathbf{y}}_0dA, \qquad (47)$$

where ω^+ is the upper surface of the film at a distance h from ω, $\mathbf{k}$ and $-\mathbf{k}$ are the exterior unit normals to the film at ω^+ and ω, the superscript $+$ is used to denote the values of variables at $\varsigma=h$, and $\boldsymbol{\nu}$ is the external unit normal to the cylindrical generating surface $\partial\omega\times[0,h]$.

Traction continuity at the film/substrate interface Ω implies that

$$\mathbf{P}_0\mathbf{k} = \mathbf{P}_s\mathbf{k}, \qquad (48)$$

where $\mathbf{P}_s$ is the limiting value of the *substrate* stress on Ω. Assuming the upper surface of the film to be traction free, i.e. $\mathbf{P}^+\mathbf{k}=\mathbf{0}$, and using the rule (44), we then have

$$\int_{\partial\pi}\mathbf{PN}\cdot\dot{\mathbf{y}}dA = h\int_{\partial\omega}\mathbf{P}_0\mathbf{1}\boldsymbol{\nu}\cdot\dot{\mathbf{y}}_0dS-\int_\omega\mathbf{P}_s\mathbf{k}\cdot\dot{\mathbf{y}}_0dA+o(h). \qquad (49)$$

Substituting this, together with (45) and (46), into (38), we conclude that

$$\int_{\omega} \mathbf{P}_s \mathbf{k} \cdot \dot{\mathbf{y}}_0 dA = O(h) \tag{50}$$

and hence, from the arbitrariness of ω and $\dot{\mathbf{y}}_0$, that $\mathbf{P}_s\mathbf{k} = O(h)$, i.e.

$$\mathbf{P}_s \mathbf{k} = h\mathbf{l} + o(h), \tag{51}$$

in which $\mathbf{l}(\mathbf{r}, t)$ is independent of h. Substituting back into the balance (38), dividing by h and passing to the limit then yields

$$\int_{\omega} [\mathbf{P}_0 \mathbf{1} \cdot \nabla \dot{\mathbf{y}}_0 + \mathbf{P}_0 \mathbf{k} \cdot \dot{\mathbf{d}} + \dot{\mathbf{y}}_0 \cdot (\rho_\kappa \mathbf{y}_{0tt} + \mathbf{l})] dA = \int_{\partial\omega} \mathbf{P}_0 \mathbf{1} \nu \cdot \dot{\mathbf{y}}_0 dS. \tag{52}$$

Applying Green's theorem in the form

$$\int_{\partial\omega} \mathbf{P}_0 \mathbf{1} \boldsymbol{\nu} \cdot \dot{\mathbf{y}}_0 dS = \int_{\partial\omega} \boldsymbol{\nu} \cdot (\mathbf{P_0 1})^t \dot{\mathbf{y}}_0 dS =$$

$$\int_{\omega} div[(\mathbf{P_0 1})^t \dot{\mathbf{y}}_0] dA = \int_{\omega} [\dot{\mathbf{y}}_0 \cdot div(\mathbf{P}_0 \mathbf{1}) + \mathbf{P}_0 \mathbf{1} \cdot \nabla \dot{\mathbf{y}}_0] dA, \tag{53}$$

we reduce (52) to

$$\int_{\omega} \{\mathbf{P}_0 \mathbf{k} \cdot \dot{\mathbf{d}} - \dot{\mathbf{y}}_0 \cdot [div(\mathbf{P}_0 \mathbf{1}) - \mathbf{l} - \rho_\kappa \mathbf{y}_{0tt}]\} dA = 0, \tag{54}$$

and then invoke the arbitrariness of ω and the independence of $\dot{\mathbf{y}}_0$ and $\dot{\mathbf{d}}$ to extract the local equations

$$\mathbf{P}_0 \mathbf{k} = \mathbf{0} \quad \text{and} \quad div(\mathbf{P}_0 \mathbf{1}) - \mathbf{l} = \rho_\kappa \mathbf{y}_{0tt} \quad \text{on} \quad \Omega. \tag{55}$$

On multiplying the second of these by h, using (51) and neglecting terms of order $o(h)$ we obtain

$$h div(\mathbf{P}_0 \mathbf{1}) - \mathbf{P}_s \mathbf{k} = h \rho_\kappa \mathbf{y}_{0tt}. \tag{56}$$

This is the rigorous leading-order (in h) boundary condition for the substrate at the film/substrate interface Ω, reducing to the usual traction-free condition $\mathbf{P}_s\mathbf{k} = \mathbf{0}$ in the absence of the film ($h = 0$). It is also seen to furnish the leading order equation of motion for the film/substrate interface. Similarly, the first of (55) is the leading-order approximation of the traction continuity condition (48), with (51). This condition implies that, to leading order, the film is in a state of plane stress.

In these equations the stress $\mathbf{P}_0$ is given by

$$\mathbf{P}_0 = W_{\mathbf{F}}(\nabla \mathbf{y}_0 + \mathbf{d} \otimes \mathbf{k}) \tag{57}$$

and so (55) may be regarded as a system for the independent fields $\mathbf{y}_0$ and $\mathbf{d}$ on Ω.

It happens that in the presence of strong ellipticity $(55)_1$ may be solved for $\mathbf{d}$ in terms of $\nabla \mathbf{y}_0$. To see this we fix $\mathbf{y}_0$ and define $G(\mathbf{d}) = W(\nabla \mathbf{y}_0 + \mathbf{d} \otimes \mathbf{k})$. Let $\sigma(u) = G(\mathbf{d}(u))$, for some parameter u. Then,

$$\dot{\sigma}(u) = W_{\mathbf{F}}(\mathbf{F}_0) \cdot \dot{\mathbf{d}} \otimes \mathbf{k} = \dot{\mathbf{d}} \cdot \mathbf{P}_0 \mathbf{k}, \quad \text{and thus} \quad G_{\mathbf{d}} = \mathbf{P}_0 \mathbf{k}. \tag{58}$$

Further,

$$\ddot{\sigma}(u) = \ddot{\mathbf{d}} \cdot \mathbf{P}_0 \mathbf{k} + \dot{\mathbf{d}} \otimes \mathbf{k} \cdot \mathcal{M}(\mathbf{F}_0)[\dot{\mathbf{d}} \otimes \mathbf{k}], \tag{59}$$

where

$$\mathcal{M} = W_{\mathbf{FF}}, \tag{60}$$

and so

$$G_{\mathbf{dd}} = \mathbf{A}(\mathbf{F}_0), \tag{61}$$

where $\mathbf{A}$ is the acoustic tensor defined by

$$\mathbf{A}\mathbf{v} = \{\mathcal{M}(\mathbf{F}_0)[\mathbf{v} \otimes \mathbf{k}]\}\mathbf{k} \tag{62}$$

for all vectors $\mathbf{v}$. In terms of components,

$$A_{ij} = \partial^2 W / \partial F_{i3} \partial F_{j3}, \tag{63}$$

having made the identification $\mathbf{e}_3 = \mathbf{k}$. It follows from (30) that $G_{\mathbf{dd}}$ is positive definite and hence, from the implicit function theorem, that $(55)_1$ (i.e. $G_{\mathbf{d}} = \mathbf{0}$), has a unique solution $\mathbf{d} = \bar{\mathbf{d}}(\nabla \mathbf{y}_0)$, say, as claimed. Further, the foregoing implies that this solution minimizes the energy $W(\nabla \mathbf{y}_0 + \mathbf{d} \otimes \mathbf{k})$ with respect to $\mathbf{d}$.

In this work it is convenient to work with strain-dependent moduli. To elaborate, consider a one-parameter family $\mathbf{F}(u)$ of deformations and let $\boldsymbol{\epsilon}(u)$ be the associated strain. Using the connection (27) we then have

$$\mathcal{M}[\dot{\mathbf{F}}] = \dot{\mathbf{P}} = \dot{\mathbf{F}}\mathbf{S} + \mathbf{F}\mathcal{C}[\dot{\boldsymbol{\epsilon}}], \quad \text{with} \quad \dot{\boldsymbol{\epsilon}} = \tfrac{1}{2}(\dot{\mathbf{F}}^t\mathbf{F} + \mathbf{F}^t\dot{\mathbf{F}}), \tag{64}$$

where the superposed dots are derivatives with respect to the parameter, and

$$\mathcal{C} = \bar{W}_{\boldsymbol{\epsilon}\boldsymbol{\epsilon}} \tag{65}$$

are the strain-dependent moduli. We note that this possesses both major and minor symmetries whereas $\mathcal{M}$ possesses only major symmetry. Accordingly,

$$\mathcal{M}[\mathbf{B}] = \mathbf{BS} + \mathbf{F}\mathcal{C}[Sym(\mathbf{B}^t\mathbf{F})], \quad \text{for all tensors} \quad \mathbf{B}, \tag{66}$$

and the strong-ellipticity condition (30) is thus seen to be equivalent to

$$(\mathbf{b}\cdot\mathbf{Sb})\,|\mathbf{a}|^2 + \mathbf{F}^t\mathbf{a}\otimes\mathbf{b}\cdot\mathcal{C}[\mathbf{F}^t\mathbf{a}\otimes\mathbf{b}] > 0. \tag{67}$$

For our purposes the relevant restriction pertains to small perturbations of the reference configuration associated with $\mathbf{F} = \mathbf{I}$. This is

$$(\mathbf{b}\cdot\mathbf{S}_R\mathbf{b})\,|\mathbf{a}|^2 + \mathbf{a}\otimes\mathbf{b}\cdot\mathcal{C}_R[\mathbf{a}\otimes\mathbf{b}] > 0, \tag{68}$$

where $\mathbf{S}_R$ is the residual stress in that configuration and $\mathcal{C}_R$ is the associated tensor of elastic moduli. There are equal respectively to the values of $\mathbf{S}$ and $\mathcal{C}$ at $\boldsymbol{\epsilon} = \mathbf{0}$.

4 Linearization

To linearize the equations we introduce the displacement field

$$\mathbf{u}(\mathbf{x}, t) = \chi(\mathbf{x}, t) - \mathbf{x}, \tag{69}$$

and assume that $\sup_{\mathbf{x}\in\kappa} |\mathbf{H}(\mathbf{x}, t)| \ll 1$, where

$$\mathbf{H} = Grad\mathbf{u} \tag{70}$$

is the displacement gradient. From (1) and (69) we have the exact expressions

$$\mathbf{F} = \mathbf{I} + \mathbf{H} \quad \text{and} \quad \boldsymbol{\epsilon} = \tfrac{1}{2}(\mathbf{H} + \mathbf{H}^t + \mathbf{H}^t\mathbf{H}), \tag{71}$$

and our assumptions imply that $\sup_{\mathbf{x}\in\kappa} |\boldsymbol{\epsilon}(\boldsymbol{x}, t)| \ll 1$. Accordingly, the estimate

$$\bar{W}_{\boldsymbol{\epsilon}} = \bar{W}_{\boldsymbol{\epsilon}}(\mathbf{0}) + \bar{W}_{\boldsymbol{\epsilon}\boldsymbol{\epsilon}}(\mathbf{0})[Sym\mathbf{H}] + o(|\mathbf{H}|) \tag{72}$$

is appropriate, in which the coefficients are the values of the stress and moduli at $\boldsymbol{\epsilon} = \mathbf{0}$, and furnishes the linearized stress-deformation relations

$$\mathbf{S} \simeq \mathbf{S}_R + \mathcal{C}_R[\mathbf{H}] \quad \text{and} \quad \mathbf{P} = (\mathbf{I} + \mathbf{H})\mathbf{S} \simeq \mathbf{S}_R + \mathbf{HS}_R + \mathcal{C}_R[\mathbf{H}]. \tag{73}$$

The residual stress and associated moduli are necessarily uniform if the material is homogeneous. Assuming the body to be in equilibrium without tractions prior to undergoing the small displacement, we have

$$Div\mathbf{S}_R = \mathbf{0} \quad \text{in} \quad \kappa \quad \text{and} \quad \mathbf{S}_R\mathbf{N} = \mathbf{0} \quad \text{on} \quad \partial\kappa_t, \tag{74}$$

the first of which is then identically satisfied.

The thin-film condition $(55)_1$ may be expressed in the form

$$\mathbf{S}_R\mathbf{k} + \mathbf{H}_0\mathbf{S}_R\mathbf{k} + (\mathcal{C}_R[\mathbf{H}_0])\mathbf{k} = \mathbf{0}, \tag{75}$$

and as this purports to hold for all deformations it follows that

$$\mathbf{S}_R\mathbf{k} = \mathbf{0} \quad \text{and} \quad (\mathcal{C}_R[\mathbf{H}_0])\mathbf{k} = \mathbf{0}, \tag{76}$$

the first of these implying that $\mathbf{S}_R$ is a (symmetric) two-tensor of the form $\mathbf{S}_R = S_{R\alpha\beta}\mathbf{e}_\alpha \otimes \mathbf{e}_\beta$, where $\{\mathbf{e}_\alpha\}$ is an orthonormal basis in the plane Ω. To investigate the consequences of the second restriction we write $\mathbf{H}_0$, the restriction of the film displacement gradient to Ω, in the form (40), obtaining

$$\mathbf{H}_0 = \nabla\mathbf{u}_0 + \mathbf{u}_0' \otimes \mathbf{k}, \tag{77}$$

where $\mathbf{u}_0(\mathbf{r}, t)$ is the displacement of the film/substrate interface and $\mathbf{u}_0'$ is the restriction to Ω of the through-thickness derivative $\mathbf{u}'$ of the displacement field *in the film*. The stated restriction may then be written in the form

$$(\mathcal{C}_R[\nabla\mathbf{u}_0])\mathbf{k} + \mathbf{A}_R\mathbf{u}_0' = \mathbf{0}, \tag{78}$$

where $\mathbf{A}_R$ is the relevant acoustic tensor, defined for all $\mathbf{v}$ by

$$\mathbf{A}_R\mathbf{v} = (\mathcal{C}_R[\mathbf{v} \otimes \mathbf{k}])\mathbf{k}, \tag{79}$$

and which is positive definite by (68) and $(76)_1$. Consequently,

$$\mathbf{u}_0' = \mathbf{a}(\nabla\mathbf{u}_0), \quad \text{with} \quad \mathbf{a}(\cdot) = -\mathbf{A}_R^{-1}(\mathcal{C}_R[\cdot])\mathbf{k}, \tag{80}$$

implying that $\mathbf{H}_0$ is determined entirely by the interfacial displacement.

The interfacial equation of motion (56) requires an expression for $\mathbf{P}_0\mathbf{1}$, which, on making use of $(73)_2$, is given to linear order by

$$\mathbf{P}_0\mathbf{1} = \mathbf{S}_R + \mathbf{H}_0\mathbf{S}_R + (\mathcal{C}_R[\mathbf{H}_0])\mathbf{1}, \quad \text{with} \quad \mathbf{H}_0 = \nabla\mathbf{u}_0 + \mathbf{a}(\nabla\mathbf{u}_0) \otimes \mathbf{k}. \tag{81}$$

This is used in (56) in the form

$$\mathbf{P}_s\mathbf{k} = h[div(\mathbf{P}_0\mathbf{1}) - \rho_\kappa\mathbf{u}_{0tt}], \tag{82}$$

in which $\mathbf{P}_s$ is the restriction to Ω of the *substrate* stress, assumed here to be given constitutively by $\mathbf{P}_s = \boldsymbol{\sigma}_0$, where

$$\boldsymbol{\sigma} = \mathcal{E}[\mathbf{G}]; \quad \mathbf{G} = Grad\mathbf{w}, \tag{83}$$

in which $\mathcal{E}$ is the substrate elasticity tensor (possessing major and minor symmetries) and $\mathbf{w}(\mathbf{x}, t)$ is the substrate displacement field. This satisfies $\mathbf{w}_0 = \mathbf{u}_0$ in a perfectly bonded film-substrate system but of course $\mathbf{w}_0' \neq \mathbf{u}_0'$, in general. This expression for the stress presumes the substrate to be free of residual stress. Generalizations are of course possible, but the present simplification suffices for our purposes.

To make the equations explicit it is convenient to decompose the interfacial displacement into tangential and normal parts, i.e.

$$\mathbf{u}_0 = \mathbf{v} + w\mathbf{k}, \quad \text{where} \quad \mathbf{v} = \mathbf{1}\mathbf{u}_0 \quad \text{and} \quad w = \mathbf{k} \cdot \mathbf{u}_0. \tag{84}$$

In the same way we write

$$\mathbf{a} = \boldsymbol{\alpha} + a\mathbf{k}, \quad \text{where} \quad \boldsymbol{\alpha} = \mathbf{1}\mathbf{a} \quad \text{and} \quad a = \mathbf{k} \cdot \mathbf{a}. \tag{85}$$

These furnish

$$\nabla \mathbf{u}_0 = \nabla \mathbf{v} + \mathbf{k} \otimes \nabla w \quad \text{and} \quad \mathbf{a} \otimes \mathbf{k} = \boldsymbol{\alpha} \otimes \mathbf{k} + a\mathbf{k} \otimes \mathbf{k}, \tag{86}$$

and hence afford the representation

$$\mathcal{C}_R[\mathbf{H}_0] = (\mathcal{C}_{ij\alpha\beta} v_{\alpha,\beta} + \mathcal{C}_{ij3\alpha} w_{,\alpha} + \mathcal{C}_{ij\beta 3}\alpha_\beta + a\mathcal{C}_{ij33})\mathbf{e}_i \otimes \mathbf{e}_j, \tag{87}$$

in which the subscript $_R$ has been suppressed on the right-hand side.

The material properties considered in this work exhibit reflection symmetry with respect to the unit normal $\mathbf{k}$, i.e.

$$\bar{W}(\boldsymbol{\epsilon}) = \bar{W}(\mathbf{Q}\boldsymbol{\epsilon}\mathbf{Q}^t), \quad \text{with} \quad \mathbf{Q} = \mathbf{I} - 2\mathbf{k} \otimes \mathbf{k}. \tag{88}$$

These have the property that all components $\mathcal{C}_{ijkl}$ of the elastic moduli having an odd number of subscripts equal to 3 vanish [5]; hence the simplification

$$\begin{aligned} \mathcal{C}_R[\mathbf{H}_0] \quad = \quad & \mathcal{C}_{\lambda\mu\alpha\beta} v_{\alpha,\beta} \mathbf{e}_\lambda \otimes \mathbf{e}_\mu + a\mathcal{C}_{\alpha\beta 33}\mathbf{e}_\alpha \otimes \mathbf{e}_\beta + (\mathcal{C}_{33\alpha\beta} v_{\alpha,\beta} + a\mathcal{C}_{3333})\mathbf{k} \otimes \mathbf{k} \\ & + \mathcal{C}_{\alpha 3\beta 3}(w_{,\beta} + \alpha_\beta)(\mathbf{e}_\alpha \otimes \mathbf{k} + \mathbf{k} \otimes \mathbf{e}_\alpha). \end{aligned} \tag{89}$$

Using the definition (79) of the acoustic tensor we then obtain

$$\mathbf{A}_R\mathbf{b} = \mathcal{C}_{\alpha 3\beta 3} b_\beta \mathbf{e}_\alpha + Cb_3\mathbf{k}, \quad \text{where} \quad C = \mathcal{C}_{3333}, \tag{90}$$

yielding

$$\mathbf{b} \cdot \mathbf{A}_R\mathbf{b} = \mathcal{C}_{\alpha 3\beta 3} b_\alpha b_\beta + Cb_3^2. \tag{91}$$

The acoustic tensor is then positive definite as required if and only if $C > 0$ and $(\mathcal{C}_{\alpha 3\beta 3})$ is positive definite. Further, (84) and (85) give

$$\mathbf{A}_R\mathbf{a} = \mathcal{C}_{\alpha 3\beta 3}\alpha_\beta \mathbf{e}_\alpha + Ca\mathbf{k} \quad \text{and} \quad (\mathcal{C}_R[\nabla \mathbf{u}_0])\mathbf{k} = \mathcal{C}_{33\alpha\beta}v_{\alpha,\beta}\mathbf{k} + \mathcal{C}_{\alpha 3\beta 3}w_{,\beta}\mathbf{e}_\alpha, \tag{92}$$

and it follows from (78) that

$$\boldsymbol{\alpha} = -\nabla w, \quad a = -C^{-1}\mathcal{C}_{33\alpha\beta}v_{\alpha,\beta}. \tag{93}$$

The restriction $\mathbf{H}_0$ to Ω of the film displacement gradient is thus given by

$$\mathbf{H}_0 = \nabla \mathbf{v} + a\mathbf{k} \otimes \mathbf{k} + \mathbf{k} \otimes \nabla w - \nabla w \otimes \mathbf{k}, \tag{94}$$

and (89), together with the minor symmetry of $\mathcal{C}_R$, yields

$$\mathcal{C}_R[\mathbf{H}_0] = \mathcal{D}[\nabla \mathbf{v}] = \mathcal{D}_{\lambda\mu\alpha\beta}v_{\alpha,\beta}\mathbf{e}_\lambda \otimes \mathbf{e}_\mu, \tag{95}$$

where

$$\mathcal{D}_{\lambda\mu\alpha\beta} = \mathcal{C}_{\lambda\mu\alpha\beta} - C^{-1}\mathcal{C}_{33\lambda\mu}\mathcal{C}_{33\alpha\beta} \tag{96}$$

are the *plane-stress moduli*. This in turn furnishes

$$\mathbf{P}_0\mathbf{1} = \mathbf{S}_R + (\nabla \mathbf{v})\mathbf{S}_R + \mathbf{k} \otimes (\mathbf{S}_R\nabla w) + \mathcal{D}[\nabla \mathbf{v}], \tag{97}$$

and eq. (82) for the interfacial motion reduces to

$$\boldsymbol{\sigma}_0\mathbf{k} = h[div\{(\nabla \mathbf{v})\mathbf{S}_R + \mathcal{D}[\nabla \mathbf{v}]\} + \mathbf{k}div(\mathbf{S}_R\nabla w) - \rho_\kappa \mathbf{v}_{tt} - \rho_\kappa w_{tt}\mathbf{k}]. \tag{98}$$

The substrate displacement is described by the classical equation of motion

$$Div\boldsymbol{\sigma} = \rho_s \mathbf{w}_{tt}, \tag{99}$$

where ρ_s is the substrate mass density.

5 Surface waves: Love modes in hexagonal and cubic crystal films

We are interested in localized surface waves of the form

$$\mathbf{w}(\mathbf{x}, t) = F(\mathbf{x}, t)\mathbf{d} \tag{100}$$

in which $\mathbf{d}$ is the fixed polarization vector, $\mathbf{x}$ is decomposed as in (31) in which $\varsigma < 0$ for the substrate, and

$$F(\mathbf{x}, t) = \exp(\eta k\varsigma)\exp[ik(\mathbf{n} \cdot \mathbf{r} - ct)], \tag{101}$$

in which η is a constant - assumed positive to ensure decay with depth into the substrate, $\mathbf{n} \in \Omega$ is the propagation direction, c is the wave speed, and k is the wave number. The induced interfacial displacement is

$$\mathbf{u}_0 = \mathbf{w}_0 = G\mathbf{d}, \quad \text{where} \quad G = F_0 = \exp[ik(\mathbf{n} \cdot \mathbf{r} - ct)]. \tag{102}$$

The gradient of the interfacial displacement is

$$\nabla \mathbf{u}_0 = \mathbf{d} \otimes \nabla G = ikG\mathbf{d} \otimes \mathbf{n}. \tag{103}$$

It proves convenient to decompose the polarization in the form (84), i.e.

$$\mathbf{d} = \boldsymbol{\delta} + d\mathbf{k}; \quad \boldsymbol{\delta} = \mathbf{1d}, \quad d = \mathbf{k} \cdot \mathbf{d}. \tag{104}$$

Then,

$$\nabla \mathbf{v} = ikG\boldsymbol{\delta} \otimes \mathbf{n} \quad \text{and} \quad \nabla w = ikGd\mathbf{n}. \tag{105}$$

Using these results with $\nabla\nabla G = -k^2 G\mathbf{n} \otimes \mathbf{n}$ and $\mathbf{u}_{0tt} = -k^2c^2G\mathbf{d}$, after some effort we reduce the bracketed term on the right-hand side of (82) to

$$div(\mathbf{P}_0\mathbf{1}) - \rho_\kappa \mathbf{u}_{0tt} = Gk^2\{(\rho_\kappa c^2 - \mathbf{n} \cdot \mathbf{S}_R\mathbf{n})\mathbf{d} - \mathcal{A}\boldsymbol{\delta}\}, \tag{106}$$

where

$$\mathcal{A} = \mathcal{D}_{\beta\alpha\lambda\mu} n_\alpha n_\mu \mathbf{e}_\beta \otimes \mathbf{e}_\lambda \tag{107}$$

is the (symmetric) plane-stress acoustic tensor associated with the propagation direction.

The induced stress in the substrate is given by (83) with

$$\mathbf{G} = \mathbf{d} \otimes GradF, \quad \text{where} \quad GradF = kF(i\mathbf{n} + \eta\mathbf{k}), \tag{108}$$

yielding

$$\mathbf{G} = kF(i\mathbf{d} \otimes \mathbf{n} + \eta\mathbf{d} \otimes \mathbf{k}) \tag{109}$$

and hence

$$\boldsymbol{\sigma} = kF\mathbf{B}, \quad \text{where} \quad \mathbf{B} = i\mathcal{E}[\mathbf{d} \otimes \mathbf{n}] + \eta\mathcal{E}[\mathbf{d} \otimes \mathbf{k}]. \tag{110}$$

Using this in the interfacial equation of motion (82) leads to the algebraic problem

$$\mathbf{Bk} = \epsilon\{(\rho_\kappa c^2 - \mathbf{n} \cdot \mathbf{S}_R\mathbf{n})\mathbf{d} - \mathcal{A}\boldsymbol{\delta}\}, \tag{111}$$

where

$$\epsilon = hk \ll 1 \tag{112}$$

is the dimensionless film thickness.

5.1 Substrate motion

From (100) and (101) we have $\mathbf{w}_{tt} = -k^2c^2F\mathbf{d}$ and

$$Div\boldsymbol{\sigma} = k\mathbf{B}(GradF) = k^2F\mathbf{B}(i\mathbf{n} + \eta\mathbf{k}), \tag{113}$$

which reduce the substrate equation of motion (cf. (99)) to the algebraic problem

$$-(\mathcal{E}[\mathbf{d}\otimes\mathbf{n}])\mathbf{n} + i\eta\{(\mathcal{E}[\mathbf{d}\otimes\mathbf{k}])\mathbf{n} + (\mathcal{E}[\mathbf{d}\otimes\mathbf{n}])\mathbf{k}\} + \eta^2(\mathcal{E}[\mathbf{d}\otimes\mathbf{k}])\mathbf{k} = -\rho_s c^2\mathbf{d}. \tag{114}$$

In *isotropic* substrates, to which attention is restricted in this work,

$$\mathcal{E}[\mathbf{G}] = \lambda_s(tr\mathbf{G})\mathbf{I} + 2\mu_s\mathbf{G}, \tag{115}$$

where λ_s and μ_s are the substrate Lamé moduli, assumed here to satisfy the usual strong ellipticity conditions $\lambda_s + 2\mu_s > 0$ and $\mu_s > 0$. In this case straightforward calculation reduces (114) to the system

$$\begin{aligned} \mu_s(id\mathbf{n} + \eta\boldsymbol{\delta}) &= \epsilon[(\rho_\kappa c^2 - \mathbf{n}\cdot\mathbf{S}_R\mathbf{n})\boldsymbol{\delta} - \mathcal{A}\boldsymbol{\delta}] \\ i\lambda_s(\mathbf{n}\cdot\boldsymbol{\delta}) + \eta(\lambda_s + 2\mu_s)d &= \epsilon(\rho_\kappa c^2 - \mathbf{n}\cdot\mathbf{S}_R\mathbf{n})d. \end{aligned} \tag{116}$$

Further,

$$(\mathcal{E}[\mathbf{d}\otimes\mathbf{k}])\mathbf{k} = (\lambda_s + 2\mu_s)d\mathbf{k} + \mu_s\boldsymbol{\delta}, \quad (\mathcal{E}[\mathbf{d}\otimes\mathbf{n}])\mathbf{k} = \lambda_s(\boldsymbol{n}\cdot\boldsymbol{\delta})\boldsymbol{k} + \mu_s d\mathbf{n},$$

$$(\mathcal{E}[\mathbf{d}\otimes\mathbf{n}])\mathbf{n} = (\lambda_s+\mu_s)(\mathbf{n}\cdot\boldsymbol{\delta})\mathbf{n}+\mu_s\mathbf{d}, \quad (\mathcal{E}[\mathbf{d}\otimes\mathbf{k}])\mathbf{n} = \lambda_s d\mathbf{n}+\mu_s(\mathbf{n}\cdot\boldsymbol{\delta})\mathbf{k}. \tag{117}$$

Love waves are polarized in the plane Ω. Accordingly, $d = 0$ and $(116)_2$ requires that

$$\mathbf{n}\cdot\boldsymbol{\delta} = 0. \tag{118}$$

Eqs. (117) simplify dramatically to

$$(\mathcal{E}[\mathbf{d}\otimes\mathbf{k}])\mathbf{k} = \mu_s\boldsymbol{\delta}, \quad (\mathcal{E}[\mathbf{d}\otimes\mathbf{n}])\mathbf{k} = \mathbf{0}, \quad (\mathcal{E}[\mathbf{d}\otimes\mathbf{n}])\mathbf{n} = \mu_s\boldsymbol{\delta}$$
$$\text{and} \quad (\mathcal{E}[\mathbf{d}\otimes\mathbf{k}])\mathbf{n} = \mathbf{0}, \tag{119}$$

and (99) delivers

$$\eta = \sqrt{1 - s^2}, \quad \text{where} \quad s = c/c_s \tag{120}$$

and $c_s = \sqrt{\mu_s/\rho_s}$ is the shear-wave speed in the substrate. Finally, $(116)_1$ reduces to the propagation condition

$$\mu_s\eta\boldsymbol{\delta} = \epsilon[(\rho_\kappa c^2 - \mathbf{n}\cdot\mathbf{S}_R\mathbf{n})\boldsymbol{\delta} - \mathcal{A}\boldsymbol{\delta}], \tag{121}$$

which requires that $\boldsymbol{\delta}$ be an eigenvector of the acoustic tensor $\mathcal{A}$. The restriction (118) and the symmetry of the acoustic tensor imply that the propagation direction $\mathbf{n}$ is then also an eigenvector.

5.2 Hexagonal (fibre) symmetry

In this subsection explicit dispersion relations are derived for films having hexagonal symmetry. In the linear theory, the associated constitutive equations are of precisely the same form as those for materials exhibiting transverse isotropy, or fibre symmetry. Accordingly, the results derived are applicable to both fibre-reinforced film materials or hexagonal crystalline materials.

In particular, the components of $\mathcal{C}$ relative to an orthonormal basis $\{\mathbf{e}_i\}$ are (see [11])

$$\begin{aligned}\mathcal{C}_{ijkl} = \lambda\delta_{ij}\delta_{kl} + \mu_T(\delta_{ik}\delta_{jl} + \delta_{il}\delta_{jk}) + \alpha(\delta_{ij}m_k m_l + m_i m_j \delta_{kl})\\ +(\mu_L - \mu_T)(m_i m_k \delta_{jl} + m_i m_l \delta_{jk} + m_j m_k \delta_{il} + m_j m_l \delta_{ik})\\ +\beta m_i m_j m_k m_l,\end{aligned} \tag{122}$$

where δ_{ij} is the Kronecker delta; $\alpha, \beta, \lambda, \mu_T$ and μ_L are material constants; and the unit vector $\mathbf{m}$, with components m_i, is the fiber axis, assumed here to be uniform. Spencer [11] shows that μ_T is the shear modulus for shearing in planes transverse to $\mathbf{m}$, whereas μ_L is the shear modulus for shearing parallel to $\mathbf{m}$. The remaining material constants in (122) may be interpreted in terms of extensional moduli and Poisson ratios [11].

The general form of the residual stress may be derived by enumerating the strain invariants for transverse isotropy that are linear in the (infinitesimal) strain. These are [11] $\mathbf{I}\cdot\boldsymbol{\epsilon}$ and $\mathbf{m}\otimes\mathbf{m}\cdot\boldsymbol{\epsilon}$. Comparison with the leading term in (72) then furnishes

$$\mathbf{S}_R = S_T(\mathbf{I} - \mathbf{m}\otimes\mathbf{m}) + S_L\mathbf{m}\otimes\mathbf{m}, \tag{123}$$

where S_T is the constant residual stress in the isotropic plane and S_L is the constant residual uniaxial stress along $\mathbf{m}$.

Necessary and sufficient conditions for strong ellipticity in the absence of residual stress are [8; 12]:

$$\mu_L > 0, \quad \varphi > 0, \quad \mu_T > 0, \quad \lambda + 2\mu_T > 0, \tag{124}$$

and

$$|\lambda + \alpha + \mu_L| < \mu_L + \sqrt{\varphi(\lambda + 2\mu_T)}, \tag{125}$$

where

$$\varphi = \lambda + 4\mu_L - 2\mu_T + 2\alpha + \beta. \tag{126}$$

We first assume the axis of transverse isotropy to coincide with the unit normal $\mathbf{k}(= \mathbf{e}_3)$ to the film, and later consider the case when the axis lies in the interfacial plane; the film material exhibits reflection symmetry with respect to the interface in both cases.

(a) Fibre axis orthogonal to the interfacial plane

In this case the plane-stress condition $(76)_1$, with $\mathbf{m} = \mathbf{k}$, yields

$$\mathbf{S}_R = S\mathbf{1}, \tag{127}$$

with S constant. Using $(93)_2$, a straightforward but involved calculation [12] leads to

$$a = -(\bar{\lambda} + \bar{\alpha})div\mathbf{v}, \tag{128}$$

where $\bar{\lambda} = \lambda/\varphi$ and $\bar{\alpha} = \alpha/\varphi$. Further,

$$\mathcal{D}[\nabla\mathbf{v}] = \varphi\{[\bar{\lambda} - (\bar{\lambda} + \bar{\alpha})^2](div\mathbf{v})\mathbf{1} + \bar{\mu}_T[\nabla\mathbf{v} + (\nabla\mathbf{v})^t]\}, \tag{129}$$

where $\bar{\mu}_T = \mu_T/\varphi$, yielding

$$\begin{aligned} \mathcal{A}\boldsymbol{\delta} &= (\mathcal{D}[\boldsymbol{\delta} \otimes \boldsymbol{n}])\boldsymbol{n} \\ &= \varphi\{[\bar{\lambda} - (\bar{\lambda} + \bar{\alpha})^2](\boldsymbol{\delta} \cdot \mathbf{n})\mathbf{n} + \bar{\mu}_T[\boldsymbol{\delta} + (\boldsymbol{\delta} \cdot \mathbf{n})\mathbf{n}]\}, \end{aligned} \tag{130}$$

and hence

$$\mathcal{A}\boldsymbol{\delta} = \mu_T\boldsymbol{\delta} \tag{131}$$

in the case of Love waves. Substituting into (121), we conclude that the polarization $\boldsymbol{\delta}$ is an arbitrary vector in the interfacial plane and from (120) that

$$\sqrt{1 - s^2} = \epsilon(rs^2 - \frac{S + \mu_T}{\mu_s}), \tag{132}$$

where

$$r = \rho_\kappa/\rho_s \tag{133}$$

is the ratio of film density to substrate density. This is the relevant dispersion relation. To solve it we assume that $1 - s^2 = O(\epsilon^2)$ and derive the consistent estimate [12]

$$s \sim 1 - \tfrac{1}{2}\epsilon^2(r - \frac{S + \mu_T}{\mu_s})^2 + o(\epsilon^2). \tag{134}$$

(b) Fibres lying in the interfacial plane

In this case $(76)_1$ yields

$$\mathbf{S}_R = S\mathbf{m}\otimes\mathbf{m}, \tag{135}$$

a uniform uniaxial stress along the fibres, while $(93)_2$ gives

$$a = -\tfrac{1}{\lambda+2\mu_T}[\lambda div\mathbf{v} + \alpha\mathbf{m}\cdot(\nabla\mathbf{v})\mathbf{m}]. \tag{136}$$

With some effort (95) and (96) may be reduced to [13]

$$\begin{aligned}\mathcal{D}[\nabla\mathbf{v}\,] &= [\lambda(\theta+a)+\alpha\mathbf{m}\cdot(\nabla\mathbf{v})\mathbf{m}]\mathbf{I}+[\alpha(\theta+a)+\beta\mathbf{m}\cdot(\nabla\mathbf{v})\mathbf{m}]\mathbf{m}\otimes\mathbf{m}\\ &\quad +2\mu_T(Sym\nabla\mathbf{v}+a\mathbf{k}\otimes\mathbf{k})\\ &\quad +2(\mu_L-\mu_T)[(Sym\nabla\mathbf{v})\mathbf{m}\otimes\mathbf{m}+\mathbf{m}\otimes(Sym\nabla\mathbf{v})\mathbf{m}].\end{aligned} \tag{137}$$

For Love waves the latter is used to derive

$$\begin{aligned}\mathcal{A}\boldsymbol{\delta} &= (\mathcal{D}[\boldsymbol{\delta}\otimes\boldsymbol{n}])\boldsymbol{n}\\ &= \alpha(1-\frac{\lambda}{\lambda+2\mu_T})(\mathbf{m}\cdot\mathbf{n})(\mathbf{m}\cdot\boldsymbol{\delta})\mathbf{n}+\mu_T\boldsymbol{\delta}\\ &\quad +(\beta-\frac{\alpha^2}{\lambda+2\mu_T})(\mathbf{m}\cdot\mathbf{n})^2(\mathbf{m}\cdot\boldsymbol{\delta})[(\mathbf{m}\cdot\mathbf{n})\mathbf{n}+(\mathbf{m}\cdot\boldsymbol{\delta})\boldsymbol{\delta}]\\ &\quad +(\mu_L-\mu_T)[(\mathbf{m}\cdot\mathbf{n})^2\boldsymbol{\delta}+2(\mathbf{m}\cdot\mathbf{n})(\mathbf{m}\cdot\boldsymbol{\delta})\mathbf{n}+(\mathbf{m}\cdot\boldsymbol{\delta})^2\boldsymbol{\delta}],\end{aligned} \tag{138}$$

and the propagation condition (121), projected onto the directions of $\boldsymbol{\delta}$ and $\mathbf{n}$, furnishes

$$(\mathbf{m}\cdot\mathbf{n})(\mathbf{m}\cdot\boldsymbol{\delta})[\boldsymbol{\delta}(\mathbf{m}\cdot\mathbf{n})^2+\alpha(1-\frac{\lambda}{\lambda+2\mu_T})+2(\mu_L-\mu_T)]=0 \quad \text{and}$$

$$\epsilon[\rho_\kappa c^2 - S(\mathbf{m}\cdot\mathbf{n})^2-\mu_L+\delta(\mathbf{m}\cdot\mathbf{n})^2(\mathbf{m}\cdot\boldsymbol{\delta})^2]=\mu_s\eta, \tag{139}$$

where

$$\delta=\beta-\frac{\alpha^2}{\lambda+2\mu_T}. \tag{140}$$

Typical data on carbon fibre/epoxy composites furnish a non-zero value of the bracketed expression in the first relation, implying that

$$(\mathbf{m}\cdot\mathbf{n})(\mathbf{m}\cdot\boldsymbol{\delta})=0, \tag{141}$$

and hence that either the direction of propagation or the polarization is parallel to the fibres.

In the first case we have $\mathbf{m}\cdot\mathbf{n}=\pm 1$ and $(139)_2$ delivers the associated dispersion relation

$$\mu_s\eta=\epsilon(\rho_\kappa c^2-S-\mu_L), \tag{142}$$

which is solved as before to obtain the estimate

$$s\sim 1-\tfrac{1}{2}\epsilon^2(r-\frac{S+\mu_L}{\mu_s})^2+o(\epsilon^2). \tag{143}$$

In the second case $\mathbf{m}=\pm\boldsymbol{\delta}$ and the dispersion relation is

$$\mu_s\eta=\epsilon(\rho_\kappa c^2-\mu_L), \tag{144}$$

yielding

$$s\sim 1-\tfrac{1}{2}\epsilon^2(r-\frac{\mu_L}{\mu_s})^2+o(\epsilon^2). \tag{145}$$

We observe that in both cases the deformation is a shear, not in the isotropic plane, but rather in the plane containing the fibres. The operative material property is therefore μ_L, the longitudinal shear modulus [15].

5.3 Cubic symmetry

In the case of cubic crystal symmetry we assume the cubic axes to be aligned with $\{\mathbf{e}_i\}=\{\mathbf{e}_\alpha,\mathbf{k}\}$. The residual stress is necessarily a pure pressure which vanishes by virtue of the plane-stress condition $(76)_1$. Accordingly, the strain energy $\bar{W}(\boldsymbol{\epsilon})$ is a homogeneous quadratic function which depends on the strain via the combinations [10]

$$(\epsilon_{11}+\epsilon_{22}+\epsilon_{33})^2,\quad \epsilon_{11}\epsilon_{22}+\epsilon_{11}\epsilon_{33}+\epsilon_{22}\epsilon_{33}\quad\text{and}\quad \epsilon_{12}^2+\epsilon_{13}^2+\epsilon_{23}^2.$$

These are common to all five subclasses of cubic symmetry.

It proves convenient to express the strain-energy function in terms of the spherical and deviatoric part of the strain, the latter being defined by

$$\bar{\boldsymbol{\epsilon}}=\boldsymbol{\epsilon}-\tfrac{1}{3}(tr\boldsymbol{\epsilon})\boldsymbol{I}, \tag{146}$$

yielding

$$\epsilon_{11}\epsilon_{22}+\epsilon_{11}\epsilon_{33}+\epsilon_{22}\epsilon_{33}=\tfrac{1}{3}(tr\boldsymbol{\epsilon})^2-\tfrac{1}{2}(\bar{\epsilon}_{11}^2+\bar{\epsilon}_{22}^2+\bar{\epsilon}_{33}^2) \tag{147}$$

and hence

$$\bar{W}(\boldsymbol{\epsilon})=\tfrac{1}{2}[C_1(\epsilon_{11}+\epsilon_{22}+\epsilon_{33})^2+C_2(\bar{\epsilon}_{11}^2+\bar{\epsilon}_{22}^2+\bar{\epsilon}_{33}^2)]+C_3(\epsilon_{12}^2+\epsilon_{13}^2+\epsilon_{23}^2), \tag{148}$$

where $C_{1,2,3}$ are material constants. To ensure strong ellipticity in accordance with our assumptions thus far it is enough to require that $\bar{W}(\boldsymbol{\epsilon})$ be

positive definite. Because (148) is the sum of independent quadratic forms this in turn is equivalent to the restrictions

$$C_1 > 0, \quad C_2 > 0 \quad \text{and} \quad C_3 > 0. \tag{149}$$

According to (73) the stress in the film is then given by

$$\begin{aligned}\mathbf{P} &= \mathcal{C}[\boldsymbol{\epsilon}] \\ &= C_1(tr\boldsymbol{\epsilon})\boldsymbol{I} + C_2(\bar{\epsilon}_{11}\mathbf{e}_1 \otimes \mathbf{e}_1 + \bar{\epsilon}_{22}\mathbf{e}_2 \otimes \mathbf{e}_2 + \bar{\epsilon}_{33}\mathbf{e}_3 \otimes \mathbf{e}_3) \\ &+C_3[\epsilon_{12}(\mathbf{e}_1\otimes\mathbf{e}_2+\mathbf{e}_2\otimes\mathbf{e}_1)+\epsilon_{13}(\mathbf{e}_1\otimes\mathbf{e}_3+\mathbf{e}_3\otimes\mathbf{e}_1)+\epsilon_{23}(\mathbf{e}_2\otimes\mathbf{e}_3+\mathbf{e}_3\otimes\mathbf{e}_2)],\end{aligned} \tag{150}$$

and the plane-stress condition $(76)_2$ yields the restrictions

$$C_1(tr\boldsymbol{\epsilon}) + C_2\bar{\epsilon}_{33} = 0 \quad \text{and} \quad \epsilon_{\alpha 3} = 0 \tag{151}$$

on the interfacial values of the strain in the film.

Using (84) and (85) and the fact that $\boldsymbol{\epsilon}$ is the symmetric part of the displacement gradient, we have

$$\boldsymbol{\epsilon} = Sym(\nabla\mathbf{v}) + a\mathbf{k}\otimes\mathbf{k} + \tfrac{1}{2}[\mathbf{k}\otimes(\nabla w + \boldsymbol{\alpha}) + (\nabla w + \boldsymbol{\alpha})\otimes\boldsymbol{k}], \tag{152}$$

and thus conclude that $(151)_2$ is equivalent to $(93)_1$. Further, $a = \epsilon_{33}$, $tr\boldsymbol{\epsilon} = \theta + a$, where $\theta = div\mathbf{v}$, $\bar{\epsilon}_{33} = \frac{2}{3}a - \frac{1}{2}\theta$ and $(93)_2$ delivers

$$a = -(C_1 + \tfrac{2}{3}C_2)^{-1}(C_1 - \tfrac{1}{3}C_2)\theta. \tag{153}$$

The plane-stress moduli are defined by (95) and (96) and hence given by

$$\mathcal{D}[\nabla\mathbf{v}] = C_1(\theta+a)\mathbf{1} + C_2(\bar{\epsilon}_{11}\mathbf{e}_1\otimes\mathbf{e}_1 + \bar{\epsilon}_{22}\mathbf{e}_2\otimes\mathbf{e}_2) + C_3\epsilon_{12}(\mathbf{e}_1\otimes\mathbf{e}_2 + \mathbf{e}_2\otimes\mathbf{e}_1), \tag{154}$$

where

$$\bar{\epsilon}_{11} = \tfrac{1}{3C_1+2C_2}[(3C_1+2C_2)v_{1,1}+C_2v_{2,2}], \quad \bar{\epsilon}_{22} = \tfrac{1}{3C_1+2C_2}[(3C_1+2C_2)v_{2,2}+C_2v_{1,1}] \tag{155}$$

and

$$\theta + a = \tfrac{3C_2}{3C_1+2C_2}(v_{1,1} + v_{2,2}). \tag{156}$$

To obtain $\mathcal{D}[\boldsymbol{\delta}\otimes\boldsymbol{n}]$ for use in (121) we simply replace $\nabla\mathbf{v}$ by $\boldsymbol{\delta}\otimes\boldsymbol{n}$, arriving at

$$\begin{aligned}\mathcal{A}\boldsymbol{\delta} &= (\mathcal{D}[\boldsymbol{\delta}\otimes\boldsymbol{n}])\boldsymbol{n} \\ &= \tfrac{3C_1C_2}{3C_1+2C_2}(\delta\cdot\mathbf{n})\mathbf{n} + \tfrac{C_2}{3C_1+2C_2}[(3C_1+C_2)\delta_1n_1^2 + C_2\delta_2n_1n_2]\mathbf{e}_1 \\ &\quad + \tfrac{C_2}{3C_1+2C_2}[(3C_1+C_2)\delta_2n_2^2 + C_2\delta_1n_1n_2]\mathbf{e}_2 \\ &\quad + \tfrac{1}{2}C_3(\delta_1n_2^2 + \delta_2n_1n_2)\mathbf{e}_1 + \tfrac{1}{2}C_3(\delta_1n_1n_2 + \delta_2n_1^2)\mathbf{e}_2.\end{aligned} \tag{157}$$

An explicit expression for $\mathcal{A}$ follows by using $\delta_\alpha = \mathbf{e}_\alpha \cdot \boldsymbol{\delta}$ with $\delta_1\mathbf{e}_1 = (\mathbf{e}_1\otimes\mathbf{e}_1)\boldsymbol{\delta}$, $\delta_1\mathbf{e}_2 = (\mathbf{e}_2\otimes\mathbf{e}_1)\boldsymbol{\delta}$, etc.; thus, in the case of Love waves ($\boldsymbol{\delta}\cdot\boldsymbol{n} = 0$),

$$\begin{aligned}\mathcal{A} &= (C_2\tfrac{3C_1+C_2}{3C_1+2C_2}n_1^2 + \tfrac{1}{2}C_3n_2^2)\mathbf{e}_1\otimes\mathbf{e}_1 + (C_2\tfrac{3C_1+C_2}{3C_1+2C_2}n_2^2 + \tfrac{1}{2}C_3n_1^2)\mathbf{e}_2\otimes\mathbf{e}_2\\ &\quad + n_1n_2(\tfrac{C_2^2}{3C_1+2C_2} + \tfrac{1}{2}C_3)(\mathbf{e}_1\otimes\mathbf{e}_2 + \mathbf{e}_2\otimes\mathbf{e}_1).\end{aligned} \tag{158}$$

Recalling that the propagation condition (121) implies that $\mathbf{n}$ is an eigenvector, we have $\mathcal{A}\mathbf{n} = \xi\mathbf{n}$ for some $\xi\in\mathbb{R}$, where

$$\begin{aligned}\mathcal{A}\mathbf{n} &= (C_2\tfrac{3C_1+C_2}{3C_1+2C_2}n_1^2 + \tfrac{1}{2}C_3n_2^2)n_1\mathbf{e}_1 + (C_2\tfrac{3C_1+C_2}{3C_1+2C_2}n_2^2 + \tfrac{1}{2}C_3n_1^2)n_2\mathbf{e}_2\\ &\quad + n_1n_2(\tfrac{C_2^2}{3C_1+2C_2} + \tfrac{1}{2}C_3)(n_2\mathbf{e}_1 + n_1\mathbf{e}_2).\end{aligned} \tag{159}$$

Taking the scalar product of the equation $\mathcal{A}\mathbf{n} = \xi\mathbf{n}$ with $n_2\mathbf{e}_1$ and $n_1\mathbf{e}_2$ yields two equations for ξn_1n_2, which we subtract to derive

$$n_1n_2(n_1^2 - n_2^2)\tfrac{3C_1+C_2}{3C_1+2C_2} = 0, \tag{160}$$

and with (149) this yields the possibilities

$$n_1n_2 = 0 \quad \text{or} \quad n_1^2 = n_2^2. \tag{161}$$

The first alternative implies that $\mathbf{n}\in\{\mathbf{e}_\alpha\}$ and hence that $\boldsymbol{\delta}\in\{\boldsymbol{e}_\alpha\}$; the propagation and polarization directions are aligned with the crystallographic axes. Eq. (157) then provides

$$\mathcal{A}\boldsymbol{\delta} = \tfrac{1}{2}C_3\boldsymbol{\delta} \tag{162}$$

and (121) yields the dispersion relation

$$\mu_s\eta = \epsilon(\rho_\kappa c^2 - \tfrac{1}{2}C_3), \tag{163}$$

which is solved as before to obtain

$$s \sim 1 - \tfrac{1}{2}\epsilon^2(r - \frac{C_3}{2\mu_s})^2 + o(\epsilon^2). \tag{164}$$

The second alternative implies that $n_1^2 = n_2^2 = n^2$, with $n = \pm 1/\sqrt{2}$. These yield the two families

$$\begin{aligned}\mathbf{n}_{(1)} &= \tfrac{1}{\sqrt{2}}(\mathbf{e}_1 + \mathbf{e}_2), \quad \text{with} \quad \boldsymbol{\delta}_{(1)} = \tfrac{1}{\sqrt{2}}(\mathbf{e}_1 - \mathbf{e}_2), \quad \text{and}\\ \mathbf{n}_{(2)} &= \tfrac{1}{\sqrt{2}}(\mathbf{e}_1 - \mathbf{e}_2), \quad \text{with} \quad \boldsymbol{\delta}_{(2)} = \tfrac{1}{\sqrt{2}}(\mathbf{e}_1 + \mathbf{e}_2),\end{aligned} \tag{165}$$

corresponding to propagation and polarization at 45 degrees to the crystallographic axes. In either case we have

$$\mathcal{A} = \tfrac{1}{2}(C_2 \tfrac{3C_1+C_2}{3C_1+2C_2} + \tfrac{1}{2}C_3)\mathbf{1} + n_1 n_2 (\tfrac{C_2^2}{3C_1+2C_2} + \tfrac{1}{2}C_3)(\mathbf{e}_1 \otimes \mathbf{e}_2 + \mathbf{e}_2 \otimes \mathbf{e}_1), \quad (166)$$

implying that

$$\mathcal{A}\boldsymbol{\delta} = \tfrac{3}{2}\tfrac{C_1 C_2}{3C_1+2C_2}\boldsymbol{\delta}. \quad (167)$$

Finally, substitution into (121) furnishes the dispersion relation

$$\mu_s \eta = \epsilon(\rho_\kappa c^2 - \tfrac{3}{2}\tfrac{C_1 C_2}{3C_1+2C_2}), \quad (168)$$

and thus

$$s \sim 1 - \tfrac{1}{2}\epsilon^2 [r - \tfrac{3}{2\mu_s}\tfrac{C_1 C_2}{(3C_1+2C_2)}]^2 + o(\epsilon^2). \quad (169)$$

6 Survey of nonlinear and linearized electroelasticity

Here we review the basic theory of nonlinear electroelasticity as a prelude to the development of a model for thin electro-elastic films. For further background reference may be made to [4; 7; 14] In nonlinear electroelasticity we assume the existence of a free energy per unit mass, φ say, that depends on the deformation gradient $\mathbf{F}$ and electric field $\mathbf{e}$. Here we restrict attention to the purely electromechanical theory and suppress thermal and electrical conduction. We also assume the material to be non-magnetizable.

The Cauchy stress is [7]

$$\mathbf{T} = \rho\varphi_{\mathbf{F}}\mathbf{F}^t + \mathbf{T}_M, \quad (170)$$

where

$$\mathbf{T}_M = \varepsilon_0(\mathbf{e} \otimes \mathbf{e} - \tfrac{1}{2}e^2\mathbf{I}), \quad \text{with} \quad e = |\mathbf{e}|, \quad (171)$$

is the Maxwell stress in which ε_0 is the free-space permittivity. The material polarization is

$$\mathbf{p} = -\rho\varphi_{\mathbf{e}}. \quad (172)$$

By an argument similar to that leading from (3) to (23) [7], we find that the free energy depends on the deformation and electric field via the Cauchy-Green deformation tensor $\mathbf{C} = \mathbf{F}^t\mathbf{F}$ and the pullback $\mathbf{E} = \mathbf{F}^t\mathbf{e}$; thus,

$$\varphi(\mathbf{F}, \mathbf{e}) = \Phi(\mathbf{C}, \mathbf{E}). \quad (173)$$

Straightforward application of the chain rule yields

$$\varphi_{\mathbf{e}} = \mathbf{F}\Phi_{\mathbf{E}} \quad \text{and} \quad \varphi_{\mathbf{F}} = 2\mathbf{F}\Phi_{\mathbf{C}} + \mathbf{e} \otimes \Phi_{\mathbf{E}}, \quad (174)$$

and hence

$$\mathbf{T} = \boldsymbol{\sigma} + \boldsymbol{T}_M, \tag{175}$$

where

$$\boldsymbol{\sigma} = 2\rho\mathbf{F}\Phi_{\mathbf{C}}\mathbf{F}^t, \tag{176}$$

together with

$$\mathbf{p} = -\rho\mathbf{F}\Phi_{\mathbf{E}}. \tag{177}$$

In the absence of a magnetic induction field or volumetric distributions of charge, the equations to be solved are

$$div\mathbf{T} = \rho\boldsymbol{\chi}_{tt}, \quad curl\mathbf{e} = \mathbf{0} \quad \text{and} \quad div\mathbf{d} = 0, \tag{178}$$

where

$$\mathbf{d} = \varepsilon_0\mathbf{e} + \mathbf{p} \tag{179}$$

is the electric displacement and *curl* is the spatial curl operator, together with $curl\mathbf{h} = \mathbf{0}$, where $\mathbf{h}$ is the magnetic field. The latter is valid in the absence of currents under the so-called quasi-electrostatic approximation [4], according to which time derivatives appearing in Maxwell's equations are negligible compared to time derivatives occurring in the equation of motion. Further, for non-magnetizable bodies it is possible to show that $\boldsymbol{h} = \boldsymbol{\chi}_t \times \mathbf{p}$. This is a nonlinear term and hence negligible in the linear theory to be discussed; the restriction $curl\mathbf{h} = \mathbf{0}$ is then effectively reduced to an identity and plays no role in the linear theory.

Appended to this system are the boundary conditions

$$\mathbf{t}_a + \mathbf{T}_M^+\mathbf{n} = \mathbf{T}\mathbf{n}, \quad \mathbf{n}\cdot[\mathbf{d}] = \sigma \quad \text{and} \quad \mathbf{n}\times[\mathbf{e}] = \mathbf{0}, \tag{180}$$

the first applying on a part of the boundary where the applied traction $\mathbf{t}_a$ is specified, where $\mathbf{n}$ is the exterior unit normal to the boundary, σ is the areal density of surface charge on the boundary, and where $[\cdot] = (\cdot)^+ - (\cdot)^-$, with the superscripts $\pm$ referring respectively to limits as the boundary is approached from the exterior and interior of the body.

We require the referential forms of the equations, expressed in terms of differential operators with respect to $\mathbf{x}$. To derive the relevant version of $(178)_2$, we use Stokes' theorem

$$\int_s \mathbf{n}\cdot curl\mathbf{e}da = \int_{\partial s} \mathbf{e}\cdot d\mathbf{y} = \int_{\partial S} \mathbf{e}\cdot\mathbf{F}d\mathbf{x} = \int_{\partial S} \mathbf{E}\cdot d\mathbf{x} = \int_S \mathbf{N}\cdot Curl\mathbf{E}dA, \tag{181}$$

where S is an arbitrary material surface with $s = \chi(S,t)$ its image in the current configuration, and *Curl* is the referential curl operator, to conclude that $(178)_2$ is equivalent to

$$Curl\mathbf{E} = \mathbf{0}, \tag{182}$$

which implies that

$$\mathbf{E} = -\,Grad V \tag{183}$$

for some scalar potential V. A slight generalization of the argument delivers the referential version of the jump condition $(180)_3$:

$$\mathbf{N} \times [\mathbf{E}] = \mathbf{0}. \tag{184}$$

In the same way we use the divergence theorem to deduce that, for an arbitrary material subvolume π with $P = \chi(\pi, t)$,

$$\int_P div\mathbf{d}dv = \int_{\partial P} \mathbf{d}\cdot\mathbf{n}da = \int_{\partial\pi} \mathbf{d}\cdot\mathbf{F}^*\mathbf{N}dA$$

$$= \int_{\partial\pi} J\mathbf{F}^{-1}\mathbf{d}\cdot\mathbf{N}dA = \int_\pi Div(J\mathbf{F}^{-1}\mathbf{d})dV, \tag{185}$$

and thus that $(178)_3$ is equivalent to

$$Div\mathbf{D} = 0, \quad \text{where} \quad \mathbf{D} = J\mathbf{F}^{-1}\mathbf{d}. \tag{186}$$

Again the procedure may be generalized to derive the appropriate version of $(180)_2$:

$$\mathbf{N}\cdot[\mathbf{D}] = \Sigma, \tag{187}$$

where $\Sigma = \sigma\,|\mathbf{F}^*\mathbf{N}|$ is the referential surface charge density.

A convenient definition of the referential polarization is

$$\mathbf{\Pi} = J\mathbf{F}^{-1}\mathbf{p}. \tag{188}$$

This yields (cf. (177))

$$\mathbf{\Pi} = -\rho_\kappa \Phi_{\mathbf{E}} \tag{189}$$

and thus (cf. (179))

$$\mathbf{D} = \mathbf{\Pi} + \varepsilon_0 J\mathbf{C}^{-1}\mathbf{E}. \tag{190}$$

Lastly, the referential equation of motion is given precisely by (2) in which $\mathbf{T}$ is now given by (170) or (175). Then,

$$\mathbf{P} = (\boldsymbol{\sigma} + \mathbf{T}_\mathbf{M})\mathbf{F}^* = 2\mathbf{F}W_\mathbf{C} + \mathbf{T}_M\mathbf{F}^*, \tag{191}$$

with

$$\mathbf{T}_M\mathbf{F}^* = \varepsilon_0\mathbf{F}^*[\mathbf{E}\otimes(\mathbf{C}^{-1}\mathbf{E}) - \tfrac{1}{2}e^2\mathbf{I}], \tag{192}$$

and where $W = \rho_\kappa\Phi$ is the strain-energy function.

To linearize the theory we suppose the norms of the electric field and the displacement gradient to be small and use the strain measure defined by (25) to obtain

$$\begin{aligned}\sigma\mathbf{F}^* &= \mathbf{F}\bar{W}_\epsilon \\ &= (\mathbf{I}+\mathbf{H})\{\mathcal{C}[\boldsymbol{\epsilon}]+\boldsymbol{\mathcal{S}}\boldsymbol{E}+\ldots\} \\ &\simeq \mathcal{C}[\mathbf{H}]+\mathbf{SE},\end{aligned} \tag{193}$$

where $\bar{W}$ is the strain energy expressed as a function of $\boldsymbol{\epsilon}$ and $\mathbf{E}$, and $\mathcal{C}$ and $\mathcal{S}$ respectively are the values of $\bar{W}_{\boldsymbol{\epsilon\epsilon}}$ and $\bar{W}_{\boldsymbol{E\epsilon}}$ when the strain and electric field vanish. Here and henceforth, for convenience, we assume that the associated values of stress and polarization vanish. Thus we assume the absence of residual stress and residual polarization. To linear order we also have

$$\mathbf{P} \simeq \boldsymbol{\sigma}\mathbf{F}^*, \tag{194}$$

since the Maxwell stress is quadratic in the electric field.

In the same way we have

$$-\boldsymbol{\Pi} = \bar{W}_{\mathbf{E}} \simeq \mathcal{Q}\mathbf{E}+\mathcal{R}\boldsymbol{\epsilon}, \tag{195}$$

where $\mathcal{Q}$ and $\mathcal{R}$ respectively are the values of $\bar{W}_{\mathbf{EE}}$ and $\bar{W}_{\boldsymbol{\epsilon E}}$ at zero strain and electric field. Combining this with (190) and $J\mathbf{C}^{-1}\mathbf{E} \simeq \mathbf{E}$ we obtain

$$\mathbf{D} \simeq \varepsilon_0\mathbf{E} - \bar{W}_{\mathbf{E}}. \tag{196}$$

In component form, eqs. (5) and (186) are given, to linear order, by

$$\rho_\kappa u_{itt} = \mathcal{C}_{ijkl}u_{k,jl} + \mathcal{S}_{ijk}E_{k,j} \tag{197}$$

and

$$[(\varepsilon_0\delta_{ij} - Q_{ij})E_j]_{,i} = \mathcal{S}_{ijk}u_{j,ki}, \tag{198}$$

where

$$\mathcal{S}_{ijk} = \partial^2\bar{W}/\partial E_k\partial\epsilon_{ij}, \tag{199}$$

u_i are the displacement components, $E_i = -V_{,i}$ and commas followed by subscripts are used to denote partial derivatives with respect to the initial Cartesian coordinates x_i.

Relevant to our analysis of thin-film substrate problems are restrictions on the various moduli ensuring the existence of propagating plane harmonic waves. To explore this we consider plane harmonic bulk waves of the form

$$u_i = a_i\exp[i(\mathbf{k}\cdot\mathbf{x}-\omega t)], \quad V = v\exp[i(\mathbf{k}\cdot\mathbf{x}-\omega t)], \tag{200}$$

where a_i are the (constant) components of the displacement polarization, v is a constant, ω is the frequency and $\mathbf{k}$ is the wave vector. The direction of propagation is $\mathbf{n}$ and $\mathbf{k} = k\mathbf{n}$, where k is the wave number; the wavespeed c is then given by $\omega = kc$. Substitution into (197) and (198) furnishes the algebraic system

$$-\rho_\kappa \omega^2 u_i = -\mathcal{C}_{ijkl} k_j k_l u_k + \mathcal{S}_{ijk} k_j k_k V \quad \text{and} \quad \mathcal{S}_{ijk} k_i k_k u_j + \eta_{ij} k_i k_j V = 0, \tag{201}$$

where

$$\eta_{ij} = \varepsilon_0 \delta_{ij} - Q_{ij}. \tag{202}$$

We assume that $\boldsymbol{\eta}$ is non-singular so that $\mathbf{k} \cdot \boldsymbol{\eta}\mathbf{k} \neq 0$ for any non-zero $\mathbf{k}$. Then,

$$V = -(\mathbf{k} \cdot \boldsymbol{\eta}\mathbf{k})^{-1} \mathcal{S}_{ijk} k_j k_k u_j \tag{203}$$

and

$$\rho_\kappa c^2 u_i = [A_{ij} + (\mathbf{k} \cdot \boldsymbol{\eta}\mathbf{k})^{-1} \Gamma_i \Gamma_j] u_j, \tag{204}$$

where

$$A_{ij} = \mathcal{C}_{ijkl} n_k n_l \quad \text{and} \quad \Gamma_i = \mathcal{S}_{ijk} n_j n_k. \tag{205}$$

Accordingly, *sufficient* conditions for propagation are the positivity of the tensors $\mathbf{A}$ and $\boldsymbol{\eta}$ [2], the former generalizing the classical propagation condition of conventional elasticity theory.

7 Thin-film model

Suppose the film is coated with a very thin layer of perfectly conducting electrode material carrying a charge density Σ. We assume that the substrate to which the film is attached is also a perfect conductor. Then the electric and polarization fields exterior to the film vanish. The jump conditions $(180)_{2,3}$, applied at the interfaces between the film and the electrode and substrate, then yield

$$\mathbf{n} \cdot \mathbf{d}^{(i)} = -\sigma \quad \text{and} \quad \mathbf{n} \times \mathbf{e}^{(i)} = \mathbf{0}, \tag{206}$$

where the superscript (i) refers to the limit as the interface is approached from the interior of the film. The associated referential forms are

$$\mathbf{N} \cdot \mathbf{D}^{(i)} = -\Sigma \quad \text{and} \quad \mathbf{N} \times \mathbf{E}^{(i)} = \mathbf{0}. \tag{207}$$

To make the first of these explicit we write $\mathbf{N} \cdot \mathbf{D}^+ = -\Sigma^+$ and $\mathbf{N} \cdot \mathbf{D}_0 = -\Sigma_0$, these being respectively equal to the surface charges at the electrode/film interface and the film/substrate interface where $\mathbf{N} = \pm\mathbf{k}$.

The weak form of the equation of motion in the film material is given by (38), but with the stress $\mathbf{P}$ now given by (194). The weak form of (186) is given by

$$\int_\pi \mathbf{D}\cdot Grad\dot{V}dV = \int_{\partial\pi}\mathbf{D}\cdot\mathbf{N}\dot{V}dA, \tag{208}$$

in which $\dot{V}$ is the variation of the electric potential and the integrand on the right-hand side is the limit from the interior of the film.

Proceeding as in (47) we decompose the electric displacement into a part in the interfacial plane and a part orthogonal to it, i.e.

$$\mathbf{D} = \mathbf{1D} + D\mathbf{k}, \quad \text{with} \quad D = \mathbf{k}\cdot\mathbf{D}. \tag{209}$$

Thus,

$$\int_{\partial\pi}\mathbf{D}\cdot\mathbf{N}\dot{V}dA = \int_{\partial\omega}(\int_0^h \mathbf{1D}\cdot\boldsymbol{\nu}\dot{V}d\varsigma)dS + \int_{\omega^+} D^+\dot{V}^+dA - \int_\omega D_0\dot{V}_0dA, \tag{210}$$

where $\omega\subset\Omega$ is an arbitrary part of the film/substrate interface Ω and ω^+ is its projection onto the electrode/film interface. Using $(207)_1$ and the estimate (44) we derive

$$\int_{\partial\pi}\mathbf{D}\cdot\mathbf{N}\dot{V}dA = h\int_{\partial\omega}\mathbf{1D}_0\cdot\boldsymbol{\nu}\dot{V}_0dS - \int_{\omega^+}\Sigma^+\dot{V}^+dA - \int_\omega\Sigma_0\dot{V}_0dA + o(h). \tag{211}$$

This is further reduced, using

$$V^+ = V_0 + hV_0' + o(h), \tag{212}$$

to obtain

$$\int_{\partial\pi}\mathbf{D}\cdot\mathbf{N}\dot{V}dA = -\int_\omega(\Sigma_0+\Sigma^+)\dot{V}_0dA + h\int_{\partial\omega}\mathbf{1D}_0\cdot\boldsymbol{\nu}\dot{V}_0dS - h\int_\omega\Sigma^+\dot{V}_0'dA + o(h). \tag{213}$$

In the same way,

$$\int_\pi\mathbf{D}\cdot Grad\dot{V}dV = h\int_\omega(\mathbf{1D}_0\cdot\nabla\dot{V}_0 + D_0\dot{V}_0')dA + o(h), \tag{214}$$

having used the decomposition

$$Grad\dot{V} = \nabla\dot{V} + \dot{V}'\mathbf{k}, \tag{215}$$

and the balance law (208) yields

$$-\int_\omega(\Sigma_0+\Sigma^+)\dot{V}_0dA + h(\int_{\partial\omega}\mathbf{1D}_0\cdot\nu\dot{V}_0dS - \int_\omega\Sigma^+\dot{V}_0'dA)$$

$$= h \int_\omega (\mathbf{1D}_0 \cdot \nabla \dot{V}_0 + D_0 \dot{V}_0') dA + o(h). \tag{216}$$

We have implicitly imposed (182) and $(207)_2$ as constraints, the latter in the form $\mathbf{k} \times \mathbf{E}^{(i)} = \mathbf{0}$. Thus, $Curl\dot{\mathbf{E}} = \mathbf{0}$ and $\mathbf{k} \times \dot{\mathbf{E}}^{(i)} = \mathbf{0}$, implying that $\dot{\mathbf{E}} = -Grad\dot{V}$ with $\mathbf{k} \times Grad\dot{V}^{(i)} = \mathbf{0}$ at the interfaces. From (215) we then have $\mathbf{k} \times \nabla \dot{V}_0 = \mathbf{0}$ in particular, implying that $\dot{V}_0$ is uniform on Ω. On Ω^+ we have

$$\mathbf{0} = \mathbf{k} \times \nabla \dot{V}^+ = \mathbf{k} \times \nabla \dot{V}_0 + h\mathbf{k} \times \nabla \dot{V}_0' + o(h), \tag{217}$$

yielding

$$\nabla \dot{V}_0' = h^{-1} o(h) \tag{218}$$

and hence

$$-\dot{V}_0 \int_\omega (\Sigma_0 + \Sigma^+) dA + h\dot{V}_0 \int_{\partial\omega} \mathbf{1D}_0 \cdot \nu dS - h\dot{V}_0' \int_\omega (D_0 + \Sigma^+) dA + o(h) = 0. \tag{219}$$

Because $\dot{V}_0$ and ω are arbitrary it follows that $\Sigma_0 + \Sigma^+ = O(h)$. At leading order we have

$$\Sigma^+ = -\Sigma_0, \tag{220}$$

leaving

$$\dot{V}_0 \int_{\partial\omega} \mathbf{1D}_0 \cdot \boldsymbol{\nu} dS - \dot{V}_0' \int_\omega (D_0 + \Sigma^+) dA + h^{-1} o(h) = 0. \tag{221}$$

Passing to the limit and invoking the arbitrariness and independence of $\dot{V}_0$ and $\dot{V}_0'$ results in

$$\int_\omega div(\mathbf{1D}_0) dA = 0 \quad \text{and} \quad \int_\omega (D_0 - \Sigma_0) dA = 0, \tag{222}$$

and the arbitrariness of ω finally yields

$$div(\mathbf{1D}_0) = 0 \quad \text{and} \quad D_0 = \Sigma_0, \tag{223}$$

pointwise on Ω.

Under the stated conditions the Maxwell stress exterior to the film vanishes. The traction boundary condition $(180)_1$ is then identical in form to (4), after making the appropriate adjustment in the definition of the stress. The procedure used in Section 3 to derive the equation of motion for the film/substrate interface carries over unchanged and culminates in (55) in the case when the upper surface of the film is traction free.

8 Linear theory for cubic symmetry: Love modes and extinguished waves

In the linear approximation the constitutive equations are

$$\mathbf{P} = \bar{W}_{\boldsymbol{\epsilon}} \quad \text{and} \quad \mathbf{D} = \varepsilon_0 \mathbf{E} - \bar{W}_{\mathbf{E}}, \tag{224}$$

and to make these explicit we require an expression for $\bar{W}(\boldsymbol{\epsilon}, \mathbf{E})$ that is homogeneous of degree two.

Here we consider various subclasses of cubic symmetry. For example, the strain-energy function pertaining to the *hextetrahedral* subgroup is [10]

$$\begin{aligned} \bar{W}(\boldsymbol{\epsilon}, \boldsymbol{E}) \;=\; & \tfrac{1}{2}[C_1(\epsilon_{11}+\epsilon_{22}+\epsilon_{33})^2 + C_2(\bar{\epsilon}_{11}^2+\bar{\epsilon}_{22}^2+\bar{\epsilon}_{33}^2)] + C_3(\epsilon_{12}^2+\epsilon_{13}^2+\epsilon_{23}^2) \\ & + \tfrac{1}{2}D_1(E_1^2+E_2^2+E_3^2) + 2D_2(E_1\epsilon_{23}+E_2\epsilon_{13}+E_3\epsilon_{12}), \end{aligned} \tag{225}$$

where $C_{1,2,3}$ and $D_{1,2}$ are material parameters and we impose inequalities (149) to ensure that a sufficient condition for propagation, discussed in Section 6, is satisfied. The associated stress is

$$\begin{aligned} \mathbf{P} \;=\; & C_1(tr\boldsymbol{\epsilon})\boldsymbol{I} + C_2(\bar{\epsilon}_{11}\mathbf{e}_1\otimes\mathbf{e}_1 + \bar{\epsilon}_{22}\mathbf{e}_2\otimes\mathbf{e}_2 + \bar{\epsilon}_{33}\mathbf{e}_3\otimes\mathbf{e}_3) \\ & + (C_3\epsilon_{12}+D_1E_3)(\mathbf{e}_1\otimes\mathbf{e}_2+\mathbf{e}_2\otimes\mathbf{e}_1) + (C_3\epsilon_{13}+D_1E_2)(\mathbf{e}_1\otimes\mathbf{e}_3+\mathbf{e}_3\otimes\mathbf{e}_1) \\ & + (C_3\epsilon_{23}+D_1E_1)(\mathbf{e}_2\otimes\mathbf{e}_3+\mathbf{e}_3\otimes\mathbf{e}_2), \end{aligned} \tag{226}$$

and the electric displacement is

$$\mathbf{D} = (\varepsilon_0 - D_1)\mathbf{E} - 2D_2(\epsilon_{23}\mathbf{e}_1 + \epsilon_{13}\mathbf{e}_2 + \epsilon_{12}\mathbf{e}_3). \tag{227}$$

Equation $(223)_2$ then furnishes the restriction $\Sigma_0 = (\varepsilon_0 - D_1)E_3 - 2D_2\epsilon_{12}$, implying that $E_3 (= -V_0')$ satisfies

$$(\varepsilon_0 - D_1)E_3 = \Sigma_0 + 2D_2\epsilon_{12}, \tag{228}$$

whereas the restriction $(55)_1$ on the film stress at the film/substrate interface reduces to

$$\mathbf{0} = \mathbf{P}_0\mathbf{k} = [C_1(tr\boldsymbol{\epsilon}) + C_2\bar{\epsilon}_{33}]\mathbf{k} + (C_3\epsilon_{13}+D_1E_2)\mathbf{e}_1 + (C_3\epsilon_{23}+D_1E_1)\mathbf{e}_2, \tag{229}$$

yielding

$$\epsilon_{13} = -(D_1/C_3)E_2 \quad \text{and} \quad \epsilon_{23} = -(D_1/C_3)E_1. \tag{230}$$

Recalling that $\mathbf{1E} = -\nabla V_0$ at the interface, and hence that $E_\alpha = -V_{0,\alpha} = 0$, we conclude that $\epsilon_{3\alpha} = 0$ in the film at the interface, as in the purely elastic theory. Further, E_3 is uniform at the interfacial plane because $\nabla V_0'$ vanishes. Thus, if the assigned surface charge Σ_0 is uniform,

and if $D_2 \neq 0$, then (228) implies that ϵ_{12} *is uniform on* Ω. This situation pertains not only to the hextetrahedral subgroup of the cubic symmetry group, but also to the *tetardoidal* and *gyroidal* subgroups [10]. In contrast, $D_2 = 0$ in higher-symmetry materials characterized by the *hexoctahedral* and *diploidal* subgroups, and so for these there is no requirement that ϵ_{12} be uniform.

Proceeding, we have

$$\mathbf{1D}_0 = (\varepsilon_0 - D_1)\mathbf{1E} - 2D_2(\epsilon_{23}\mathbf{e}_1 + \epsilon_{13}\mathbf{e}_2), \tag{231}$$

which vanishes identically, ensuring that $(223)_1$ is automatically satisfied. The equation of motion for the film/substrate interface is

$$\boldsymbol{\sigma}_0\mathbf{k} = h[div(\mathbf{P}_0\mathbf{1}) - \rho_\kappa \mathbf{u}_{0tt}] \tag{232}$$

in which $\boldsymbol{\sigma}$ is the stress in the substrate, assumed to be an isotropic, non-polarizable elastic solid, and

$$\mathbf{P}_0\mathbf{1} = C_1(tr\boldsymbol{\epsilon})\mathbf{1} + C_2(\bar{\epsilon}_{11}\mathbf{e}_1\otimes\mathbf{e}_1 + \bar{\epsilon}_{22}\mathbf{e}_2\otimes\mathbf{e}_2) + (C_3\epsilon_{12} + D_1E_3)(\mathbf{e}_1\otimes\mathbf{e}_2 + \mathbf{e}_2\otimes\mathbf{e}_1). \tag{233}$$

Our results yield

$$div\{E_3(\mathbf{e}_1 \otimes \mathbf{e}_2 + \mathbf{e}_2 \otimes \mathbf{e}_1)\} = \mathbf{0}, \tag{234}$$

implying that (232) reduces to the purely elastic problem treated in Section 5. Accordingly a *uniform* surface charge on a polarizable cubic crystal film has no effect on propagating waves.

However, we have seen that $\nabla\epsilon_{12} = \mathbf{0}$ on Ω if the film properties are such that $D_2 \neq 0$. For Love waves, the in-plane displacement gradient is (cf. $(105)_1$) $\nabla\mathbf{v} = ikG\boldsymbol{\delta} \otimes \mathbf{n}$, with $\boldsymbol{\delta} \cdot \boldsymbol{n} = 0$. Writing $\mathbf{n} = \cos\theta\mathbf{e}_1 + \sin\theta\mathbf{e}_2$ and $\boldsymbol{\delta} = -\sin\theta\mathbf{e}_1 + \cos\theta\mathbf{e}_2$, we use this to derive

$$2\nabla\epsilon_{12} = -k^2G(\cos^2\theta - \sin^2\theta)\mathbf{n} \tag{235}$$

and thus conclude that $\cos^2\theta = \sin^2\theta$, yielding $\theta = \pm 45°$. This implies that waves propagating along the crystallographic axes are extinguished by the application of a uniform surface charge in polarizable cubic films belonging to the hextetrahedral, tetardoidal or gyroidal subclasses. We know of no experimental corroboration of this remarkable and potentially useful prediction.

Bibliography

[1] S. S. Antman, *Nonlinear Problems of Elasticity*. Springer, Berlin, 2005.

[2] E. Baesu, D. Fortune and E. Soós, *Incremental behaviour of hyperelastic dielectrics and piezoelectric crystals.* ZAMP, **5**4 160-178, 2003.

[3] P. G. Ciarlet, *Mathematical Elasticity, Vol. 1: Three-Dimensional Elasticity.* North-Holland, Amsterdam, 1988.

[4] A. C. Eringen and G. A. Maugin, *Electrodynamics of Continua, Vol. 1.* Springer, N.Y., 1990.

[5] A. E. Green and W. Zerna, *Theoretical Elasticity, 2nd edn.* Oxford University Press, 1968.

[6] Y. B Fu, *Linear and nonlinear wave propagation in coated or uncoated elastic half spaces. Waves in Nonlinear Pre-Stressed Materials* (M. Destrade & G. Saccomandi, Eds). *CISM Courses and Lecture Notes.* Springer, Wien, 2007.

[7] A. Kovetz, *Electromagnetic Theory.* Oxford University Press, 2000.

[8] J. Merodio and R.W. Ogden, *A note on strong ellipticity for transversely isotropic linearly elastic solids.* Q. Jl. Mech. Appl. Math. 56, 589-591, 2003.

[9] R. W. Ogden, *Non-linear Elastic Deformations.* Dover, N.Y., 1997.

[10] G. F. Smith, M. M. Smith and R. S. Rivlin, *Integrity bases for a symmetric tensor and a vector: The crystal classes.* Arch. Ration. Mech. Anal. **1**2, 93-133, 1963.

[11] A. J. M. Spencer, *Constitutive theory for strongly anisotropic solids*, in: *Continuum Theory of the Mechanics of Fibre-Reinforced Composites* (A.J.M. Spencer, Ed.). *CISM Courses and Lectures* No. 282, pp. 1-32. Springer, Wien, 1984.

[12] D. J. Steigmann and R. W. Ogden, *Surface waves supported by thin-film/substrate interactions.* IMA J. Appl. Math., 72, 730-747, 2007.

[13] D. J. Steigmann, *Linear theory for the bending and extension of a thin, residually stressed, fiber-reinforced lamina.* Int. J. Engng. Sci. , 47, 1367-1378, 2009a.

[14] D. J. Steigmann, *On the formulation of balance laws for electromagnetic continua.* Math. Mech. Solids, 14 390-402, 2009b.

[15] D. J. Steigmann, *Elastic waves interacting with a thin, pre-stressed, fiber-reinforced surface film.* Int. J. Engng. Sci., 48, 1604-1609, 2010.